

IMAGING AGENTS FOR MULTIMODAL *IN VIVO* IMMUNE CELL TRACKING

by

LINDSEY VAN GEMEREN

A thesis submitted to
The University of Birmingham
for the degree of
DOCTOR OF PHILOSOPHY

School of Chemistry
College of Engineering and Physical Sciences
The University of Birmingham
March 2016

**UNIVERSITY OF
BIRMINGHAM**

University of Birmingham Research Archive

e-theses repository

This unpublished thesis/dissertation is copyright of the author and/or third parties. The intellectual property rights of the author or third parties in respect of this work are as defined by The Copyright Designs and Patents Act 1988 or as modified by any successor legislation.

Any use made of information contained in this thesis/dissertation must be in accordance with that legislation and must be properly acknowledged. Further distribution or reproduction in any format is prohibited without the permission of the copyright holder.

Abstract

The aim of this work was to develop tri-modal cell labels for tracking immune cells *in vivo*, particularly for longitudinal studies of immune cell therapies. Localisation and quantification of the cells is invaluable in determining the effectiveness of these treatments, so imaging agents for fluorescence, ^1H MRI and ^{19}F MRI were combined.

Four combinations of agents in a robust scaffold were investigated: luminescent dyes and a ^1H MRI contrast agent were trapped electrostatically in a silica matrix; luminescent dyes and proton MRI agents were bound to silica and gold nanoparticle surfaces; a fluorinated fluorescent dye was investigated briefly; and all three modalities' agents were combined by filling and functionalising a silica shell. All of these combinations were characterised and imaged using a clinical 3T MRI scanner.

Lead compounds from each section were incubated with white blood cells, examining uptake in monocytes and lymphocytes, with preliminary observations of viability. Detection of labelled cells by their luminescence and MRI contrast enhancement was possible in some cases, though ^{19}F MRI still poses some challenges.

Detection limits by ^{19}F MRI were determined for a range of fluorinated compounds, elucidating the possibilities of translating ^{19}F MRI into the clinic with current technology.

ACKNOWLEDGEMENTS

I would like to thank all my supervisors for their advice and support: Professor M. J. Hannon; Professor Z. Pikramenou; Dr. N. P. Davies; Dr. J. P. Dicks; Professor D. H. Adams; Dr. S. M. Curbishley.

To Mike and Zoe, thank you for your advice and support on chemistry and nanotechnology aspects, and to Mike for your feedback on this thesis. To Nigel and James, thank you for your help and training in using the scanner and advice on MRI. To Stuart, thank you for your patient help and advice in the cell work, flow cytometry and microscopy.

Thanks also to Ela Claridge for her support and advice on computational aspects of this work.

I would like to thank Dr. N. J. Rogers for our joint work on the gold nanoparticles and providing the IrBpySAC, and Dr. D. J. Lewis for his advice and help on the silica nanoparticles and providing the GdQSH. Also thanks to S. Adams for providing the ruthenium tris-phenanthroline and for carrying out all the luminescence lifetime measurements.

Many thanks also to Dr. R. Williams for facilitating use of the furnace for calcination, and for carrying out the nanoparticle density measurements. Thanks also to Professor L. M. Grover for use of his furnace.

I would also like to thank Paul Stanley and Theresa Morris from the Centre for Electron Microscopy for their training and advice in TEM and SEM, and the preparation of the cell samples for TEM.

Thanks to Eva Valsami-Jones from the School of Earth Sciences for generously allowing use of her Zetasizer. Thanks also to the Analytical Facilities in the School of Chemistry for mass spectrometry measurements.

Thanks to Michael Clancy and Siobhan King for their contributions to this work through their PSIBS mini-projects.

On a more personal note, thanks to the other PSIBS 4th years. Special thanks to Joscelyn Sarsby for her support and for keeping me going. Thanks also to Stephen Cardinal for looking after me through the less-good times and for proof reading this!

Finally I would like to thank the EPSRC for funding through the PSIBS DTC and the University of Birmingham for the chance to carry out this work.

CONTENTS

Acronyms	ix
1 Introduction	1
1.1 Project background summary	1
1.2 Immune cell therapies	4
1.2.1 Stem cell therapies	5
1.2.2 Dendritic cell vaccines	6
1.2.3 T cell therapies	11
1.2.4 Current trends in immune cell therapies	13
1.2.5 Clinical need for new cell tracking agents	14
1.2.6 Summary	21
1.3 Imaging techniques	22
1.3.1 Luminescence imaging	22
1.3.2 Magnetic resonance imaging	23
1.4 Imaging agents	26
1.4.1 Luminescent probes	27
1.4.2 ^1H MRI contrast agents	30
1.4.3 ^{19}F MRI tracers	32
1.4.4 Multimodality	34
1.5 Nanotechnology	35
1.5.1 Silica nanoparticles	35
1.5.2 Gold nanoparticles	37

1.6	Multimodal molecules	38
1.6.1	Fluorinated fluorescent dyes	38
1.7	Project design and aims	40
1.7.1	System design: imaging agent requirements	41
1.7.2	System design: delivery vehicle requirements	42
1.7.3	Project aims: MR imaging capabilities investigation	42
1.7.4	Project aims: imaging agent development	43
1.7.5	Project aims: Cellular interactions investigations	43
2	General Experimental Details and Imaging Capabilities	45
2.1	Materials	45
2.1.1	Common reagents and solvents	45
2.1.2	Imaging agents	45
2.1.3	Other equipment	46
2.2	Instrumental details and methods	46
2.2.1	Preparation and analysis of samples by DLS	46
2.2.2	Preparation and analysis of samples by TEM	47
2.2.3	Density analysis of nanoparticles	47
2.2.4	Preparation of samples for ICP-MS analysis	47
2.2.5	Preparation and analysis for luminescence measurements	48
2.2.6	Preparation and analysis for UV-visible spectroscopy	48
2.2.7	NMR characterisation	49
2.2.8	MR imaging	49
2.3	Cell preparation and analysis	50
2.3.1	Peripheral blood mononuclear cell isolation and treatment	50
2.3.2	Cell analysis by flow cytometry	50
2.3.3	PBMC analysis by light microscopy	51
2.3.4	Cell analysis by TEM	52
2.3.5	Cell analysis by MRI	52

2.4	^1H MR capabilities	53
2.4.1	Imaging with the birdcage coil	53
2.4.2	^1H imaging with the ^{19}F coil	55
2.5	^{19}F MR capabilities	56
2.5.1	Fluorine imaging background	56
2.5.2	Coil capabilities	57
2.6	Detection limits of various molecules by ^{19}F MRI at 3 T	60
2.6.1	Molecules with 3 equivalent fluorines	60
2.6.2	Molecules with 6 equivalent fluorines	61
2.6.3	Molecules with 9 equivalent fluorines	62
2.6.4	Molecules with 24 equivalent fluorines	64
2.6.5	Discussion	65
3	Trapping Imaging Agents in a Nanoparticle Matrix	67
3.1	Background and design	67
3.2	Experimental details	69
3.2.1	Materials	69
3.2.2	Nanoparticle synthesis	70
3.2.3	Nanoparticle characterisation	72
3.3	Synthesis and characterisation results	73
3.3.1	Negatively charged silica nanoparticles	73
3.3.2	Primary aminated silica nanoparticles	77
3.3.3	Quaternary aminated nanoparticles	88
3.4	Cell treatment results	93
3.4.1	Flow cytometry results	93
3.4.2	Microscopy	98
3.4.3	MR imaging	100
3.5	Conclusions	102

4 Binding Imaging Agents to a Nanoparticle Surface	104
4.1 Background and introduction	104
4.1.1 Gold nanoparticles	104
4.1.2 Silica nanoparticles	105
4.1.3 Other nanoparticles	106
4.1.4 Project plan	107
4.2 Experimental details	110
4.2.1 Materials	110
4.2.2 APTES-DTPA conjugation	110
4.2.3 Nanoparticle syntheses	111
4.3 Synthesis and characterisation results	112
4.3.1 Silica nanoparticles	113
4.3.2 Gold nanoparticles	119
4.4 Cell treatment results	128
4.4.1 Silica nanoparticles	128
4.4.2 Gold nanoparticles	137
4.5 Summary and conclusions	143
4.5.1 Silica nanoparticles	143
4.5.2 Gold nanoparticles	144
4.5.3 Cell treatments	145
5 Multiple Imaging Agent Capabilities in Molecular Structures	146
5.1 Background and introduction	146
5.2 Characterisation results	148
5.2.1 Luminescence	148
5.2.2 MRI signal	149
5.3 Cell treatment results	150
5.3.1 Flow cytometry	150
5.3.2 Fluorescence microscopy	154

5.3.3	MRI detection	155
5.4	Conclusions	155
6	Trapping Imaging Agents in a Nanoparticle Core	157
6.1	Introduction	157
6.2	Overview and system design	158
6.3	Experimental details	163
6.3.1	Materials	163
6.3.2	Hollow silica nanoparticle syntheses	164
6.3.3	Hollow nanoparticle characterisation	167
6.4	Synthesis and characterisation results	168
6.4.1	Hollow particle synthesis by dissolution-regrowth	169
6.4.2	Hollow particle synthesis by latex templating	172
6.4.3	Hollow particle synthesis by selective etching	180
6.5	Conclusions	201
7	Image Analysis Methods	203
7.1	Automated particle sizing from TEM images	203
7.1.1	Background and overview	204
7.1.2	Algorithm I: Rapid circle detection (RCD)	205
7.1.3	Algorithm 2: Compass gradients edge detection (CGED)	211
7.1.4	Combined algorithms: StarRCD	215
7.2	Automated relaxation time calculation from MR images	225
7.2.1	Background and overview	225
7.2.2	Algorithm	226
7.2.3	Discussion	228
7.3	Conclusions	229
8	Conclusions and Further Work	230
8.1	Trapping imaging agents in a nanoparticle matrix	231

8.2	Binding imaging agents to a nanoparticle surface	233
8.3	Multimodal imaging agent molecules	234
8.4	Trapping imaging agents in nanoparticle cores	235
8.5	Image analysis	237
8.5.1	Electron microscopy image analysis	237
8.5.2	MRI image analysis	238
8.6	Future directions	238
	Appendices	240
	A Flow cytometry of IrGdAuNPs in PBMCs	241
	B Characterisation data for synthesised molecules	243
B.1	Diethylenetriamine tetraacetic acid 3-amidopropyl triethoxysilane	244
B.1.1	NMR	244
B.1.2	ESI-MS	245
B.1.3	FT-IR	245
	List of References	246

ACRONYMS

C₁₈TMS Octadecyltrimethoxysilane.

Me₃APTMS trimethyl[3-(trimethoxysilyl)propyl]ammonium chloride.

Me₃ASiNPs quaternary aminated silica nanoparticles.

AFC 7-amino-4-trifluoromethyl coumarin.

APTES 3-aminopropyl triethoxysilane.

AuNPs gold nanoparticles.

CEST chemical exchange saturation transfer.

CGED compass gradients edge detection.

DCs dendritic cells.

DLS dynamic light scattering.

EMA European Medicines Agency.

ESI-MS electrospray ionisation mass spectrometry.

FDA Food and Drug Administration.

FITC fluorescein isothiocyanate.

FT-IR Fourier transform infrared spectroscopy.

HFC 7-hydroxy-4-trifluoromethyl coumarin.

HPCs haematopoietic progenitor cells.

HSCs haematopoietic stem cells.

HSiNPs hollow silica nanoparticles.

ICP-MS inductively coupled plasma mass spectrometry.

MRI magnetic resonance imaging.

NMR nuclear magnetic resonance spectroscopy.

PBMCs peripheral blood mononuclear cells.

PBS phosphate buffered saline.

PET positron emission tomography.

PFC perfluorocarbon.

PFCE perfluoro-15-crown-5-ether.

PFOB perfluorooctyl bromide.

RCD rapid circle detection.

ROIs regions of interest.

RuGdSiNPs gadolinium-functionalises RuSiNPs.

RuSiNPs ruthenium tris-phenanthroline-doped silica nanoparticles.

SiNPs silica nanoparticles.

SNR signal to noise ratio.

SPECT single photon emission computed tomography.

SPIOs superparamagnetic iron oxide nanoparticles.

TEOS tetraethyl orthosilicate.

TMOS tetramethyl orthosilicate.

UTE ultrashort echo time.

CHAPTER 1

INTRODUCTION

This thesis explores multimodal imaging agents for the *in vivo* tracking of immune cell therapies. Imaging agents for multinuclear MRI and fluorescence techniques have been designed and used to treat immune cells in this work. The theory and background behind the project is described in this chapter.

1.1 Project background summary

Cellular therapies are a relatively recent field in healthcare. Under normal conditions the innate functionality and capabilities of cells are effective at restoring the body. When these natural processes become ineffective, cellular therapies use cultured and possibly modified cells to correct them. Examples range from stem cell therapies for the regeneration of tissue, such as heart tissues after myocardial infarction [1] to immune cell therapies, such as dendritic cell vaccines for cancers [2] or autoimmune diseases [3]. This work focuses on immune cell therapies, but the principles are similar for other forms.

The modification of cells for these therapies often occurs *in vitro*, before they are administered to the patient. Once they have been administered however there is no label-free way of distinguishing them from the rest of the cells in the body *in situ*, so evaluation of the treatment has previously been based on outcomes, such as in some early trials [4, 5], or through antigen challenge or cytokine testing [6]. If the cells are labelled such that they

can be tracked through the body however, then information about the cells themselves can be included in the evaluation. For example, the location of the cells will inform as to whether they reach and remain in crucial sites such as the lymph nodes.

In this project, the aim is to develop labels that will simultaneously allow the location and quantification of the cells. The principles used here are transferable to functional information, so similar work could be developed for observing the longevity or effectiveness of therapeutic cells, which would show whether they have enough time and capability to produce the observed outcomes.

The preferred label would depend on the technique being used to track the cells. Non-invasive imaging techniques are ideal for this; they do not involve surgery, or risk the removal of any of the therapeutic cells, and they are relatively unobtrusive for the patient.

Currently nuclear imaging techniques are the ‘gold standard’ for tracking cells, for which radiotracers are taken up by the cells and imaged *in vivo* by single photon emission computed tomography (SPECT) or positron emission tomography (PET). The radiotracer lifetime will however limit the length of the tracking study, so in this project the aim is to create an alternative label whose detectability will not decay.

Magnetic resonance imaging (MRI) is increasingly of interest too [7], and has been used here since it is a widely clinically available alternative to nuclear imaging. The isotopes used are stable, and so the signal decay will depend mainly on the cellular concentration and retention of the label.

At present no single MRI technique will provide effective information on both the location and number of cells at a given site. Data from multiple modes of MRI could however be combined to do this; ^1H MRI can provide localization information, as discussed in Section 1.3.2, while ^{19}F MRI can provide quantification, also discussed in Section 1.3.2. Multinuclear MRI is therefore an invaluable combination to be added to clinical capabilities. This project investigates the possibilities of using these two techniques with one label for immune cell tracking, with a long-term view of its effectiveness in the clinic.

These methods however only provide information on the tissue level. Observing the location of tracers within the cells is also necessary in order to examine the interaction of the label with the cells. More sensitive techniques than MRI are needed for this, so the incorporation of a fluorescent tag is also highly beneficial. This will allow the use of fluorescence microscopies, as well as flow cytometry, which can provide bulk rather than microscopic information on the label uptake and retention.

One essential component for clinical translatability is the robustness of the proposed system. For a dual modal imaging agent to be accepted, the results by both modalities must be reliable. Incorporating the imaging agents into one vehicle is a logical step that will ensure that the two agents are delivered and retained at the same rates.

Nanotechnology, as discussed in Section 1.5 provides a means for this, in that the imaging agents can be built or added into a structure on the scale of tens or hundreds of nanometres. There has been much research into the interaction of nano-sized materials with cells [8, 9, 10], so this can be drawn on in the design of vehicles for imaging agents. Chemistry also provides some answers to this problem. The different agents could be components of one molecule, covalently combined into one robust structure, as discussed in Section 1.6.

In this project therefore, the incorporation of proton and fluorine MRI agents and fluorescent tags into nanoparticles was investigated. Three methods of trapping these agents in nanostructures were considered, as well as the vehicle simply being a molecule.

Immune cells were treated with the lead vehicles from these experiments to observe the uptake and localization within the cells. Of particular interest was whether the labels were taken up to a high enough concentration for MR imaging at realistic cellular concentrations.

Much research into this area has used pre-clinical scanners with high field strengths [11, 12, 13, 14], partly due to MRI being a relatively insensitive technique. Studies which have used lower field strengths have generally used custom-made setups such as small solenoid coils, or small surface coils on small animals [15, 16, 17]. Although these

studies demonstrate that ^{19}F MRI is possible at clinical field strengths, the choice of coil to demonstrate the clinical feasibility is questionable. Considering that the aim of the research is eventual use in humans, the capabilities of a standard clinical MRI scanner, equipped with a large surface coil designed for liver imaging, were explored here.

Automated analysis of the images obtained was implemented in order to produce a reliable and high-throughput method of analysing the TEM and MRI data.

The TEM images required the measurement of particle sizes, which is a lengthy task when carried out manually, and subject to some user bias in terms of edge selection. Automated analysis processes a series of images and combines the measured sizes, thus vastly reducing analysis time and providing a reproducible and reliable method of analysing the images.

The MRI data is a stack of images, though usually these are not arranged in the correct order. The automated method orders them from information in the metadata, then analyses the stacks it creates. After selection of the regions of interest (ROIs), which is semi-automated, the algorithm fits the intensity values to a model equation, which thus determines the relaxation times for each ROI. The relaxation times quantify the contrast enhancement, so allow quantitative comparison between contrast agents.

1.2 Immune cell therapies

Cellular immunotherapies were first developed using stem cells as a way to regenerate particular parts of the body. The immune system, for example, could be reconstituted after destruction by radiation or drug treatment to remove blood cancers [18], or in cases of severe genetic immunodeficiency [19].

Other immune cell therapies have grown from this, with the specific aim of treating diseases by *ex vivo* treatment and readministration of cells. The modification of the cells can be specialised so as to target the disease, such as a tumour, but by using the body's own resources.

Haematopoietic stem cell therapies, dendritic cell vaccines and T cell therapies, discussed below, are based on this principle of using the cells' innate capabilities to intercept and rectify problems in the immune pathway.

1.2.1 Stem cell therapies

Stem cells are a crucial range of cells in the body which are responsible for the regeneration of tissues. They are specialised so as to generate a subset of cell types by division and differentiation, such as haematopoietic stem cells (HSCs), which differentiate into all the various blood and immune cells. Patients who are genetically highly immunodeficient can therefore have their immune cells produced by infused HSCs [19]. Similarly, haematopoietic cancers, including some leukemias and myelomas, are treated by destruction of the patient's immune system, including the cancer, followed by regeneration of a theoretically healthy immune system with HSCs [18, 20].

Only one stem cell therapy has been approved for marketing by the time of writing in the European Union. Holoclar, a treatment of autologous *ex vivo* expanded limbal stem cells for regenerating the cornea in cases of ocular burns, was approved by the European Medicines Agency (EMA) in December 2014.

A range of HSC transplantation therapies have been given orphan designation by the EMA, which allows clinical investigation and later protection on the market to incentivise development for rare conditions. They have not, to date, been given market approval.

In the USA, the Food and Drug Administration (FDA) has approved immunotherapies including products such as Hemacord (New York Blood Center, Inc), and Allocord (SSM Cardinal Glennon Children's Medical Center). These use haematopoietic progenitor cells (HPCs), which can differentiate into the immune cells in a similar way to HSCs, in order to reconstitute the immune system. They are also approved in cases of severe immunodeficiency, either for genetic reasons or after destruction of the immune system, referred to as myeloablation.

After the therapeutic stem cells are administered in these treatments, they must cir-

culate throughout the blood. In mesenchymal stem cell therapies however, a loss of therapeutic cells has been noted as a result of their becoming stuck in the lung and other small capillaries [21]. For HSCs, the cells should localise in bone marrow niches, which regulates their differentiation [22, 23]. Tracking the cells can therefore verify the location of the stem cells [22] and how they differentiate [24].

Labelling of stem cells for tracking is however complicated by their proliferation *in vivo* diluting many of the typical imaging agents. Exceptions to this involve engineering to make the cells express reporter genes, a sequence encoding a fluorophore, such as green fluorescent protein [24, 22] or a lysine-rich protein as a chemical exchange saturation transfer (CEST) agent [25], which are passed on to the progeny. Alternatively, both bioluminescence and SPIO-enhanced MRI have been used in animal models to track neural stem cells [26].

In terms of immunotherapies, HSC transplantation was a revolutionary step in being able to treat blood cancers and restore immune systems. It is however a highly aggressive and risky process, leaving the patient vulnerable to minor infections. More targeted approaches have therefore been explored, as discussed below, which use specific cell populations.

1.2.2 Dendritic cell vaccines

Dendritic cells (DCs) are antigen-presenting cells acting as part of the immune system. In the body they are derived from HSCs, existing initially as immature dendritic cells. They sample their environment for pathogens until they are activated; this involves a process of phagocytosis, processing of possible antigens, and antigen presentation on the cell surface. Once activated the dendritic cells mature and migrate to the lymphoid tissues (the lymph nodes and spleen), where they in turn activate T cells, which continue the chain of immune responses [27].

Immunotherapies have been developed which use the antigen-presenting abilities of DCs to induce an immune response [28, 29]. DCs are however naturally spread around

the body, and circulate in low concentrations, so direct isolation would yield very low cell counts. Monocytes from peripheral blood were found to also derive into DCs with suitable stimulation [30, 31], and are naturally found in much higher counts. Monocyte-derived DCs have consequently been used for generating *ex vivo* vaccines.

In vaccine production, monocytes from a peripheral blood sample are isolated, derived into immature DCs, treated with tumour antigens to activate them and matured in culture. Upon administration to the patient, the cells should migrate to the lymph nodes and spleen, and similarly induce an immune response against a tumour or infection [32, 5, 33]. This process is illustrated in Figure 1.1.

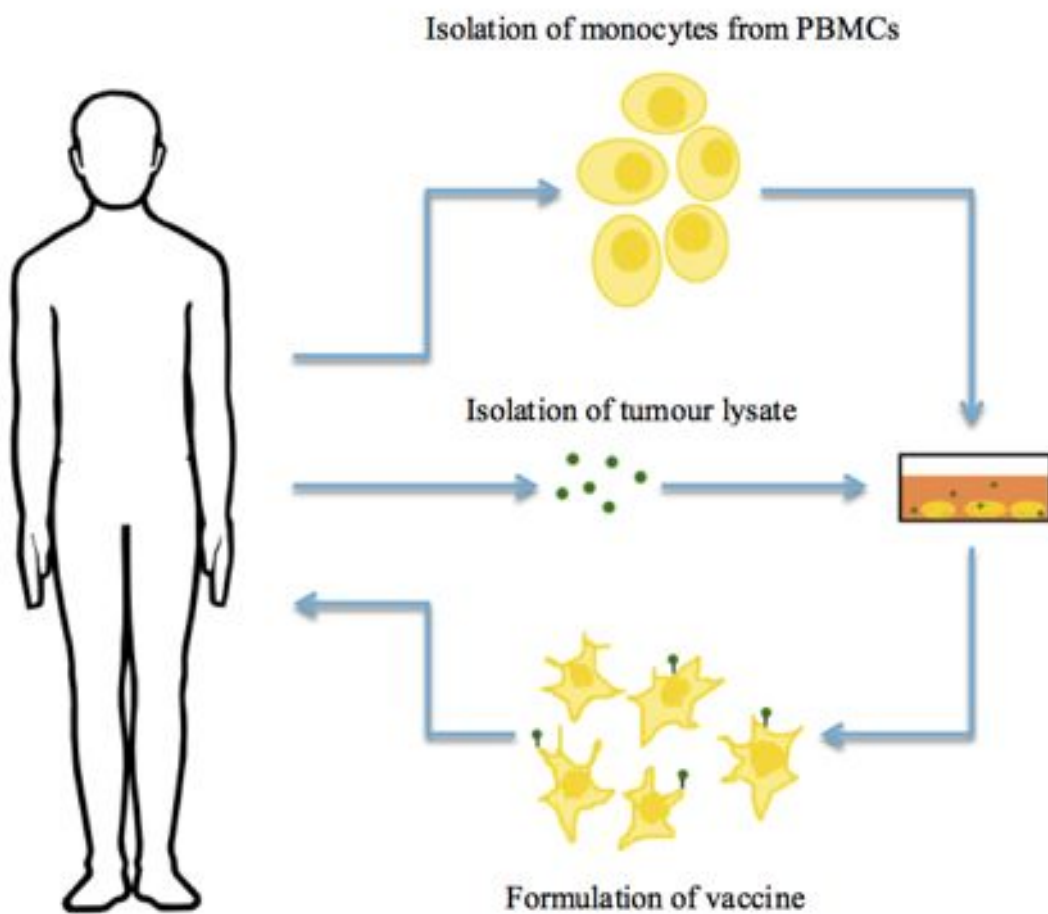


Figure 1.1: Illustration of a simplified workflow for preparing dendritic cell vaccines.

Various forms of this therapy have been developed and moved into clinical use or clinical trials.

A formulation of autologous DCs, sipuleucel T (marketed as Provenge by Dendreon) is licensed for prostate cancer therapy. It is approved for use in the USA by the FDA (BL 125197), and the European Medicines Agency (EMA) (EMEA/H/C/002513). In the UK it is not recommended by the National Institute for Health and Clinical Excellence (NICE) on the basis that it is not more effective than other treatments for the price (ID573). On the contrary, it was approved by Germany's equivalent to NICE, the IQWiG, which noted some added benefits.

Due to difficulties in the manufacturing process however, the company producing Provenge, Dendreon, filed for bankruptcy and was recently taken over by the pharmaceutical company Valeant. This indicates that there are still significant challenges in the development of these processes, but that there is also still commercial motivation to overcome them.

A number of DC vaccine clinical trials are underway in the USA. Some of these trials are referenced in Table 1.1.

Condition	Phase	Trial reference
Glioblastoma	III	NCT00045968
	II	NCT00576537
Renal cell cancer	III	NCT01582672
Melanoma	III	NCT01875653
	II	NCT00197912
Breast cancer	II	NCT00622401
	II	NCT01431196
Soft tissue sarcoma	II	NCT01883518
Early stage HIV-1	II	NCT00402142
	II	NCT00833781
Metastatic colorectal cancer	II	NCT01348256
	II	NCT01413295
	II	NCT00228189
Ovarian cancer	II	NCT00799110

Table 1.1: Examples of dendritic cell vaccines in clinical trials in the USA for a range of diseases. Source: <https://clinicaltrials.gov>.

Similarly in the UK there are a number of trials underway, some being carried out in both the UK and the USA, listed in Table 1.2.

Condition	Phase	Trial reference
Glioblastoma	III	NCT00045968
	II	NCT00576537
Renal cell cancer	III	NCT01582672
Hepatocellular carcinoma	II	ISRCTN11889464
Rheumatoid arthritis	I	NCT01352858

Table 1.2: Examples of dendritic cell vaccines in clinical trials in the UK. Source: <https://clinicaltrials.gov>.

The number of conditions this therapy is undergoing trials for shows its versatility. From cancers of the brain, skin, liver and kidneys, to autoimmune diseases such as rheumatoid arthritis and HIV, the potential of these therapies is wide ranging and revolutionary for healthcare.

The work in this thesis was being carried in connection with the trial for the treatment of hepatocellular carcinoma, and consequently the focus of future tissue and *in vivo* studies would have particular regard to the liver tissues and associated pathways.

Dendritic cell vaccines rely on the cells reaching the lymphoid tissues, which can be assessed by the outcome, such as tumour regression. This however provides no quantifiable information on the therapy's direct effectiveness, so tracking of the DCs *in vivo* by a range of imaging techniques, which are discussed in detail in Section 1.2.5, would demonstrate that a given number of cells at a given site are suitably placed to produce the outcome.

The need for cell tracking has been emphasised by a study using a ^{111}In oxinate as a radiotracer, which showed that after intradermal injection, fewer than 4% of the DCs reached the lymph nodes [34]. Current DC vaccine research is therefore focused on improving the DC migratory capacity, such as by priming the injection site so cytokines

associated with migration are upregulated [35], or by using fresher natural DCs rather than monocyte-derived DCs [36].

It has also been noted that multiple approaches to restoring the immune system may be necessary to boost the clinical efficacy. DC vaccines are therefore now being considered in combination with other immunotherapies [37, 38], as discussed in more detail in Section 1.2.4.

1.2.3 T cell therapies

An alternative point to intercept the immune response is the T cells themselves. T lymphocytes are immune cells that recognise pathogens via the antigens receptors on their surface. They must generally be activated and only recognise the specific antigens they have been primed with. Recognition occurs through simultaneous binding to the T cell receptor and to another, co-stimulatory, receptor.

Some T cell therapies involve modifying the surface receptors, usually by genetic engineering to recognise the target pathogens [39, 40, 41]. The T cell receptor can either be modified alone to improve its affinity, or it can be engineered to be combined with an artificial co-stimulatory receptor to form a chimeric antigen binding site that is specific to its target [42, 40].

No T cell therapies have currently been approved to the author's knowledge at the time of writing, but many clinical trials are underway. Some of these are listed in Table 1.3.

Condition	Phase	Trial reference
Leukemia	III	NCT00914628
	II	NCT01013441
Probable multiple sclerosis	III	NCT00228228
Glioblastoma	III	NC00807027
Hepatocellular carcinoma	III	NCT00699816
Metastatic breast cancer	III	NCT01741038
	II	NCT01431196
Adenocarcinomas (gastric, colorectal, lung and solid tumour)	II	NCT01723306
HIV	II	NCT00407836
Progressive multiple sclerosis	II	NCT01448252
Metastatic melanoma	II	NCT00871481

Table 1.3: Examples of T cell therapies in clinical trials. Source: <https://clinicaltrials.gov>.

As can be seen from the range of clinical trials, T cell therapies are versatile in that they can be applied to many disease states. As with the dendritic cell vaccines, they hold the potential to tackle conditions that are at present otherwise incurable, such as multiple sclerosis.

T cell therapies have the advantage of avoiding the need for migration to the lymph nodes, since the T cells themselves are active. The disadvantage is that the small circulating numbers of lymphocytes require expansion of the T cell population either *in vivo* or

in vitro in order to generate therapeutic numbers rapidly [43, 44]. Conversely, dendritic cells can each activate many T cells, so have an intrinsically multiplying effect.

As with dendritic cell vaccines there is no label-free way of detecting modified T cells *in vivo*, so the therapies suffer from similar tracking problems to dendritic cells, as discussed in Section 1.2.5. The interest lies in whether the primed T cells arrive at the tumour site, and so could therefore affect the local immune response. For example, engineered T cells were labelled with ^{111}In -oxinate (see Figure 1.2 for the structure) and tracked by SPECT to the bone marrow and other sites of interest in patients with acute myeloid leukemia. In another example, engineered T cells were tracked using ^{111}In -oxinate (also referred to as ^{111}In -oxine) in a phase I trial for ovarian cancer. Most of the radiation was seen in the lungs, liver and spleen [45] however, showing that either only a small portion is reaching the tumour, or that the tracer is being trafficked out of the cells soon after injection [46].

MRI has also been used to track T cells, mostly using superparamagnetic iron oxide nanoparticles (SPIOs). Splenocytes (lymphocytes from the spleen) labelled with SPIOs were tracked in mice using MRI at 7T. Similarly, T cells labelled with fluorescent peptide-coated SPIOs were tracked in mice at 4.7T [47]. See Section 1.2.5 for more information on the use of SPIOs.

Small animal PET has similarly been used to track genetically-engineered T cells *in vivo* by transfecting them with a reporter gene designed to specifically accumulate a PET probe [48, 49].

1.2.4 Current trends in immune cell therapies

As mentioned above, current immunotherapy trends involve combining different treatments, thus targeting multiple aspects of the immune response in the same treatment [37, 38, 35].

One development is the removal of immune suppression by checkpoint blockade [50]. Under normal conditions checkpoints are cell surface receptors that prevent the immune system from responding to self-antigens, which would otherwise lead to autoimmune re-

sponses and excessive T cell proliferation. Cancer cells possess these self-antigens, so similarly suppress the immune response, and can exploit this mechanism by checkpoint up-regulation [51]. This locally inhibits T lymphocyte activity, resulting in decreased reaction to the tumour's other antigens [50].

A modern trend is therefore to use inhibitors for these receptors to re-stimulate the immune response, with reported durable clinical effects [52]. Several checkpoint inhibitors have been approved for clinical use in the USA; examples include Ipilimumab (Bristol-Myers Squibb Company), a monoclonal antibody targeting the CTLA-4 receptor, and Pembrolizumab (Merck Sharp & Dohme Corp.), a monoclonal antibody binding to the PD-1 receptor. In the EU Ipilimumab also has marketing authorisation, while Nivolumab (Bristol-Myers Squibb International Corp.), another PD-1 inhibitor, is authorised for a paediatric investigation, though not yet market approval.

There is however a proportion of patients who do not respond to checkpoint inhibitors as a single therapy [53], and it is thought that this could be in patients with weak immune systems. The current movement is therefore towards using other therapies to boost the immune system, as well as the checkpoint blockade to remove the suppression [52, 54, 53]. Since immune cell therapies such as DC vaccines and T cell therapies will enhance the immune response, they are a vital component of therapy innovation, making robust tracking and quantification of their *in vivo* distribution all the more pressing.

1.2.5 Clinical need for new cell tracking agents

Currently, the clinical gold standard for immune cells tracking *in vivo* is nuclear imaging, though preclinically other techniques are of interest too. This section examines a few examples of the current clinical imaging agents used for tracking, and explores others which are under investigation.

Labelling with clinically approved agents

Radiotracers Radiolabelling is attractive because it is not limited by depth, as light microscopy techniques are, and gives real-time information on the cells *in situ*. It can also provide a quantifiable signal, indicating the number of cells that reach target sites in the body.

The standard method for tracking cells is SPECT. This requires a suitable radioisotope to be created, incorporated into a metal complex, and incubated with the cells.

Labelling with indium chelates such as indium oxinate (also known as indium oxine, see Figure 1.2e) allows tracking by SPECT, and some of the lighter isotopes such as ¹⁸F-fludeoxyglucose (FDG), by PET. Some examples of the clinically approved formulations are listed in Table 1.4, with the structures of the more complex ones shown in Figure 1.2.

Isotope	Generic name	Imaging technique	Indicated condition
^{99m} Tc	^{99m} Tc sestamibi	SPECT	Myocardial perfusion
	^{99m} Tc exametazime	SPECT	Cerebral perfusion
¹⁸ F	Florbetapir	PET	Amyloid plaques
¹¹¹ In	¹¹¹ In pentetreotide	SPECT	Neuroendocrine tumours with somostatin receptors
	¹¹¹ In oxine	SPECT	Leukocyte labelling
⁸² Rb	⁸² Rb chloride	PET	Myocardial perfusion
¹³ N	Ammonia- ¹³ N	PET	Myocardial perfusion

Table 1.4: Examples of radioisotopes, their formulations, and their associated imaging modality and condition. These are all currently licensed for use in clinics.

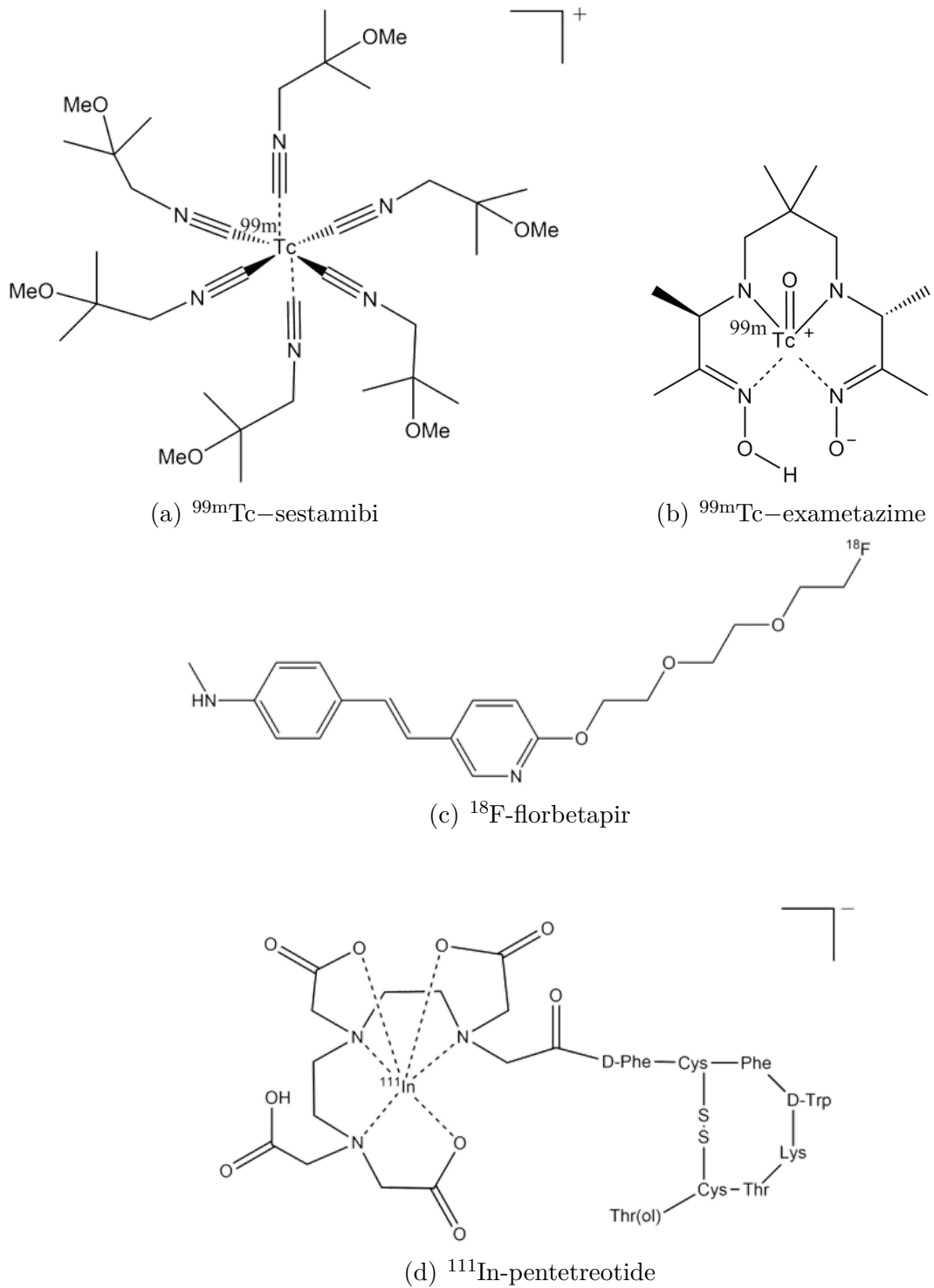


Figure 1.2: Structures of the example clinical radiotracers presented in Table 1.4.

^{111}In -oxine, an oxyquinoline complex shown in Figure 1.2e, is the most widely used for cell tracking, being the only approved complex for cell labelling, and a gold standard against which new methods are compared [55, 56, 57]. It localises in the cytoplasm of

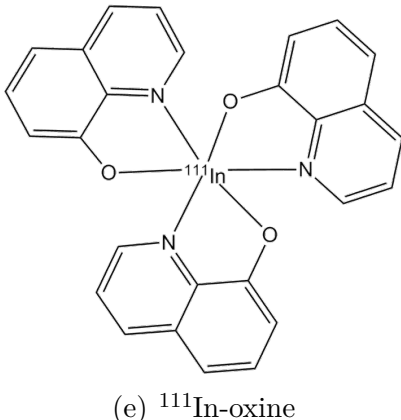


Figure 1.2: Structures of the example clinical radiotracers presented in Table 1.4 (continued).

platelets [58], but in leukocytes is more concentrated around the nucleus [59].

$^{99\text{m}}\text{Tc}$ -HMPAO, also known as $^{99\text{m}}\text{Tc}$ -exametizime, shown in Figure 1.2b, has been loaded into DCs, but was found in one study to be unsuitable for DC labelling [60]. In leukocytes there were more promising results reported, though radioactivity in other organs such as the bladder was also noted [61]. Like the indium complexes, it also appears to localise in the cytoplasm, possibly towards the nucleus [62, 63].

^{18}F , ^{13}N and ^{82}Rb have not been used for immune cell tracking, probably due to their short half lives (109.8 minutes, 10 minutes and 75 seconds respectively). ^{18}F -labelled compounds have been used to track cardiac stem cells after myocardial infarction, but not for long periods [64, 65], whereas the half lives of the other two are too short for any cell tracking.

When compared to other techniques nuclear imaging does have some advantages. In one study the higher sensitivity of radiolabelling provided better cell tracking by SPECT than T_2 -weighted MRI [66]. In a dog model of myocardial infarction, HSCs were co-labelled with SPIOs and ^{111}In -oxine before infusion. While the indium was visible by SPECT and scintigraphy, the SPIOs were not detected using MRI. This study highlights the challenges of optimising co-label concentrations, and the limited sensitivity of MRI compared to nuclear imaging.

With a half-life of 2.8 days for ^{111}In , tracking is only usually feasible for up to 4 days

after labelling [67]. Radiotracers therefore do not allow tracking in longer term studies after *ex vivo* labelling. There is also limited resolution using SPECT, making precise localisation within lymph nodes only possible using scintigraphy after resection [34].

There are also risks from labelling cells with ionising radiation. For example, HPCs were labelled with ^{111}In -oxine and tracked by scintigraphy in a rat myocardial infarction model [68]. Although the conclusion from this study was that the tracking was feasible, a loss of proliferation was noted in the labelled HPCs, suggesting that the tracer was affecting the cells. In a similar way in a different study, T cell proliferation was limited by the same tracer until the complex had been depleted from the cells [46], indicating that label concentrations may need to be optimised to balance these effects.

Gadolinium complexes Gadolinium chelates, which are discussed in detail in Section 1.4.2, have also been used for cell tracking, though with modified formulations or functionalisation compared to the clinical preparations. Reformulation of the clinically available compound GdDTPA by addition of transfection agents improved uptake into stem cells, producing sufficient labelling for imaging by MRI [25]. Similarly, a membrane translocation peptide was conjugated to GdDOTA, leading to detectable uptake into lymphocytes [69], and with further modification, to the nucleus of cancer cells [70].

Pre-clinical labelling

SPIOs SPIOs have attracted considerable interest as alternative MRI contrast agents to the standard gadolinium chelates. They are typically iron oxide cores of 2-3 nm trapped in a hydrophilic coating of dextrans or other polymers, but the cores can be much larger, reaching the micrometre range for particular applications [71]. The coatings make the particles hydrophilic, enabling cell treatments and the tuning of uptake. There is nevertheless often a need for transfection agents, though this can be overcome by amination of the SPIO surface [72].

SPIOs are reported to provide effective negative contrast in MRI, and a further functionalisable surface [73, 74]. An extra advantage is the potential for magnetic manipulation, such as magnetic sorting of labelled cells [75]. The disadvantage is that they do only provide negative contrast, making them less distinguishable from other short-T₂ image regions, and leading to local distortion which could mask other structures. They have previously been clinically approved, but are currently withdrawn from the market due to a combination of lack of demand [76] and concern about efficacy expressed by the EMA and manufacturers.

SPIOs have been used to track dendritic cell vaccines [55], though this required intranodal injection of the DCs in order to achieve sufficient contrast, followed by *ex vivo* quantification in a higher strength MR scanner. They have also been used as haematopoietic stem cell labels [77] and for *in vivo* tracking [78], as well as for lymphocyte tracking [57, 79].

An alternative method for tracking cells by T₂ negative contrast is to engineer the cells to over-express ferritin. This up-regulates iron storage when the cells are incubated in iron-enriched medium, leading to a T₂ contrast that is detectable by MRI [80, 81].

Ferritin up-regulation has been used for tracking of neurons and glial cells [82], cardiac stem cells [83], and as a label for embryonic stem cells [84]. When compared with SPIO-labelling, ferritin up-regulation was found to produce lower signals, but to give the advantage of distinguishing between live and dead grafts [85]. This is therefore a potentially very interesting technique for dendritic cells, and has been demonstrated using a transduction of the gene into a DC line [86], though both the sensitivity, and the effect of the cytological changes would need to be thoroughly investigated.

Hyperpolarised MRI Hyperpolarised MRI has also received increasing interest recently. The normal limitation of MRI is its sensitivity, which is due to only a small excess of nuclei contributing to the net magnetization. If however the nuclei are hyperpolarised at the time of imaging, there will be a significantly larger excess of nuclei in one spin state,

leading to an increase in the net magnetization and hence the signal. Xenon has been investigated as it can be readily hyperpolarised before being inhaled for lung imaging [87], or perfused into cell medium for cell labelling [88].

The problem with this technique at present is that it involves subjecting the nuclei to extreme conditions such as low temperature and high magnetic fields, to optical pumping, or to catalytic hydrogenation with hyperpolarised parahydrogen, none of which could be carried out *in vivo*. Since the lifetime of the hyperpolarisation is limited to minutes [89], or at most hours [90], this would be a problem for longitudinal studies. While hyperpolarized MRI has been used for a number of applications [91], it would not be suitable for *in vivo* cell tracking unless the technology or techniques develop further.

CEST agents An alternative MRI method which is being increasingly explored is chemical exchange saturation transfer (CEST) agents. These are molecules with exchangeable protons, where one frequency is excited until the protons are saturated. During this pulse however there is a rapid exchange of the saturated protons with the surrounding water. As a result, a much higher number of protons than the concentration of the agent are excited in the local area, and the saturated magnetisation is transferred to the bulk, thus decreasing the water signal and leading to negative contrast. This means that one or more specific frequencies can be excited, leading to hotspot imaging and the potential for multicolour imaging [92, 93], and that the effect on the image is amplified by the rapid exchange [94, 95].

CEST can be achieved either through the saturation of exchangeable protons such as hydroxyl or amine hydrogens, or through paramagnetic complexes, which are spectrally further separated from the water peak. Both have been explored for cell tracking, either through the introduction of a reporter gene, such as a lysine-rich protein [93], or through modifications to common lanthanide metal complexes [96, 97].

While CEST agents are therefore an interesting option, especially if a dual-modal CEST and luminescence compound could be designed, difficulty in quantifying the cells

and the negative MRI contrast make them less useful than other methods discussed below.

Ultrasound Ultrasound is an attractive technique because it is widely available, non-intrusive and relatively inexpensive. The disadvantages are that it has low resolution, highly localised signals and is largely not quantitative [98]. Therefore, although it has been used for guidance in cell administration (and even this has come under scrutiny for its effectiveness [99]), it is not ideal for tracking.

Optical imaging *In vivo* fluorescence techniques have been explored for cell tracking [7], usually involving intravital fluorescent microscopy [100], and labelling with organic fluorophores [101], quantum dots [102, 103], or genetic engineering to introduce fluorescent proteins [104] or luciferase [105]. They are however limited by the depth penetration of light through tissue, *i.e.* a few hundred micrometres, and consequently they require the cells to be close to the skin or to be accessible by endoscopy. These techniques are therefore intrinsically restricted to certain volumes of the body, or require a highly invasive procedure [7]. Moreover, these procedures all involve either fluorophores with limited photostability, high toxicity, or they involve modifying the genome of the cells, the consequences of which have not been fully investigated.

1.2.6 Summary

Current therapies have been shown to be effective in a range of cases by their outcomes, as discussed above, and some longer-term cell tracking has been carried out using radiotracers. In order to track these cells for longer than the decay time of a radiotracer however, ideally for more than a week, longer-lived tracers are required. This would allow observation of the cell migration through the body on a scale of weeks rather than days.

While the techniques used clinically and pre-clinically have some advantages, none of them alone provides an effective solution to this. One notably absent item from this

section is fluorine containing agents for ^{19}F MRI, which are discussed in detail in Section 1.4.3.

The imaging modalities selected for tracking in this work are discussed below, with a discussion about the benefits of combining them for cell tracking.

1.3 Imaging techniques

This section explores some of the theory and research in imaging techniques of interest for novel methods of cell tracking: luminescence-based techniques, ^1H MRI, and ^{19}F MRI.

1.3.1 Luminescence imaging

Fluorophores are detected by various imaging techniques. Essentially, a sample is illuminated with a light source at the wavelength of maximum fluorescence excitation. The emitted light is then collected, often with filtering to remove the excitation light, and formed into an image either by scanning and detection by a photomultiplier tube or wide-field imaging and detection by a camera (usually a charge-coupled device, CCD).

Fluorescence microscopy is widely used in research, with many biological and clinical laboratories having the necessary equipment already in place. This makes it a useful technique to use in novel processes. For example, if an immune cell is fluorescently labelled, the sub-cellular location of the label can be readily determined [106]. Of particular interest are whether the fluorophore is in the cytoplasm, whether it has entered the nucleus and might be interacting with the DNA, or whether it is trapped inside vesicles, and therefore is being trafficked through the cell.

Luminescence imaging is intrinsically limited by the interaction of light with tissue. The water and haemoglobin in tissues will absorb and scatter light to different degrees depending on its wavelength, thus limiting the penetration depth to millimetres [107] and restricting the *in vivo* use of light microscopy. Methods such as two-photon microscopy try to overcome this by using multiple low energy photons hitting the sample simultaneously

to excite it to high energy states. This enables the use of near IR excitation, where the scattering and absorption effects are minimised, but produces emission in a readily detectable blue region of the visible spectrum. Even with this technique however the depth penetration is very limited [108, 109].

Flow cytometry is also an attractive technique because it allows the quantification of the probe within a population of cells. The population is distinguished by co-labelling with a suitable fluorescent tag. The number of cells containing the probe of interest is then counted (denoted as the percent of positive cells), and the amount of probe per cell quantified by the median fluorescence of the gated-channel.

1.3.2 Magnetic resonance imaging

Magnetic resonance imaging (MRI) is a non-invasive, non-ionising medical imaging technique. It uses radio frequency pulses to excite the nuclei in the sample, and detects their relaxation back to equilibrium. The relaxation rate is dependent on environment, so different tissues will often relax at different rates, thus creating image contrast.

Proton MRI is by far the most widespread form of MRI. Clinical scanners are tuned to the frequency of ^1H nuclei, and the properties and abundance of protons make them ideal for imaging. It is very effective in the discrimination between soft tissues, contrasting with and complementing techniques such as computed tomography.

^{19}F nuclei also have useful magnetic properties, and are considered to be a viable alternative mode of MRI. Fluorine has an advantage over protons since the concentration of fluorine endogenously present in the body is below the detection limit of MRI, being reportedly less than a nanogram per gram of wet tissue [110]. Clinical equipment tends not to be tuned to the frequency of the ^{19}F nuclei however, so extra hardware is usually required for imaging.

¹H MRI

Three factors are the main properties of the tissues which affect the image produced by MRI; they are the proton density, the T₁ and the T₂.

Various longitudinal recovery pulse sequences are used to measure the T₁ of a sample. The two used in this work are inversion recovery and a fast low angle saturation recovery.

Inversion recovery involves a 180° pulse, then various inversion times, TI, before a 90° pulse to tip the spins into the imaging plane, which is perpendicular to the static field, traditionally denoted as B₀. The spins will relax from their excited states by different degrees during TI depending on their T₁. By using a range of TIs the T₁ can be calculated according to the equation (1.1) [111].

$$Intensity_{sample,IR}(TI) = M_0 \left[e^{-\frac{TI}{T_1}} (-2 + e^{-\frac{TR}{T_1}}) + 1 \right] \quad (1.1)$$

Saturation recovery with a low flip angle consists of rapid low flip angle pulses and a spoiler gradient to destroy the transverse magnetisation between them. The advantage is that the repetition time, TR (the time between repetitions of the pulse sequence) is significantly reduced. There is however a greater susceptibility to artefacts, which must also be accounted for in the sequence preparation. A range of TRs are used, which allow the calculation of T₁ according to equation (1.2) [111].

$$Intensity_{sample,SR}(TR) = M_0 \left[1 - e^{-\frac{TR}{T_1}} + k \right] \quad (1.2)$$

The high tissue penetration capabilities, versatility and lack of ionising radiation make MRI a highly suitable technique for *in vivo* clinical use. It is widely used and understood in clinical settings, meaning that it can be readily applied to a range of applications. MR images moreover have high tissue contrast, allowing high accuracy localisation within a body.

The main disadvantage of MRI is low sensitivity. Since the magnetisation being detected is only a slight net excess, most of the proton spins are intrinsically unavailable for

imaging as their spins are equalled by spins in the opposite direction.

There are also general disadvantages of MRI scans such as that they can be unsuitable for some patients with metal implants. A contrast agent is also often required, which can be contraindicated in patients with renal problems. Contrast agents are discussed in Section 1.4.2.

¹⁹F MRI

¹⁹F MRI uses the same principles as proton MRI. The nuclei are aligned and excited in the same way, though the frequency used to excite them is slightly lower ($\omega = \gamma^*B_0$, where ω is the Larmor frequency, γ is the gyromagnetic ratio and B_0 is the static magnetic field. $\gamma(^1H)$ is 42.58 MHz/T as opposed to $\gamma(^{19}F)$, which is 40.08 MHz/T). Fluorine also has a 100% natural abundance of the ¹⁹F isotope and a spin 1/2 nucleus, resulting in no intrinsic isotopic splitting or quadrupolar splitting in the signal.

Fluorine can therefore also be imaged in a similar way to protons. The sequence does however need to be selected and optimised carefully based on the environment of the fluorine. Ultrashort echo time (UTE), steady state free precession (SSFP) and rapid acquisition with refocused echoes (RARE) sequences have all been used with fluorine imaging in the past.

Fluorine is an interesting nucleus specifically for *in vivo* MRI because of the low endogenous concentrations of fluorine [110]. The highest levels that are present are in solid tissues such as teeth and bone, and thus have such short relaxation times that they would not generally interfere with samples with fluid properties.

Consequently any fluorine introduced into the body (provided that it is in a fluid form) will have no background signal, and should therefore be quantifiable. This contrasts conveniently with proton MRI which is not quantifiable, but does provide *in vivo* localisation, and can be imaged with the same equipment.

One main disadvantage of the use of fluorine is that it generally does require extra equipment, such as multi-frequency transmit and receive coils. While these can be incor-

porated into current clinical setups, an initial investment is necessary.

The other disadvantage is that fluorine-containing molecules can carry some risks, either in the toxicity of the compounds themselves or their degradation products. Meanwhile perfluorocarbons (PFCs), which have been used clinically in the past, are difficult to formulate, since PFCs are immiscible with water.

One formulation of a perfluorocarbon, a crown ether with 20 MR-equivalent nuclei, has been marketed and has undergone early phase clinical trials particularly for cell tracking. In research other groups have also made perfluorocarbon emulsions for cell tracking. These are discussed in detail in Section 1.4.3.

1.4 Imaging agents

Imaging agents are chemical compounds that aid in imaging by a given modality. They can be either contrast agents or tracers.

A contrast agent improves the contrast of an image in its environment. Examples include gadolinium chelates in proton MRI and microbubbles in ultrasound imaging. The tissues of the body will already have some inherent contrast, but an additional contrast agent can help to highlight lesions or objects of interest. The advantage of contrast agents is that the inherent image contrast provides information on their relative anatomical localisation.

Tracers are used when there is no or little inherent contrast in an image, and hence any signal observed is considered to come from the tracer. Examples include radionuclides for positron emission tomography (PET) such as fluorodeoxyglucose (FDG). The advantage of tracers is that due to the low background in the signal, provided the modality detects all the relevant response, the signals are assumed to be quantitative. The disadvantage is that with a single modality there is usually no indication of the anatomical localisation.

1.4.1 Luminescent probes

Luminescent probes can be either a tracer or a contrast agent depending on the modality by which they are observed, and the spectral properties of both the probe and the sample.

Fluoresceins Fluorescein and its derivatives are among the most common of fluorescent probes. Microscopes and flow cytometers even with a small range of filter sets will generally include settings suitable for the detection of fluorescein isothiocyanate (FITC). The ease of imaging and its low price make it appealing as an imaging agent. It is moreover known to be biocompatible, being used in ophthalmic eye drops and for angiography. The disadvantage is that in solution it is highly susceptible to photobleaching, making modifications to stabilise the molecule desirable.

The fluorescence profile of fluorescein depends on its environment, principally on the pH [112], and on any appended moieties [113]. FITC was used in early investigations of lymphocyte tracking, showing no effect on viability [114]. It was superseded however by other derivatives [115]. Its succinimidyl ester derivative, CFSE, has been used for tracking lymphocyte proliferation by flow cytometry [116], and its diacetate derivative, CFDA, has been used for leukocyte tracking in eye vasculature [117], though CFDA was found to leak out of the cells so to be unsuitable for longer term tracking [118].

Coumarins The coumarin dyes form another range of organic fluorophores. Various coumarins have been found to affect mononuclear cells and have pharmacological effects [119]. 7-amino-4-trifluoromethyl coumarin (AFC) is frequently conjugated to a peptide and used as a marker of apoptosis (see [120] and commercial products, e.g. CAS number 201608-14-2). It is mentioned particularly here because of its bifunctional nature; the molecule is fluorescent but also possesses three MR equivalent fluorines, making it intrinsically a dual modal agent. No examples were found of it being used as a general cell

label, for tracking or otherwise.

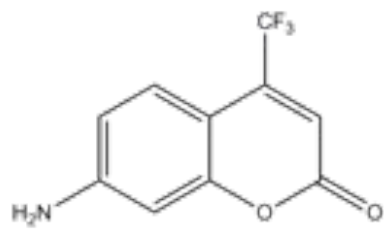
Charge transfer complexes Charge transfer complexes are also an interesting variety of luminescent dye. They are reported to show good photostability and strong luminescence with a large Stokes shift [121].

Ruthenium trisphenanthroline is a readily available and well-studied example complex. Its main charge transfer band has maximum absorption around 450nm, with emission between 500 and 700nm [122]. It binds to DNA [122, 123], but has not been found reported as a cell label, except to note that it is cytotoxic to mouse lymphocyte leukaemic cells [124]. An analogous complex with enhanced lipophilicity has been demonstrated as cell probe, though it was designed for lifetime imaging to probe binding rather than for cell tracking [125].

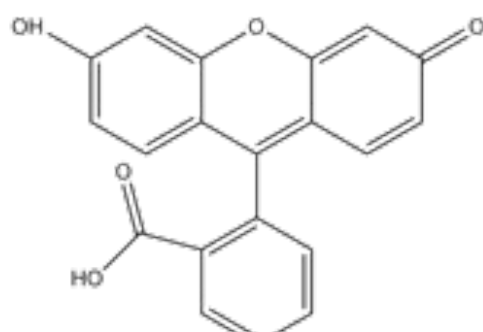
Iridium polypyridyl based complexes have also been found to emit bright luminescence, with a range of colours and binding properties depending on the ligands [126, 127, 128]. Several of these complexes have been tested as environment-sensitive cell labels [129, 130] which can be targeted to particular cellular compartments [127, 131, 129]. They have not, at the time of writing, been previously used for *in vivo* cell tracking, or for labelling immune cells.

The iridium complex used, $[\text{Ir}(\text{Bpy})_2(\text{BpySH})]^+$, was specifically designed for stable luminescence and binding to a gold surface. The complex and subsequent nanoparticle development were carried out by Dr. N.J. Rogers [132].

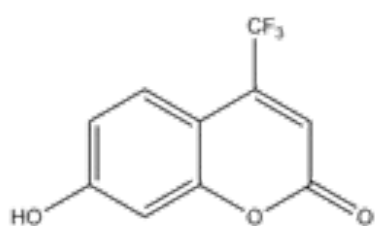
The structures of the luminescent dyes used in this project are shown in Figure 1.3.



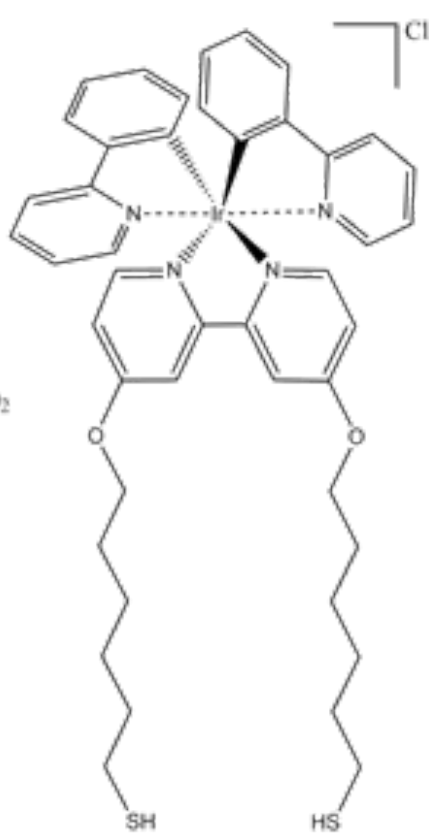
7-amino-4-trifluoromethyl coumarin



Fluorescein



7-hydroxy-4-trifluoromethyl coumarin



Ruthenium tris-phenanthroline

Iridium bipyridyl-SH

Figure 1.3: Structures of various luminescent dyes used in this project.

These dyes are usually incorporated simply by incubation with the cells [133], though extra factors such as pendant peptides and serum free conditions can affect both the uptake and sub-cellular localisation [134]. Some lipophilic ruthenium complexes appear

to enter the cells by passive diffusion [135], and others by a non-endocytotic temperature dependent route [133, 136], indicating dependence not only on cell type and the available transporters, but also on the complex itself.

1.4.2 ^1H MRI contrast agents

A number of ^1H MRI contrast agents are clinically available, which makes these attractive for research. Some of these are presented in Figure 1.4. The ligands are changed to suit their particular indications, which is one consideration for the choice of complex. For example, Gd-EOB-DTPA, marketed as Primovist, specifically targets hepatocytes, thus improving liver contrast in MRI scans [137].

The other major consideration for gadolinium contrast agents is the balance between the water access to the inner sphere of the gadolinium centre, and the kinetic stability of the complex. High kinetic stability is necessary to minimise patient risk, since the free ion is considered to be toxic [138]. Generally however higher ligand denticity is associated with lower toxicity [138, 139].

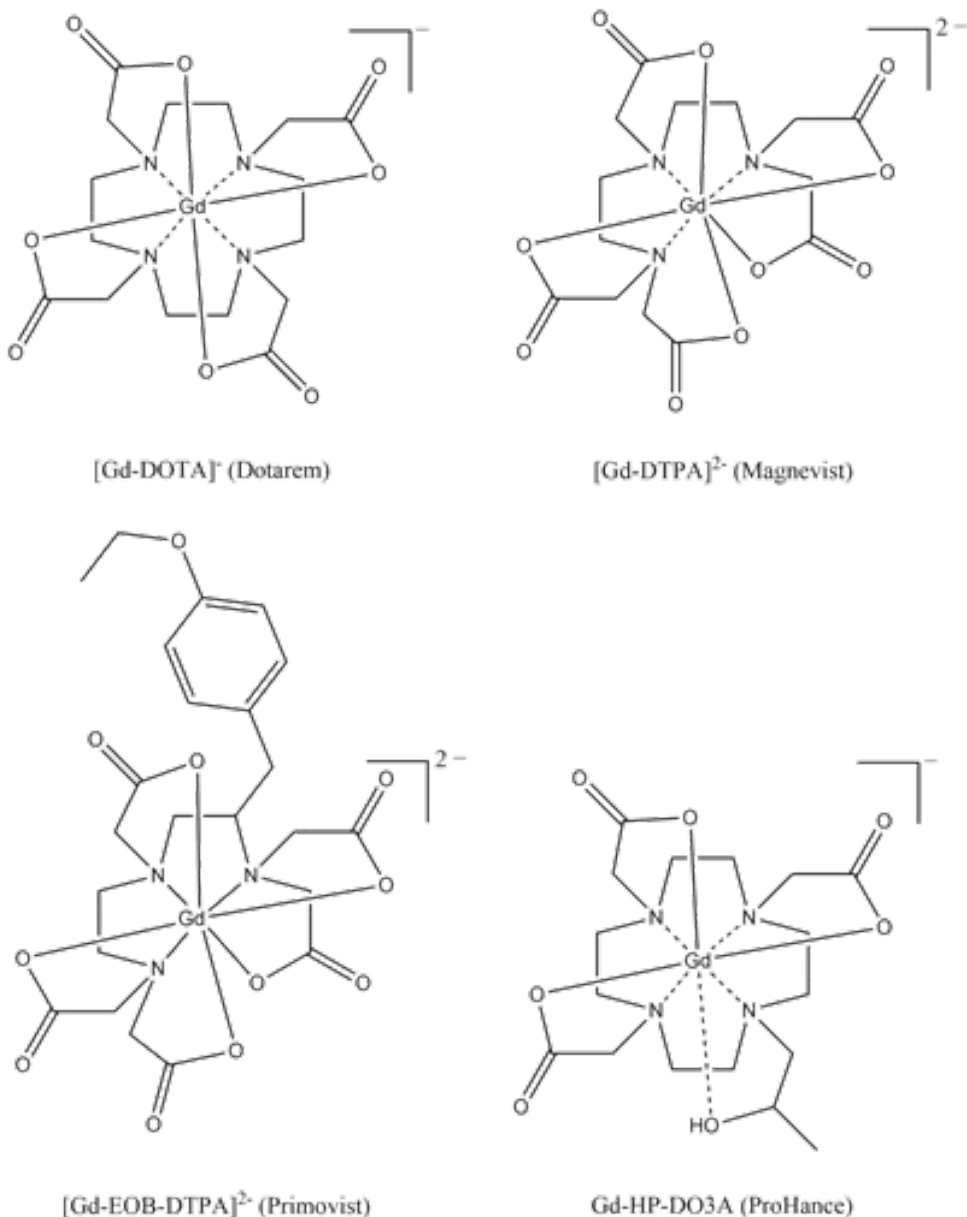


Figure 1.4: Structures of various ¹H MRI contrast agents used currently in clinics.

In terms of cell labelling, uptake of simple gadolinium complexes is often very low [140], though $[\text{Gd-HP-DO3A}]^{2-}$ (see Figure 1.4) has been used to label pancreatic islets by co-incubation, which was then imaged *in vivo* in a 7 T scanner [141]. It was noted however that with a less stable complex, a transmetallation process led to Gd^{3+} ions, rather than the whole complex, being taken up by two types of cancer cells, leading to a significant fall in cell viability [140].

In an attempt to boost the effect of the agent, GdDTPA complexes were conjugated to

a fluorescent dextran, creating a dual-modal stem cell label. The compound was diluted out of proliferating cells within seven days, but remained within non-proliferating cells, with little or no reuptake by surrounding cells [142]. Other attempts to improve contrast using MR images have included trapping gadolinium ions in fullerene cages [143], and binding to nanoparticles, which is explored in Section 1.5.

The main ^1H MRI agent used in this project was a gadolinium DTPA derivative used for hepatic imaging, marketed as Primovist. The ligand has a pendant ethoxybenzyl group as shown in Figure 1.4. This is a clinically available compound with known properties, which would be helpful for clinical translatability.

The other ^1H MRI agent used here is a gadolinium bound to a derivative of DTPA, denoted as APTES-DTPA, which has been conjugated to a silane moiety to allow binding to a silica surface (see Chapter 4).

1.4.3 ^{19}F MRI tracers

^{19}F MRI tracers are a relatively novel concept. The lack of clinical setups capable of imaging ^{19}F MRI and the small range of tracers available make it a more challenging option than some other contrast agents. The potential benefits nevertheless make investigation worthwhile.

There are three fields in which fluorinated compounds have been used clinically: medicines and anaesthetics [144], blood substitutes [145], and ultrasound contrast agents [146].

Medicines and anaesthetics have obvious disadvantages as imaging agents in their lack of biological inertness. Both blood substitutes and ultrasound contrast agents, consisting of perfluorocarbon (PFC) emulsions or bubbles, are a promising avenue for imaging research [146]. It should be noted though that these frequently have several MR-inequivalent fluorines, which lead to chemical shift artefacts in MRI [147]. They are nevertheless biocompatible and MRI active, and would be strong choices when considering translatability. On the other hand, as mentioned above, the higher the degree of fluorination, the higher

the immiscibility in water, making processing for human use more difficult.

One of the most widely used perfluorocarbons is perfluorooctyl bromide (PFOB), which has been used as a blood substitute [148], as a fluorine MRI tracer in small animals [149], and as a multimodal agent for ultrasound, fluorine MRI and CT [150, 151].

One set of commonly used agents for fluorine MRI are the perfluoropolyethers. They are often a linear chain form that, due to the low symmetry, has split peaks in its spectrum [152], which could result in chemical shift artefacts in the images.

One significant development in perfluoropolyethers for MRI was perfluoro-15-crown-5-ether (PFCE), which has 20 equivalent fluorines [153]. PFCE has been emulsified by trapping it in a PVA-stabilised PLGA nanoparticles of 200 or 2000nm in size, which could simultaneously be co-labelled with fluorescent dyes [147]. It has also been emulsified, and co-labelled with fluorophores for the tracking of DCs *in vivo* [154].

Immune cell labelling with PFCs is summarised in [147], with all the PFC molecules discussed above reported for *ex vivo* labelling of dendritic cells and stem cells. The structures of PFOB, PFCE and an example PFPE are shown in Figure 1.5.

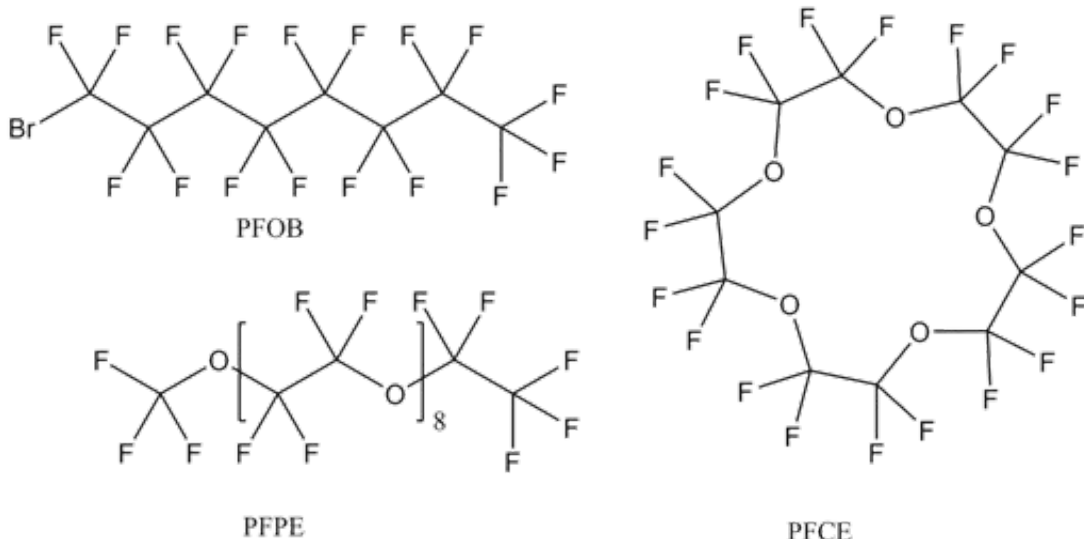


Figure 1.5: The structures of PFOB, PFCE and an example perfluoropolyether (PFPE).

A highly fluorinated suspension of molecular aggregates has recently been reported for therapeutic cell tracking [155]. The molecule possesses 36 MR-equivalent fluorines, and is

attractive due to the consequently strong ^{19}F MR signal it produces. This structure will not readily be modified to produce a multimodal system without losing the strong fluorine signal. Its incorporation into a multimodal vehicle could however prove an interesting avenue for future research.

In this work various ^{19}F tracers are examined. PFOB is used as it has been widely studied and is readily available. Trifluoromethylated molecules have also been explored, as well as some weakly coordinating anions such as hexafluorophosphate (which has 6 fluorines split into two peaks by the phosphorous) and tetrakis 3,5-bis(trifluoromethyl)phenyl borate (which has 24 equivalent fluorines, though some weak splitting by the boron).

1.4.4 Multimodality

Using more than one imaging technique on a sample or patient provides at least confirmatory if not complementary information. This results in higher confidence for diagnosis and therapy.

For example, ^1H MRI will non-invasively produce anatomical localisation, and ^{19}F MRI would enable the quantification of a tracer at that location. This is similar to the combination of positron emission tomography and computed tomography (PET/CT) which is current clinical practice, but avoids the use of ionising radiation.

If therefore tracers and contrast agents can be combined into a single vehicle and delivered as a unit, the multimodal probe will be more readily located and traced quantifiably *in vivo*.

This however requires a reliable method of combining the imaging agents at consistent proportions in a form robust enough to withstand physiological environments. This can be challenging, depending on the imaging agents in question.

For example, fluorinated substances as might be used for ^{19}F MRI will often be immiscible with water, forming a separate fluorous phase. Solutions to this have involved forming emulsions with fluorinated surfactants or surfactant cocktails, or encapsulating the PFC in a polymer shell [156]. Both the liposomes and polymer shells have been

modified to include fluorophores, making them dual modal [147, 157, 11]. Forming such nano-sized emulsions however often requires specialised equipment such as microfluidizers, and can nevertheless be susceptible to Ostwald ripening [158], so a more robust system is desirable.

1.5 Nanotechnology

Nanotechnology is often defined as involving structures with at least one dimension between 1 and 100nm in size. The definition is sometimes extended to particles below 1 micron in one dimension. The term nanoparticles will be used here in the more loose sense of spheres having diameters between 1nm and 1 micron.

The size of nanoparticles, along with various other properties such as their surface charge, can significantly affect their interaction with biological systems. Small nanoparticles are reported to be able to enter cells by diffusion through the membrane [159, 160, 161], whereas most nanoparticles enter by an endocytotic, usually phagocytotic, pathway [162]. Treatments usually involve simple incubation of the cells with the nanoparticles.

Nanotechnology is a versatile field with many possibilities for combining different components into one self-contained vehicle. Methods explored in this work include; trapping molecules inside nanoparticles in Chapter 3, using the nanoparticles' surface as a scaffold in Chapter 4, and carrying molecules in the cores of the particles in Chapter 6.

1.5.1 Silica nanoparticles

A method for the controlled synthesis of silica nanoparticles (SiNPs) were first reported by Stober in 1968 [163]. They are solid silica spheres with a generally regular morphology, though varying size distributions.

SiNPs are formed, according to the Stober method [163], by the basic hydrolysis of tetraethylorthosilicate (TEOS). Reagent concentrations are varied to control the size and

shape of the SiNPs, along with other factors such as the temperature and reaction time.

Modifications of Stober's method have involved replacing some of the TEOS with functionalised silanes, thus incorporating the functional groups into the bulk matrix or on to the surface of the NPs [164, 165, 166, 167], as discussed in Chapters 3 and 4 respectively.

The morphology of SiNPs can also be changed by adding porogenic molecules, frequently surfactants, to the synthesis mixture. This can create well-ordered pore systems widely considered useful for drug delivery and some imaging applications [168, 169, 170]. The disadvantage of these methods is that the template molecules need to be removed after the synthesis, without disrupting the structure of the particle, without losing any added functional groups, and ensuring that all of the template has been removed. The usual method is to extract the surfactant into a solvent, but this can lead to incomplete removal, and so poorly characterised micro-environments in the pores [171, 172, 173].

Even with a more comprehensive method such as calcination [174], which would destroy any organic functionalisation, there would still be a risk of micro-environments within the structure with different properties to the bulk, *e.g.* pH surface functional groups [170]. While there could be advantages to systems with micro-environments, they would need to be reliably characterised, especially if it might have clinical applications.

An extension of these porous systems is hollow silica nanoparticles (HSiNPs), which have been formed by a number of methods, as discussed in detail in Chapter 6. They consist simply of silica shells with a higher loading capacity than mesoporous structures, and a single cavity, making them easier to characterise.

SiNPs are inert, robust and highly versatile in terms of their functionalisation. Their surface can be modified with silanes, allowing conjugation to most biomolecules of interest.

These properties are valuable for cell tracking applications. An inert vehicle is important as the cell label should ideally not have any effect on the activity of the cell. The ability to functionalise the surface moreover means that SiNPs can be targeted to particular biological vectors [175, 176, 177]. Imaging agents can readily be incorporated into them in various modes, as explored through this thesis.

1.5.2 Gold nanoparticles

Gold nanoparticles (AuNPs) are often found in the 10-30 nm diameter range. They are formed readily by the reduction of tetrachloroaureate in the presence of citrate molecules [178, 179]. though other synthetic methods are also described in Chapter 4.

AuNPs are particularly useful because of their versatility in functionalisation through gold-sulphur bonds [180]. Being relatively small for nanoparticles they have a high surface area to volume ratio, allowing high levels of surface modification. They are dense heavy metal structures which can consequently be easily discerned by electron microscopy, thus providing another mode of intracellular localisation, uptake and release [181, 182]. One disadvantage is that the metal surface can quench luminescence, so a spacer is necessary to distance dyes from the nanoparticle surface [183, 184].

AuNPs are generally considered to be biocompatible [181], although some cytotoxicity has been observed with cationic AuNPs [185] and small (1-2nm) AuNPs [186], which should be taken into account in the design. The particles must also be colloidally stabilised, which somewhat limits the functionalisation capacity. For example, it is difficult to change the surface charge from the negatively charged citrate groups to a positively charged species without significant aggregation.

There is consequently much research on gold nanoparticles for many applications, ranging from drug delivery [187, 188, 180], photothermal and photodynamic therapy [189, 190], and combinations of diagnostic and therapeutic agents (so called ‘theranostics’) [191, 192, 193].

Gold nanoparticles are of interest for cell tracking because of the high surface loading capacity for imaging agents. Any molecules that has, or can be modified to have, a thiol group could potentially bind to a gold nanoparticle surface. They have been explored in the context of photoacoustic imaging of melanoma cells, with the notion that the technique could be extended to circulating cancer cells [194]. They have also been functionalised with fluorescent and gadolinium labelled DNA to create dual-modal labels [195], and with sugars for receptor-mediated targeting to particular cells [196].

1.6 Multimodal molecules

Nanotechnology can be an efficient and elegant solution to the problem of designing a multimodal imaging agent system, as discussed above. It can however have several disadvantages: in the loss of colloidal stability in salt or protein solutions such as cell medium [197]; leakage of imaging agents; and the size distribution of the nanoparticles, coupled with the size dependent response of biological systems [186, 198, 199].

Multimodal alternatives to nanotechnology were therefore considered; these could include small molecules where multiple functional moieties are present on one structure. For example, having a fluorophore with a conjugated gadolinium complex, or a gadolinium complex with a conjugated fluorine group, could potentially allow multimodal detection of the label.

1.6.1 Fluorinated fluorescent dyes

Numerous fluorinated fluorescent dyes (FFDs) exist. The electron withdrawing effects of the fluorines can have significant effects on the fluorescence [113, 200]. Two FFDs, the first marketed by Life Technologies, are fluorescein derivatives: Oregon Green 488 and Pennsylvania Green. Both have reported improved photostability compared to fluorescein [201]. The advantage of the fluorines is largely limited to the fluorescence properties, since the inequivalent placement and low number of the fluorines make these molecules unsuitable for ^{19}F MRI.

BODIPY dyes are also a popular set of fluorinated fluorophores [202, 203]. The attachment of the fluorines to the boron will however result in quadrupolar splitting of the fluorine signal, risking chemical shift artefacts in ^{19}F MRI.

The fluorinated coumarin dyes mostly look more promising. 6,8,difluoro-7-hydroxy coumarin would suffer from similar artefacts to the fluorescein dyes. The three equivalent fluorines on AFC, 7-hydroxy-4-trifluoromethyl coumarin (HFC) and coumarin 153 however make them attractive FFDs for further investigation.

Similarly, Atto514, marketed by Atto-tec, might potentially be promising, especially considering the presence of the six fluorines, but would be prohibitively expensive to use at the concentrations required for ^{19}F MRI in preliminary experiments

The structures of these dyes are shown in figures 1.6 and 1.7.

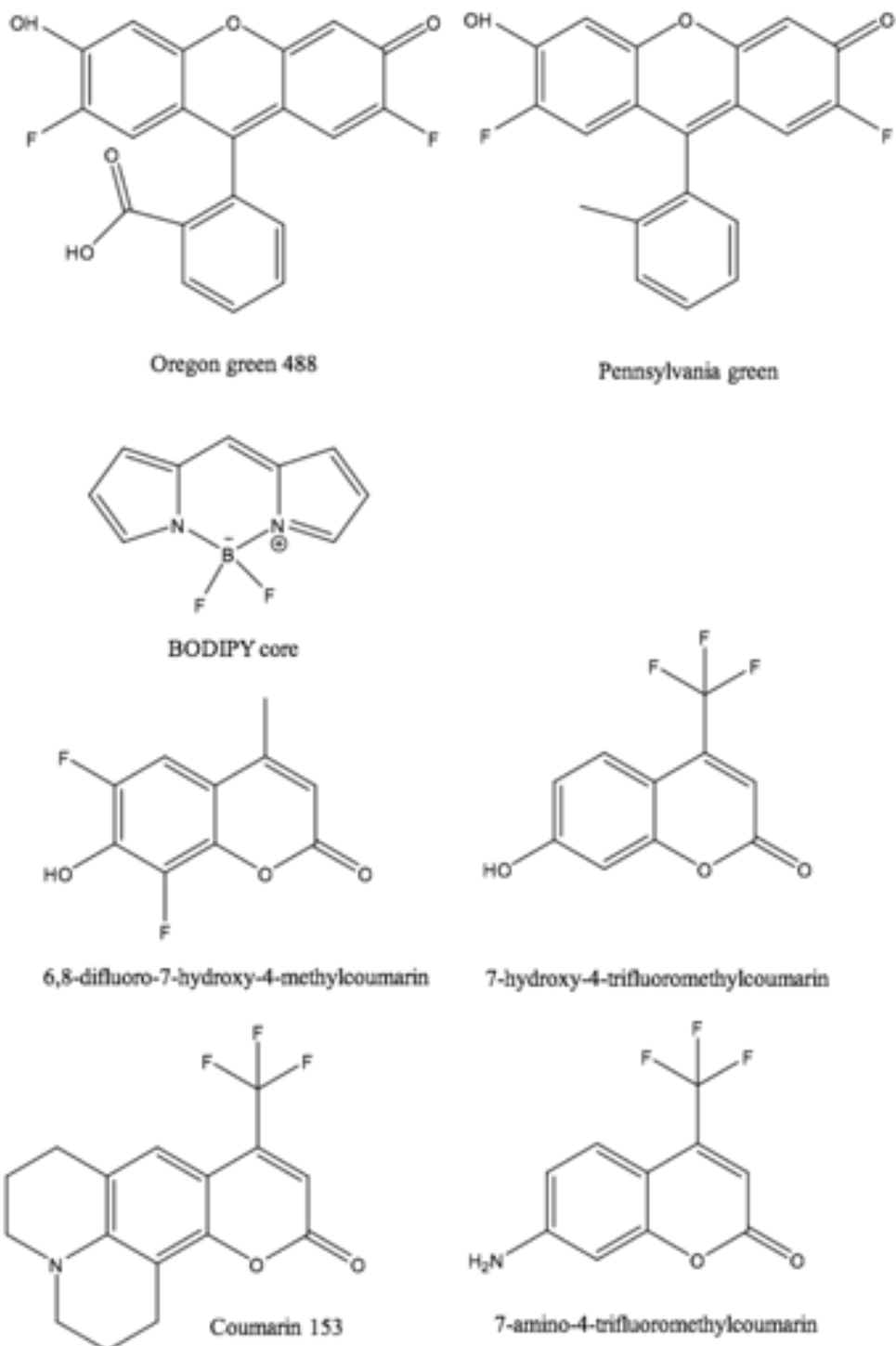


Figure 1.6: Structures of some fluorinated fluorescent dyes.

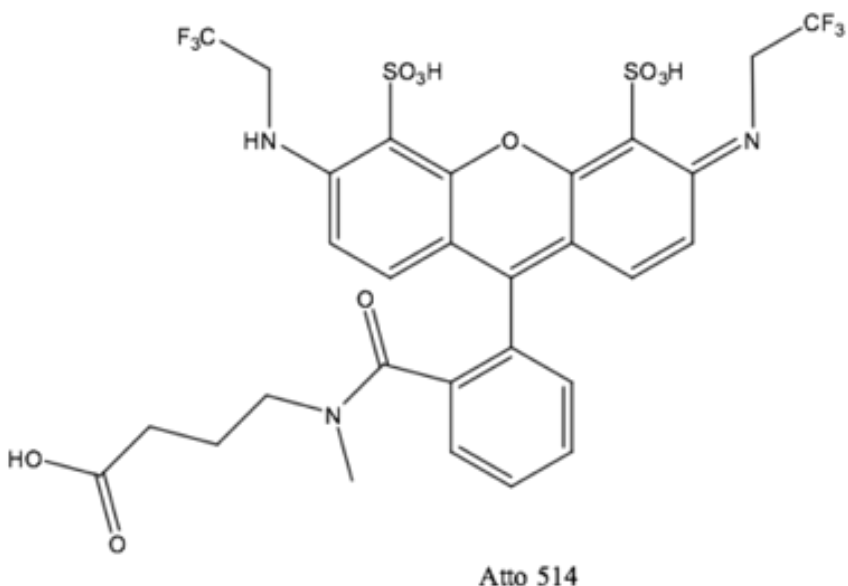


Figure 1.7: Structures of some fluorinated fluorescent dyes (cont.).

These coumarin dyes are not significantly water soluble, possibly in part due to the presence of the fluorine groups. They are however soluble in alcohols and DMSO, so can be dissolved sufficiently for use in cell studies.

Atto514 has higher water solubility and a good excitation and emission range for multicolour fluorescence imaging, but is a proprietary brand as in considerably more expensive than the coumarin dyes.

In this project therefore AFC was primarily used, since it offered an inexpensive dual modal molecule with the potential to be functionalised further through the amine group.

1.7 Project design and aims

The broad aim of this work is to create and explore vehicles for the simultaneous delivery of multiple imaging agents. The required concentrations of the various agents are investigated, and the design optimised where possible to account for the sensitivity of the different modalities.

1.7.1 System design: imaging agent requirements

The design requirement of the various imaging agents has been described in Table 1.5, which has guided the strategies used.

Requirements	Fluorophores	Gadolinium chelates	Fluorinated agents
Structure	Aromatic moiety not disrupted	Effective chelation of metal centre	High ^{19}F NMR-equivalence
Freedom of movement	None	Rotational correlation	Rotational correlation
Solvent access	None preferably	Access to water	None
pH control	Depends on structure	Necessary	None

Table 1.5: Table specifying design considerations for the three classes of imaging agents in this project

In practice the requirements described in Table 1.5 can be implemented as follows.

Fluorophores can be incorporated into any part of a nanoparticle structure as long as the particles are not disrupted by the process. They may benefit from a pH-controlled environment if their fluorescent properties depend upon this.

The toxicity of gadolinium-based contrast agents is highly dependent on a minimal presence of free gadolinium ions. These agents require that effective chelation of the gadolinium is maintained both during the incorporation into a nanoparticle structure, so limiting the usable pH range that can be withstood during the synthesis, and through foreseeable pH changes the system will undergo physiologically. Moreover, these contrast agents require access to the water, so cannot be trapped in a non-aqueous medium in an impermeable shell. There must also be sufficient rotation to ensure a rotational correlation with the surrounding molecules, thus enabling faster relaxation.

Fluorinated agents have few requirements, but do need enough freedom of rotation to allow relaxation of the spins by interaction with surrounding molecules. The only other consideration is ensuring that the NMR-equivalence of any fluorine species is maintained, ensuring a high signal and avoiding the introduction of chemical shift artefacts.

1.7.2 System design: delivery vehicle requirements

For the design of the delivery vehicle, the most important property is that the final system should be bioinert. The vehicle should enter the immune cells, but interact minimally with them to reduce any effects on the cell functionality. It should be a stable and robust system, which also has a minimal effect on the capabilities of the imaging agents, as discussed above.

The aim is therefore to investigate various delivery systems, mainly consisting of silica or gold nanoparticles, but also to explore other options.

1.7.3 Project aims: MR imaging capabilities investigation

^{19}F MRI is not currently used clinically, but modifications to clinical equipment to expand the nuclear analysis capabilities to fluorine have become available. A ^{19}F coil, interface and software extension were procured for the work of which this project is a part, and as a relatively new setup, protocols are not well established.

The aim in this work is to investigate the capability of the ^{19}F MRI setup, within the limitations imposed by the research licence agreement with the manufacturer. As a clinical scanner, options for pulse sequence development are limited, and this was not feasible within the time constraints. Consequently, though there are a number of protocols reported in the literature which give promising results, such as Rapid Acquisition with Refocused Echoes (RARE) sequences at 11.7T [12, 204], or the steady state free precession sequences at 1.5T [205], these were often not available to be replicated, or did not have suitable parameters or options available, *e.g.* the number of averages or echo time. Fast

low angle single shot (FLASH) sequences however have been used on clinical strength scanners [206, 207], and were available for this work, so were focused on in this project.

The sensitivity of the coil with respect to the sample placement is important, and could have considerable effects on the results produced. Since a large portion of this project involves the development of imaging agent systems, analysis of various model phantoms demonstrated the concentration ranges that would be required.

1.7.4 Project aims: imaging agent development

Once a robust delivery system is found, the aim is to incorporate imaging agents, while maintaining the design requirements discussed above, at a sufficient concentration for imaging.

Luminescence techniques for example have relatively high sensitivity, requiring concentrations in the nanomolar to micromolar range, depending on the quantum yield. MRI on the other hand requires much higher concentrations due to its low inherent sensitivity. The delivery systems developed are therefore investigated to verify that the luminescence is bright enough for microscopy and flow cytometry applications. The relaxivity is also measured for samples containing gadolinium, and fluorine MRI carried out for fluorine-containing samples.

The relaxivity is dependent on the field strength of the scanner, and the MRI work in this project has been carried out on a clinical strength 3 tesla scanner. This immediately gives an indication of the clinical translatability of the system. This approach contrasts with many studies, in which the development is carried out in a pre-clinical scanner of higher field strength, thus giving a skewed impression of their translatability.

1.7.5 Project aims: Cellular interactions investigations

Comprehensive investigations of cellular uptake and viability of these systems are beyond the scope of this project. This is due to the number of factors that would affect

the uptake: specific cell type, temperature, donor variability, culture conditions, etc.. The viability is also complex as it will depend partly on the cell type, uptake and culture conditions, but would also be assessed differently depending on the application of interest.

This project therefore aims to carry out preliminary studies to assess the feasibility of labelling the cells, and the requirements for sufficient labelling for the various imaging modalities.

Peripheral blood mononuclear cells (PBMCs) are to be used, as they are relatively rapid, easy and inexpensive to isolate, as compared for example to dendritic cell preparations. The PBMC blood fraction contains both monocytes and lymphocytes, which are both of interest for immune cell therapies. The aim is therefore to observe the concentration-dependent uptake into both cell types, where possible by flow cytometry and fluorescence microscopy. MRI analysis will then indicate whether the labelled cells show enhanced contrast, making them dual or tri-modal imaging agents.

CHAPTER 2

GENERAL EXPERIMENTAL DETAILS AND IMAGING CAPABILITIES

This chapter details materials and methods which are common to all of the following chapters. The aim of this is to provide a central reference point and avoid repetition. The chapter also explores the capabilities of the MRI imaging systems used in the rest of the work. These experiments were carried out alongside the testing of the imaging agent systems, but are presented separately here in order to demonstrate the challenges involved, especially in fluorine MRI.

2.1 Materials

2.1.1 Common reagents and solvents

Tetraethyl orthosilicate (TEOS) (Acroseal) and 3-aminopropyl triethoxysilane (APTES) were purchased from Sigma Aldrich. Ammonium hydroxide (28 - 30%) was purchased from VWR. Ethanol was purchased from Fisher Scientific (UK).

2.1.2 Imaging agents

Fluorescein sodium salt, 1-bromo-heptadeca-fluorooctane (PFOB) and trifluoroethanol were purchased from Sigma-Aldrich. Primovist (GdDTPA-EOB) was produced by Bayer.

Sodium tetrakis(3,5-bistrifluoromethylphenyl)borate was purchased from ABCR. Gadolinium chloride hexahydrate was purchased from Alfa Aesar.

2.1.3 Other equipment

200 mesh copper transmission electron microscopy (TEM) grids were purchased from Agar Scientific (UK) or Electron Microscopy Supplies (USA).

The centrifuge used in the nanoparticle preparation was a Gallenkamp fixed head angle rotor or a Corning LSE Compact with a fixed angle rotor. The sonicator used here was a Decon FS200b 35-45kHz ultrasonic cleaning system.

2.2 Instrumental details and methods

2.2.1 Preparation and analysis of samples by DLS

As-prepared nanoparticle samples were diluted until visibly clear with the stated solvent – usually deionised water or ethanol. For dynamic light scattering (DLS) measurements, sample suspensions were placed in 1 ml plastic disposable cuvettes (Sarstedt polystyrene cuvettes) and analysed using a ZEN3600 Zetasizer Nano (Malvern, UK).

Samples were equilibrated to 25°C for 2 minutes prior to measurements. Light was detected at 173° backscattered. Each sample was measured 3 times, with each measurement consisting of at least 10 runs.

For zeta potential analysis the same sample was used as for DLS. The suspension was placed in a polystyrene folded capillary cell (Malvern, DTS1061), and analysed by the Zetasizer Nano (Malvern, UK). Each sample was measured 3 times, with each measurement having an automatic number of runs.

2.2.2 Preparation and analysis of samples by TEM

8 µl of as-prepared nanoparticles were dropped onto a Formvar coated 200 mesh copper TEM grid held in opposable tweezers. The drop was left to settle for 1-2 minutes then the excess was blotted by touching the droplet with filter paper. The grid was left to air dry in the tweezers for a minimum of 30 minutes, and usually overnight.

The grids were analysed using a Jeol 1200EX transmission electron microscope with an accelerating voltage of 80keV.

2.2.3 Density analysis of nanoparticles

All density measurements were carried out by Dr. R. Williams.

The true density of all samples was evaluated using an AccuPyc II 1340 (Micromeritics, U.S.A) helium pycnometer; each sample was subject to ten purge and measurement cycles with helium. Average density of the samples were calculated from measuring the mass of a known volume of sample (typically 0.75 ml) in powder form. Relative density was calculated as the average density divided by the true density. Porosity was then calculated as 1 minus the relative density and multiplied by 100%.

2.2.4 Preparation of samples for ICP-MS analysis

Samples were analysed by inductively coupled plasma mass spectrometry (ICP-MS) to find the gadolinium and ruthenium content, where relevant. The nanoparticles were dissolved to release the ions prior to analysis. All samples were prepared and analysed in triplicate.

350-400 mg of oven-dried silica nanoparticles were weighed accurately and placed in a 100 ml PTFE beaker. 4 ml of hydrofluoric acid (47-51% trace analysis from Sigma Aldrich) and 15 ml of nitric acid (67% trace metals from VWR) were added and the suspension was stirred using a PTFE-coated stirrer bar at approximately 400 rpm for 3 hours at room temperature. The temperature was gradually raised (10°C every 30

minutes) to heat the samples at 50°C for 24 hours and then to 75°C for 24 hours, until dry.

67% nitric acid was added then carefully diluted with distilled water to yield a 1:100 (w:v of original solid mass) solution in 2% nitric acid. For example, with 398 mg of silica used initially, the solution was made up to 39.8 ml using 2% nitric acid, by adding 1.2 ml of 67% nitric acid then diluting with 38.6 ml of distilled water. Samples were stirred for one hour then filtered through a 450 nm syringe filter (Minisart RC25, Sartorius) into polypropylene centrifuge tubes. No particulates were visible prior to filtering; this step was required by the ICP-MS operator as a precaution.

Samples were analysed by Dr. S. Baker, using an Agilent 7500ce inductively-coupled plasma mass spectrometer with an Octopole reaction system (ORS) for the removal of polyatomic interferences. A Miramist nebuliser was used for sample introduction. The plasma was run with an RF power of 1500 W. Gd was analysed at mass 157 and Ru at mass 101.

2.2.5 Preparation and analysis for luminescence measurements

As prepared nanoparticles were diluted to the stated concentration and placed in quartz cuvettes. Excitation and emission analyses were performed using an FLSP920 Time Resolved Spectrometer (Edinburgh Instruments), using a xenon lamp and a visible light photomultiplier tube (PMT).

2.2.6 Preparation and analysis for UV-visible spectroscopy

As-prepared nanoparticles were scanned in quartz cuvettes and, where necessary, diluted so as to obtain a maximum absorbance below 1. Measurements were carried out in a Cary 5000 spectrometer.

2.2.7 NMR characterisation

NMR characterisation of ^1H and ^{19}F nuclei was performed on an automated Avance AVIII 300MHz spectrometer (Bruker). ^1H analysis was with a standard 1D 30° pulse sequence (denoted as zg30). ^{19}F analysis was carried out by a standard inverse-gated decoupled 1D ^{19}F pulse sequence (zgig).

2.2.8 MR imaging

MRI was carried out on a 3 T Magnetom Verio (Siemens).

^1H scans were carried out using a 16 channel birdcage head coil with a spoiled 2D gradient recalled echo saturation recovery sequence. The samples were raised to the middle of the coil and centred laterally. Falcon tubes of distilled water were also placed in the coil to aid localisation and calibration. The slice thickness was 4.5 mm, and the sequence had a repetition time (TR) of ranging from 235 - 9200 ms, echo time (TE) of 1.4 ms, a flip angle of 8° , 100% sampling and 32 averages (NA) per slice.

^{19}F scans were carried out using a flexible surface coil with ^1H and ^{19}F transmit and receive capabilities. A proton localiser scan was carried out to locate the samples, then the frequency was switched to approximately 115.957 Hz and centred on the peak of interest. The pulse sequence was based on a 3D gradient echo FLASH programme, with a slice thickness of 4 mm, a TR of 2.1 ms, a TE of 0.96 ms, 32 averages and an 8° flip angle unless stated otherwise. Samples were placed directly on top of the upturned coil and were grouped in the centre over the area which had been found to contain the coil element by earlier measurements, as discussed in section 2.5.

The field of view for both sequences varied as necessary to provide the maximum signal to noise ratio (SNR) while avoiding aliasing artefacts.

2.3 Cell preparation and analysis

The following section describes the methods used in all chapters that include cell treatments.

2.3.1 Peripheral blood mononuclear cell isolation and treatment

Peripheral blood mononuclear cells (PBMCs) were isolated from the peripheral blood of volunteer donors. Total blood was layered onto a Lymphoprep density gradient medium and centrifuged at 700 x g for 20 minutes. The mononuclear layer was removed and placed in phosphate buffered saline (PBS). The pellet was washed three times by centrifugation and resuspension in PBS, then the cells counted by haemocytometer, with Trypan blue staining to verify viability. The PBMCs were incubated at 2×10^6 cells/ml in RPMI 1640 with gentamycin, penicillin and streptomycin, and 10% foetal calf serum, and any stated treatments. Cell suspensions were placed in plastic well-plates and stored at 37°C in 5% CO₂.

2.3.2 Cell analysis by flow cytometry

The treated PBMCs were centrifuged (5 minutes at 650 x g) and resuspended in PBS three times. The suspended cells were then placed in flow cytometry tubes at a concentration of 2×10^6 per ml. Samples were reagitated by gentle vortex mixing prior to analysis.

PBMCs were analysed on a CyAn ADP 9 colour flow cytometer (Beckman Coulter, UK). The detection was gated so that only single cells were recorded.

Flow cytometry analyses cell populations by creating a laminar flow which passes individual cells through a LASER light beam. The forward and side scattered light are detected by photomultiplier tubes, and filters can be placed in the light path to gate out wavelengths of interest.

2.3.3 PBMC analysis by light microscopy

Various methods were attempted for preparing the PBMCs for microscopy. Being non-adherent, the natural spherical morphology of the PBMCs exist only when in suspension. Techniques which preserved this however, such as sealing the cell suspension in an imaging chamber (Grace Biolabs) did not reliably lead to clear images being produced, as seen in section 5.3.2. All other light microscopy images presented in this thesis were therefore produced by the following method.

PBMCs were washed by centrifugation at 650 x g and re-suspension in PBS to a concentration of 2×10^6 per ml. 200 μ l of the cell suspension was pipetted into the funnel of a cytocentrifuge slide attachment, and then spun onto poly-L-lysine coated glass microscope slides for 3 minutes at 300 rpm. The slides were air dried for 30 minutes.

The cells were fixed by immersion in methanol for 2 minutes and allowed to air dry. The slides were then wrapped in aluminium foil and stored at -20°C.

For brightfield cell staining, a Kwik-Diff preparation (Fisher Scientific, UK) was carried out. This stain combination consists of methanol as a fixative and permabiliser, eosin as a red stain and methylene blue as a blue stain. The expected results, according to the product insert, are that red blood cells should appear pink, lymphocytes should have a clear blue cytoplasm, possibly with red-purple granules, and monocytes should have a pink and blue cytoplasm, possibly with blue granules.

Slides were defrosted while wrapped, then stained according to the manufacturer instructions and rinsed under a gentle stream of deionised water. The samples were mounted while still wet using Immu-Mount (Fisher Scientific, UK), and covered with cover-slips. Slides were stored at 4°C until required. Microscopy was carried out within 3 days, but usually within hours of mounting.

Imaging was carried out on an Zeiss Axioskop 40 microscope equipped with a mercury arc lamp and a DAPI 420 nm long pass filter.

2.3.4 Cell analysis by TEM

PBMCs were washed by centrifugation at 650 x g and re-suspension in PBS twice. The cells were then washed into glutaraldehyde buffer (2% glutaraldehyde in PBS) and stored at 6°C.

Embedding and sectioning was carried out by the Centre for Electron Microscopy at the University of Birmingham.

Briefly, the fixed cells were centrifuged to form a pellet and embedded in resin. The resin was microtomed to produce thin sections, stained with uranyl acetate, and placed on copper TEM grids coated with holey carbon.

The cell sections were imaged on a Jeol 1200EX transmission electron microscope at 80 keV.

2.3.5 Cell analysis by MRI

The PBMCs settled in aqueous suspension, and therefore two methods were used in this project for imaging cells by MRI.

Cells were initially suspended in 10% gelatin (w/v in PBS) at a known concentration and placed either in polypropylene deep-well plates or in microcentrifuge tubes.

It was found however that, especially where a high concentration of imaging agent was required, such as with the ¹⁹F MRI experiments, that this method produced no signal. Cells were therefore pelleted in microcentrifuge tubes, before having 10% gelatin (w/v in PBS) layered on top to prevent movement.

Samples were then placed in the centre of the MRI scanner coil, and imaged as described above.

2.4 ^1H MR capabilities

In exploring the capabilities of the equipment available, one aim was to establish how much variation in the results occurred as a consequence of sample placement. For proton imaging, this was tested both with the birdcage (head) coil, and the dual frequency surface coil used also for the ^{19}F MRI.

2.4.1 Imaging with the birdcage coil

The dependence of sample location within the coil was investigated by the variation across a rack filled with microcentrifuge tubes containing deionised water. This mimicked the set-up for sample imaging used during this project but on a larger scale as the whole rack was filled.

The relaxation time of the water was measured from each of the tubes, and plotted on a scale of distance across the rack, see Figure 2.1. The centre of the surface plot should correspond to the centre of the head coil, which was placed in the centre of the scanner.

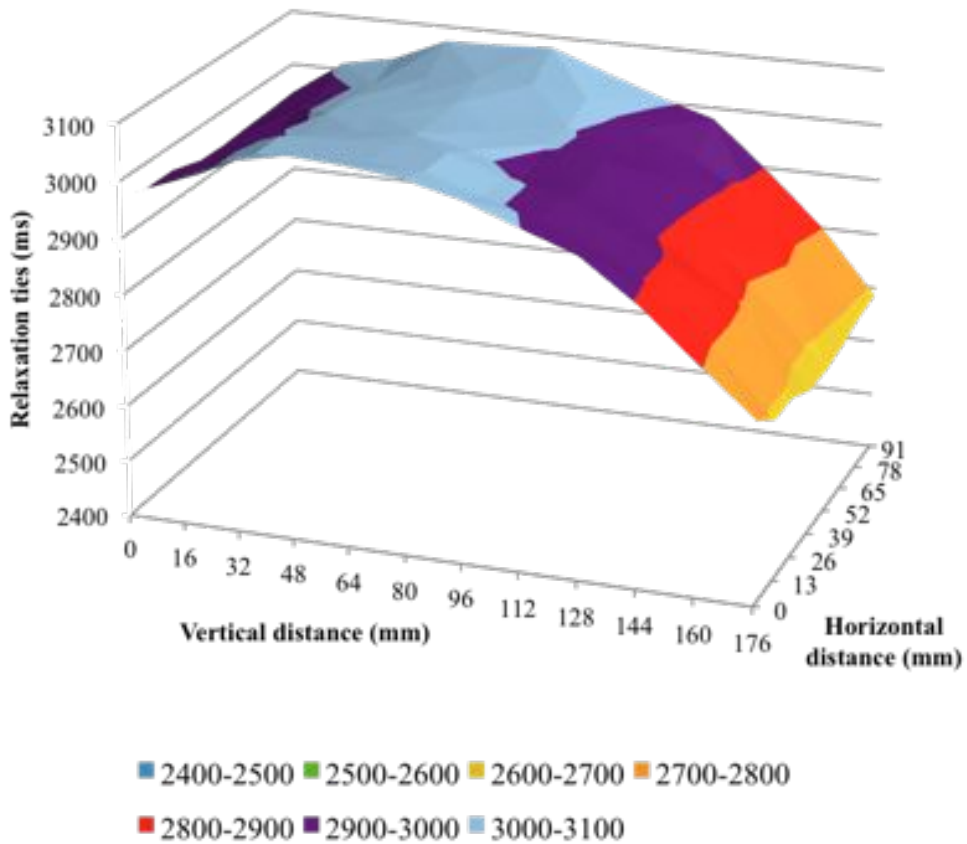


Figure 2.1: Variation in relaxation time of distilled water measured horizontally through the 16 channel ^1H birdcage coil. Vertical distance indicates the direction from the top of the head towards the neck. Horizontal distance indicated the direction from ear-to-ear.

The plot shows variation in the direction corresponding to the conventional z axis of the scanner, labelled as vertical in Figure 2.1, which passes through the centre of the bore. From roughly the centre of the coil to close to the top of the coil (0 mm on the vertical distance axis), the relaxation times vary by 0.1 seconds in a gradual reduction moving outwards. From the centre to the bottom of the coil the change is greater, with the relaxation time falling by 0.35 seconds. This might be improved where a larger sample area is necessary by also using a neck coil, though the sensitivity profile of the combined coils would have to be checked too.

There appears to be less variation horizontally across the coil, with the highest values appearing by the edge of the sampled area, though the centre only relaxing 0.07 seconds slower than the outer samples. This can be explained by the shape of the coil, as the

coils in the sides of the birdcage would be closer to the samples than the coils above the central ones.

These results suggest that the measured relaxation times would be most consistent if samples are placed within the central area of the coil, of roughly 5 cm x 5 cm. If they cannot be within this area however the variation could be corrected using calibration plots.

2.4.2 ^1H imaging with the ^{19}F coil

The same rack of microcentrifuge tubes containing deionised water as were used for the birdcage proton coil were scanned using the dual band $^1\text{H}/^{19}\text{F}$ coil.

The relaxation times are plotted in Figure 2.2.

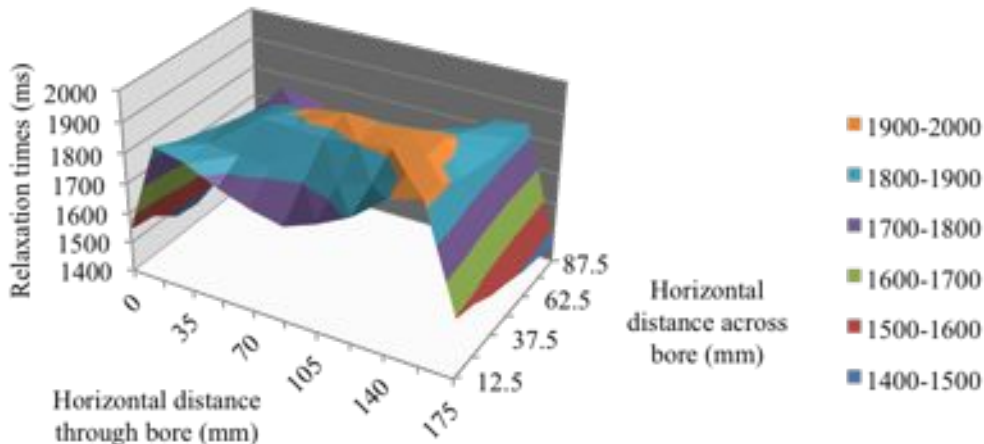


Figure 2.2: Variation in relaxation time of distilled water measured across the $^1\text{H}/^{19}\text{F}$ surface coil.

There is some variation across the coil, though it is only at the edges that there is a large drop in the relaxation times by several hundred milliseconds. This is probably simply due to the distance from the active part of the coil to the sample. There is not however an obvious pattern to the variation in the middle 5 x 15 cm rectangle above this coil, so proton measurements within this area can be expected to have an error of up to

200 ms in measured relaxation times as a result of the location.

The other significant point to note is that the relaxation times of the water samples are considerably lower than those measured using the head coil. With the head coil, the measured T_1 of water was roughly 2.9 - 3.1 seconds, whereas on the fluorine coil, the same samples are showing T_1 s of 1.8 - 2.0 seconds.

2.5 ^{19}F MR capabilities

The capabilities of the ^{19}F MRI system determine the requirements for a multimodal probe. The fluorine coil used in this work is a dual-frequency transmit and receive surface coil.

The detection capabilities of the coil were explored initially using an array of bottles containing 1 M trifluoroethanol (data not shown). It was then explored further, both in terms of lateral range and distance from the surface, by imaging a box containing a solution of 0.3 M trifluoroethanol.

This study was then extended to find the signal-to-noise ratios with compounds containing a range of equivalent fluorine substituent groups. This encompasses molecules comparable to those of direct clinical relevance, such as tri-fluorinated drugs, to molecules which would require special formulation due to their low solubility.

2.5.1 Fluorine imaging background

Fluorine MRI was first carried out by Holland in 1977 [208]. A glass tube containing 1.4 M sodium fluoride was imaged on a 0.7 T MRI scanner [110].

Since then field strengths have increased, and ^{19}F imaging has been carried out on a range of scanners. On the clinical strength end of the spectrum, samples were spectroscopically detected at 1.5T, with fluorinated drugs in the micromolar range and thousands of averages [15, 209]. Similarly, a 10 mM concentration of trifluoroethanol was examined at 3T, but again with 900 to 1800 averages [210].

On the research end of the spectrum, much development has been carried out on 11.7 T MRI scanners with perfluorocarbon emulsions in the low millimolar range, so requiring fewer averages in general [211, 12, 204].

These experiments were all carried out on systems with varying scanners, coils and pulse sequences. A significant problem with ^{19}F MRI being used clinically is the insensitivity of the technique. Many clinical studies to date have involved using high field MRI pre-clinical scanners, which can demonstrate the principle, but can give an overly optimistic view of what is currently possible clinically.

In the following section the capabilities of the available equipment for this project were investigated. A 3 T clinical MRI scanner was used with a commercially available coil and accompanying software extension. This provides a realistic picture of the challenges facing ^{19}F MRI.

2.5.2 Coil capabilities

The equipment was set up as indicated in Figure 2.3. A box containing 0.3 M trifluoroethanol was placed directly on the surface of the fluorine coil so that it covered the central area.



Figure 2.3: Arrangement of ^{19}F surface coil for imaging of a box of 0.3 M trifluoroethanol (TFE). The shape of the coil and its housing relative to the sample are illustrated.

Slices were imaged through the box, parallel with the surface coil, with increasing flip

angles. The closest slice to the coil is shown in figures 2.4a and 2.4b for high (40°) and low (3°) flip angles respectively. The area of the sample showing signal varies from the edge of the sample box (with high flip angle) to the location and shape of the coil in the centre (for low flip angle).

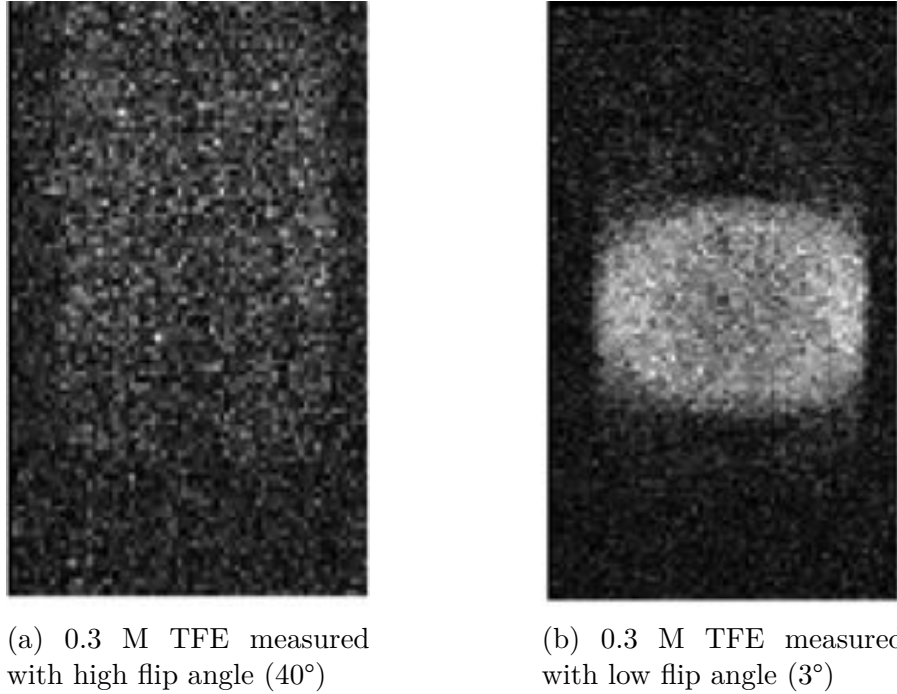
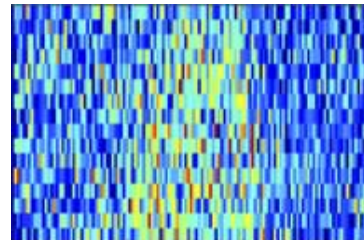


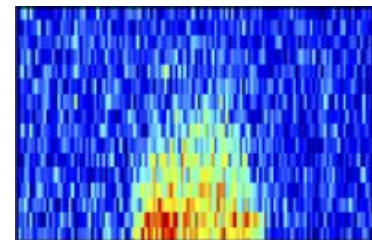
Figure 2.4: Comparison of images produced by ^{19}F MRI at high (a) and low (b) flip angles.

A cross section vertically through the slices is illustrated in Figure 2.5 to show the depth of the signal from the surface of the coil, which corresponds to the bottom of the images. For the high flip angle case the images are noisy, with the signal largely and most consistently coming from the area above the coil itself. The range of the signal is approximately 50 mm above the surface of the coil. For the low flip angle case there is a stronger signal from the area above the coil, but this is essentially lost within 30 mm of the surface. False colours are added for clarity.

The SNR through the centre of this cross section was plotted with distance, as shown in Figure 2.6. For the high flip angle case, the SNR remains roughly constant but is low, starting at 3 and dropping to 2.5 within 60 mm. In the low flip angle case, the SNR has dropped by 50% within 30 mm.



(a) 0.3 M TFE measured with high flip angle (40°)



(b) 0.3 M TFE measured with low flip angle (3°)

Figure 2.5: Comparison of cross sections of image stacks produced by ^{19}F MRI at high (a) and low (b) flip angles. The bottom of the images are directly on top of the coil, while the top of the images are 6 cm above.

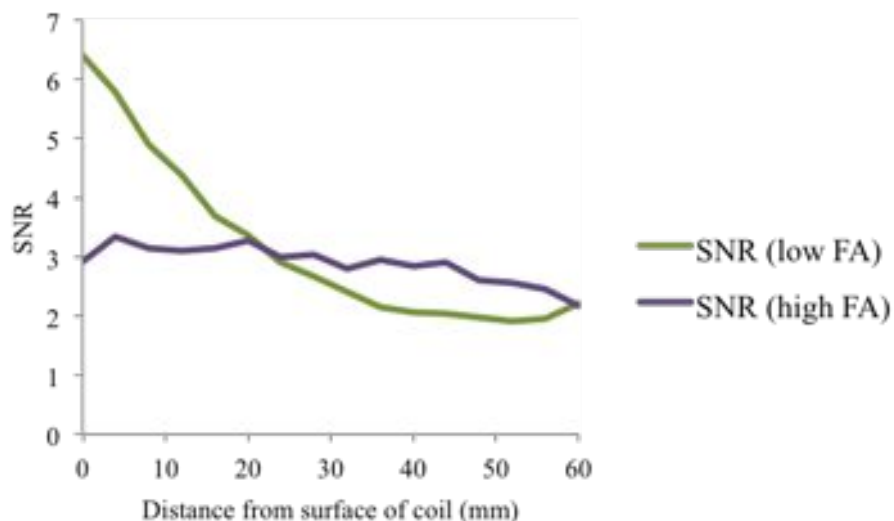


Figure 2.6: Comparison of SNR changing with distance from the coil surface. The image stacks were produced by ^{19}F MRI of 0.3 M TFE at high (40°) and low (3°) flip angles.

This indicates the limited range both in terms of the lateral area over which the coil can detect signal, and the distance from the coil the sample can be. This could potentially cause problems for *in vivo* imaging, since in the body the ^{19}F tracers could easily be more than 50 mm away from the coil.

For practical purposes this means that the amount of fluorine incorporated into a multimodal system must not only be high enough for detection with the most focused sequences (which will image close to the coil), but also with higher flip angles, which will allow a greater volume in which the fluorine can be detected.

Since much of the previous work on ^{19}F MRI has involved either high field strengths or small surface coils fitted directly over a small animal, a systematic and consistent investigation of the detection limits was undertaken for a range of fluorinated species. The broad aim is to provide a reference point for future work on clinical field strength ^{19}F MRI.

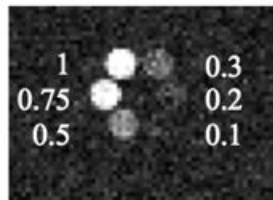
2.6 Detection limits of various molecules by ^{19}F MRI at 3 T

Before multimodal imaging agents can be created it is helpful to know the rough concentrations of the various components that will be required. There are competing effects in the selection of a fluorine tracer; a higher number of fluorines per molecule will produce a higher SNR but lower aqueous solubility or miscibility. Conversely lower numbers of fluorine will be more soluble in water, so more suitable for cell culture, but will have a reduced SNR.

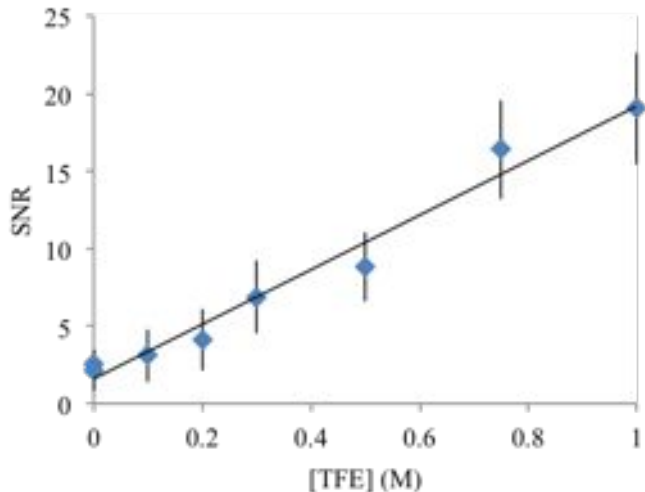
The effect of the number of fluorines per molecule on the SNR of ^{19}F MR images was therefore investigated to provide a reference point for the development of the multimodal agents.

2.6.1 Molecules with 3 equivalent fluorines

The detection limit for molecules with three equivalent fluorines was measured by the imaging of a range of concentrations of trifluoroethanol in water. The resulting image and the plot of the calculated signal to noise ratio is displayed in Figure 2.7.



(a) ^{19}F image of TFE. Concentrations are indicated in white in mol/L.



(b) Plot of SNRs vs. concentration.

Figure 2.7: Trifluoroethanol (TFE) imaged by ^{19}F MRI at a range of concentrations, and the corresponding plot of the SNRs. The error bars represent the error due to noise and variation across the region of interest.

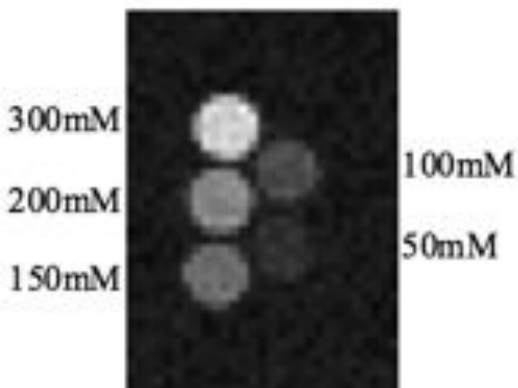
In Figure 2.7 it can be seen that an SNR of at least 15 is preferable, as this gives a distinct outline of the sample tube. This corresponds however to a molecular concentration of 0.73M, which is an unfeasibly high concentration for cell tracking purposes.

The lower concentration samples can be distinguished with an SNR of 5, produced by samples of 0.19 M. Such a high concentration is still unlikely to be possible in cell tracking situations. Moreover, though the sample can be delineated from this image, the contrast may still not be great enough for confident detection with unknown sample locations.

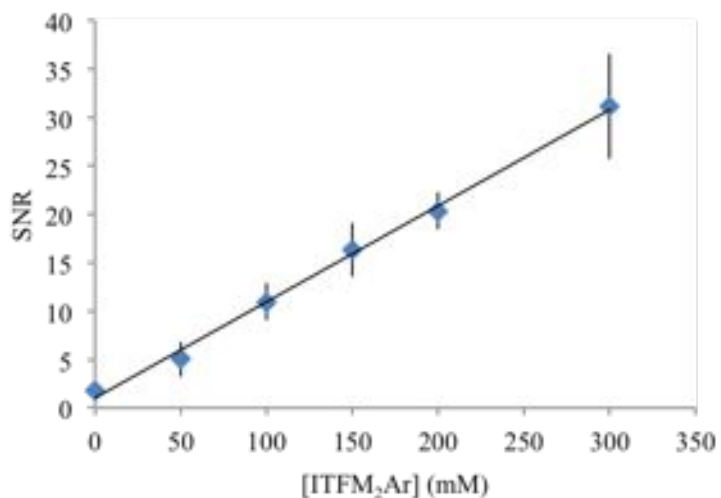
2.6.2 Molecules with 6 equivalent fluorines

1-iodo-3,5-bis(trifluoromethyl) benzene was used as a model for molecules with six MR-equivalent fluorines. The highest SNR was observed with a flip angle of 4° , so one of

the acquired images is shown in Figure 2.8a, and the SNR was calculated from this. The SNR is plotted against concentration in Figure 2.8b.



(a) ^{19}F image of ITFM₂Ar. Concentrations are indicated next to each sample.



(b) Plot of SNRs vs. concentration.

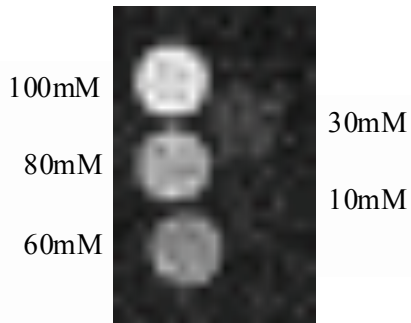
Figure 2.8: 1-iodo-3,5-bis(trifluoromethyl) benzene (ITFM₂Ar) imaged by ^{19}F MRI at a range of concentrations, and the corresponding plot of the SNRs. The error bars represent the error due to noise and variation across the region of interest.

For a SNR of 5, a concentration of 40 mM is required, whereas for an SNR of 15, a 141 mM solution is necessary.

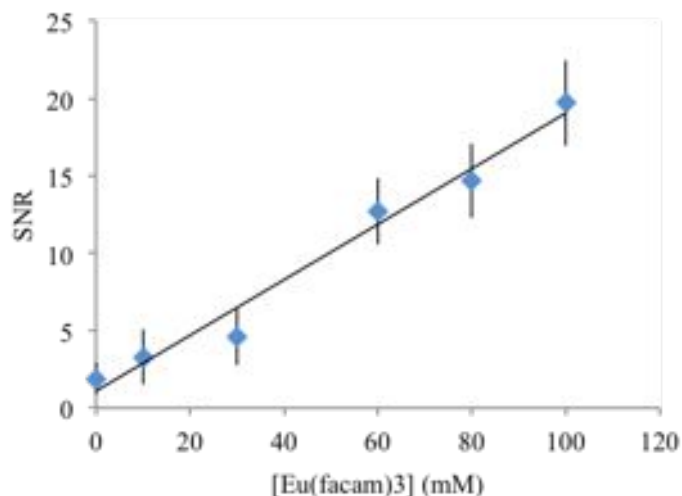
2.6.3 Molecules with 9 equivalent fluorines

Europium tris[3-(trifluoromethylhydroxymethylene)-(D)-camphorate] ($\text{Eu}(\text{facam})_3$) has 3 equivalent fluorine nuclei on each of its ligands, so was investigated as a complex with

9 equivalent fluorines. The SNR of the complex dissolved in methanol was examined at a range of concentrations and flip angles. The highest SNR appeared with a flip angle of 4°, and an image using this is shown in Figure 2.9 along with a plot of the SNR against concentration.



(a) ^{19}F image of $\text{Eu}(\text{facam})_3$. Concentrations are indicated next to each sample.



(b) Plot of SNRs vs. concentration.

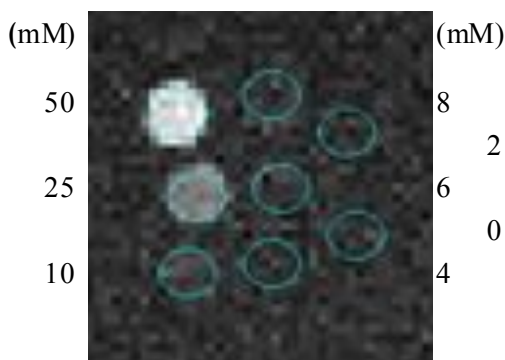
Figure 2.9: Europium tris[3-(trifluoromethylhydroxymethylene)-(D)-camphorate] ($\text{Eu}(\text{facam})_3$) imaged by ^{19}F MRI at a range of concentrations, and the corresponding plot of the SNRs.

For a SNR of 5, a concentration of 22 is needed in order to be able to detect the sample. As can be seen however from the image, this will not be clearly delineated. For a SNR of 15 a concentration of at least 77 mM is necessary.

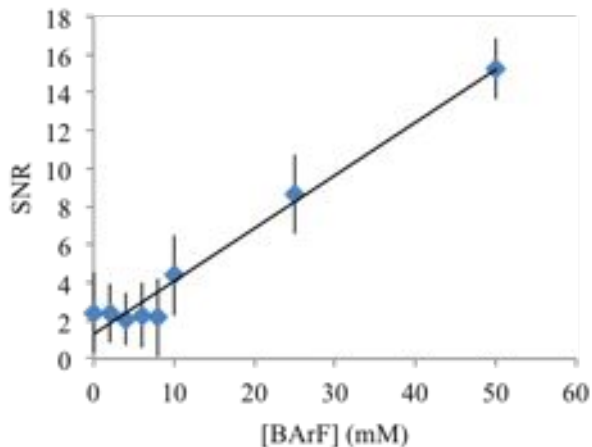
2.6.4 Molecules with 24 equivalent fluorines

The SNR of a molecule with twenty four equivalent fluorines was investigated. Tetrakis(3,5-bis(trifluoromethyl)phenyl)borate, known as BArF, was dissolved in diethyl ether and imaged at various flip angles. The SNR was highest using a flip angle of 8° , so data using this flip angle is presented.

A plot of the SNR varying with concentration is shown in Figure 2.10, along with an image of the regions of interest.



(a) ^{19}F image of BArF. Concentrations are indicated next to each sample.



(b) Plot of SNRs vs. concentration.

Figure 2.10: Tetrakis(3,5-bis(trifluoromethyl)phenyl)borate (BArF) imaged by ^{19}F MRI at a range of concentrations, and the corresponding plot of the SNRs.

For an SNR of 5, a concentration of 13 mM would be necessary, based on the fitted line in Figure 2.10. Ideally a much higher concentration of between 25 and 50 mM would

be present, since, as above, a clear signal should be visible for quantification, as can be seen in the image.

2.6.5 Discussion

The above results are summarised in Figure 2.11 as a plot of the concentrations needed to produce SNRs of 5 and 15, which correspond to distinguishable and clearly delineated samples respectively.

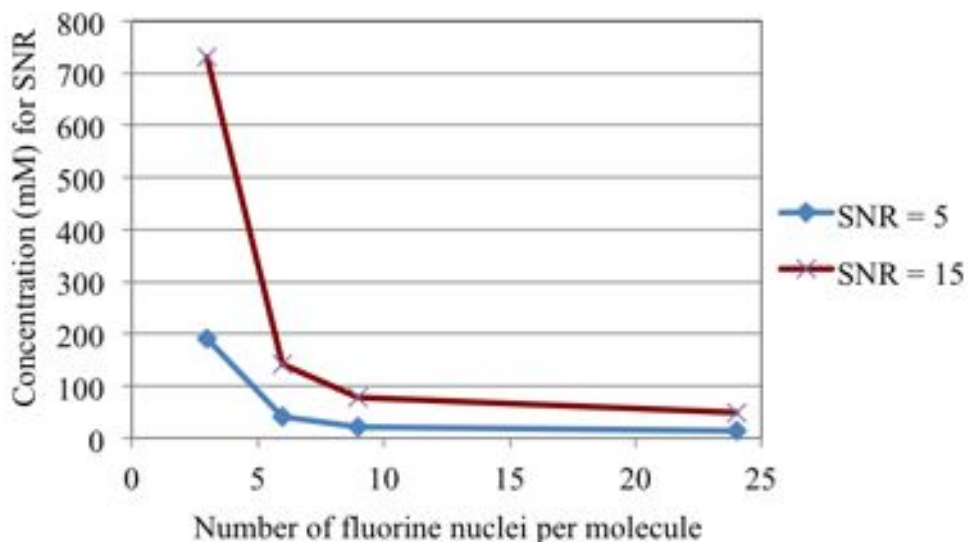


Figure 2.11: Plot of the required concentrations (in mM) to produce a given SNR (5 or 15) plotted against the number of fluorines per molecule.

It is interesting to note that the required concentrations do not correspond if considered in terms of fluorine concentrations, suggesting that there are other factors than concentration affecting the signal. These could include the viscosity of the sample, but also coil loading, the reception field distribution, the T_1 and T_2^* of the samples and the tip angle [212].

All of these need therefore to be carefully considered in future work, especially involving quantitation, so that these are taken into account when comparing, for example, a fluorine compound in tissue to a reference sample outside the body. These samples will not only have very different environments, affecting their viscosity, T_1 and T_2^* , but will

also be in different locations in the coil, leading to variation from coil sensitivity, receptor field distribution, and the tip angle experienced by the sample.

CHAPTER 3

TRAPPING IMAGING AGENTS IN A NANOPARTICLE MATRIX

Some nanoparticles consist of an extended network, such as a silica, in which other small molecules can be trapped. This can be achieved chemically by covalently linking the molecule to a monomeric component of the network, such as a silane [213, 214]. It can also be achieved physically by selecting both the nanoparticle and the molecule for their positive interaction. This chapter explores the physical trapping of imaging agents inside silica matrices.

3.1 Background and design

Imaging agents often rely on their molecular structure for their physical and chemical properties. For example, the fluorescent properties of fluorophores often depend on the presence of a planar aromatic system [215]. If imaging agents are incorporated into nanoparticles, it is therefore usually preferable for the molecular structure to be undisturbed.

While covalent linking of an imaging agent into the structure will have the advantage of more reliable entrapment and lower leakage levels (see examples in [216, 217]), it risks changing the imaging agent's structure by requiring a physical linker in some cases, and hence its properties. For some agents the change may be an improvement, as with some

fluorophores where an increase in the quantum efficiency is observed [218]. This limits the available agents however to ones where a linker can be attached without disrupting the agent's capabilities.

Physical entrapment into the nanoparticle matrix can be highly effective while maintaining the structural integrity of the imaging agent. It is also highly versatile, since to trap an alternative molecule only requires that they have similar physical properties, rather than requiring a reaction with a monomer of the network.

The nanoparticle matrix should have suitable properties to accommodate the molecules to be trapped. It should also be able to carry a high concentration of the imaging agents with the structure remaining fit for purpose.

Silica networks, for example, are robust covalent structures which have been modified extensively to tune their physical and chemical properties. Methods include the incorporation of silanes to modify the charge or hydrophobicity [219], to add fluorescence [214] and to introduce porogens to create mesoporous networks [168]. In this chapter silica and amine-modified silica have been used to electrostatically trap positively and negatively charged molecules respectively.

In terms of the nanoparticles' cargo, almost any small imaging agent could potentially be incorporated into a larger structure such as a nanoparticle. The main limiting factors are the interaction of the matrix with the molecules, the size of both structures, and the permeability of the matrix, for the molecules where this is relevant.

In this chapter the encapsulation of two modality agents were attempted: fluorophores for fluorescence techniques, and contrast agents for proton MRI. Where possible, clinically approved molecules were used as they have been studied thoroughly and their effects in the body are generally known. This was the case for proton MRI contrast agents, where Gd EOB-DTPA (marketed as Primovist by Bayer, UK) was used, and for fluorescein which is used in ophthalmic eye drops and angiography [220].

Initially ruthenium tris phenanthroline was trapped electrostatically inside a simple silica matrix. This method has been previously reported [165], and provided a basis for

early investigations. The versatility of silica nanoparticles however allows further surface functionalization in order to also image them by other modalities, as explored in Chapter 4.

Many imaging agents of interest, such as gadolinium chelates for MRI and organic fluorophores such as fluorescein, are negatively charged. These cannot be trapped electrostatically in a negatively charged silica matrix and hence positively charged silica matrices were explored in order to trap them. In this system, Gd DTPA-EOB and fluorescein were trapped inside a silica nanoparticle which was created by co-condensation with an aminated silane during the synthesis.

This idea was explored further in an attempt to create particles with no pH dependence in their properties (unlike the primary amine functionalised particles), which could potentially lead to a variable interaction with the imaging agents. The APTES was therefore replaced by a quaternary aminated silane, trimethyl[3-(trimethoxysilyl)propyl]ammonium chloride (Me_3APTMS). The synthesis was otherwise replicated, except for the addition of a base to catalyse the reaction. This was necessary since the reaction with APTES is autocatalysed.

3.2 Experimental details

The experimental details described here are used specifically in this chapter. All materials and experimental methods used in multiple chapters are described in the general experimental details in Chapter 2 to avoid repetition.

3.2.1 Materials

Silanes

Silanes used in this chapter are: tetraethyl orthosilicate (Acroseal, Fisher Scientific); (3-aminopropyl) triethoxysilane (98%, Alfa Aesar); trimethyl [3-(trimethoxysilyl)propyl]

ammonium chloride (ca. 50% in methanol, TCI Europe).

3.2.2 Nanoparticle synthesis

The synthesis of silica nanoparticles consisting of negatively charged and positively charged silica matrices are described here. Methods for doping these particles are also provided here.

Negatively charged silica nanoparticles

53.5 ml EtOH, 3.2 ml NH₄OH (28%), 1.6 ml TEOS and 1 ml [Ru(phen)₃](PF₆)₂ (1 mg/ml in acetonitrile) were placed in a round-bottomed flask. The solution was stirred for 24 hours, during which it became turbid.

The suspension was washed by centrifugation at 5000 rpm (approximately 3300 x g) for 30 minutes and resuspension in clean solvent. The nanoparticles were washed twice with ethanol and twice with water.

For storage the nanoparticles were resuspended in ethanol.

Primary aminated silica nanoparticles (ASiNPs)

Primary aminated silica nanoparticles (ASiNPs) were synthesised by a sonochemical method described in [221].

2 ml of tetraethyl orthosilicate (TEOS) and 0.5 ml of (3-aminopropyl)triethoxysilane were added to 15 ml of ethanol in a glass vial. The mixture was sonicated for 5 minutes, then 0.5 ml of distilled water was added dropwise.

The mixture was sonicated for 3 hours, during which time the solution became turbid and usually gelled.

The resulting gel or suspension was washed by centrifugation at 5000 rpm (approximately 3400 x g) for 20 minutes and resuspension in clean solvent. The nanoparticles were washed twice in ethanol and twice in distilled water.

For storage nanoparticles were resuspended in ethanol.

Gadolinium doped ASiNPs Instead of 0.5 ml of water, 0.5 ml of 12.5 mM GdEOB-DTPA was added dropwise to the silane mixture. The gadolinium solution was clinical grade Primovist (at 0.25 M) diluted with distilled water.

Fluorescein doped ASiNPs 5mg of fluorescein sodium was added to the silane mixture before the addition of the water.

Gadolinium and fluorescein doped ASiNPs 5mg of fluorescein sodium was added to the initial silane mixture, and 0.5 ml of 12.5 mM Gd EOB-DTPA was added as for the GdASiNPs.

Quaternary aminated silica nanoparticles (Me_3ASiNPs)

Quaternary aminated silica nanoparticles (Me_3ASiNPs) were synthesised by an analogous sonochemical method to the ASiNPs.

2 ml of tetraethyl orthosilicate (TEOS), 1.07 ml ethylamine and 1.2 ml of Me_3APTMS were added to 15 ml of ethanol in a glass vial. The mixture was sonicated for 5 minutes, then 0.5 ml of distilled water was added dropwise.

The mixture was sonicated for 3 hours, during which time the solution became turbid and usually gelled.

The resulting gel or suspension was washed by centrifugation at 5000 rpm (approximately $3400 \times g$) for 20 minutes and resuspension in clean solvent. The nanoparticles were washed twice in ethanol and twice in distilled water.

For storage nanoparticles were resuspended in ethanol.

The above synthesis was modified to incorporate various imaging agents.

Gadolinium doped Me_3ASiNPs Instead of 0.5 ml of water, 0.5 ml of 12.5 mM Gd EOB-DTPA was added dropwise to the silane mixture. The gadolinium solution was clinical grade Primovist (at 0.25 M) diluted with distilled water.

Fluorescein doped Me_3ASiNPs 5mg of fluorescein sodium was added to the silane mixture before the addition of the water.

Gadolinium and fluorescein doped Me_3ASiNPs 5mg of fluorescein sodium was added to the initial silane mixture, and 0.5 ml of 12.5 mM Gd EOB-DTPA was added as for the $\text{GdMe}_3\text{ASiNPs}$.

3.2.3 Nanoparticle characterisation

Nanoparticles were characterised by DLS and TEM as described in Section 2.2.1 and 2.2.2.

Encapsulation efficiency

The amount of gadolinium trapped in the nanoparticles was measured by ICP-MS. Samples were prepared according to Section 2.2.4.

MR contrast enhancement

Nanoparticle samples were diluted with ethanol to a range of concentrations as stated and placed in glass vials or polyethylene microcentrifuge tubes. ^1H MRI was carried out on a 3T clinical scanner; details and pulse sequences are described in Section 2.2.8.

3.3 Synthesis and characterisation results

Silica nanoparticles were created by the hydrolysis and condensation of silanes by two different methods. They are capable of electrostatically trapping a range of molecules in their matrix in order to deliver them into immune cells.

Positively charged species can be readily trapped in typical (negatively charge) silica structures, which were formed in this case by a modification of the Stober synthesis [163, 214]. This was carried out as a precursor to the dual-modal particle created in Chapter 4.

Negatively charged species however require a positively charged silica matrix for electrostatic trapping. Nanoparticles with positively charged networks were therefore created by sonochemical co-condensation of the silanes tetraethyl orthosilicate (TEOS) and 3-aminopropyl triethoxysilane (APTES), and doped with various negatively charged imaging agents.

3.3.1 Negatively charged silica nanoparticles

Doping silica nanoparticles with positively charged metal complexes is a well established technique [165]. Here ruthenium tris-phenanthroline-doped silica nanoparticles (RuSiNPs) were created.

This work is described here for completeness but, since this project is application-driven, the particles are characterised more fully in chapter 4 as the dual-modal system of interest.

Light scattering (DLS)

RuSiNPs diameters were measured by dynamic light scattering (DLS). The results are displayed in Table 3.1. Three repeat runs of the measurement were carried out, and the distributions produced, as well as the closest Gaussian fit to the distribution, are displayed in Figure 3.1.

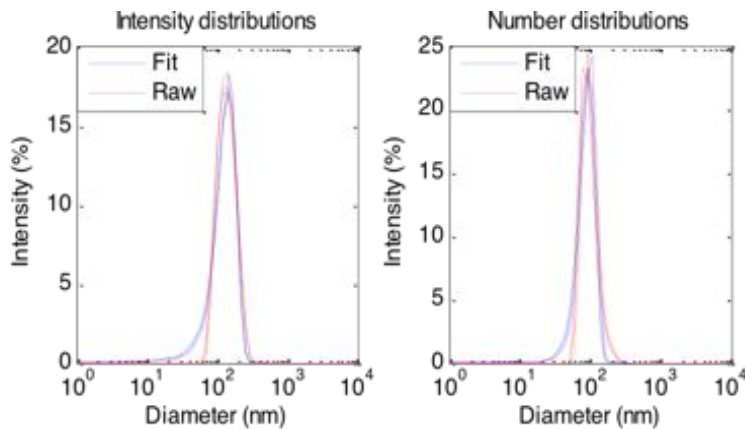


Figure 3.1: Histogram of RuSiNP radii measured by DLS analysis.

	Diameter (nm) (by intensity)	Diameter (nm) (by number)	Zeta potential (mV)
Mean	146	98	-55
Standard deviation	43	24	1

Table 3.1: DLS measurements of RuSiNPs

The number distribution was considered to indicate the more accurate diameter, making these particles 98 nm in hydrodynamic diameter with a standard deviation of 24 nm corresponding to a hydrodynamic radius of 49 nm, with a standard deviation of 12 nm.

Electron microscopy (TEM)

The size of the nanoparticles was also measured by electron microscopy. Images were analysed using the automated TEM analysis algorithm described in Section 7.1. Briefly, the magnitude and direction of changes in the image intensity were used to determine the edge locations, and then a heuristic circle detection method was used to find circular shapes matching the edges. These shapes, constrained by the direction of the intensity

changes, approximate the nanoparticle perimeters, and hence provide a diameter for each individual nanoparticle.

The mean radius of the RuSiNPs measured from 401 nanoparticles in such images was found by the above method to be $43 \text{ nm} \pm 6 \text{ nm}$. Characteristic images are shown in Figure 3.2. The plotted histogram of radii is shown in Figure 3.3.

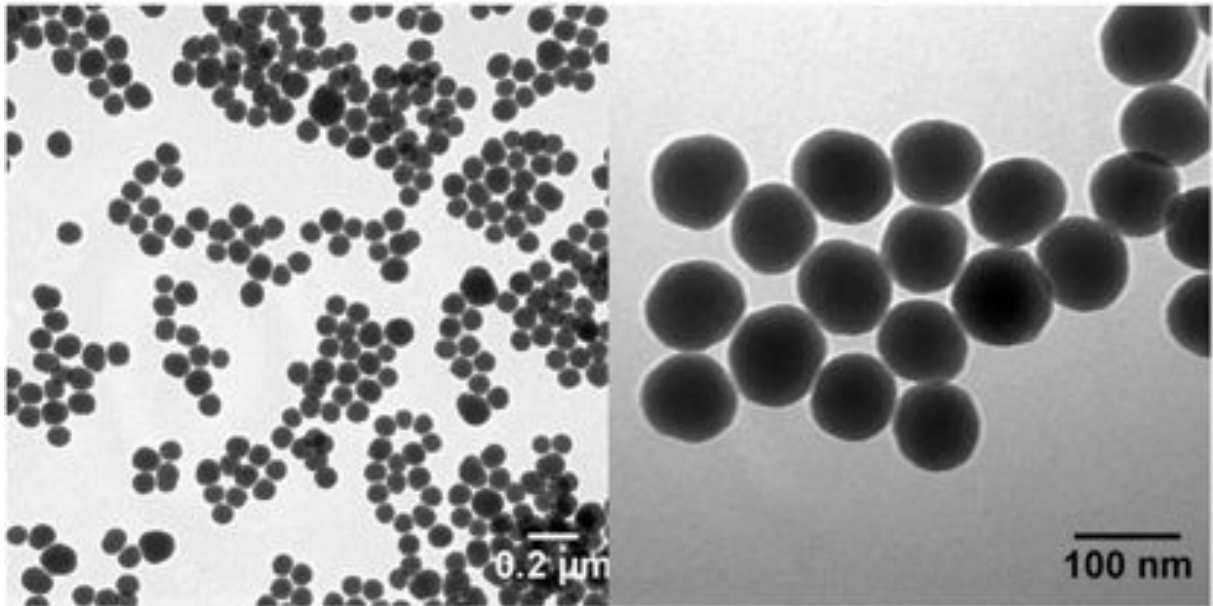


Figure 3.2: TEM images of ruthenium doped silica nanoparticles (RuSiNPs).

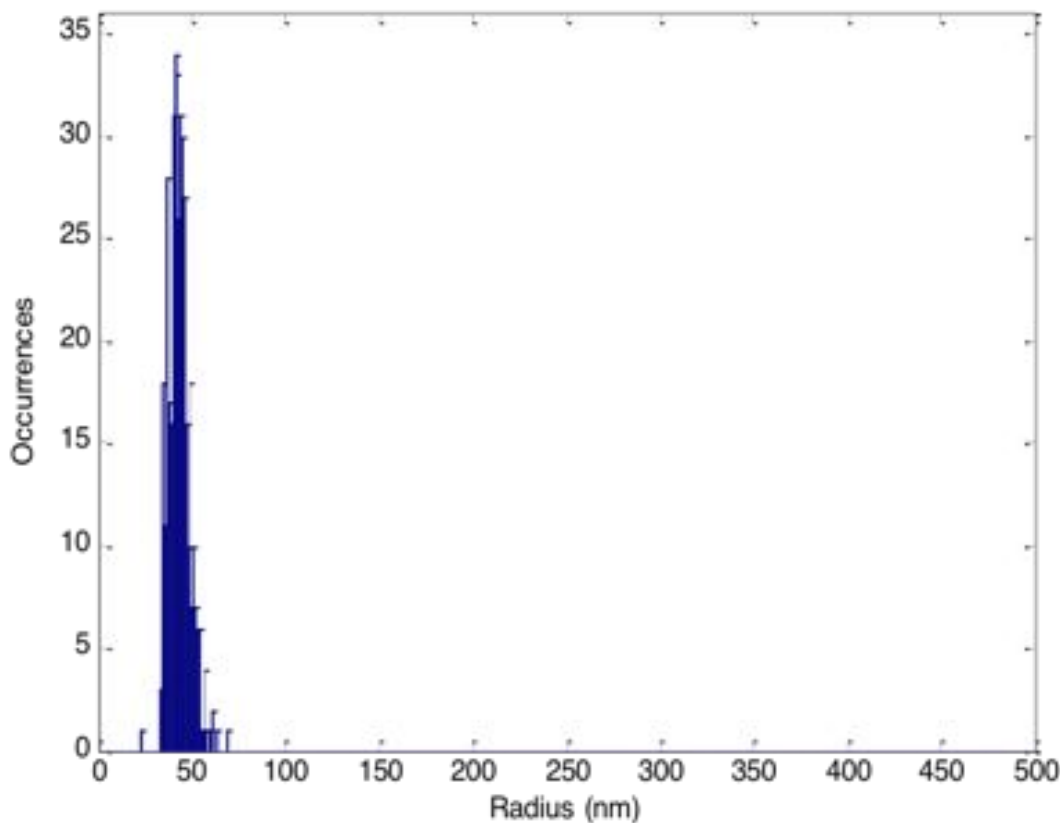


Figure 3.3: Histogram of RuSiNP radii measured from TEM images by automated segmentation.

As would be expected, the radius as measured by TEM, 43 nm, is slightly smaller than that measured by DLS, *i.e.* 49 nm. This could be due to TEM measuring only the dense core of the silica rather than the particle plus its hydration spheres, as with DLS [222]. It could also be an effect of TEM measuring only a microscopic sample, as opposed to the bulk measured with DLS, since these values are both within the standard deviation of each other.

Luminescence and luminescence lifetimes

The luminescence excitation and emission spectra are shown in Figure 3.4. Excitation scans were monitored at 590 nm and emission scans were excited at 480 nm.

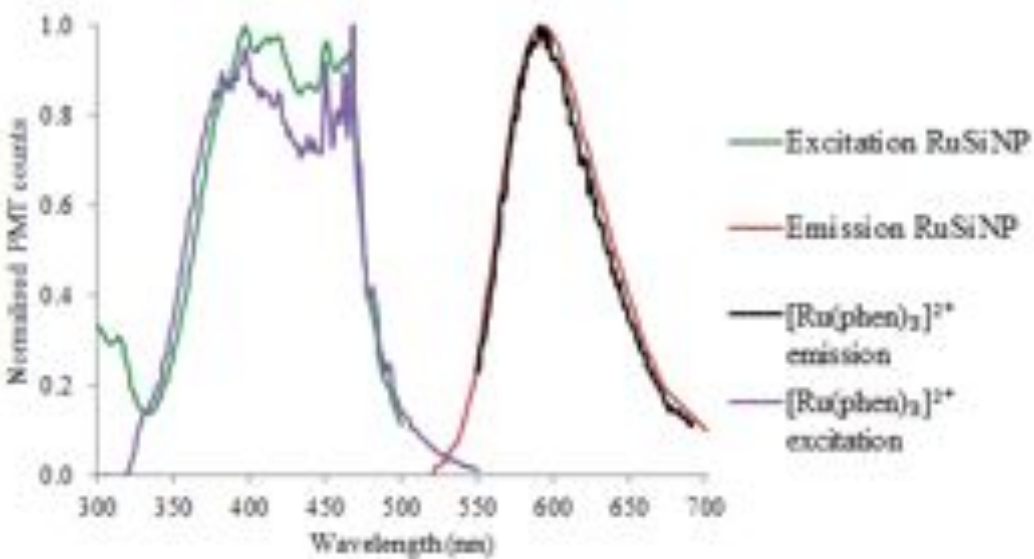


Figure 3.4: Excitation and emission spectra of RuSiNPs and $[\text{Ru}(\text{phen})_3]^{2+}$ in water and acetonitrile respectively. $\lambda_{ex} = 480 \text{ nm}$; $\lambda_{em} = 590 \text{ nm}$.

The ruthenium luminescence emission is not significantly affected by the trapping process, whereas the excitation spectrum appears to have broadened slightly. This might however be attributed to scattering by the particles. The emission spectrum has broadened very slightly upon trapping, but the maximum remains at 590 nm upon encapsulation. The spectra are comparable to those reported in the literature [122, 165].

The luminescence lifetimes for these nanoparticles are presented in Table 3.2. These are discussed in detail in Section 4.3.1, but are comparable with literature values.

Sample	t1 (ns)	t1 (%)	B1	t2 (ns)	t2 (%)	B2	t	A	χ^2
RuSiNP	547	13	280	1836	87	557	1405	7.7	1.03

Table 3.2: Luminescence lifetime measurements of the RuSiNPs

3.3.2 Primary aminated silica nanoparticles

Aminated silanes have frequently been conjugated to molecules of interest in order to functionalise silica nanoparticles; examples include references [223, 224, 225].

They have rarely been used to modify the entire structure of the nanoparticle at greater than dopant concentrations. Such nanoparticles have been described in the context of ceramics [221], but were not developed for biomedical ends. Mesoporous silica nanoparticles have been created also using a co-condensation method combining TEOS and a quaternary aminated silane [170], though here they claimed that due to the different hydrolysis rates of the silanes the amine groups are mainly localised on the surfaces. Consequently they claimed to trap indocyanine green into the pores by multiple interactions, and hence have not necessarily demonstrated trapping into the silica matrix.

The aminated particles developed for ceramics in reference [221] were therefore created by sonochemical co-condensation of TEOS and APTES in the presence of fluorescein and GdDTPA-EOB (Primovist). These are referred to as FlASiNPs, GdASiNPs and FlGdASiNPs for particles doped with fluorescein, GdDTPA-EOB and both compounds, respectively. Although the FlGdASiNPs are really the dual-modal system of interest, where relevant the separately doped ones were analysed in some cases to clarify the origin of a given effect.

Light scattering (DLS)

The FlGdASiNPs were analysed by DLS in various solvents. The results are displayed in Figure 3.5 and Table 3.3.

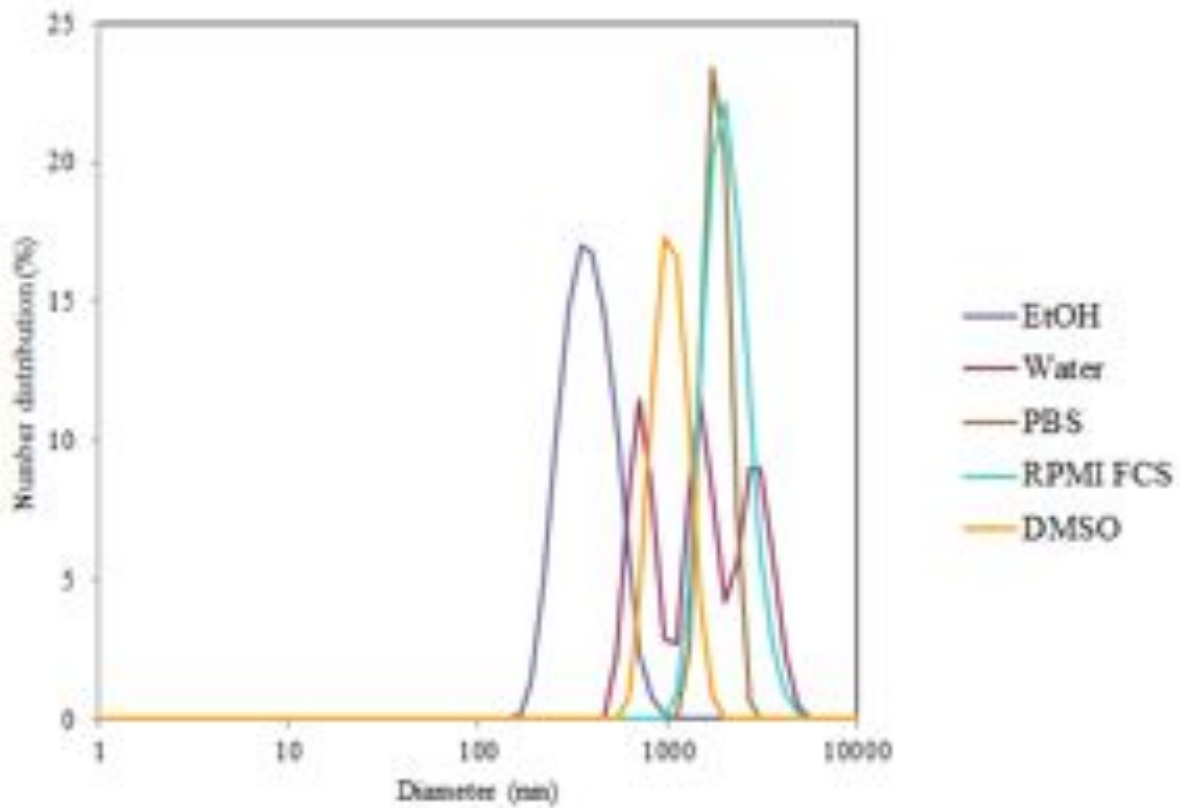


Figure 3.5: Distributions by number of diameters of FlGdASiNPs, measured by DLS. The FlGdASiNPs were suspended in a range of solvents to assess their level of aggregation. (N.B. In RPMI the samples were too unstable in suspension to obtain reliable measurements.)

Mean diameters (nm) per peak	EtOH	Water	PBS	RPMI + FCS	DMSO
Peak 1	373	729	1734	2192	986
Peak 2		1516			
Peak 3		2989			

Table 3.3: Peak means of the FlGdASiNPs' diameters, as measured by DLS and shown in Figure 3.5.

The FlGdASiNPs showed a concerning level of polydispersity. Given the particles' morphologies in the electron microscopy images (see Section 3.3.2), this could be a conse-

quence of aggregation. This is evident even in the ethanol dispersion, though this solvent produced the fewest aggregates greater than a micron in diameter.

Dispersion in aqueous salt-containing media, *i.e.* PBS and cell culture medium (RPMI 1640, both with and without 10% FCS), appears to cause the greatest level of aggregation. The effect of the peptides and salts in the RPMI itself could be disrupting the FlGdASiNPs' stability, since their presence has been shown to cause aggregation in variety of silica nanoparticles [226]. The distribution in the serum-containing medium however is consistent with reports of a protein corona, which occurs when proteins deposit on the nanoparticle surface [227]. This could be stabilising the particles enough to allow dispersion in the RPMI, though still creating aggregates.

The dispersion in water appeared to be aggregating during the experiment, as seen by the shifting in the distributions, which is also consistent with studies of aminated silica nanoparticles [226]. Dispersion in DMSO appears to result in significant aggregation, producing micron sized clusters, but which were stable, at least in the short term.

These results could be affected by the solvent polarity, but the calculations involved in obtaining them also rely on given solvent properties, which will be slightly different for each solvent. While this data was included where possible, some approximations were necessary. For example, the FCS containing RPMI would have had a higher viscosity than that with RPMI only. The RPMI was also coloured with an indicator, which would change the optical properties of the solution somewhat. Therefore, although the aqueous suspensions were treated as having similar colloidal properties, this may have skewed the results.

These results do suggest however that the nanoparticles have a low colloidal stability. The stability will be affected by a number of factors, including the surface charge of the particles, the density of the particles, the solvent and any excipients in the solvent (such as salts or peptides). These are discussed further below.

The zeta potential measurement of the FlGdASiNPs produced more reproducible results. Samples were measured in deionised water, and the obtained values are presented

in Table 3.4.

NP sample	Zeta potential (mV)	Standard deviation
FlGdASiNPs	30	0.2

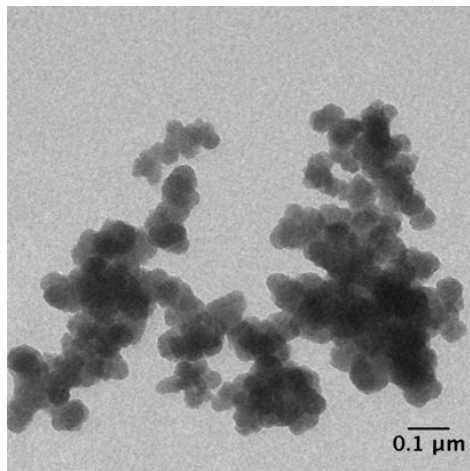
Table 3.4: The mean zeta potential of FlGdASiNPs and the standard deviation from the mean.

The standard deviation of the three measurements is small, suggesting that the surface charge is overall stable. The positive charge is expected due to the presence of the amine groups in the particles, and more promising than reports of the amine groups folding back in to interact with the negatively charged silane network, effectively neutralising the charge [228].

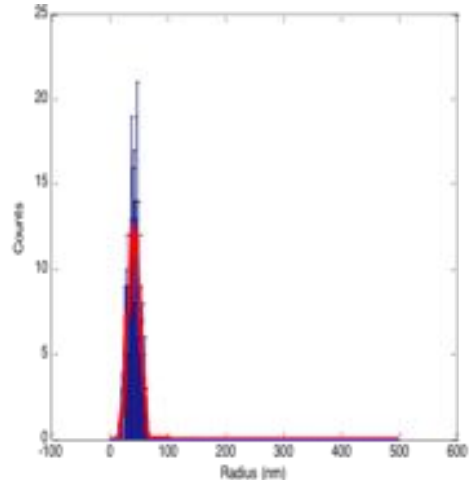
The low stability of the suspension indicated by the sizing experiment is somewhat explained by the relatively low surface charge; the colloidal stability should be improved by greater positive charge.

Electron microscopy (TEM)

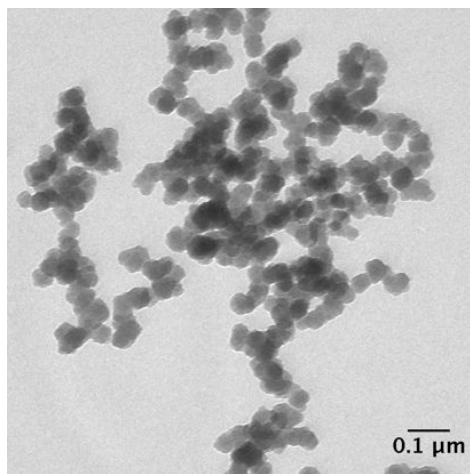
The FlGdASiNPs were analysed by transmission electron microscopy. Typical images of the nanoparticles doped with fluorescein (FlASiNPs), gadolinium-DTPA-EOB (GdASiNPs) and both agents (FlGdASiNPs) are displayed in Figure 3.6.



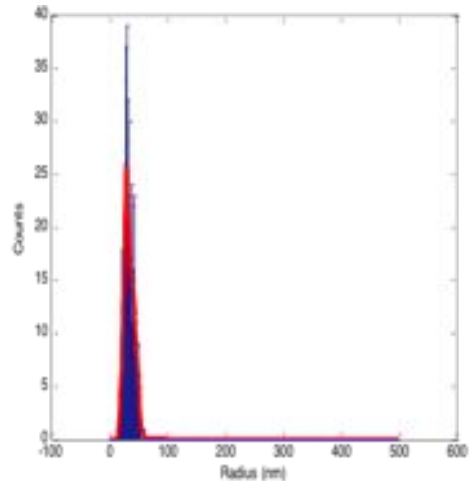
(a) FLASiNPs



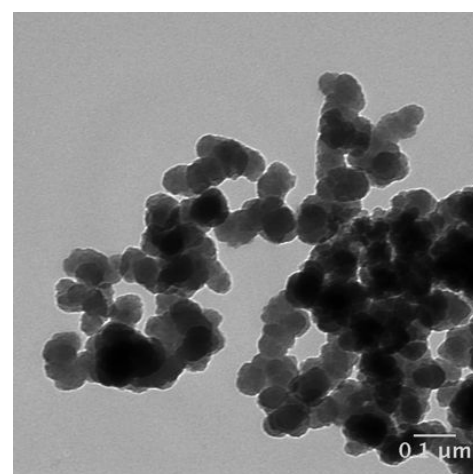
(b) Histogram of FLASiNP radii (nm)



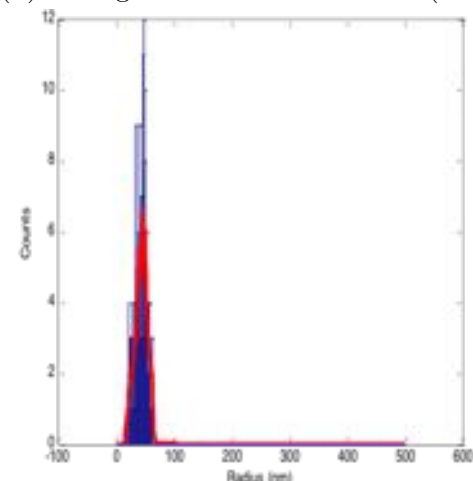
(c) GdASiNPs



(d) Histogram of GdASiNP radii (nm)



(e) FLGdASiNPs



(f) Histogram of FLGdASiNP radii (nm)

Figure 3.6: TEM images of doped ASiNPs containing (a) fluorescein, (b) gadolinium DTPA-EOB and (c) fluorescein and the gadolinium complex.

The radii were measured using the custom-written TEM analysis algorithm described

in Section 7.1, and are summarised in table 3.5.

ASiNP sample	Mean radius (nm)	Standard deviation	No. NPs measured
FlASiNPs	42	12	395
GdASiNPs	34	10	618
FlGdASiNPs	44	13	195

Table 3.5: Radii of ASiNPs as measured by TEM.

The dual modal fluorescein and gadolinium labelled nanoparticles are 44 nm in radius by TEM. This is considerably smaller than the sizes measured by DLS, though this can be explained by the aggregates that are visible in the TEM images, which would be all the DLS would detect if they existed as such in suspension as well as when dry.

The morphology is consistent with other silica gels, which have been reported to form fractal-like aggregates in some cases [229, 230]. These structures and their properties would need to be investigated thoroughly if these particles were found to be of interest for this project or future work.

The other point to note is that the particles labelled with gadolinium were consistently smaller than those which incorporated fluorescein. The reason for this is unclear since the mechanism of formation of these particles has not been explored. This does not affect the dual modal system investigated here, but is a consideration for further development of this system to include other imaging agents.

Encapsulated concentration

The gadolinium content of the dual modal fluorescein gadolinium nanoparticles was measured by ICP-MS, as described in Section 2.2.4.

A 10 mg/ml solution of FlGdASiNPs was found to contain an average of 5.16 µg of

gadolinium per ml (standard deviation of 0.22 µg (Gd) / ml). Therefore the nanoparticles contained 0.516 µg(Gd) per mg of nanoparticles.

The fluorescein concentration could not be calculated accurately by absorption because the quantum yield would have been changed by interaction with the nanoparticle matrix, as suggested by the lifetimes, presented below in Section 3.3.2. As indicated by the same luminescence results however and by the cell study experiments below (Section 3.4), the combination of the concentration of fluorescein and the remaining fluorescence is readily sufficient for cell labelling purposes.

Luminescence

The luminescence of the fluorescein labelled ASiNPs were measured and compared to free fluorescein in solution.

The fluorescence spectrum of the FlGdASiNPs, see Figure 3.7 is not shifted significantly, with the excitation wavelength maximum remaining at 492 nm when free and trapped alone, but rising to 499 nm when trapped with the gadolinium complex. The emission maximum changes slightly, with the free fluorescein at 518 nm, the FlASiNPs shifting to 516 nm and the FlGdASiNPs at 517.5 nm. The peak width for both the excitation and emission appears to have narrowed upon trapping.

It is worth noting however that the fluorescence spectrum of fluorescein is quite variable in these small ways depending on the protonation state and solvent [231, 232]. It indicates however that the fluorophore has not been significantly disrupted.

Sample	t1 (ns)	t1 (%)	B1	t2 (ns)	t2 (%)	B2	t	A	χ^2
FlASiNPs	1.737	24.4	0.062	3.87	75.5	0.086	2.98	106.05	1.189
FlGdASiNPs	3.448	79.5	0.06	5.48	20.5	0.01	3.74	55.85	1.06

Table 3.6: Luminescence lifetime measurements of the FlGdASiNs and FlASiNPs.

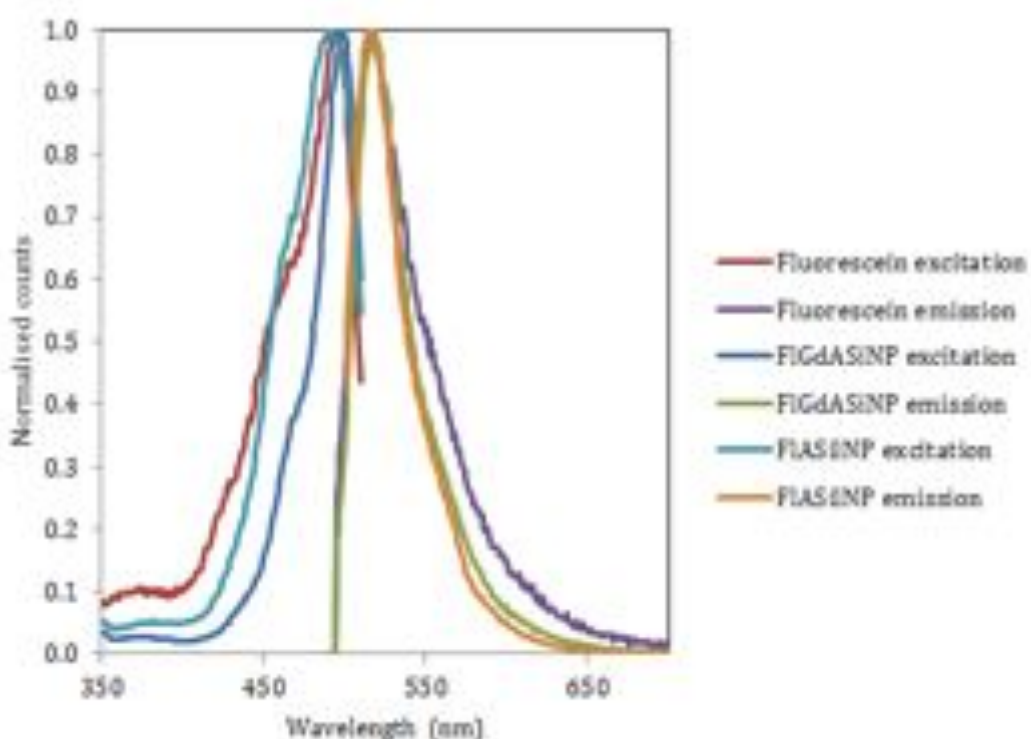


Figure 3.7: Excitation and emission spectra of FlGdASiNPs, FlASiNPs and fluorescein, all in distilled water. Excitation scans were monitored at 520 nm and emission scans were excited at 490 nm.

Luminescence lifetime data for the fluorescent ASiNPs is presented in table 3.6.

The fluorescence of free fluorescein in solution varies with pH, but can be considered to be in the region of 4.3 ns - 4.6 ns at pHs above 6.35, and shorter for lower pHs [233]. Longer lifetimes have however been observed when the molecular motion is hindered by a silica structure [234].

Neither of the fitted lifetimes of these nanoparticle formulations match the value for free fluorescein, suggesting that the fluorescein molecules are interacting with the matrix, and that there is little or no detectable free fluorescein present.

The fitted lifetimes for the FlASiNPs, (1.74 ns (24%) and 3.87 ns (76%) are similar to those reported for FITC-doped silica nanoparticles in reference [235], that is 1.6 (32%) and 3.79 (68%), though the calculated total lifetime differs due to the relative percentages.

For the FlGdASiNPs the lifetimes are considerably different, though there is still a lifetime of 3.45 ns for the majority of the emission. The second lifetime fit of 5.5 ns is similar to that seen for fluorescein doped into SBA-15 nanoparticles [234].

It should be noted however that reports are varied for the lifetimes of fluorescein in trapped and untrapped states, and these are highly dependent on the protonation state and the environment [233, 231, 235, 232]. Comparisons to literature values are therefore made with some caution, but suggest that the fluorescein is trapped in the matrix.

MRI contrast enhancement

A MR image of the FlASiNPs, GdASiNPs and FlGdASiNPs in solution is displayed in Figure 3.8, and the corresponding relaxivities are shown in Table 3.7 and Figure 3.9.

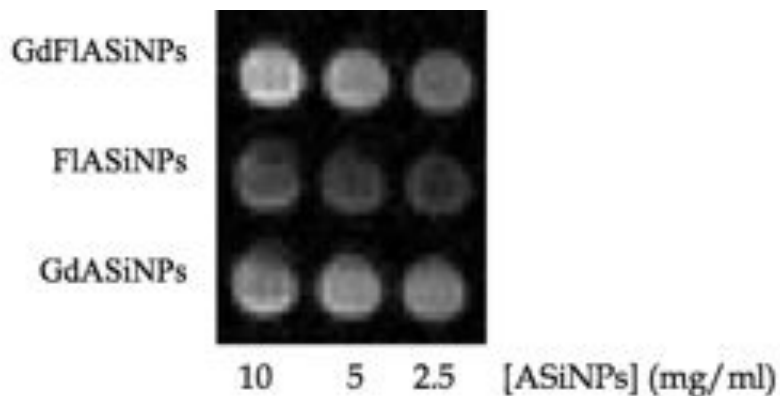


Figure 3.8: ^1H MR image of ASiNPs containing fluorescein, gadolinium and both imaging agents together.

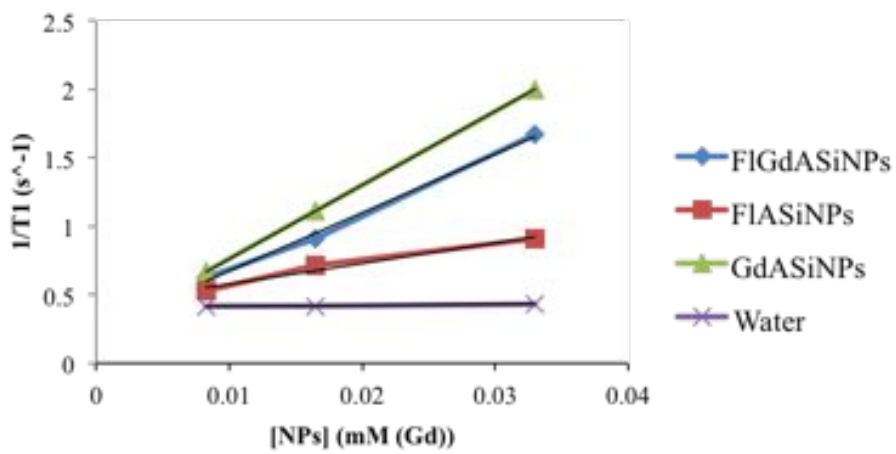


Figure 3.9: MR relaxivities ASiNPs containing fluorescein, gadolinium and both imaging agents together. Values were calculated (a) per nanoparticle and (b) per gadolinium.

ASiNP sample	Relaxivity $s^{-1}mM^{-1}$	Relaxivity $s^{-1}(mg/ml)^{-1}(NP)$
FlGdASiNPs	43	0.14
FlASiNPs	(15)	0.05
GdASiNPs	(54)	0.18
Water	(0.78)	0.003

Table 3.7: MR relaxivities of FlGdASiNPs, FlASiNPs and GdASiNPs, calculated per gadolinium ion and per nanoparticle. N.B., numbers in parenthesis are not true measured values but are provided for comparative purposes, as discussed in the main text.

Overall the GdASiNPs, labelled only with gadolinium, show the greatest concentration-dependent change in relaxation rate. The effect is slightly reduced for the FlGdASiNPs as fluorescein is expected to displace some of the gadolinium chelates in the dual-modal particles. The FlASiNPs show the least concentration-dependent change in relaxation rate, as would be expected considering the lack of gadolinium.

The relaxivity of the FlGdASiNPs is $43 \text{ s}^{-1}\text{mM}^{-1}(\text{Gd})$, and can be calculated accurately in relation to the number of gadolinium ions since the number of gadolinium ions present in a typical sample was measured by ICP-MS. The other values plotted in Figure 3.9 and table 3.7 are calculated as if the samples had the same Gd content as the FlGdASiNPs, and are therefore inaccurate, but are provided for control purposes.

Only the Gd content of the FlGdASiNPs was measured to minimise unnecessary handling of hydrofluoric acid, which was necessary for the sample preparation for ICP-MS.

The relaxivity of the water sample, $0.8 \text{ s}^{-1}\text{mM}^{-1}(\text{Gd})$, gives an indication of the error involved, since these samples contain no nanoparticles or gadolinium. The relaxivity of the FlGdASiNPs is well outside this range, suggesting that there is contrast enhancement occurring. The magnitude of the relaxivity value has been observed in mesoporous silica nanoparticles [169, 236], and could be attributed to a geometrical confinement effect [237]. The FlASiNPs however show an unexpectedly high relaxivity of 15 s^{-1} , which suggests that some of the relaxation effect is also due to the nanoparticles themselves rather than the gadolinium. The presence of the nanoparticles would increase the viscosity of the solution [238], so some concentration-dependent change in the relaxation rate is expected.

3.3.3 Quaternary aminated nanoparticles

In an extension from Section 3.3.2, there was an attempt to remove the inherent pH dependence of the system through the incorporation of quaternary amines instead of primary amines.

The synthesis was replicated, with the substitution of the relevant amines. One obstacle however was that the synthesis of the primary amines was auto-catalysed. With no basic amines present, extra base was required to initiate the hydrolysis of the silanes. Various bases were tried, including ammonium hydroxide, ethylamine and triethylamine, with added volumes controlled so the pH of the solution matched the starting conditions of the ASiNP reaction.

Fluorescein and gadolinium were incorporated as above, with the results referred to as

FlMe₃ASiNPs, GdMe₃ASiNPs and FlGdMe₃ASiNPs. The resulting gels were dispersed and characterized by DLS and TEM, as shown below.

Light scattering (DLS)

The suspensions of the Fl, Gd and FlGdMe₃ASiNPs were analysed by dynamic light scattering (DLS). The consequent distributions were fitted to Gaussian distributions, as presented in Figure 3.10. The mean diameters and standard deviations stated are those of the fitted curves.

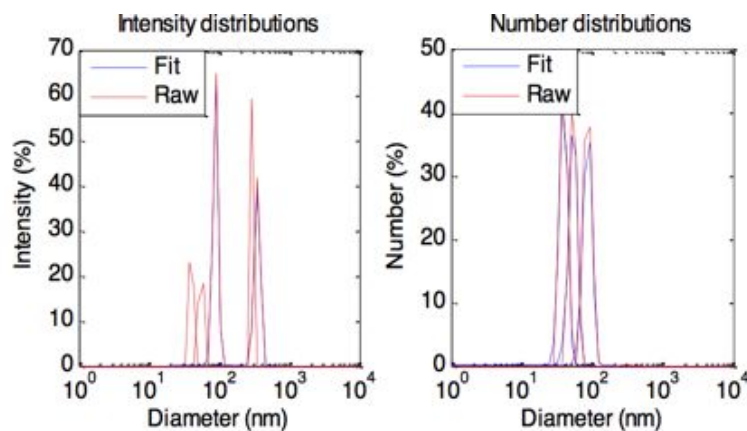


Figure 3.10: Distributions by number and intensity of diameters of FlGdMe₃ASiNPs, measured by DLS.

FlGdASiNP	Diameter (nm) (by intensity)	Diameter (nm) (by number)	Zeta potential (mV)
Mean	1085	1076	27.9
Standard deviation	332	298	6.37

Table 3.8: Mean diameter of FlGdMe₃ASiNPs as measured by DLS. N.B., only the number distribution means are shown since the intensity distributions, shown in Figure [subfig ref] were too polydisperse to provide an accurate fit.

The size distributions obtained by DLS indicate that nanoparticles did not form from

this method. The fluorescein doped silica preparation shows some particles in the tens of nanometres size range, though the variation between the three experimental runs shows that the samples are not stable. This variation and low stability is also observed for the GdMe₃ASiNPs and the FlGdMe₃ASiNPs, though this is less obvious due to the plots being presented on a logarithmic scale. Both of the preparations which contain gadolinium also have size distributions in the micron range, suggesting that they would not be suitable for labelling cells.

The surface charge of these particles is positive for all three dopant formulations. This should encourage interactions with the cell membrane, and hence improve cell uptake. The values are however unexpectedly lower than that seen for the ASiNPs, which could be due to the incomplete or unsuccessful formation of the nanoparticles. This is explored further in light of the electron microscopy results below.

Electron microscopy (TEM)

The TEM samples of the FlMe₃ASiNPs were prepared according to the standard method described in Section 2.2.2. The other Me₃ASiNPs were also similarly prepared, but no structures could be found on the grids when analysed, and since only micron-sized structures could be seen by DLS, these systems were pursued no further.

There were no discrete particle-like structures observed for the FlMe₃ASiNPs. Instead, a broad range of shapes were seen as a varying continuum across a large section of the grid. Snapshots of these are shown in Figure 3.11. It should be noted that the circular shapes in some of these snapshots could not be focused through in the same way as spherical particles, and can therefore be considered to be flat object

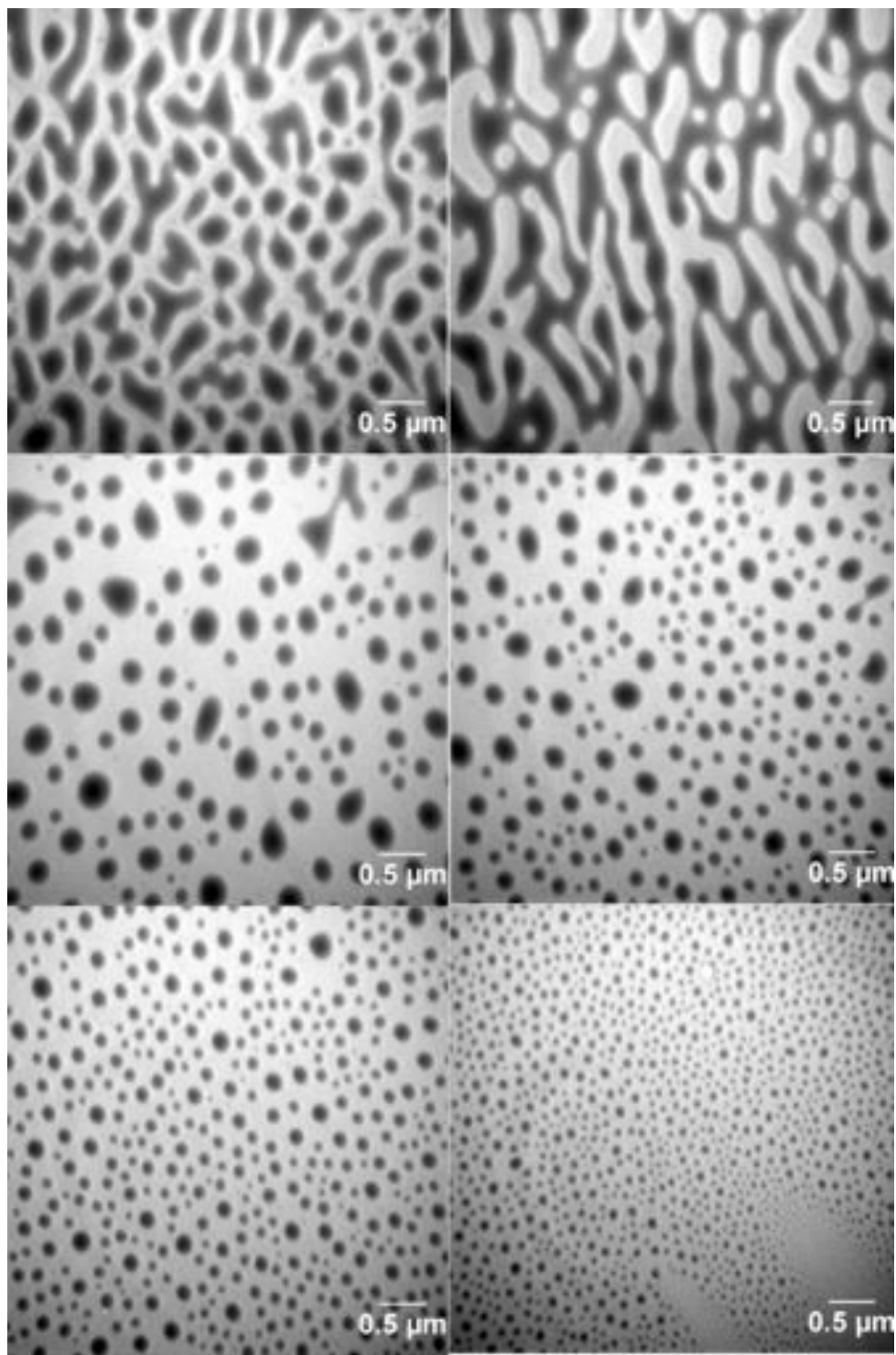


Figure 3.11: TEM images of quaternary aminated silica nanoparticles labelled with fluorescein.

One suggestion to explain these patterns is that the gel, instead of consisting of discrete particles as for typical nanoparticles, is more homogenous, and has dried flat on to the

grid. Based on the DLS results (Section 3.3.3), there may have been spherical structures prior to dehydration. Further investigations would be necessary to characterise the gel if this system were pursued.

Luminescence

The luminescence spectra of the aminated silica gels were measured in order to determine whether the gels could be used as fluorescent markers. The spectra are displayed in Figure 3.12.

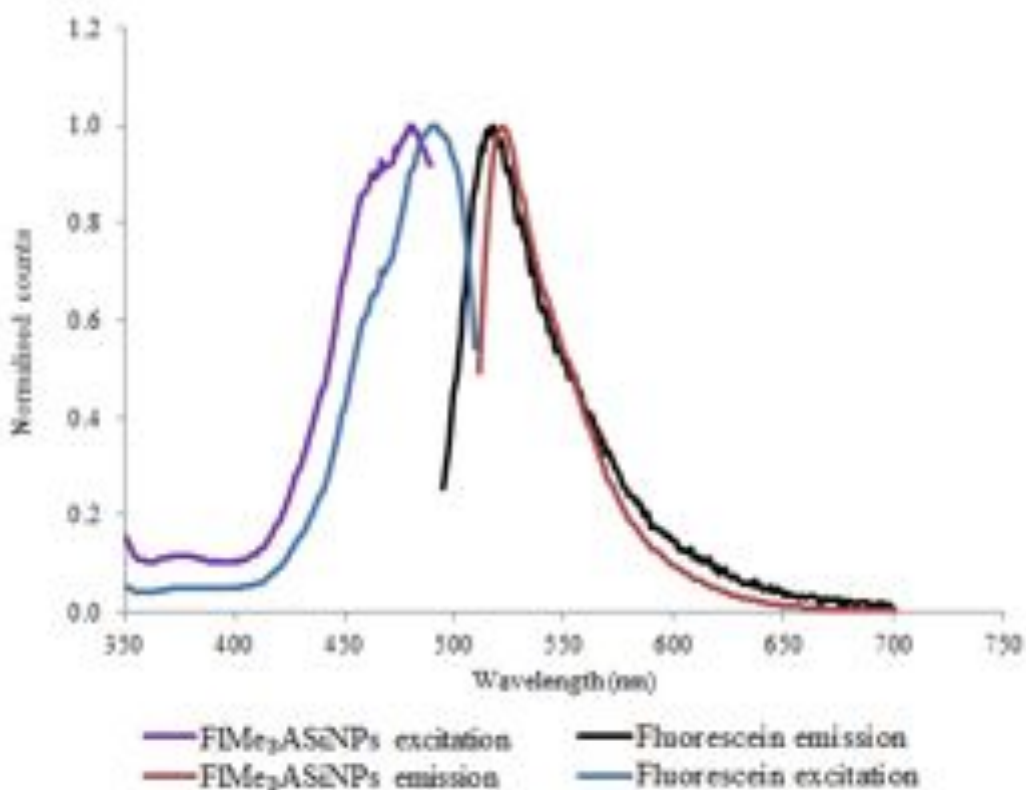


Figure 3.12: Excitation and emission spectra of FlMe₃ASiNP gels and fluorescein.

The spectra are similar to fluorescein fluorescence spectra, with some broadening in the excitation spectrum, possibly due to scattering, and a small increase in the Stokes shift.

Given the DLS and TEM results, these gels were considered to fall outside the specifications of this project so further work was halted in favour of other systems.

3.4 Cell treatment results

The interaction of developed nanoparticle systems with cells is essential to determining whether they could be a useful tool for immune cell therapies. The aim of these experiments was therefore to observe which cell types, if any, would take up the most promising nanoparticles and, if so, any significant effect on the cell morphology or viability.

Particles similar to the RuSiNPs have shown good uptake into cell types other than immune cells [236, 239]. Since the dual modality aspect is of the most interest, however, cell tests were only carried out on the particles which had been further functionalised to incorporate gadolinium. These results are presented in Section 4.4.1.

The FlGdASiNPs were carried forward due to their dual-modality. Their uptake into cells might be expected to be greater than the RuGdSiNPs since they have a positive surface charge [9]. There have however been reports of toxicity concerns with aminated silica particles, attributed at least partly to disruption of the cell membrane [240], which would need to be thoroughly investigated if the FlGdASiNPs were to be pursued further.

PBMCs include a range of white blood cells which could potentially be of interest in immune cell therapies, especially monocytes and lymphocytes. PBMCs were therefore treated with FlASiNPs, GdASiNPs and FlGdASiNPs, and observed by flow cytometry, fluorescence microscopy and ^1H MRI.

3.4.1 Flow cytometry results

The effect of the nanoparticle treatment on the cells was investigated by measuring the forward scatter and side scatter of a laser passing perpendicularly through a stream of individual cells. The forward scattered light indicates the size of the cell, since the larger the cell the more it will slightly deflect the beam. The side scatter, which is measured at a much higher angle, shows the granularity of the cell, since high granularity will deflect the beam more.

These two properties of each individual cell are plotted on a forward scatter vs. side

scatter plot to give an overview of the size and granularity of the cell population. Since different cell types will intrinsically have different such properties they will tend to cluster together, which are referred to as clouds.

The forward vs. side scatter plots for PBMCs with no nanoparticles, 0.1 mg/ml of FlGdASiNPs and 0.5 mg/ml are shown in Figure 3.13 as the extremes of the treatment results. These plots have an ellipse marking the monocyte cloud. The lymphocyte cloud is the high intensity area below and slightly to the left of the monocyte cloud.

Another rough but useful measure can be the amount the cloud of a given cell type moves with treatment. This was measured here by the percentage of the whole cell population remaining in the selected gate with increasing nanoparticle concentration treatments, and is presented in Figure 3.14 for treatments with FlGdASiNPs and FlASiNPs.

As can be seen from Figure 3.14, there is a significant reduction in the cells within the original gate at 0.5mg/ml, suggesting that the cells have undergone significant changes. From the corresponding scatter plot it is clear that the cell size is reduced, since the cloud has moved to the left. It also appears to have spread in terms of granularity, with some cells higher in the plot, so more granular, and therefore possibly containing large nanoparticle aggregates, and some cells much less granular, so either shrunk or completely disrupted.

This trend is apparent in the lower nanoparticle concentration plot, with the trend increasing with treatments.

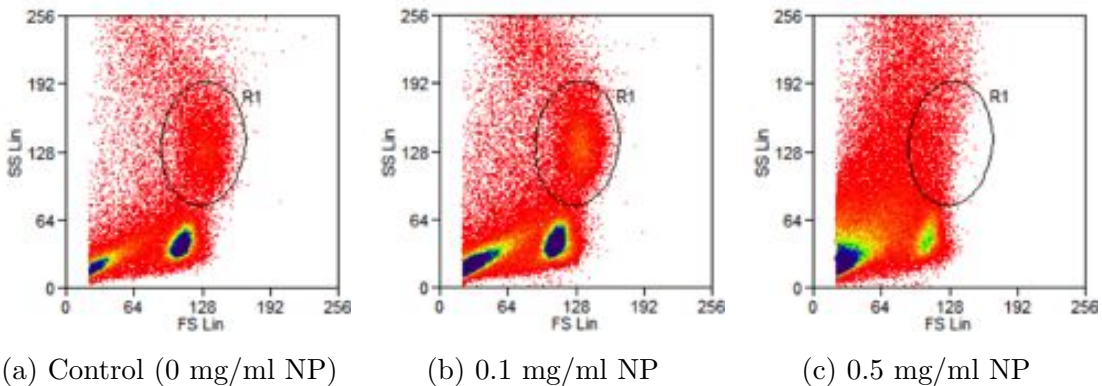


Figure 3.13: Forward scatter (FS) vs. side scatter (SS) plots for different nanoparticle treatment concentrations, showing the changes in size and granularity of the cells. The monocyte gate is highlighted by the black ellipse.

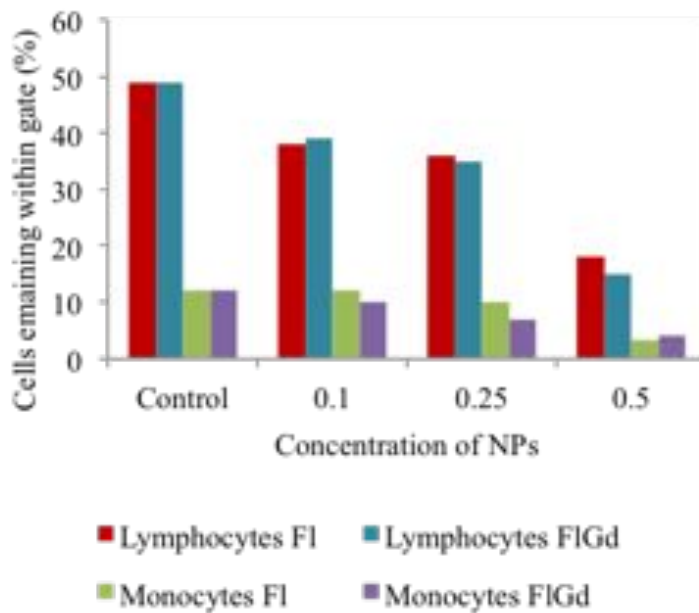


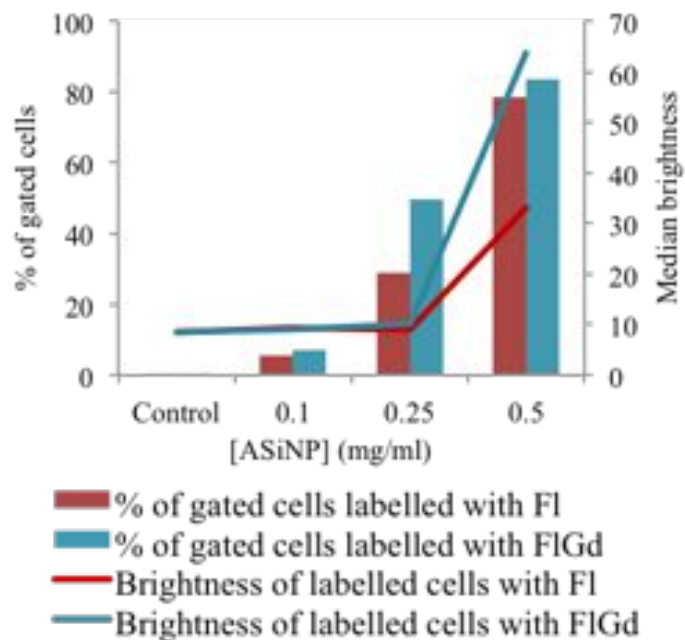
Figure 3.14: Plot showing percentage of cells (monocytes and lymphocytes) remaining within original gate with increasing nanoparticle concentration (FlASiNP and FlGdAS-iNP) treatments.

A bandpass filter was simultaneously used so as to be able to detect the fluorescein content in the cells. After the autofluorescence was gated out, the fluorescence brightness displayed by each cell was measured on a histogram. The percentage of cells showing fluorescence above the autofluorescent range, and the median of the histogram peak, were measured both within the monocyte and lymphocyte gates. This therefore suggests

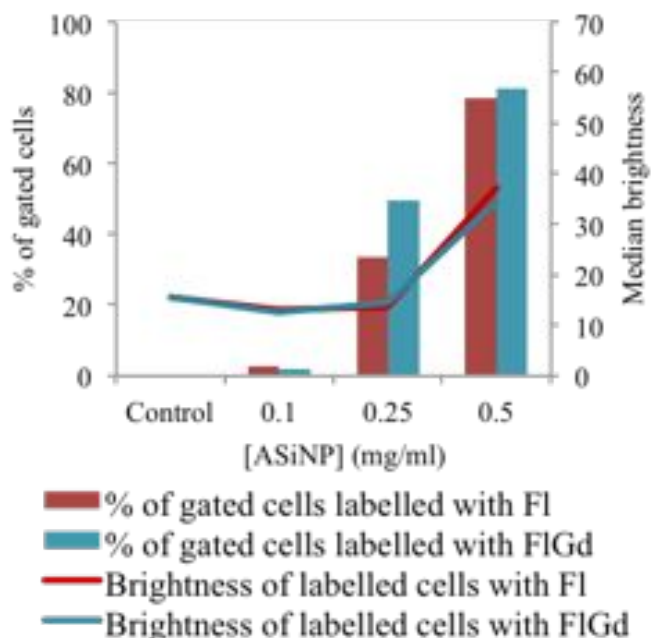
both what proportion of the cell type have taken up nanoparticles, and how much they have taken up. These values are presented in Figure 3.15, both for treatments with FlGdASiNPs and FlASiNPs.

As can be seen, at lower concentrations, only a small percentage of the cells have taken up any nanoparticles to a detectable concentration, with only a small shift in the histogram. By 0.25 mg/ml of nanoparticles the labelling has increased to 50% for both cell types with FlGdASiNPs. Curiously for both cell types the uptake of the FlASiNPs is lower, though this could have been experimental error due to treatments with very small quantities of nanoparticles, which showed some aggregation.

The brightness of the cells, *i.e.* the median fluorescence, is roughly proportional to the percentage of labelled cells at the lower concentrations. At the higher concentrations, the cells remaining within the size and granularity gate are clearly showing a high degree of fluorescence. In the monocytes there is a much greater shift in the FlGdASiNP brightness than in the FlASiNPs at the highest concentration.



(a) Monocytes



(b) Lymphocytes

Figure 3.15: Plot showing the percentage of monocytes (a) and lymphocytes(b) containing fluorescent nanoparticles and the median degree of fluorescence, plotted against the concentration of ASiNPs (either FlASiNPs or FlGdASiNPs) the cells were treated with.

3.4.2 Microscopy

The uptake in the cell was further investigated by fluorescence microscopy.

PBMCs incubated with 0.25 mg/ml FlGdASiNPs were prepared for microscopy in the same way as for the RuGdSiNPs. Unfortunately no recognisable cells could be detected. Although the flow cytometry results above suggest that there are some potentially viable cells which have been labelled with the FlGdASiNPs, the nanoparticles can be seen to be significantly aggregated, and are therefore likely to have destroyed any viable cells during the cytopsin process.

For comparison purposes the FlGdASiNPs with PBMCs preparation was imaged, and is displayed in Figure 3.16. Some purple stained shapes are visible in the bright-field image which may be remnants of cells, but this cannot be readily confirmed. The bright areas in the fluorescence image co-localise with red areas on the bright-field image, suggesting that the eosin is binding to the nanoparticles, and staining them red. This should be noted if this protocol were developed in future work as it could produce misleading counterstaining of the cells.

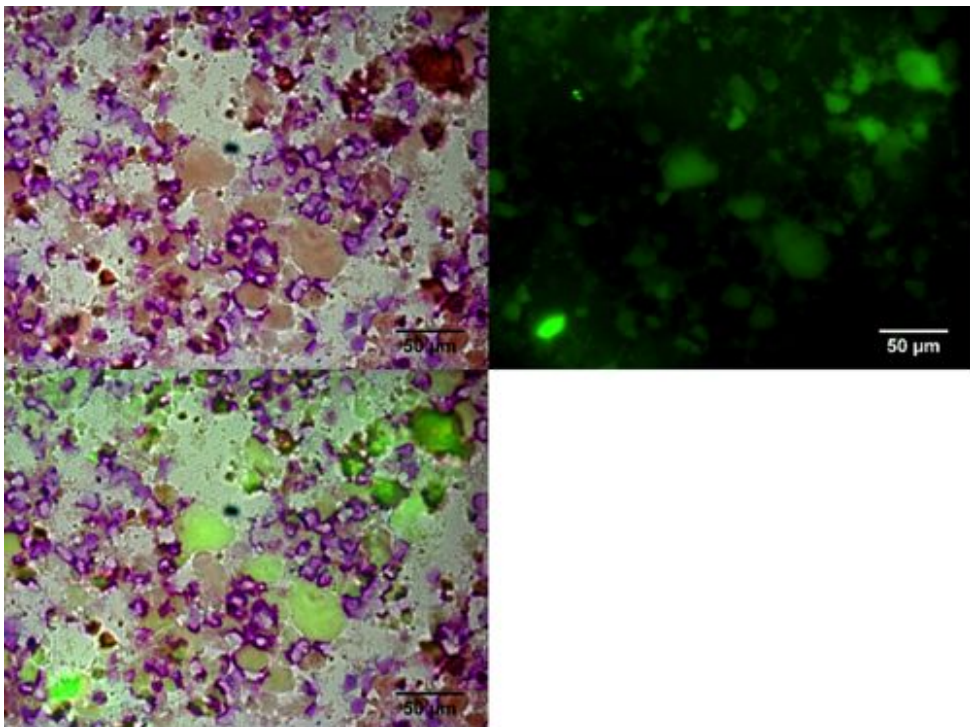


Figure 3.16: Microscopy images showing the stained cells by brightfield microscopy (top left), the corresponding fluorescence image (top right) and an overlaid combined image (below).

As an alternative gentler method, cells were labelled as above but were stained only with DRAQ5, and placed in an imaging chamber (Grace Biolabs) sealed with a coverslip. This avoided the cytopinning step, which could have caused a significant amount of damage to the cells in view of the nanoparticle aggregates spun with them.

A microscopy image of the FlGdASiNP labelled cells is shown in Figure 3.17. The green FlGdASiNPs are clearly seen clustered around the DRAQ5-stained nuclei, suggesting uptake into the cytoplasm of the cells. There are clusters of FlGdASiNPs visible which are not localised around nuclei, which were attributed to nanoparticle aggregates. This demonstrates that the FlGdASiNPs can act as fluorescent cell labels, though purification to remove aggregates and extracellular nanoparticles would be necessary to false positive identification of cells.

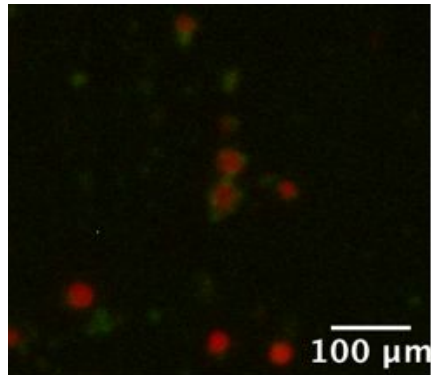


Figure 3.17: Microscopy image showing stained PBMC nuclei (red), and FlGdASiNPs (green). Images were acquired per channel and overlaid with false colours.

These microscopy experiments were however not pursued further in view of the MRI results below.

3.4.3 MR imaging

PBMCs were incubated with 0.25 mg/ml of FlGdASiNPs, washed and resuspended in 1ml of 10% gelatin at concentrations ranging from 10×10^6 to 50×10^6 . The samples were then imaged by MRI in order to measure any contrast enhancement, by measuring the relaxation rate, with gadolinium (Primovist) samples alongside them as controls. One of the images produced and the associated relaxivity plots are shown in Figures 3.18, 3.19 and 3.20

The suspension of FlGdASiNP-labelled PBMCs showed no increase in relaxation rate with concentration. This suggests that the gadolinium concentration inside the cells is too low for detection by MRI. This result indicates that these nanoparticles, while novel and having interesting other potential applications, are not suitable for cell tracking by MRI.

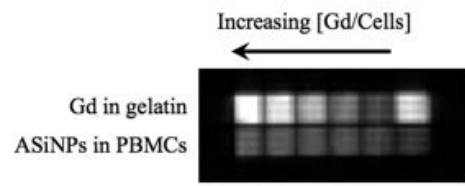


Figure 3.18: MR image of (top row) GdDTPA-EOB dissolved in 10% gelatin at a range of concentrations, and (bottom row) a range of concentrations of PBMCs treated with 0.25 mg/ml FlGdASiNPs, also in 10% gelatin.

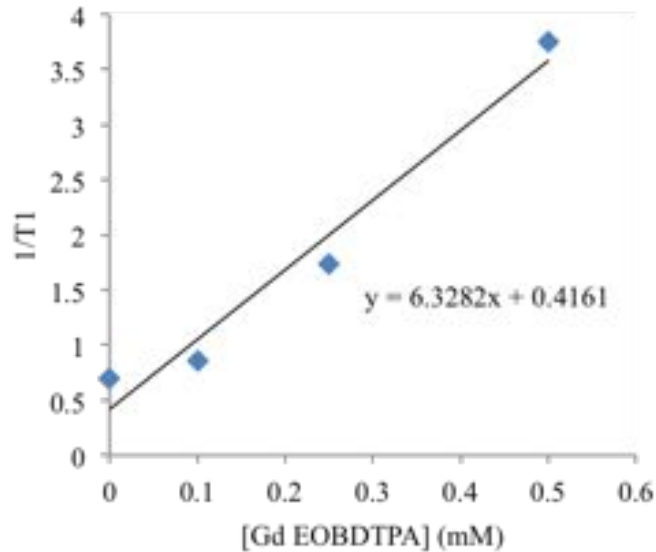


Figure 3.19: Plot of the relaxivity values calculated from GdDTPA-EOB dissolved in 10% gelatin.

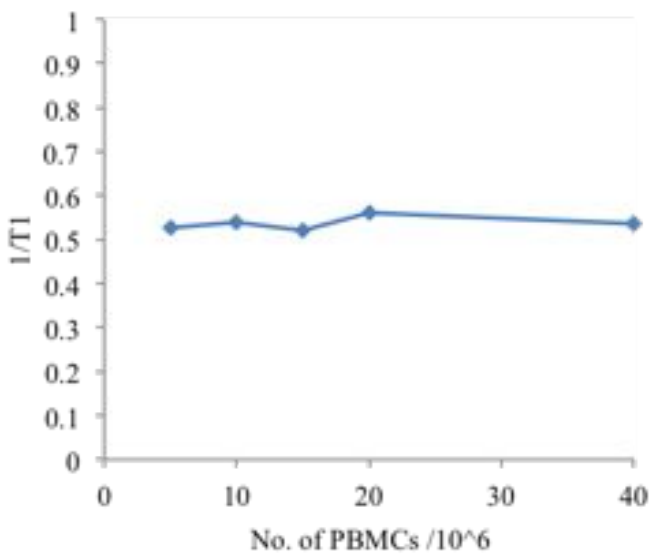


Figure 3.20: Plot of the relaxivity calculated from PBMCs treated with FlGdASiNPs, suspended in 10% gelatin.

3.5 Conclusions

Both positively and negatively charged silica matrices have been found to be effective in trapping imaging agents. This method of electrostatically trapping agents in a nanoparticles matrix has therefore been found to be a useful tool for nanotechnology.

The standard negatively charged silica particles have the disadvantage that there are few positively charged imaging agents of interest. Their synthesis is well understood however, and the particles can be readily formed with regular morphologies. In order to increase the potential of these particles, they are further developed in chapter 4 by surface functionalization.

This novel use of positively charged aminated silica matrix is more versatile in what can be electrostatically trapped, since there are many negatively charged imaging agents. The non-uniform morphology and high tendency towards aggregation of these particles are of some concern in this system. These particles might be stabilised in suspension by the deposition of an alternative layer of material, either silane, metal or polymer. In

order for this to occur however the particles would first need to be separated, otherwise the deposition would occur only on the surface of the aggregates.

While an analogous aminated silica matrix with a permanent positive charge was attempted, this route proved too problematic in the available time. This would be an interesting option in future work if stable particles could be formed with the quaternary amine throughout the matrix, perhaps by a Stober process involving co-condensation of the silanes. One factor to consider in this would be the relative hydrolysis times of the component silanes, which can affect their distribution through the matrix [170]. In order to maximise the positive charge throughout the matrix and so maximise loading capacity, the volume and addition time of the co-silane could be optimised in the same way as the distribution of dopant can be controlled [241].

CHAPTER 4

BINDING IMAGING AGENTS TO A NANOPARTICLE SURFACE

Nanoparticles, due to their small size, provide large surface areas for modification with molecules of interest. The binding of imaging agents to nanoparticle surfaces, are explored in this chapter, specifically focusing on both silica nanoparticles, as discussed in Chapter 3, and gold nanoparticles, which can reliably be formed at much smaller sizes, thus providing larger surface areas.

4.1 Background and introduction

One frequently employed method of delivering a molecule into cells is to attach it to a vehicle with good uptake properties. This ideally delivers a discrete, known and high concentration of the molecule in a well characterised and stable format. Multiple agents can similarly be bound to one surface, with the same advantages.

Nanoparticles are suitable vehicles for this purpose due to their small size, easily modifiable surfaces and readily characterisable morphology.

4.1.1 Gold nanoparticles

Gold nanoparticles are particularly of interest due to their small diameter, and hence their high surface area to volume ratio.

Modification can be carried out with any thiol-bearing imaging agents, giving them considerable versatility. They have previously been functionalised with a range of imaging agents, from luminescent lanthanide or transition metal dyes [242, 243] to gadolinium based contrast agents [244, 245]. The disadvantage is that the metal ligands usually require custom synthesis to include at least one thiol moiety, as in the four studies referenced.

AuNPs have been synthesised by a number of methods, with various reducing agents and stabilising molecules.

The Turkevich method [179] involves the reduction of heated gold salts (chloroauric acid) and stabilisation of the resulting particles, both by citrate ions. This is the simplest method, and produces citrate-stabilised gold nanoparticles between 10 - 20 nm in diameter, [178], though the size has subsequently been varied to a much wider range [246].

In the Brust method [247], the reducing agent is sodium borohydride, and tetraoctyl ammonium bromide is used to stabilise the particles in an organic phase. This allows the nanoparticles to be formed and functionalised in an organic solvent, allowing more options for surface modification. The particles are however smaller than the Turkevich method, falling between 2 and 5 nm in diameter.

The Martin method [248] also uses sodium borohydride as the reducing agent, and produces either non-stabilised or dodecanethiol-stabilised particles of between 3.2 and 5.2 nm. The non-stabilised particles require tight control of the reagent ratios, and the dodecanethiol AuNPs are soluble in solvents such as hexane.

In this work AuNPs were synthesised by the Turkevich method, then surface-functionalised to add two imaging agents; a luminescent iridium complex and a gadolinium complex for MRI contrast enhancement.

4.1.2 Silica nanoparticles

Silica nanoparticles are similarly versatile in that they can be modified, through the condensation onto the surface of alkyl silanes, with a wider range of surface groups than

gold. There are many functionalised silanes commercially available which add amine, thiol, carboxylate or phosphonate groups, to name but a few. The importance of modified silica surfaces are highlighted by noting that several other nanoparticles, including gold nanoparticles, SPIOs and quantum dots have all been coated with silica, either to improve solubility or stability, or to enable further functionalisation [249, 250, 251, 252, 253].

In terms of multimodal vehicle design, trapping in the core can provide greater protection from the environment. Conversely some imaging agents need to be on the surface, either for access to the solvent, as for T₁ MRI agents [254, 236], or for ready chelation of radionuclide labels [175, 255].

The synthesis of solid SiNPs typically proceeds either via a Stober synthesis or a microemulsion synthesis.

In the Stober synthesis [163], tetraethyl orthosilicate is hydrolysed by a base (usually ammonium hydroxide) and condensed in an alcoholic solution. This is a simple one-pot synthesis and uncomplicated purification. The size of the particles is controlled by the ratios of the silane, base and solvent (or solvents), from roughly 60 nm to 800 nm in diameter [165], or as low as 15 nm with seeded growth mechanisms [256].

Microemulsion syntheses involve the use of surfactants to form nano-sized reaction vessels [257, 258]. The hydrolysis and condensation occur inside the emulsion droplets, thus controlling the particle sizes by limiting water concentrations [258]. This method can produce smaller and more monodisperse particles than the Stober synthesis [259], but requires complete removal of the surfactant, which is often not addressed.

In order to limit the risk of contamination from residual surfactant species, and to be able to incorporate organic imaging agents, thus excluding calcination, the Stober synthesis was used in this project.

4.1.3 Other nanoparticles

As mentioned above SPIOs can have their surfaces functionalised through a silica layer, but they also have the added advantage that the core itself is an imaging agent.

Dendrimers are highly controlled and can have a range of terminal imaging agents on the surface, but they can have complex syntheses and purifications. Other nanostructures (such as hydroxyapatite, polymeric nanoparticles, silver nanoparticles, and carbon nanotubes) could also be of interest for alternative solutions for this project's goal, but they require either more complex functionalisation processes or have associated toxicity concerns.

4.1.4 Project plan

In this work luminescent RuSiNPs, as discussed in Chapter 3, were surface functionalised with gadolinium DTPA-based ligands to form RuGdSiNPs, as illustrated in Figure 4.1. The ligand was based on a modification of a gadolinium ligand presented by Rieter *et al.* [236].

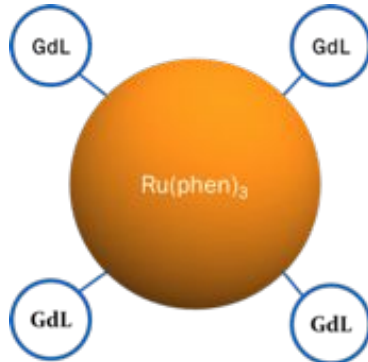


Figure 4.1: Ruthenium tris-phenanthroline labelled silica nanoparticle with gadolinium ligands bound to the surface (RuGdSiNP).

The ligand was based on a modification of a gadolinium ligand presented by Rieter *et al.* [236], and is formed by reaction of the DTPA dianhydride with an aminated silane, APTES, as shown in Figure 4.2.

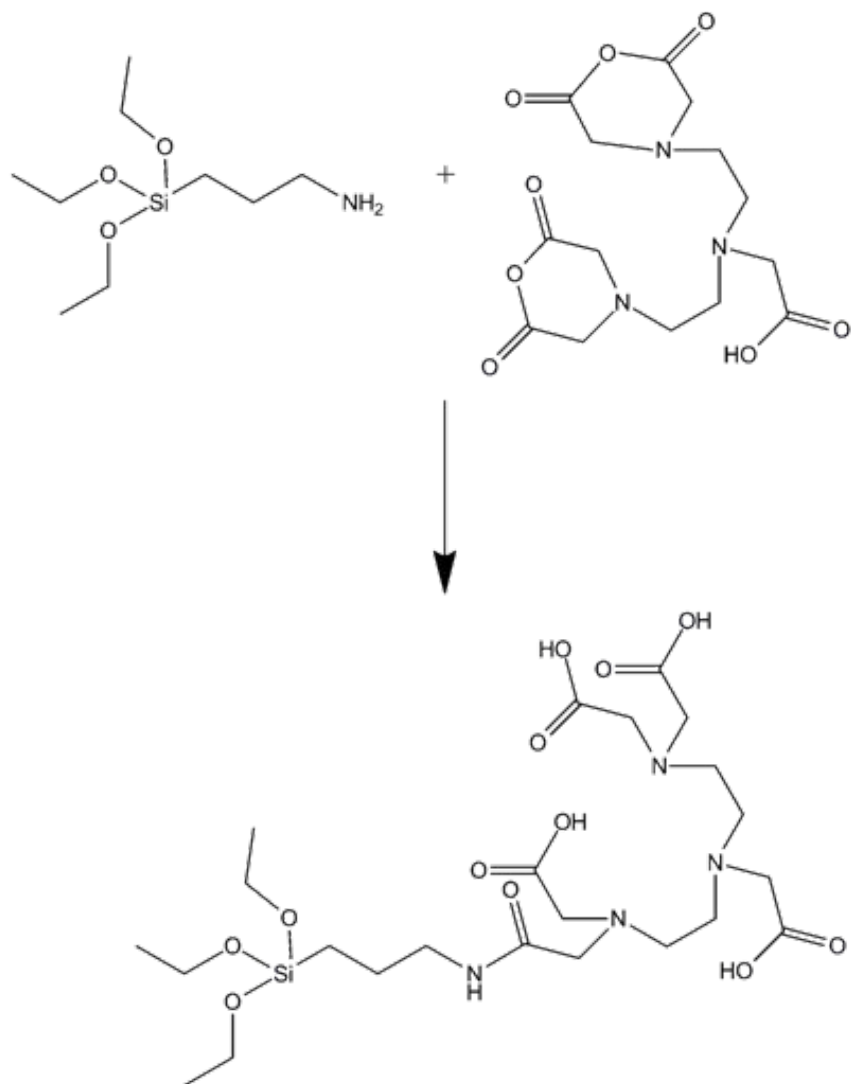


Figure 4.2: Illustration of the reaction between APTES and DTPA dianhydride to form the 3-amidopropyltrioxysilane-diethylenetriaminetetraacetic acid (APTES-DTTA).

Gold nanoparticles were coated with the neutral gadolinium DTPA-based ligands as illustrated in Figure 4.3, which displaced the citrate molecules but stabilised the particles sufficiently to allow addition of positively charged iridium bipyridyl complexes, shown in Figure 4.4. The particles are illustrated in Figure 4.5. They were characterised, tested in immune cells for cell uptake and assessed as a dual modal imaging agent.

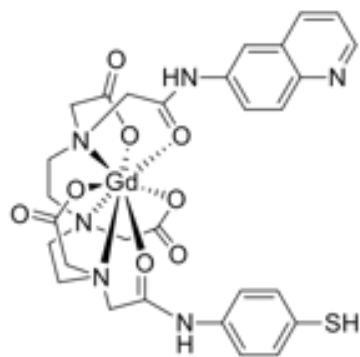


Figure 4.3: Structure of the GdQSH ligand used to functionalise the IrGdAuNPs.

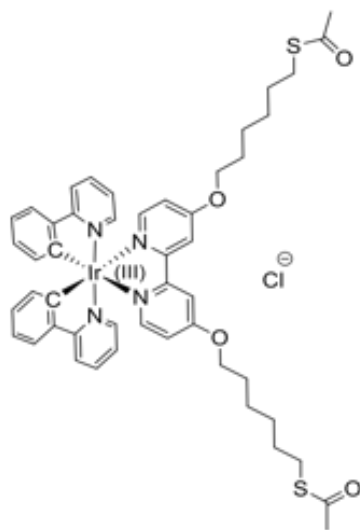


Figure 4.4: Structure of the IrBpySAC used to functionalise the IrGdAuNPs.

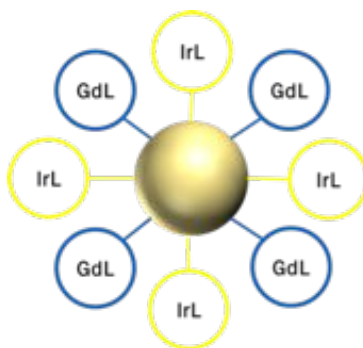


Figure 4.5: Gold nanoparticle with gadolinium ligands and iridium bipyridyl ligands bound to the surface (IrGdAuNP).

Both particles were synthesised, characterised, and tested in immune cells for cell uptake and assessed as a dual modal imaging agent.

4.2 Experimental details

The experimental details here are specific to this chapter. All materials and methods used in multiple chapter are provided in Chapter 2 to avoid repetition.

4.2.1 Materials

Gadolinium(III) chloride hexahydrate and diethylenetriaminepentaacetic dianhydride (98%) were purchased from Sigma Aldrich. Anhydrous pyridine (Acroseal over molecular sieves) was purchased from Fisher Scientific. Ru(phen)₃(PF₆)₂ was synthesised by S. Adams in the group of Prof. Z. Pikramenou,

AuNP synthesis

Chloroauric acid was purchased from Alfa Aesar. Trisodium citrate was purchased from Sigma Aldrich. IrBpySAC was prepared by Dr. N.J. Rogers, GdQSH was prepared by Dr. D.J. Lewis, all of whom were in the group of Prof. Z. Pikramenou.

4.2.2 APTES-DTPA conjugation

500 mg (1.4 mmol) of DTPA dianhydride was placed under an argon atmosphere in a 50 ml round bottomed flask and dissolved in 10 ml of anhydrous pyridine. 350 μ l (1.5 mmol) of APTES was added and the mixture was stirred with a magnetic stirrer bar for 24 hours at 800 rpm.

The DTPA-APTES was purified by precipitation with approximately 50 ml of hexane followed by separation by centrifugation. This process was repeated a further two times before drying by rotary evaporation and under high vacuum, producing 752 mg (1.25 mmol) of white powder (yield 90%).

¹H NMR of the silanetriol (300MHz, D₂O + NaOH) δ 3.10 - 2.96 (12H, m, 8H CH₂COO⁻ + 2H CH₂C(O)N + 2H CH₂NC(O)), 2.55 - 2.45 (8H, s, NCH₂CH₂N), 1.45

(2H, m, SiCH₂CH₂), 0.37 - 0.31 (2H, m, SiCH₂).

¹³C NMR (400MHz,PENDANT, DMSO) δ 173 (4C, COOH), 169 (1C, s, C(O)NH), 55 (10C, 4C CH₂(CO(NH)) + 1C CH₂(COOH) + 3C Si(OCH₂CH₃) + 2C C(O)NCH₂CH₂), 52 (4C, s, NCH₂CH₂N), 50 (4C, s, CH₂Si(OCH₂CH₃)).

ESI-MS (TOF -ve ion) of the partially hydrolyzed and deuterated silane m/z 597.8 ([M-H]⁻ 28%) 537.7 ([M-H-2 OEt + 2 OH]⁻ 9%).

FTIR (solid) 1755 (med, C=O, COOH), 1640 (s, C=O, amide), 1400 (s, C-O-H bending), 1250 (med, C-O, COOH), 1075 (s, N-C), 915 (Si-CH₂).

4.2.3 Nanoparticle syntheses

Silica nanoparticles were synthesised according to an adapted Stober synthesis [163], then modified with functionalised silanes. Gold nanoparticles were synthesised according to the Turkevich method and then modified with functionalised thiols.

Silica nanoparticles (RuGdSiNPs)

53.5 ml EtOH, 3.2 ml NH₄OH (28%), 1.6 ml TEOS and 1 ml Ru(phen)₃(PF₆)₂ (1 mg/ml in acetonitrile) were placed in a round bottomed flask. The solution was stirred for 24 hours, during which it became turbid.

Separately, 88 mg (22μmol) of APTES-DTPA was dissolved for 30 minutes in 180 μl of 1M NaOH. 18.6 mg (50μmol) of GdCl₃·6 H₂O was added and allowed to dissolve for 30 minutes. The ligand solution was then added to the nanoparticle suspension and stirred over night.

The suspension was washed by centrifugation at 5000 rpm (approximately 3300 x g) for 30 minutes and resuspension in clean solvent. The nanoparticles were washed twice with ethanol and twice with water.

For storage the nanoparticles were resuspended in ethanol.

Gold nanoparticles (IrGdAuNPs)

19.8 mg of chloroauric acid was placed in a round-bottomed flask in the dark and dissolved in 50 ml of deionised water. The solution was heated to reflux and stirred vigorously. 57.2 mg of trisodium citrate was dissolved in 5 ml of deionised water, and the solution was quickly added to the vortex.

The solution turned dark red and was heated at reflux for a further 10 minutes, then allowed to cool to room temperature with stirring.

For coating the AuNPs, the 1 mM GdQSH solution was freshly prepared in methanol. IrBpySH solution was prepared by dissolving IrBpySAc in acetonitrile to 7 mM, then freshly diluting to 3.5 mM with 30% NH₄OH before each preparation.

The SPR band was verified by UV/visible spectroscopy before and during coating. A characteristic band with λ_{max} at 520 nm was required initially.

5 aliquots of 20 μ l of GdQSH solution (100 μ l in total) were added to 1 ml of AuNPs (9 nM), causing a shift in the SPR to 526 nm. 3 aliquots of 2 μ l of the IrBpySH solution (6 μ l in total) were then added to the AuNPs, leading to a shift in the SPR to approximately 527 nm.

The IrGdAuNPs were then washed at least twice by centrifugation at 12100 x g, and resuspended in deionised water.

To create GdAuNPs, the synthesis was identical except the addition of the iridium was omitted.

4.3 Synthesis and characterisation results

Dual modal silica and gold nanoparticles were created by a modified Stober synthesis and the Turkevich method respectively, followed by surface functionalisation with custom-made imaging agent complexes. Both were designed to exhibit luminescent properties and proton MRI contrast enhancement.

4.3.1 Silica nanoparticles

One advantage of silica is that it allows the combination of trapping fluorophores in its matrix and surface functionalisation. This maximises the available surface area for the ligands which require solvent access, while also giving a high loading of those imaging agents which do not.

Here silica nanoparticles were created by a modified Stober synthesis and the surface was functionalised with gadolinium chelates. Ruthenium tris-phenanthroline was trapped in the matrix of the nanoparticle, as discussed in Chapter 3, creating in principle a dual modal system.

Light scattering (DLS)

Dynamic light scattering (DLS) measurements were carried out on the gadolinium-functionalised RuSiNPs (RuGdSiNPs). The sizes are presented in Table 4.1, along with those from Section 3.3.1 for comparison. A histogram of the radii is shown in Figure 4.6.

Sample	Diameter mean (nm) (by intensity) ± standard deviation	Diameter mean (nm) (by number) ± standard deviation	Zeta potential (mV) ± standard deviation
RuGdSiNPs	164 ± 47	115 ± 29	-30 ± 1
RuSiNPs	146 ± 43	98 ± 24	-55 ± 1

Table 4.1: Diameters and zeta potentials of the RuSiNPs and RuGdSiNPs as measured by DLS

The hydrodynamic diameter of the RuGdSiNPs is found to be 115 nm with a standard deviation of 29 nm, corresponding to a radius of 57.5 nm with a standard deviation of 14.5 nm.

By light scattering the size of the particles appears to increase upon functionalisation, and although this is to be expected, there seems to be a considerable difference in the size between the Gd-functionalised and non-Gd-functionalised RuSiNPs.

Various aspects of the RuGdSiNPs are non-ideal for DLS measurement. The presence of the $[\text{Ru}(\text{phen})_3]^{2+}$ could lead to luminescence in the sample which would disrupt the measurements. The density of these particles, although approximated by that of amorphous silica, will not be totally accurate due to the doping with the $[\text{Ru}(\text{phen})_3]^{2+}$. Therefore, since the two distribution means fall within the standard deviations of each other, both by number and intensity, these can be taken as an approximation to the size of the particles in the bulk solution to support the more reliable TEM data.

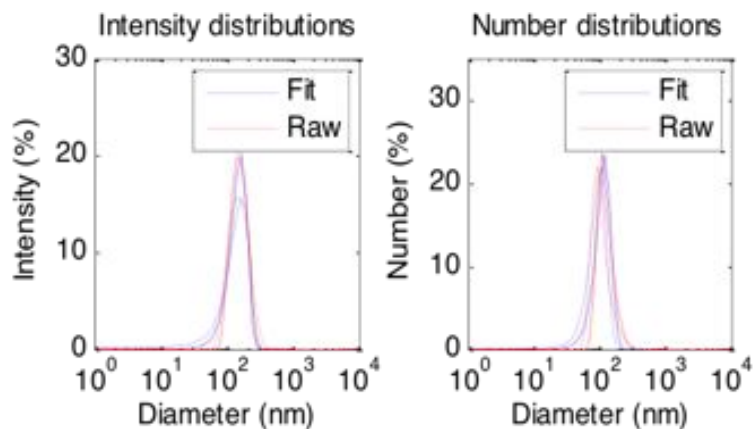


Figure 4.6: Histograms of RuGdSiNP diameters measured by DLS analysis.

Electron microscopy (TEM)

Transmission electron microscopy images were taken of the RuGdSiNPs. A characteristic image is shown in Figure 4.7, and the histogram of the measured radii is shown in Figure 4.7.

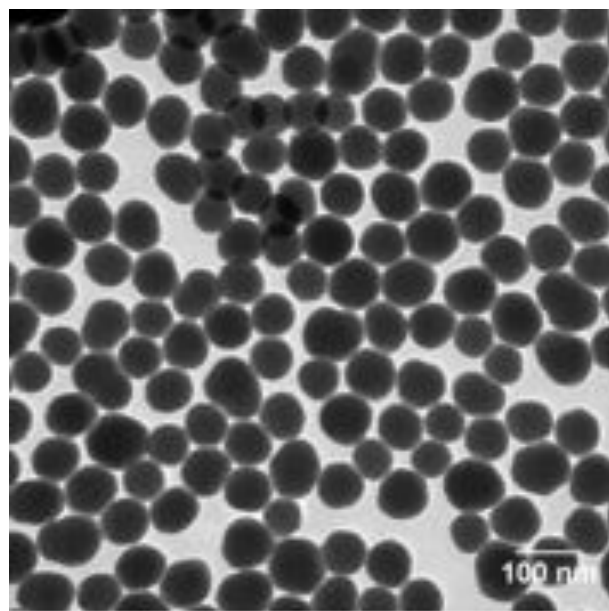


Figure 4.7: TEM images of ruthenium doped silica nanoparticles with gadolinium conjugated to the surface (RuGdSiNPs).

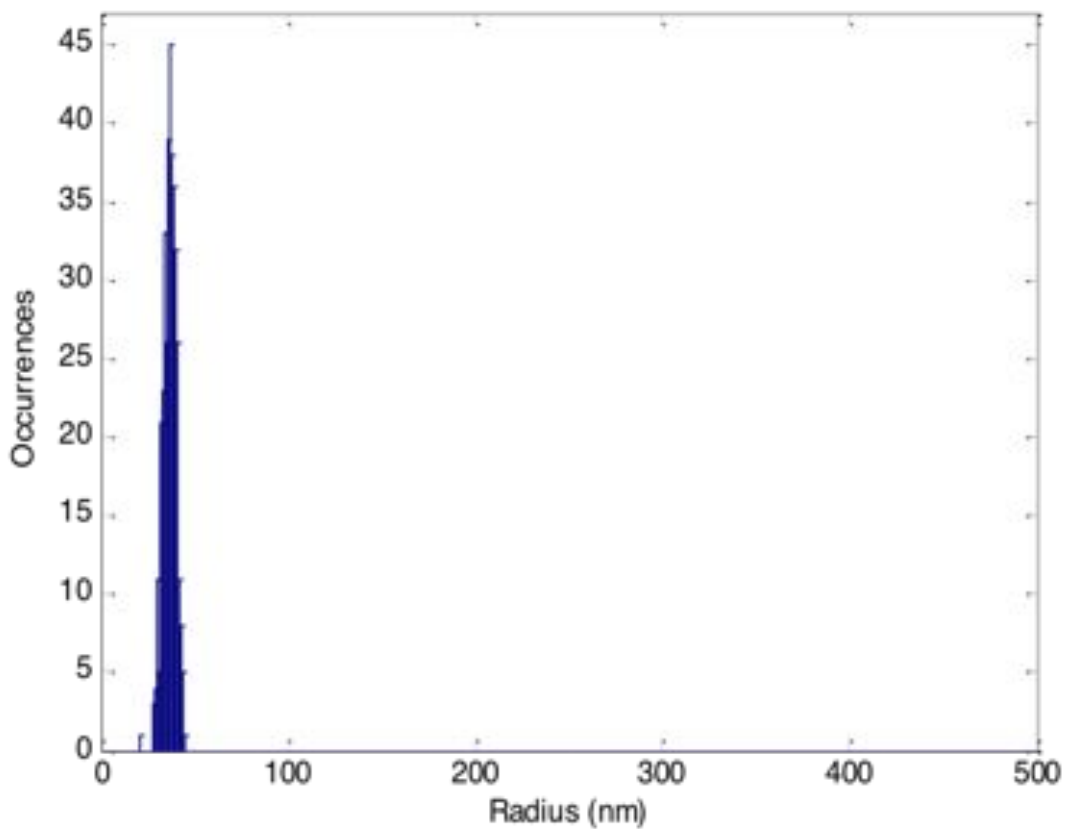


Figure 4.8: Histogram of RuGdSiNP radii measured from TEM images by automated segmentation.

The radius of the RuGdSiNPs was $37\text{ nm} \pm 4\text{ nm}$ (based on 368 measured NPs).

These particles are therefore smaller than the RuSiNPs described in Section 3.3.1, which were 43 nm in radius. While the synthesis consistently produced particles with a suitably spherical morphology, the particle radius varied between approximately 35 and 45 nm. While consistency was maintained where possible, factors such as the concentration of the ammonium hydroxide (which varied slightly between reagent bottles and decreased with use) were found to be significant.

The radius of the RuGdSiNPs as measured by DLS, 57.5 nm, is considerably larger than that measured by TEM, 37 nm. This could be due to the hydrodynamic diameters of the nanoparticles being considerably larger than the dense cores visible by TEM. It could also however be due to the microscopic number of particles being analysed by TEM, rather than the bulk quantities measured by DLS. Nevertheless, for the reasons discussed above, given the number of particles analysed by TEM, this size will be taken as representative of the particle cores.

Binding efficiency

Nanoparticle samples were diluted to a concentration of 1:100 for ICP-MS analysis.

The ruthenium concentration was found to be $1.67\text{ mg/l} \pm 0.2\text{ mg/l}$. This corresponds to a molar concentration of $17\text{ }\mu\text{M}$. This is considerably lower than expected since very little appeared to wash out, and a maximum of 40 mg/l could be expected based on the amount added.

The sample was however dissolved and stored in nitric acid, in which ruthenium can react when heated to form the volatile ruthenium tetroxide leading to loss of the metal [260], though it is unlikely that this would have had such a significant effect given the gentle heating of the sample in this case.

The gadolinium concentration was found to be $59.3\text{ mg/l} \pm 2.2$. This corresponds to a molar concentration of $378\text{ }\mu\text{M}$. This is also smaller than expected since the maximum value, based on the Gd added is 300 mg (Gd)/L . Since the ligand solution is colourless

however, a large proportion could have washed off, so this is not of major concern at this stage.

Luminescence profile and lifetimes

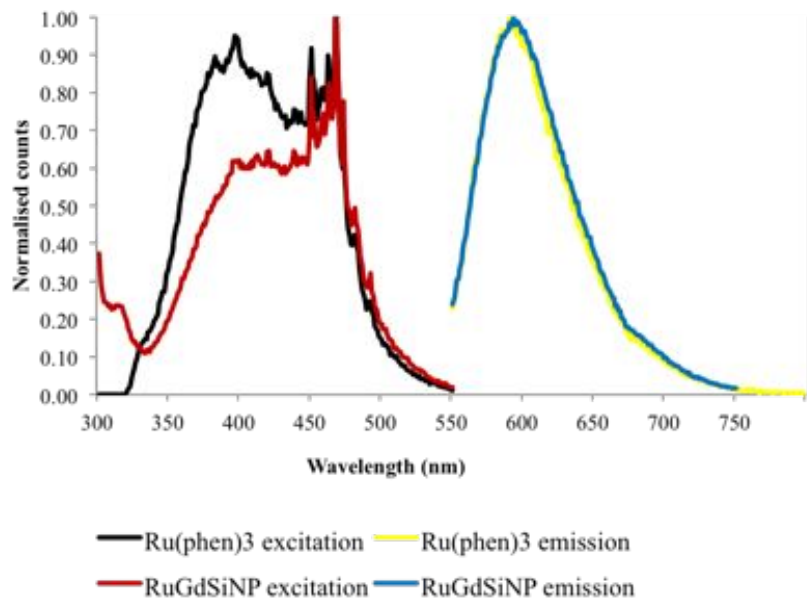


Figure 4.9: Excitation and emission spectra of RuGdSiNPs and $[\text{Ru}(\text{phen})_3]^{2+}$. Excitation scans were monitored at 590 nm and emission scans were excited at 480 nm.

The luminescence spectra of the RuGdSiNPs compared to free $[\text{Ru}(\text{phen})_3]^{2+}$ in solution are displayed in Figure 4.9. The emission spectra appear to be almost identical, with the maximum only shifting by 3 nm from 590 nm for the free complex to 593 nm for the trapped complex, and the peak shape being slightly broadened. This shift is the same as found for the RuSiNPs in Section 3.3.1, which is as expected considering the surface modification should not alter the core structure.

The lifetime data for the RuGdSiNPs are presented in Table 4.2. The lifetimes are similar to those of the RuSiNPs, also as would be expected since the surface modification should not affect the core. The changes that are observed could be a consequence of a changed permeability with the extra coating, or could be within experimental error of the fitting.

Sample	t1 (ns)	t1 (%)	B1	t2 (ns)	t2 (%)	B2	t	A	χ^2
RuGdSiNP	590	15	367	1762	85	672	1348	3.8	1.01
RuSiNP	547	13	280	1836	87	557	1405	7.7	1.03

Table 4.2: Luminescence lifetime measurements of RuGdSiNPs, along with the RuSiNP measurements from Section 3.3.1 for reference.

In broader terms, however, the values are similar to those reported for similar particles [165], *i.e.* 530 ns for the free dye and 1357 ns for $[\text{Ru}(\text{phen})_3]^{2+}$ -doped Stober silica nanoparticles. This suggests either that there was some dye free in the solution, despite the particles being thoroughly washed and none being visible under UV light, or that some of the dye is trapped in such a way as to allow enough movement and oxygen access to simulate a free environment.

MR contrast enhancement

RuGdSiNPs were imaged by ^1H MR at a range of concentrations between 0 and 20 mg/ml. The images were analysed by the automated MR analysis tools described in Section 7.2 to find the relaxivity of the samples. The relaxivity plots are shown in Figure 4.10, with the slope of the fitted line giving the relaxivity.

The relaxivity of the RuGdSiNPs was found to be $3.3 \text{ s}^{-1}\text{mM}^{-1}$ (*i.e.* mM of gadolinium ions). This is the same order of magnitude as currently available clinical contrast agents, though a little lower than expected given the similarity between the complexes. For example Primovist, measured simultaneously as a reference standard, was found to have a relaxivity of $5.7 \text{ s}^{-1}\text{mM}^{-1}$. This difference was disappointing but the system was pursued given a clear trend showing contrast enhancement and the other potential benefits of the dual modality.

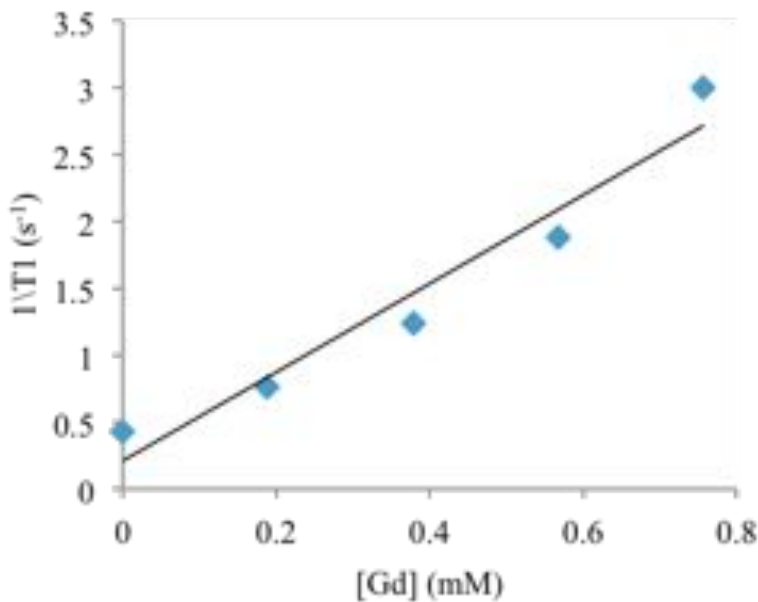


Figure 4.10: MR relaxivity plots of RuGdSiNPs imaging agents together. Values were calculated per gadolinium.

4.3.2 Gold nanoparticles

The AuNPs were prepared by the Turkevich method [178], which produced 13 - 15 nm gold nanoparticles. In order to add proton MRI contrast enhancement the citrate was replaced by the GdQSH complexes, which were not charged but helped stabilise the nanoparticles by their steric bulk. Positively charged thiolated iridium bipyridyl complexes (hydrolysed IrBpySAC from reference [261]) were then substituted in to produce dual modal IrGdAuNPs.

The synthesis was robust and reproducible when carried out under UV-visible spectroscopic observation to verify the shifts in SPR bands. The particles exhibited sufficient stability for cell treatment, but aggregated upon longer term storage, requiring the nanoparticles to be prepared freshly for each experiment.

Light scattering (DLS)

The diameters of the AuNPs and IrGdAuNPs are 14 nm and 18 nm respectively, as measured by dynamic light scattering (DLS), corresponding to radii of 7 and 9 nm respectively. The full data is shown in Table 4.3.

Sample	Diameter mean (nm) (by intensity) ± standard deviation	Diameter mean (nm) (by number) ± standard deviation	Zeta potential (mV) ± standard deviation
AuNPs	26 ± 0.5	14 ± 0.5	-41 ± 1
IrGdAuNPs	28 ± 0.5	18 ± 0.5	47 ± 0.2

Table 4.3: Diameters and zeta potentials of IrGdAuNPs and AuNPs as measured by DLS.

There is an increase in the diameter with the addition of the iridium and gadolinium complexes, as expected given the steric bulk the imaging agents would provide.

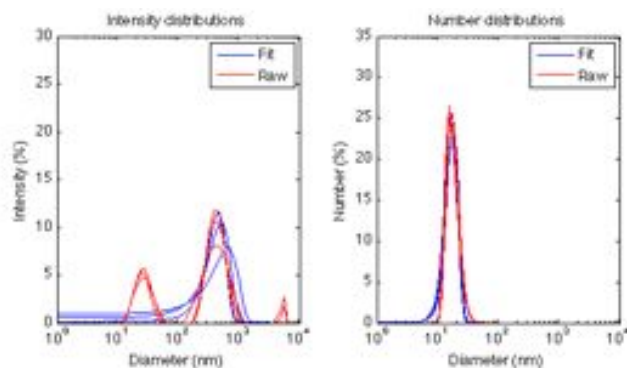


Figure 4.11: Histograms of IrGdAuNP diameter dispersions measured by DLS.

The change in the zeta potential from the functionalisation step reflects the reversing of the surface charge by the replacement of the negatively charged citrate molecules with the bulky, neutral gadolinium complexes. The positive charge then comes from the functionalisation with the iridium complexes, indicating successful functionalisation.

The zeta potential for the IrGdAuNPs does however suggest that the particles should be colloidally stable. The limited shelf life of the particles is therefore not explained by the surface charge.

A possible alternative explanation could be that the surface of the IrGdAuNPs will be covered in aromatic and alkyl ligands, so presenting a hydrophobic and largely aprotic surface. This may lead to gradual flocculation and eventually aggregation of the particles when in aqueous media. The shelf life would ideally be addressed in further work if these particles were to be pursued, but the stability was considered sufficient for reliable further testing in this project.

Electron microscopy (TEM)

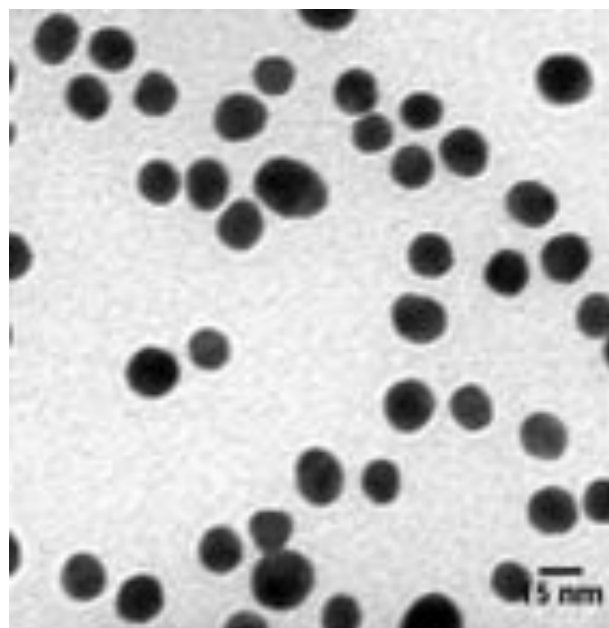


Figure 4.12: TEM image of gold nanoparticles (AuNPs).

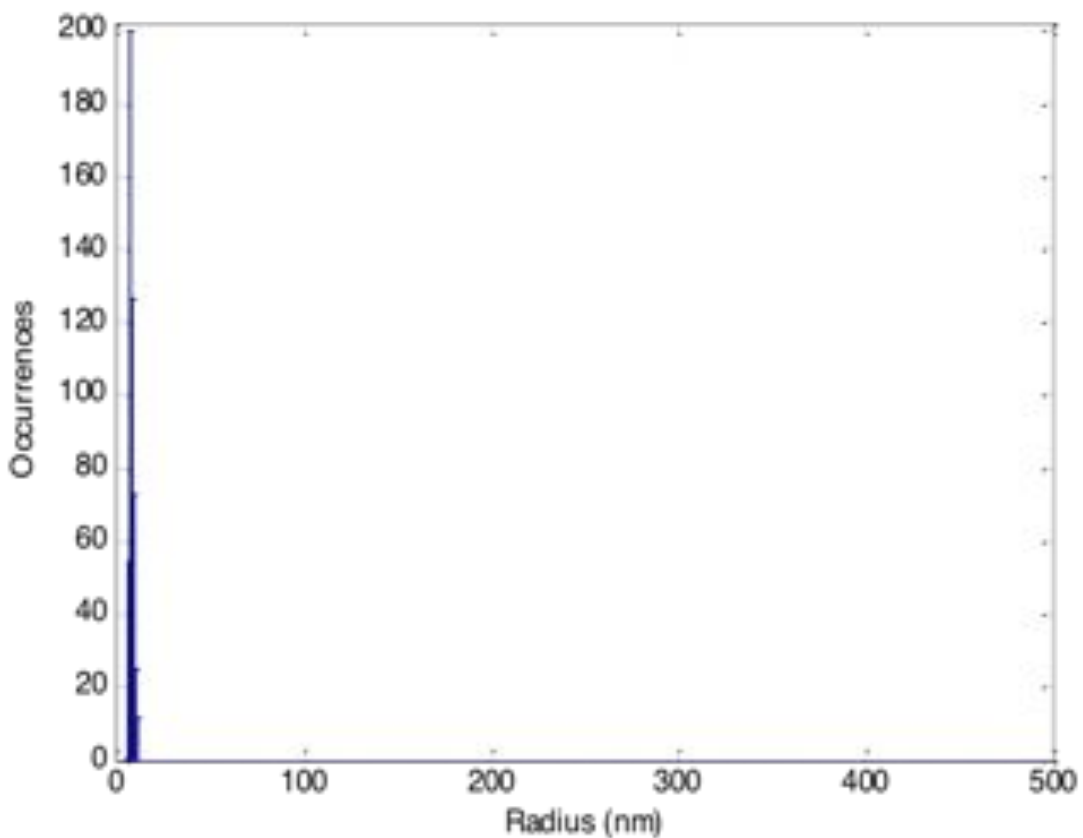


Figure 4.13: Histogram of AuNPs radii measured from TEM images by automated segmentation.

The unlabelled AuNPs were analysed by TEM. The radius was found to be 7.5 nm with a standard deviation of 1 nm based on the measurement of 493 NPs. A representative image is shown in Figure 4.12, and the histogram of the measured radii in Figure 4.13.

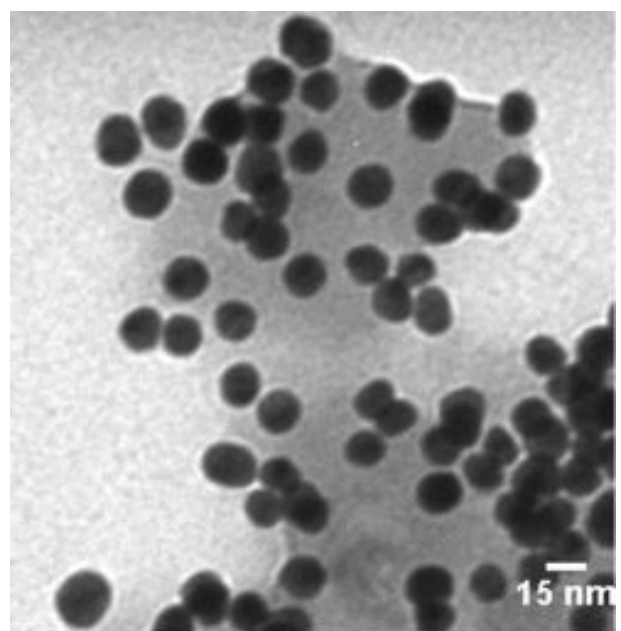


Figure 4.14: TEM images of gold nanoparticles coated with iridium and gadolinium complexes (IrGdAuNPs).

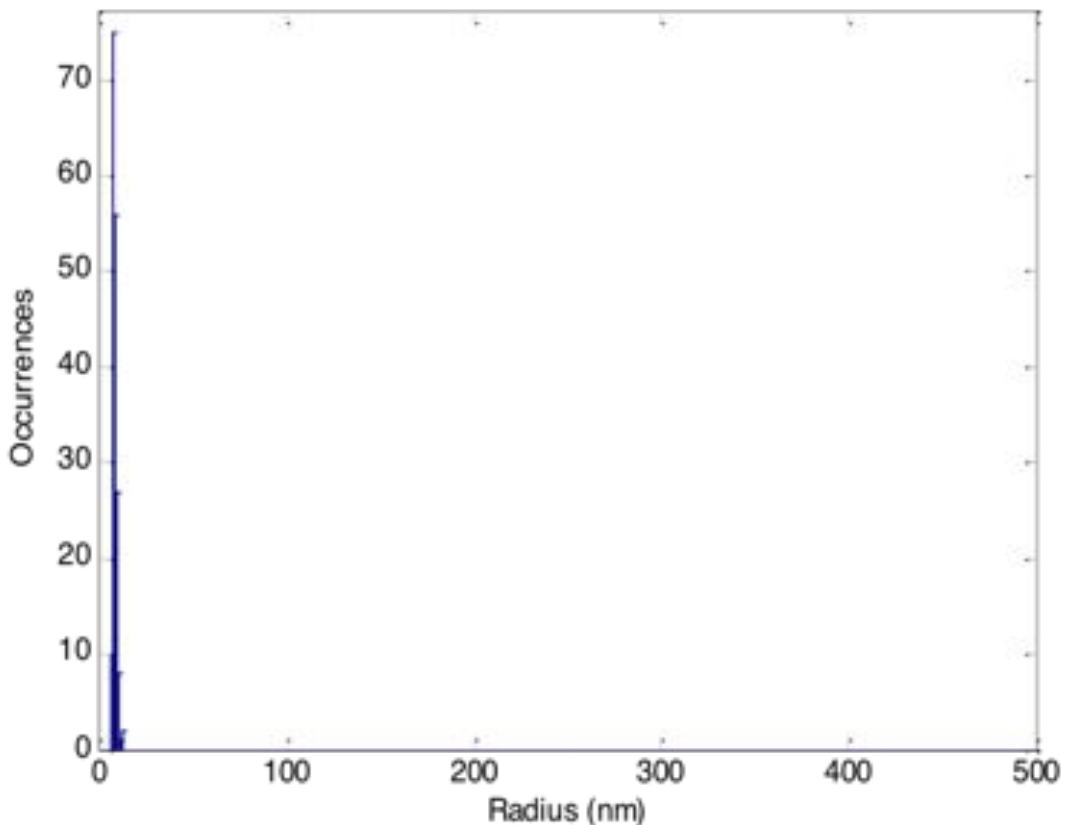


Figure 4.15: Histogram of IrGdAuNPs radii measured from TEM images by automated segmentation.

The mean radius of the IrGdAuNPs by TEM is 8 nm with a standard deviation of 1 nm, based on the measurement of 179 NPs by the method described in Section 7.1. A representative image is shown in Figure 4.14, and a histogram plot of the measured sizes is shown in Figure 4.15.

Given the microscopic nature of analysis by TEM and the standard deviations of these two measurements there appears to be no significant change between the citrate-coated and the functionalised AuNPs. This is to be expected considering the low contrast that would be produced by the organic ligands in TEM. The iridium and gadolinium, though heavy atoms, would have concentrations too low for them to contribute significantly to the nanoparticle contrast. Based on the images, the functionalisation does not appear to have had a detrimental effect on the nanoparticles' morphology or dispersion.

There is also no significant difference between the TEM and DLS size for these particles.

Luminescence

The excitation and emission spectra of the IrBpySH complex was measured by S. King, and is shown in Figure 4.16. The emission maximum is at 580 nm, with excitation at 380 nm. The excitation spectrum is characteristic of similar iridium bipyridyl-based complexes [262, 263, 264]. A non-maximal excitation was used in order to more closely match the instrumentation capabilities for analysis of cells (flow cytometry, microscopy etc.), which rely on using visible wavelength light.

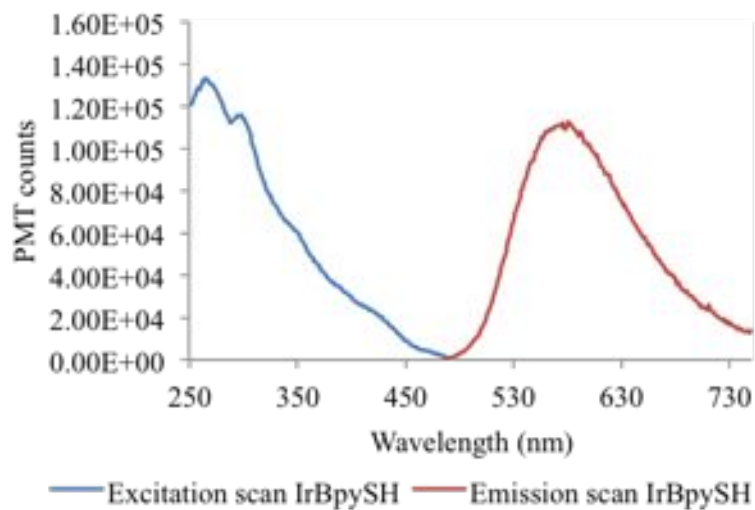


Figure 4.16: Excitation and emission spectra of the iridium bipyridyl-based ligand (20 μM) in methanol. Excitation scans were monitored at 578 nm and emission scans were excited at 380 nm.

The photochemical properties of the IrGdAuNPs were analysed and discussed by Dr. N.J. Rogers [132]. Briefly, the particles showed similar excitation and emission spectra, with the emission maximum unchanged at 580 nm.

This profile makes the particles suitable for microscopy or fluorescence techniques using a 355 nm LASER, and possibly feasible using a mercury or xenon arc lamp [265, 266]. Wavelengths lower than this should be avoided however as there is a risk of oxidative

DNA damage [267].

MR contrast enhancement

The relaxivity of the free gadolinium complex was found to be $5.1 \text{ s}^{-1}\text{mM}^{-1}$, which is comparable to commercially available contrast agents [139]. A corresponding MR image is shown in Figure 4.17, along with the plot used to calculate the relaxivity in Figure 4.18.

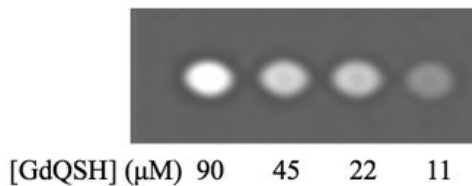


Figure 4.17: MR image of the GdQSH complex.

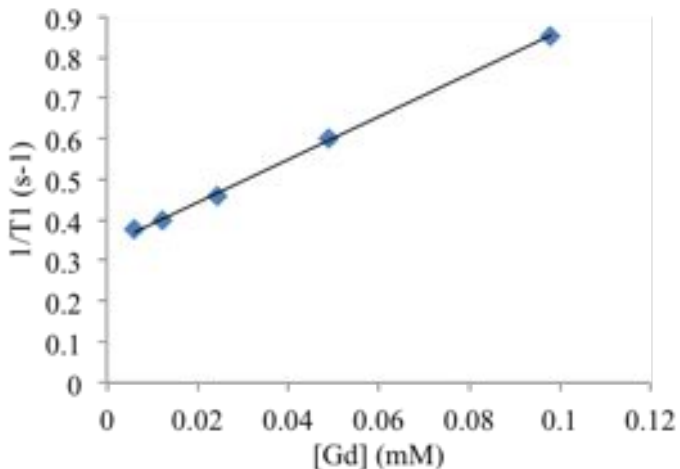


Figure 4.18: Plot of the relaxation rate against the gadolinium concentration for the GdQSH complex.

The IrGdAuNPs and GdAuNPs showed a contrast enhancing effect, as can be seen in characteristic images of a range of concentrations of both particles in Figure 4.19. This is quantified through the relaxivity, calculated from a plot of the inverse relaxation time plotted against concentration, shown in Figure 4.20.

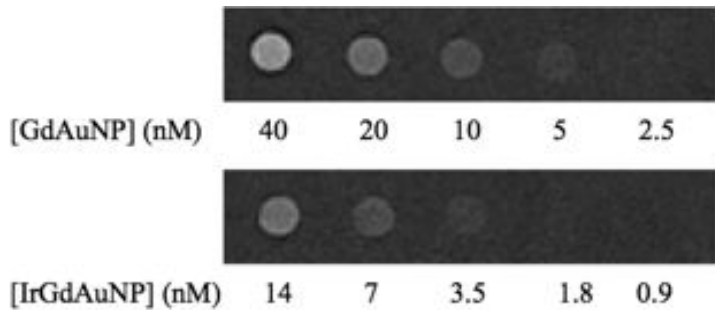


Figure 4.19: MR image of IrGdAuNPs (bottom row) and GdAuNPs (left column of samples).

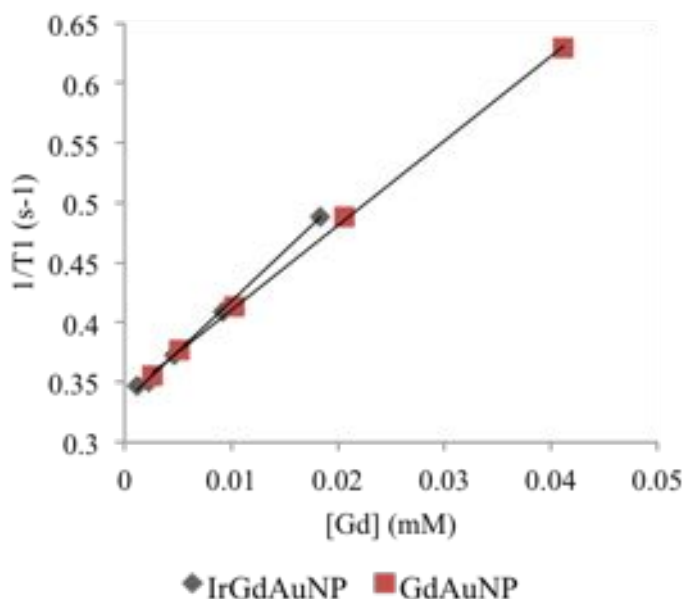


Figure 4.20: Plot used to calculate the relaxivities of the IrGdAuNPs

The particles showed relaxivities of $7.1\text{ s}^{-1}\text{mM}^{-1}$ for the GdAuNPs, and $8.4\text{ s}^{-1}\text{mM}^{-1}$ for the IrGdAuNPs. These are both considerable increases compared to the gadolinium complex alone, as would be expected from an increase in the rotational correlation time.

It would however also be expected that the GdAuNPs would have higher relaxation rates than those where some of the gadolinium complexes have been displaced by iridium complexes. This does not appear to be the case though possibly due to the higher gadolinium loading on the IrGdAuNPs compared to the GdAuNPs (1306 Gd per NP as opposed to 1043 respectively, as measured by ICP-OES by Dr. N.J.Rogers [132]).

These results demonstrate the effective gadolinium functionalisation of the AuNPs,

and that they show a greater relaxation rate than current clinical contrast agents. When combined with the luminescence results, they show the functionalisation of the AuNPs for both luminescence and MRI, making them promising dual modal agents.

4.4 Cell treatment results

Both of the nanoparticle systems developed in this chapter showed dual-modal imaging capabilities and were readily characterisable. They were therefore incubated with immune cells to observe any uptake into the various cell types, with particular focus on the monocytes and lymphocytes.

4.4.1 Silica nanoparticles

One promising nanoparticle system was the RuGdSiNPs. They were readily characterised, showing clear and regular morphologies, with good long term stability in solution, and showing dual modal imaging capabilities for ^1H MRI and fluorescence techniques.

One particular aspect of interest was how the RuGdSiNPs would interact with DCs. These cells naturally endocytose in order to process antigens, so some uptake would be expected. A preliminary study was carried out to observe the labelling of the DCs by flow cytometry.

DCs were derived from PBMCs, which were isolated by a gradient density column, and the CD14 positive cells were selected by magnetic filtering. The monocytes were cultured to mature DCs over 5 days, and RuGdSiNPs were added on the third day; the cell uptake was assessed by flow cytometry.

The other aspect of extra interest was how the flow cytometry values varied between experiments with different donors. PBMCs from five donors were treated with RuGdSiNPs and incubated for 24 hours, then the fluorescence was measured by flow cytometry. Samples were also analysed by light microscopy and MRI to assess whether the RuGdSiNPs labelled the cells sufficiently for detection by both modalities with realistic numbers of

cells. Although meaningful quantitative viability tests were beyond the scope of this project, an indication of the cell viability was obtained from the flow cytometry data in combination with the microscopy data.

Flow cytometry of RuGdSiNPs in dendritic cells

Flow cytometry was carried out on DCs loaded with the RuGdSiNPs, though aggregates in the sample caused some problems with the instrument. Forward scatter/side scatter plots are shown in Figure 4.21, indicating the change in the size and morphology of the cells with varying nanoparticle treatments.

The change in the percentage of labelled cells, and the degree of labelling (*i.e.* the median channel fluorescence) is plotted in Figure 4.22. There is some uptake by the dendritic cells at the lowest concentration of 0.19 mg(NP)/ml, with 39% of the DCs being labelled and a median channel fluorescence from those cells of 24.0. This increases to 45% with treatment at 0.375 mg(NP)/ml and a median channel fluorescence of 27.7, but at higher concentrations fewer cells are labelled and those that are, are less bright. This could be due to the aggregation of the nanoparticles being most severe above this concentration, and hence the nanoparticles not being available for uptake. It could also be due to a natural limit to the amount dendritic cells will take up.

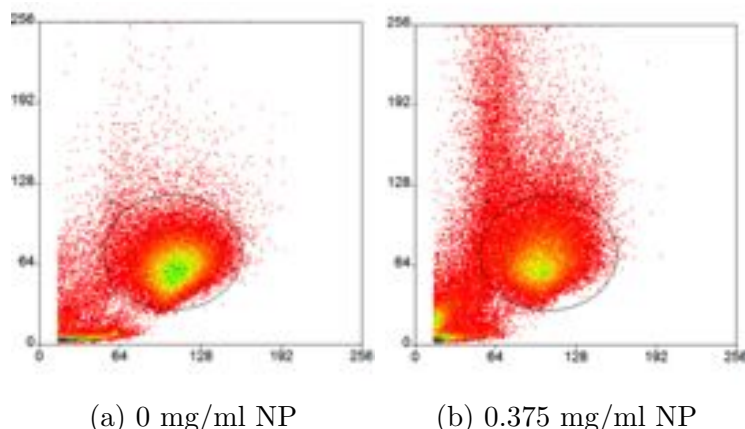


Figure 4.21: Forward scatter vs, side scatter plots for (a) DCs and (b) DCs treated with 0.375 mg/ml RuGdSiNPs, showing the changes in size and granularity of the cells. The DC gate is highlighted by the black ellipse.

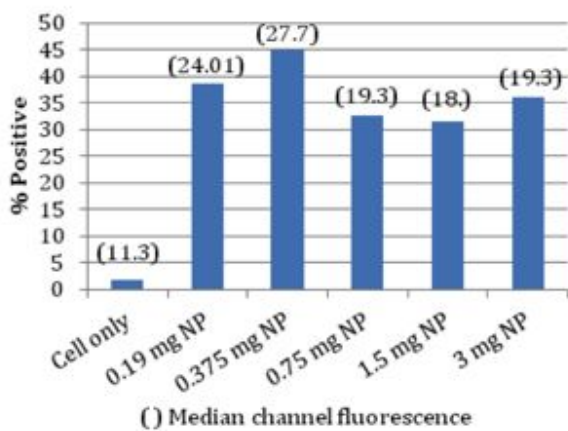


Figure 4.22: Plot showing the percentage of DCs containing RuGdSiNPs and the median degree of fluorescence, plotted against the concentration of RuGdSiNPs the cells were treated with.

Flow cytometry of RuGdSiNPs in PBMCs

PBMCs were treated with RuGdSiNPs at a range of concentration for 24 hours, then analysed by flow cytometry. The results are displayed in Figure 4.23, with the an example of the forward scatter/side scatter plots at different treatment concentrations shown in Figure 4.24. No significant uptake was observed in the lymphocytes in these experiments so only the monocyte data is presented.

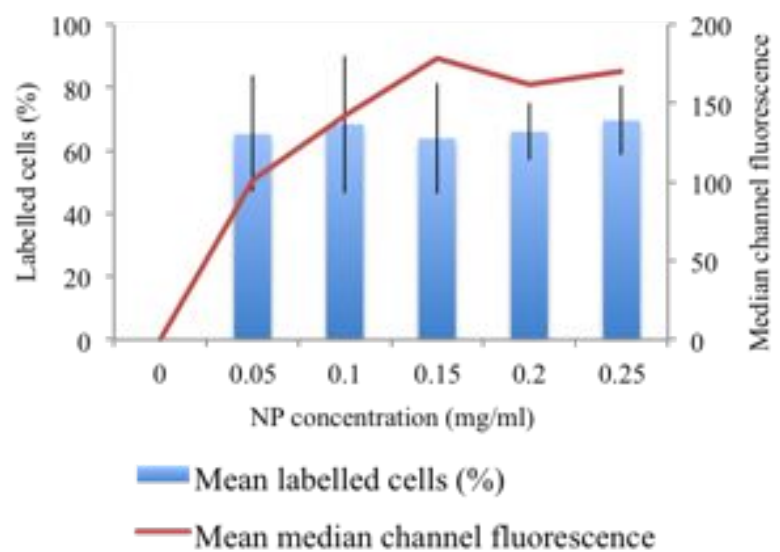
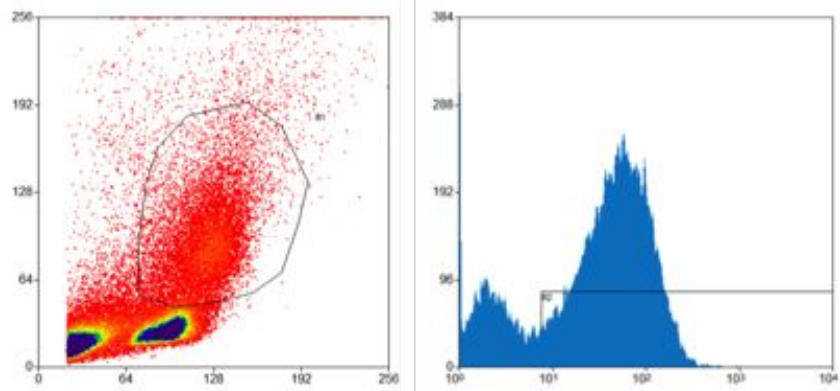
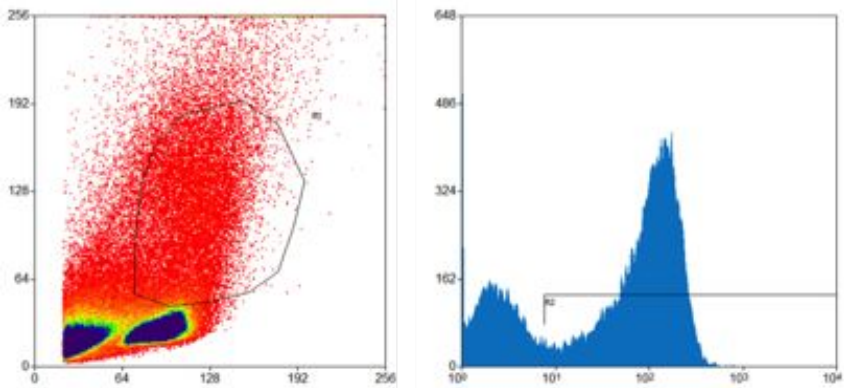


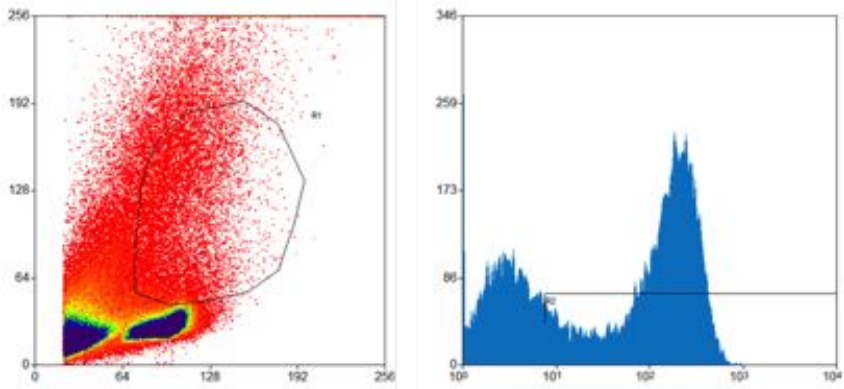
Figure 4.23: Plot showing the percentage of monocytes containing RuGdSiNPs and the median degree of fluorescence, plotted against the concentration of RuGdSiNPs the cells were treated with.



(a) 0.05 mg/ml NP



(b) 0.15 mg/ml NP



(c) 0.25 mg/ml NP

Figure 4.24: Forward scatter vs, side scatter plots for PBMCs treated with increasing concentrations of RuGdSiNPs, showing the changes in size and granularity of the cells. The monocyte gate is highlighted by the black ellipse. The histograms of the channel fluorescence are also shown for each concentration.

The uptake of the RuGdSiNPs is analysed both in terms of the number of cells which contain the label, denoted by the percentage of positive cells, and the amount of the label taken up into the labelled cells, denoted by the median channel fluorescence.

In this case the experiment was repeated with five different donors, over two days, to show the variability that can arise. The error bars show the standard deviation of the labelled cell percentage over the five experiments. There was an average 67% of monocytes labelled across all nanoparticle treatment concentrations. The median channel fluorescence on the other hand rises to a peak at a 0.15 mg/ml RuGdSiNP treatment concentration, with a plateau afterwards, suggesting that there is no benefit from increasing the concentration beyond this. A compromise must therefore be found for future work between the maximum positive labelling, the maximum label uptake, and the cell viability.

A preliminary measure of the cell viability at the different RuGdSiNP treatment concentrations is the proportion of cells remaining within the monocyte gate, which is determined on a control sample. This indicates whether there is a significant change in size or morphology within the monocyte population with increasing cell concentrations. The mean percentage of the whole cell population falling within the monocyte gate is plotted against treatment concentration in Figure 4.25.

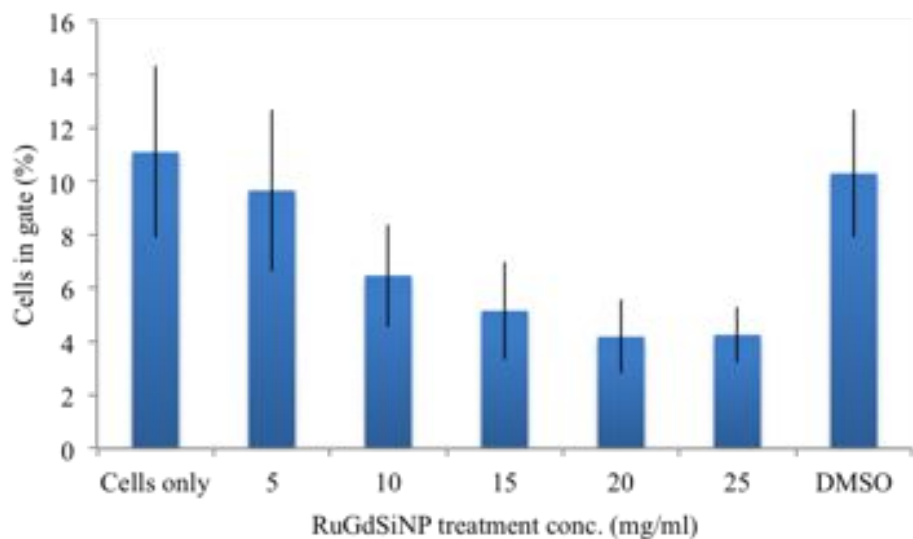


Figure 4.25: Plot showing the percentage of the whole cell population falling within the monocyte gate, plotted against the concentration of RuGdSiNPs the cells were treated with. The 'Cells only' data was a control sample with no nanoparticle treatments, while the 'DMSO' sample was a vehicle control at the highest treatment concentration, but without the nanoparticles. The error bars indicate the standard deviation over 5 donors.

There is a clear drop in the percentage of cells falling within the monocyte gate with increasing treatment concentrations. The RuGdSiNPs appear to be affecting the cells at all concentrations, but in a concentration-dependent manner. The DMSO (vehicle) control, which involved the same volume as for the 25 mg/ml RuGdSiNP treatment, may be having a small effect but a much smaller one than the nanoparticles themselves.

It should be noted that the flow cytometer used does not give any indication of the volume required to examine a given number of cells. There is therefore no measure of the number of cells which have died and disintegrated during the treatment. This highlights the need for extensive viability testing for any system that emerges as a potential multimodal imaging agent.

Microscopy of RuGdSiNPs in PBMCs

Labelling was carried out at a range of RuGdSiNP concentrations to observe the effect of the nanoparticles on the cell morphologies, which were indicated by the flow cytometry results above.

At a RuGdSiNP concentration of 0.05 mg/ml, the cells show recognisable morphologies, with nanoparticles mostly appearing to be in the cytoplasm of the cells, see the microscopy image in Figure 4.26. The fluorescence appears to be punctate, suggesting that the nanoparticles have been taken up into the cells in vesicles. The types of vesicle could be investigated further as part of future work by using vesicle specific fluorescent counterstains such as Lysotracker.

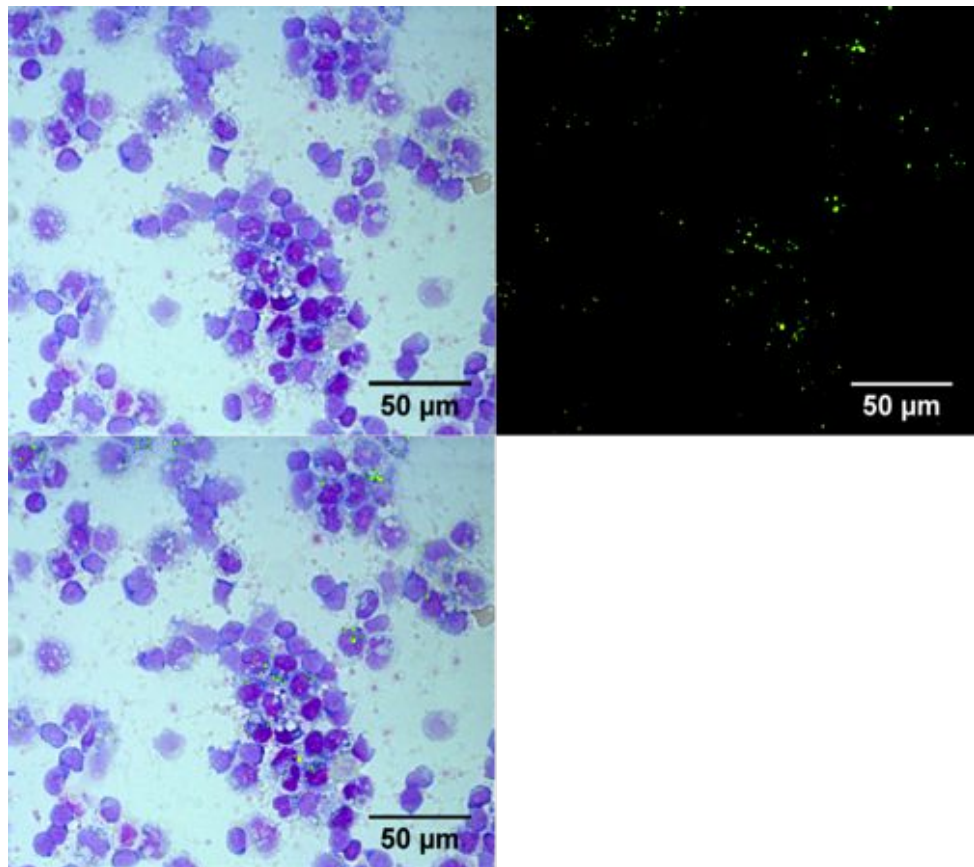


Figure 4.26: Micropscopy images showing the stained cells by brightfield microscopy (top left), the corresponding fluorescence image indicating the RuGdSiNP locations (top right) and an overlaid combined image (below).

At a higher nanoparticle concentration of 0.15 mg/ml, the nanoparticles can also be seen as punctate fluorescence which is co-localised with the cells, see Figure 4.27. The cells however look less recognisable as healthy cells, with large-lobed anuclear structures seeming to contain clusters of nanoparticles. These could be clusters of dying or dead cells. They could also be giant cells, formed to process the high concentration of foreign matter, *i.e.* the RuGdSiNPs. These could be the larger structures seen developing with the loss of the monocyte cloud in the flow cytometry results.

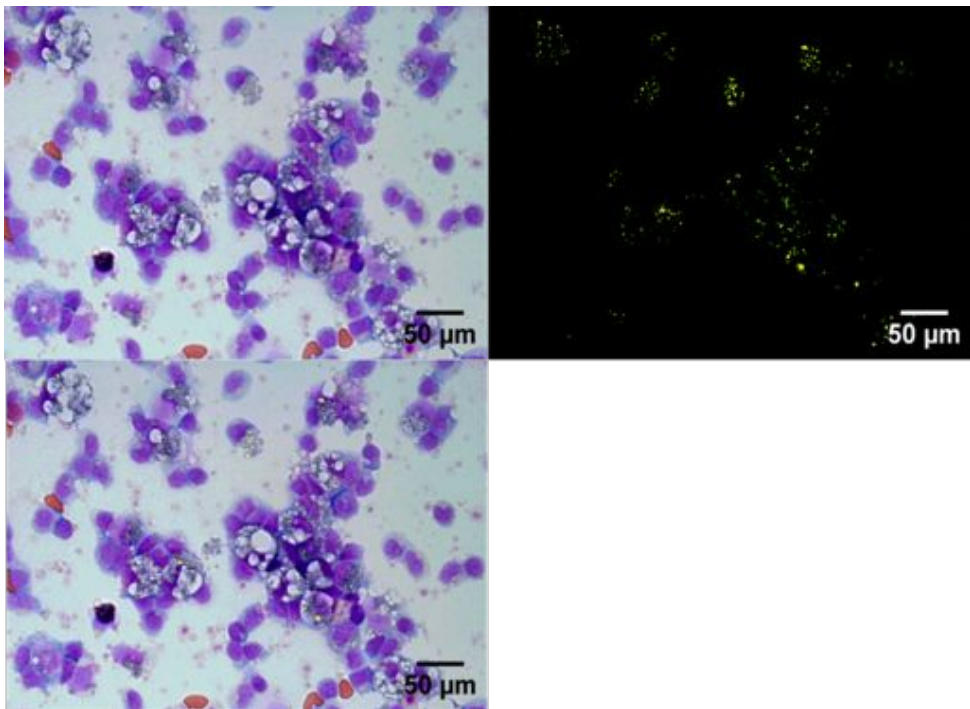


Figure 4.27: Micropscopy images showing the stained cells by brightfield microscopy (top left), the corresponding fluorescence image indicating the RuGdSiNP locations (top right) and an overlaid combined image (below).

MRI of RuGdSiNPs in PBMCs

50×10^6 PBMCs were labelled with 0.15 mg/ml of RuGdSiNPs to provide the maximum labelling, as seen by flow cytometry. Although there may be some loss of viability at this concentration, as suggested by the microscopy results, maximum labelling was considered preferable for this experiment. The RuGdSiNP labelled cells, suspended in gelatin, had a relaxation rate of 0.52 s^{-1} , while the control sample, containing gelatin, showed a rate of 0.49 s^{-1} .

The labelled cells showed a small difference from the control sample of gelatin based on the relaxivities (see Figure 4.28). This was not obvious in the corresponding images, however, as shown in Figure 4.29, indicating that the cells would not be readily localisable *in vivo* and that therefore there is insufficient uptake of nanoparticles at this concentration. This is not surprising considering the relatively low uptake of the nanoparticles (see flow cytometry results). It does suggest however that these would not be suitable for

multimodal cell tracking unless the uptake could be improved, as this high concentration of cells would be undetectable.

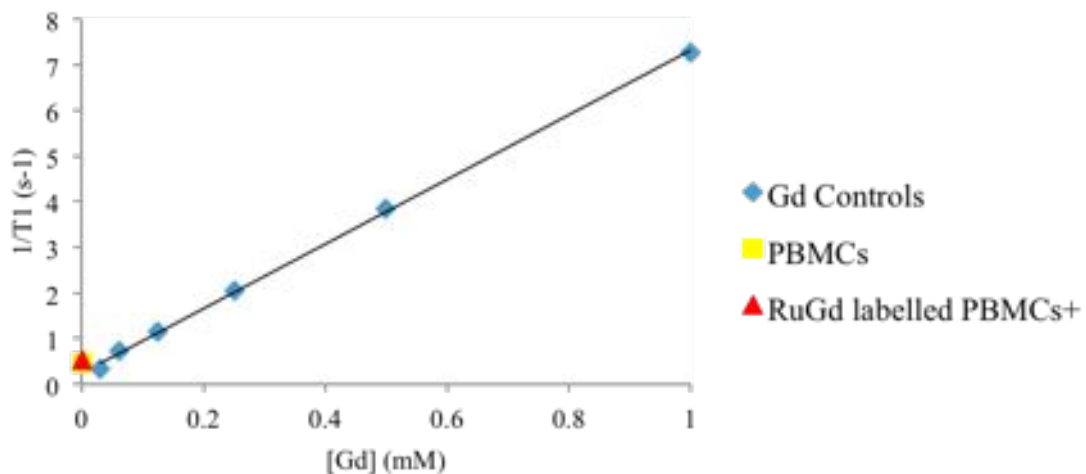


Figure 4.28: Plot of the relaxation rates against gadolinium concentration, calculated from GdDTPA-EOB and from 50×10^6 PBMCs which were labelled with 0.25 mg/ml RuGdSiNPs, washed, then suspended in 10% gelatin.

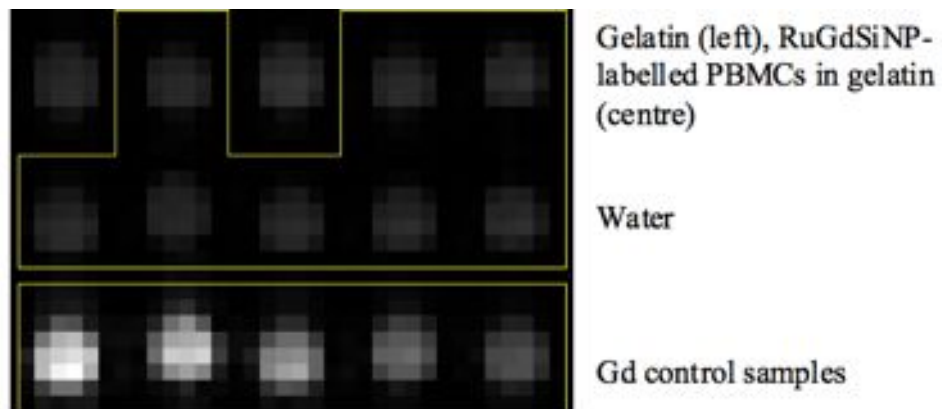


Figure 4.29: MR image of the RuGdSiNP-labelled PBMCs (top centre), a control samples of 10% gelatin, water samples around these and gadolinium (Primovist) samples (bottom row) at a range of concentrations.

4.4.2 Gold nanoparticles

Gold nanoparticles labelled with gadolinium and iridium (IrGdAUNPs) were incubated with PBMCs in order to observe any uptake by the cells. The luminescence excitation spectrum of the iridium, with absorption mainly below 400 nm, makes these particles

unsuitable for analysis by many standard biological methods. The flow cytometer carried no lasers below 405 nm in wavelength, resulting in the nanoparticles not being detectable by this method (see appendix A for flow cytometry of cells at 405 nm).

The microscopy in this project was carried out on a system with a mercury lamp which leads to some excitation in the UV range [265]. This coupled with a DAPI and FITC filter set should allow some imaging of any nanoparticles loaded into PBMCs.

Transmission electron microscopy (TEM) has also been used to observe the uptake of the IrGdAuNPs by the PBMCs. The gold nanoparticle cores provide high contrast in the images, and with a low energy electron beam the cellular structures can simultaneously be seen.

Microscopy of IrGdAuNPs in PBMCs

Initial microscopy on the IrGdAuNPs aimed to retain the native cell morphologies. The IrGdAuNP labelled cell suspension was labelled with a red nuclear stain, DRAQ5, according to the manufacturers instructions and placed in an imaging chamber (Grace Biolabs), which was sealed with a glass coverslip. The cells were imaged immediately through the glass coverslip. A typical microscopy image is shown in Figure 4.30.

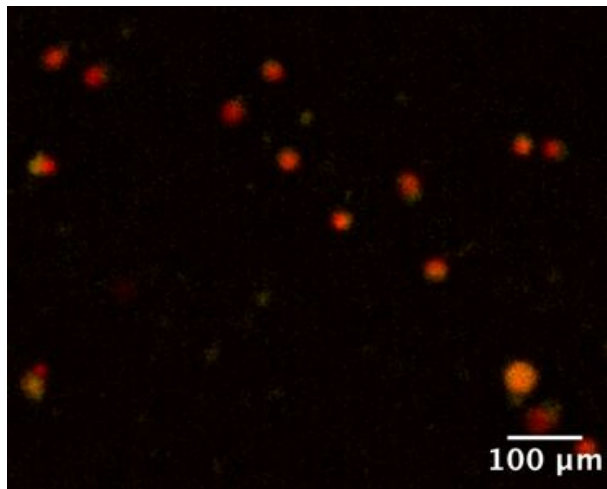


Figure 4.30: Multi-channel microscopy image showing PBMCs nuclei labelled in red and the IrGdAuNPs in yellow. (Images were acquired per channel and overlaid with false colour.)

There are IrGdAuNPs clearly clustered around the nuclei suggesting uptake into the cytoplasm. For most of the cells there does not appear to be any uptake into the nucleus, which is reassuring as interaction with the DNA could risk damage to the cells. There are however also clusters of nanoparticles with no nucleus, which could be due to uptake by anuclear cells, excessive uptake leading to apoptosis and so local labelled cell debris, or out-of-focus cells, or free nanoparticles. It is not clear without further staining which of these is the case.

Since out-of-focus cells were problematic for the imaging, the microscopy preparation was revised to produce cells in a monolayer with extra staining. The disadvantage is that the non-adherent cells must be layered on to the surface by cytopinning, where the cells are effectively centrifuged on to a slide surface. Kwik-Diff staining was then used to stain the entire cell and help differentiate between cell types.

Figure 4.31 shows an example of IrGdAuNP-treated PBMCs which appear to be healthy, with a range of cell types present. There is however no observable uptake of the IrGdAuNPs by this method, as no significant level of fluorescence co-localises with the cells in the bright-field image.

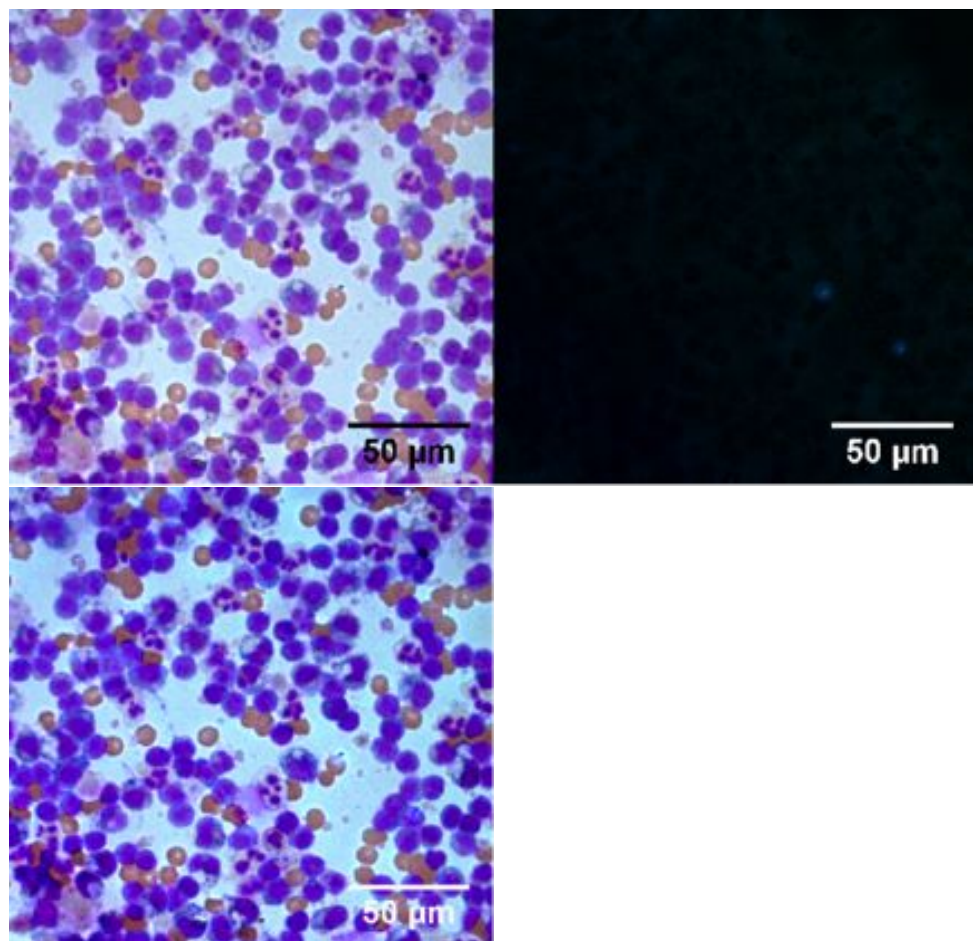


Figure 4.31: Micropscopy images showing the labelled cells by brightfield microscopy (top left), the corresponding fluorescence image (top right) and an overlaid combined image (below).

This was unexpected given the nanoparticle luminescence observed by imaging in the chamber (Figure 4.30), so was considered to be possibly a result of the cell staining process, either due to reaction of the nanoparticles with the dyes or loss of the particles during the permeabilisation step.

The microscopy of the IrGdAuNPs has therefore proved to be challenging, though a range of other stains may be preferable for these nanoparticles. For example a membrane stain or actin stain would indicate the extent of the cell, and combined with the nuclear stain and cytopinning, would provide more information on the cellular localisation of the IrGdAuNPs.

These microscopy experiments were not pursued in this work in view of the MRI

results presented below. It is anticipated however based on these preliminary results that IrGdAuNPs could be an effective cell label for luminescence-based techniques with suitable optimisation.

Electron microscopy of IrGdAuNPs in PBMCs

Gold nanoparticles can be readily discerned by TEM due to their high electron density. When taken up into cells, which are subsequently embedded in resin and sectioned, the nanoparticles can still be distinguished from the background when the cells are lightly stained.

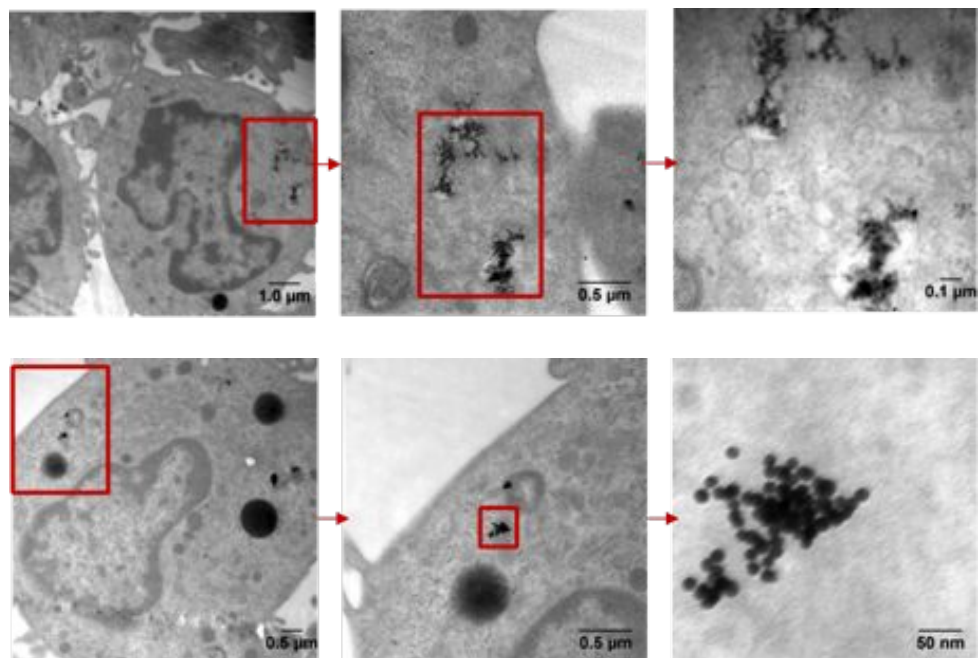


Figure 4.32: TEM images, at increasing magnifications from left to right, of PBMCs containing IrGdAuNPs.

In both cells shown in Figure 4.32 the nanoparticles are collected into clusters.

In the top image the IrGdAuNPs appear to be membrane-bound. This could be a consequence of the cell type. The large lobed nucleus suggests that the cell could be a granulocyte, which are often phagocytic, and would be expected to take up foreign particles in vesicles.

The second cell shown above appears to have taken the nanoparticles up into the

cytoplasm, as no surrounding structure is visible. While this could be an artefact from the staining process, the nucleus is much smaller and more regularly shaped, suggesting a different cell type; it could possibly be a B cell.

It should be noted however that there were many cells present on the grids which did not appear to contain any nanoparticles. Sectioning the cells necessarily will exclude much of the cell material, which might have contained nanoparticles. Nevertheless, the conclusion must be that though nanoparticles do appear to have been taken up into a variety of cell types, there is only a low level of cell labelling.

MR of IrGdAuNPs in PBMCs

50×10^6 PBMCs were labelled with IrGdAuNPs at a concentration of 0.9nM (NPs), washed and suspended in 1 ml of 10% gelatin. The cell suspension was imaged by ^1H MRI to determine whether the labels caused any contrast enhancement. A characteristic image is shown in Figure 4.34. The relaxation rate was calculated by the algorithm described in Section 7.2, and is plotted along with gadolinium controls in Figure 4.33.

A relaxation rate of $0.52 \text{ s}^{-1}\text{mM}^{-1}$ was observed. This is comparable to the signal produced by the RuGdSiNPs labelling PBMCs, which also had a relaxation rate of $0.52 \text{ s}^{-1}\text{mM}^{-1}$. As for the RuGdSiNPs this would not be considered a great enough change in contrast to localise the cells *in vivo*, so would similarly require improved uptake in order to be an effective tool for cell tracking.

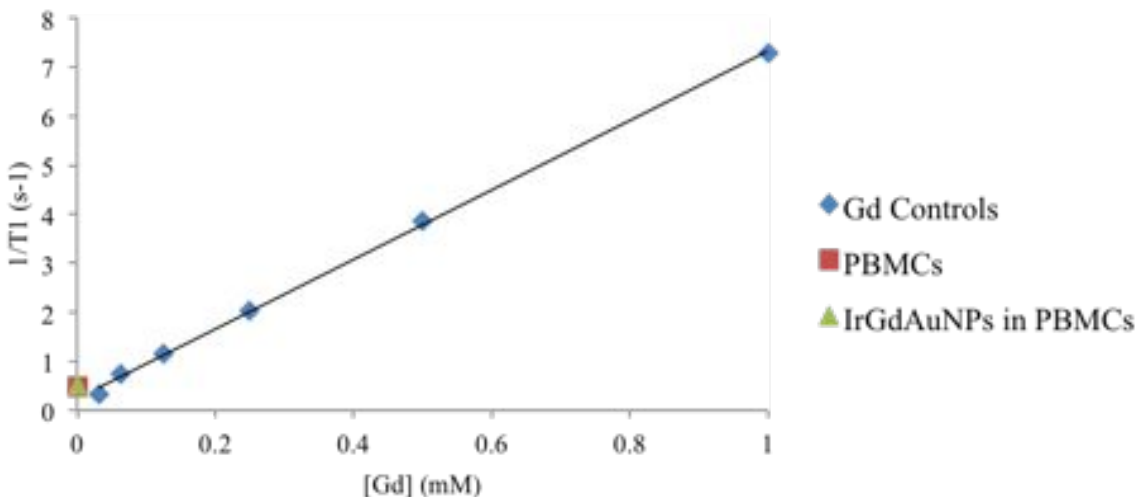


Figure 4.33: Plot of the relaxation rates against gadolinium concentration, calculated from GdDTPA-EOB and from 50×10^6 PBMCs which were labelled with 0.9nM IrGdAuNPs, washed, then suspended in 10% gelatin.

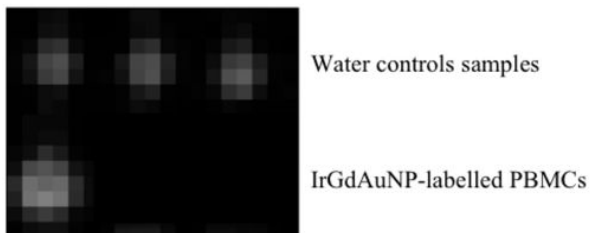


Figure 4.34: MR image of the IrGdAuNP-labelled PBMCs (bottom left), alongside samples of gelatin containing 2.5 mg/ml RuPFOBGdHSNPs (bottom centre) and RuPFOB HSNPS (bottom right). The top row shows water samples.

4.5 Summary and conclusions

4.5.1 Silica nanoparticles

RuGdSiNPs of 70 - 80 nm in diameter were synthesised and characterised. The luminescence spectra were similar to those of the free dye, and the lifetime was similar to comparable reported RuSiNPs. $[\text{Ru}(\text{phen})_3]^{2+}$, as for the RuSiNPs is therefore considered to be trapped in the matrix with no significant disruption due to the surface functionalisation.

The gadolinium complex conjugation meanwhile resulted in MRI contrast enhancement comparable to current clinical contrast agents. This is disappointing considering the increase in the relaxivity reported due to the greater rotational correlation caused by the slower tumbling of the nanoparticles [268, 269]. The rates observed however were considered to be sufficient to continue with cell treatments.

Both monocytes and lymphocytes were found to take up the RuGdSiNPs by flow cytometry. Punctate fluorescence attributable to the RuGdSiNPs was observed by fluorescence microscopy, confirming uptake with little change to the PBMCs' appearance with a treatment concentration of 0.05 mg/ml of RuGdSiNPs. Higher concentrations showed changes in the cell morphology, suggesting a limit the particles leading to healthy labelled cells.

The RuGdSiNPs were therefore considered to be useful for luminescence techniques, but requiring further work before they could be useful as MRI labels.

4.5.2 Gold nanoparticles

The IrGdAuNPs, of 16 - 18 nm in diameter, were tested as dual-modal contrast agents. The luminescence spectra were similar to the unbound complex, while MRI showed contrast enhancement greater than currently available clinical contrast agents.

When used as cell labels for PBMCs, however, while there was a suggestion of uptake seen by microscopy and TEM, MRI indicated that improved uptake would be necessary in order for the cells to be visible *in vivo*.

Binding to the nanoparticle surfaces can consequently be considered to be an additional tool for adding further functionality, but, as implemented here, only had limited abilities for cell tracking.

4.5.3 Cell treatments

Future work for cell treatments would include examining the effects of the nanoparticles on the cells. The first analysis would look at viability, in order to check how cytotoxic the nanoparticles are. Various assays could accomplish this, such as MTT, which gives an indication of mitochondrial function, or Sytox green, which permeates only into dead cells and can be analysed by flow cytometry. Other factors of interest would be to verify if the monocytes, once labelled, can still differentiate into dendritic cells, and whether either of these cell types still have phagocytotic capacity. The next stage would then be to examine the ability of the relevant cells to migrate, as the derived DCs would need to be able to travel to the lymph nodes post injection.

CHAPTER 5

MULTIPLE IMAGING AGENT CAPABILITIES IN MOLECULAR STRUCTURES

This chapter explores ways of reliably delivering multimodal agents for immune cell tracking which are alternatives to nanotechnology by using covalent structures which incorporate multiple functionalities. A commercially available fluorinated fluorescent dye is therefore investigated for its cell tracking potential.

5.1 Background and introduction

While nanotechnology can theoretically provide many of the solutions necessary for the delivery and retention of imaging agents, there are also significant disadvantages. Unless the distribution of the nanoparticle sizes is very small, there is a chance of different sizes having varying effects on biological systems [198]. Moreover, due simply to their size, some particles will often be trafficked through the cell in vesicular systems, via various uptake pathways [270].

Having relatively simple molecules that are intrinsically multimodal is therefore attractive. If the components are covalently linked, the proportions of the imaging agents will be maintained, with no question of differential leakage from a vehicle or cell unless the molecule is degraded. The size of a small molecule means that it could potentially pass through the cell membrane, as with many drugs and fluorescent dyes, possibly thus

reducing problems of vesicular segregation and trafficking.

Dendrimers could provide an interesting avenue of research since they have sizes defined by their 'generation' and are therefore monodisperse when pure. Their synthesis and purification are however complex, and therefore not as readily translatable to the clinic as is desired for this project. More accessible molecules have been considered here.

Systems such as a GdDTPA complex conjugated to a fluorinated coumarin dye [271], which would be technically trimodal by ^1H MRI, ^{19}F MRI and fluorescence, were considered. One fundamental problem however is that gadolinium moieties covalently linked to fluorine groups, even by long chains, have a significant relaxation enhancing effect on the fluorine [272]. This would dampen or remove the ^{19}F MRI signal without UTE pulse sequences. While such a system would therefore be of interest if other MRI equipment were available, it would not be suitable for this work.

A simple commercially available molecule, 7-amino-4-trifluoromethyl coumarin (AFC), see Figure 5.1, was investigated. This is a coumarin dye which also has a trifluoromethyl functionalisation that could be used for ^{19}F magnetic resonance.

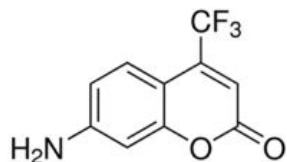


Figure 5.1: Molecular structure of 7-amino-4-trifluoromethyl coumarin (AFC).

AFC has previously been used as a marker for caspase activity [272]. The fluorophore is conjugated to a peptide (usually Ac-DEVD or Ac-LEHD), and fluoresces when the peptide is cleaved by caspase, a biomarker for apoptosis [273, 274]. It is similarly sold in plasmin assay kits attached to a plasmin substrate peptide, *e.g.* SensoLyte AFC Plasmin Activity Assay Kit.

AFC has also been used as a ^{19}F NMR probe for glutathione transferase [275], with the aim of eventually developing a probe to measure the enzymatic activity. The change in chemical shift of the singlet ^{19}F peak upon cleavage from the 'masking' group, indicated

the presence of glutathione transferase. This could potentially be of interest for work such as this as it indicates that the frequency of the ^{19}F peak will shift if the molecule is conjugated via the amine group. Hence if this molecule were further functionalised by conjugation, the bond subsequently breaking would be detectable by MRI.

The dual-modal imaging agent capability of AFC was examined. It was then incubated with PBMCs, and the uptake observed by flow cytometry, microscopy and MRI. The aim was to assess whether it is taken up at sufficient levels to be useful for cell tracking.

5.2 Characterisation results

7-amino-4-trifluoromethyl coumarin (AFC) was purchased from Sigma Aldrich, and was used as provided. The dual-modal capabilities of AFC and its PBMC labelling are assessed for cell imaging by fluorescence techniques and ^{19}F MRI.

5.2.1 Luminescence

The fluorescence excitation and emission spectra of 7 amino-4-trifluoromethyl coumarin (AFC) were measured, and are plotted in Figure 5.2. The excitation and emission maxima are 440 nm and 487 nm respectively.

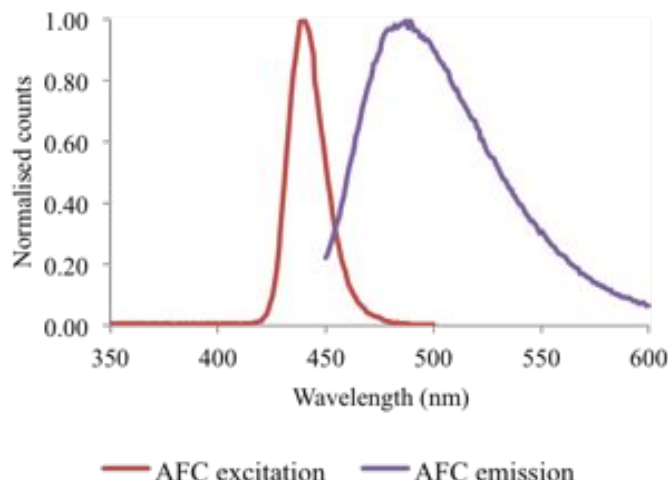


Figure 5.2: The luminescence excitation and emission spectra of 7-amino-4-trifluoromethyl coumarin in methanol. Excitation scans were monitored at 520 nm and emission scans were excited at 445 nm.

The fluorescence profile of AFC is suitable for fluorescence using visible light excitation sources. The emission is sufficiently shifted to allow filtering to distinguish it from the excitation light.

5.2.2 MRI signal

The ^{19}F MRI signal from solutions of AFC in DMSO was measured for a range of concentrations, and the resulting image is displayed in Figures 5.3 and 5.4.

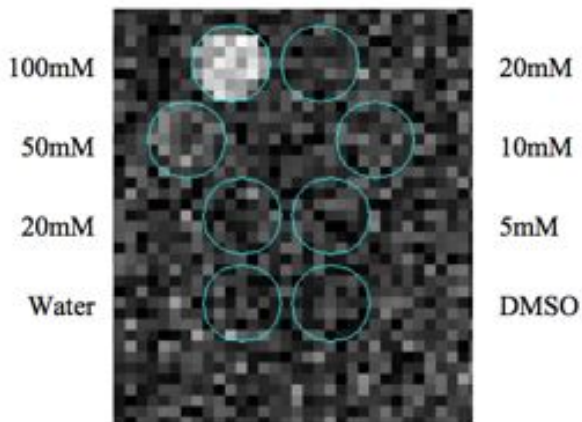


Figure 5.3: ^1H MR image of AFC at a range of concentrations, as annotated.

The samples showed a low signal-to-noise ratio, as plotted in Figure 5.4. This is comparable to the SNR obtained for trifluoroethanol (see Section 2.6.1), a molecule which also has three MR-equivalent fluorines.

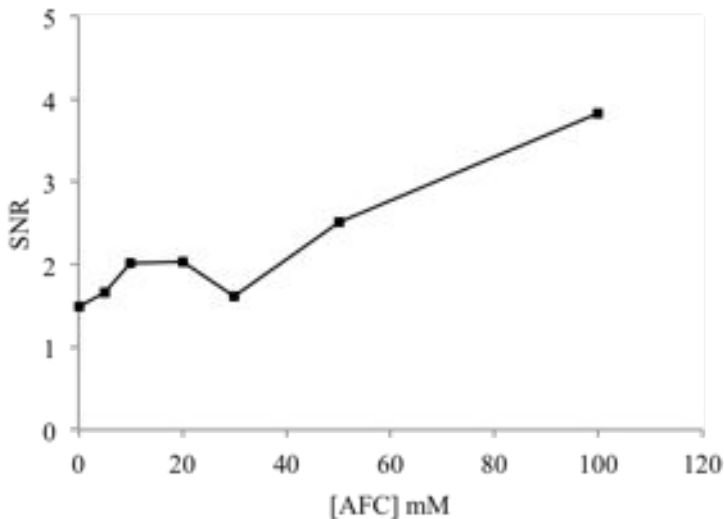


Figure 5.4: SNR of AFC samples in the ^1H MR image (see Figure 5.3).

The low SNR of the AFC indicates that, as expected from the experiments in Section 2.6.1, it would need to be taken up and retained in cells at very high concentrations in order to be of use in *in vivo* cell tracking by ^{19}F MRI.

5.3 Cell treatment results

AFC was incubated with PBMCs to test their interaction with immune cells. In particular, cellular uptake was noted, as well as the ability of the dye to label the cells for multimodal imaging. The dyes were incubated with isolated PBMCs for 24 hours and observed by flow cytometry, microscopy and ^{19}F MRI.

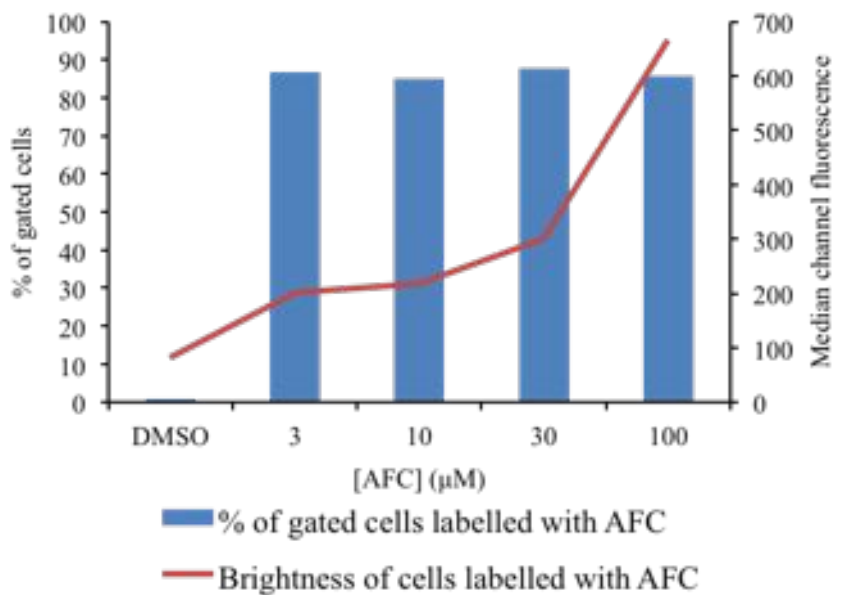
5.3.1 Flow cytometry

Flow cytometry showed that the uptake of the AFC into monocytes occurs readily, see Figure 5.5. 86% of the monocyte cloud were labelled with fluorescent material on average

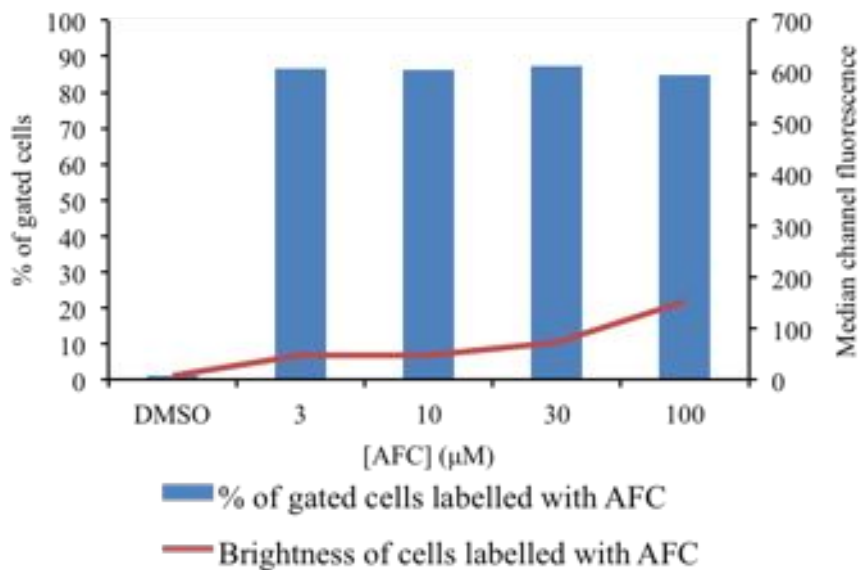
over the four treatment concentrations (with standard deviation 1%). There was also an increase in the median brightness of the labelled cells with increasing concentration, indicating a concentration dependent labelling.

86% of the lymphocyte cloud were also labelled with AFC (standard deviation 1%). The median channel fluorescence was however much lower than for the monocytes, with a maximum of 150 (arbitrary scale) for the lymphocytes compared to 670 for the monocytes, indicating that there is concentration dependent labelling, but to a more moderate level.

Typical forward scatter/side scatter plots at various AFC concentrations are shown in Figure 5.6. One point to note is that there is much less debris present than in the other flow cytometry plots in this work, due to the lack of nanoparticle aggregates. This makes the analysis more reliable as the smaller granular points are more likely to correspond to dead or dying cells.

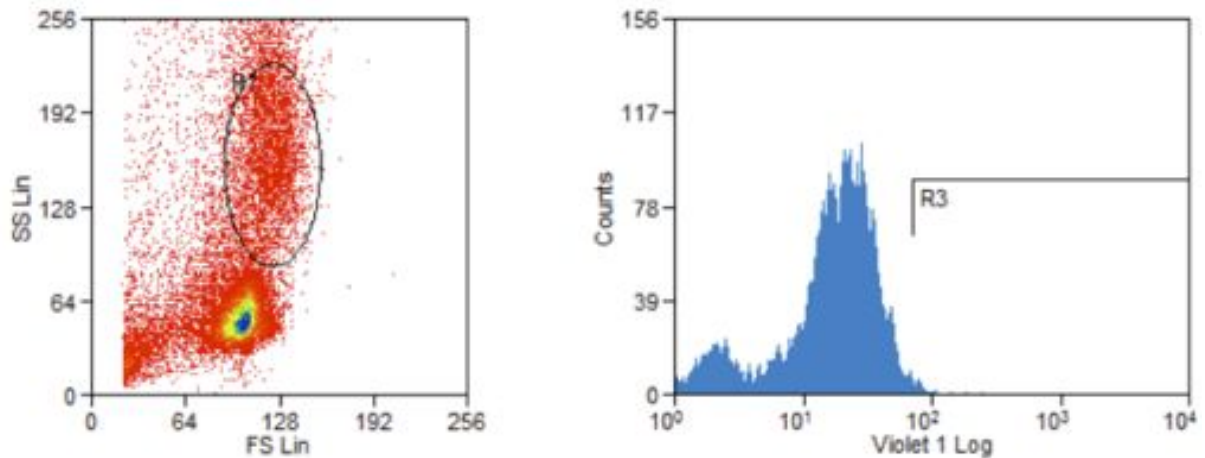


(a) Monocytes

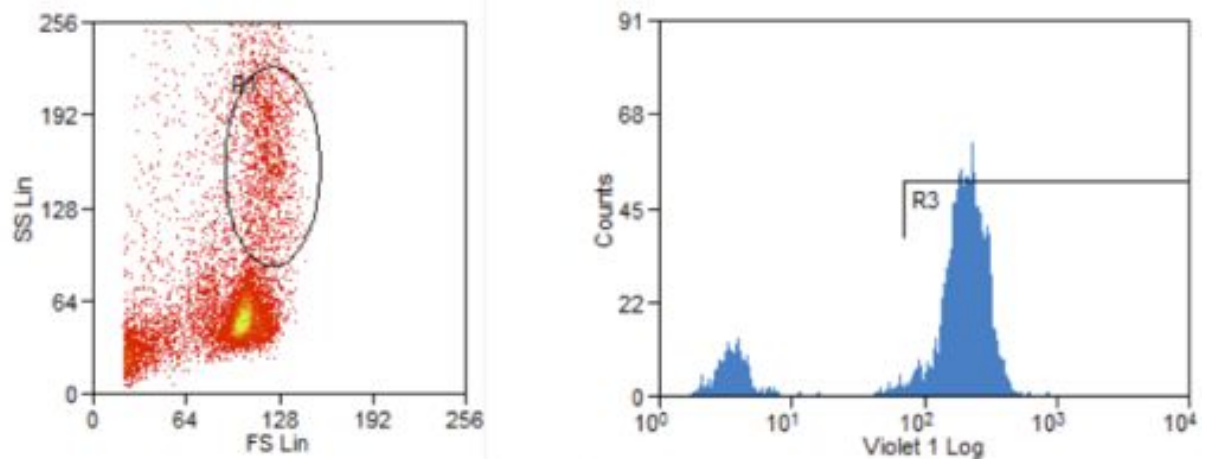


(b) Lymphocytes

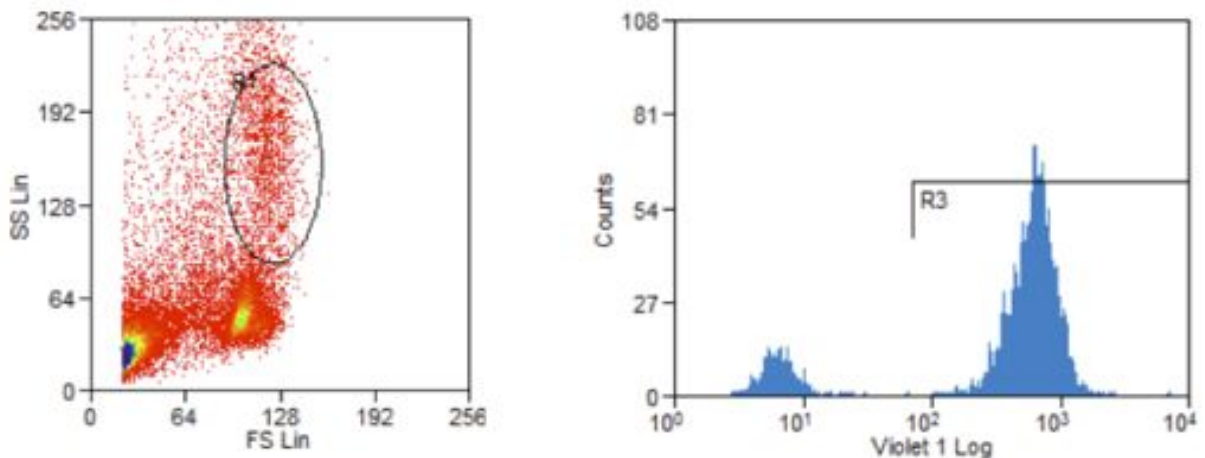
Figure 5.5: Plots showing the concentration-dependent uptake of AFC into (a) monocytes and (b) lymphocytes by flow cytometry. The blue bars indicate the percentage of the cell type which are labelled, while the red line indicates the median brightness of the labelled cells.



(a) DMSO control ($[AFC] = 0$)



(b) $10 \mu M$ AFC



(c) $100 \mu M$ AFC

Figure 5.6: Forward scatter/side scatter plots of PBMCs labelled with increasing AFC concentrations, and the corresponding fluorescence histograms.

The other point to note is that, as can be seen in Figure 5.7, fewer of monocytes and

lymphocytes are found in the cell clouds with increasing concentration of the dye. The percentages of the total cell population that fall within the gates of their control cloud decreases with concentration, most notably above 10 μM AFC. This could be due to the dye disrupting the membrane at higher concentrations, leading to increased cytotoxicity.

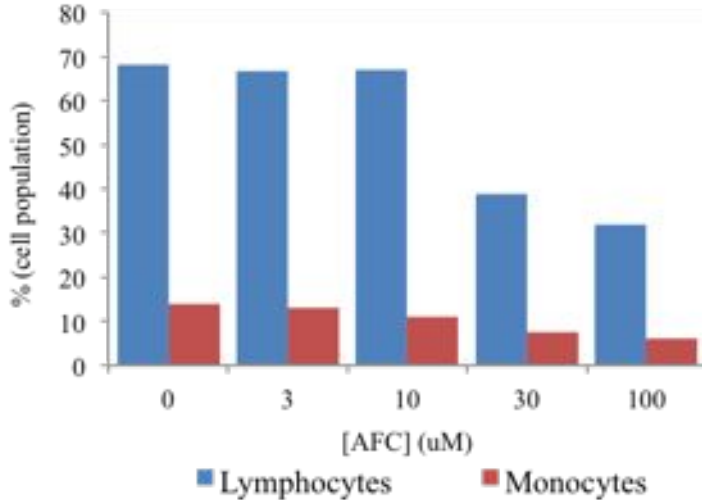


Figure 5.7: Plot of the decreasing percentage of each cell type (monocytes and lymphocytes) which remain within the same size and granularity gate (from the forward scatter/side scatter plots). Values indicate the percentage of the total cell population falling within these gates, depending on the AFC labelling concentration.

10 μM AFC would therefore be a reasonable concentration for future viability based testing, as it is expected that at this concentration the majority of the cells will be healthy.

5.3.2 Fluorescence microscopy

The AFC is unfortunately not compatible with immunohistochemistry processes such as staining with Kwik-Diff, possibly due to the methanol permeabilisation step allowing the dye to leak out. Therefore though the cells were visible by brightfield microscopy, appearing similar to the stained control cells, no fluorescence was detected.

5.3.3 MRI detection

PBMCs were treated for 24 hours with 10 μM AFC, corresponding to the highest dose that showed little change in cell size or morphology by flow cytometry.

PBMCs were pelleted at 50×10^6 and 20×10^6 cells and imaged by MRI. No signal was detectable above the level of the noise. The 50×10^6 cells pellet was then lysed by sonication, re-suspended in D_2O and analysed by fluorine NMR. No signal was detectable spectroscopically either, suggesting that the AFC is not present at a high enough concentration in the cells to be useful for cell tracking by ^{19}F MR.

5.4 Conclusions

Simple molecules are easier to work with than nanoparticles, and can bear multiple functionalities. AFC, an intrinsically dual modal agent, produced a single ^{19}F MR peak, so did avoid problems of chemical shift artefacts. It also produced a fluorescence signal involving excitation and emission well within the visible range of the spectrum and a large enough Stokes' shift to allow filtering if necessary.

AFC was readily taken up into PBMCs and detected by flow cytometry. Uptake depended on concentration, and the levels of uptake differed between monocytes, which became fluorescent at low concentrations around 3 μM , and lymphocytes, which required higher concentrations in the 100 μM range in order to shift the median channel fluorescence. Cytotoxicity at these high concentrations is a concern however, as the flow cytometry indicated a considerable change in the size and shape of the cells. There was however no ^{19}F MRI peak detectable on a clinical scanner from a cell pellet, suggesting that the local concentration of dye in the cells is not high enough to generate a signal. AFC is therefore not a suitable dual modal agent for cell tracking used alone.

The signal could potentially be boosted if the number of fluorines per molecule could be increased. For example, the molecule could be attached to a central structure such as 3,3-bis(carboxymethyl)glutaric acid to produce 4 equivalent trifluoromethyl groups per

molecule, so boosting the signal by 5. Three potential problems with this are that the solubility of the highly fluorinated molecule may be low in solvents that can be used in cell culture, that the purification of the fully conjugated structure from the partially reacted structures may be difficult, and the fluorescence excitation may be shifted into the UV. If a suitable compound were designed and these problems were resolved however the use of molecular structures could be an interesting way to label the cells for dual modal cell tracking.

As mentioned above, trimodal cell tracking by fluorescence, ^1H and ^{19}F MRI would be more challenging since the gadolinium for the ^1H contrast will exert a relaxation-enhancing effect on the fluorine groups [272, 276], making them more difficult to detect with standard MR protocols. There are ultrashort echo time (UTE) sequences [277] which might resolve this problem, and that could be of interest in future work.

CHAPTER 6

TRAPPING IMAGING AGENTS IN A NANOPARTICLE CORE

In this chapter, hollow nanoparticles were created with the aim of encapsulating imaging agents inside the cavity. A range of syntheses were explored for forming the shells, and the most promising was developed into a trimodal imaging agent for luminescence techniques, ^1H MRI and ^{19}F MRI.

6.1 Introduction

Having explored various other avenues through this work, it was found that a high loading of fluorine would be necessary in order to detect particles by ^{19}F MRI. There has been much research on porous structures, such as mesoporous silica nanoparticles, for trapping imaging agents [169, 278]. It follows however that a larger cavity, such as in hollow nanoparticles, would be beneficial in order to obtain maximum fluorine loading.

A hollow structure such as this could be modified further with other agents for luminescence or ^1H MRI contrast. This might then prove to be an effective way of delivering reliably high concentrations of multiple agents into cells.

Hollow liposomal and polymeric systems have been investigated extensively [279, 16, 146, 150, 147]. While these have advantages such as high biocompatibility and translatability, they tend to be larger and less robust than silica particles due to effects such as

Ostwald ripening. A smaller alternative system was therefore sought, as discussed below.

6.2 Overview and system design

The creation of hollow shells were investigated focusing on silica, a robust biocompatible material [280, 281]. There are reports of the permeability of silica, possibly making the inclusion of mesopores unnecessary for some agents, but the synthesis of both solid and mesoporous shell structures were explored here, thus potentially allowing for the introduction of a greater range of imaging agents.

There are many reported techniques for producing these hollow shells, ranging from homogeneous templating [282], where a solid silica particle is created then the core is degraded, to heterogeneous templating [283], where an alternative material is used for the core, which is subsequently removed. The following techniques for synthesising hollow silica nanoparticles were attempted in this project.

Method 1: Dissolution and regrowth

292 nm hollow particles were reported to be made by dissolving 400 nm solid silica particles in a borate solution, and their spontaneous regrowth on the surface [284]. The solid spheres are created by a rapid Stober process which produced highly monodisperse nanoparticles. A polymer (polyvinyl pyrrolidone) is deposited on the surface and the nanoparticles are reacted with sodium borohydride in water. The borohydride forms a borate salt, which aids in the dissolution of the nanoparticles. The dissolved silicates then redeposit on the surface, regrowing the nanoparticle shell, as illustrated in Figure 6.1. The roughness of the shells is then reportedly controlled by the temperature to which this solution is heated.

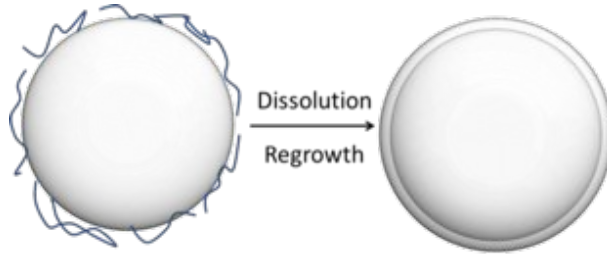


Figure 6.1: Illustration of the formation of hollow nanoparticles by simultaneous dissolution and regrowth. A silica nanoparticle is coated in polymer, the particle is dissolved and the shell spontaneously reforms.

The aim in this project was to replicate this method but with smaller nanoparticles, so forming hollow shells of approximately 100 nm.

Method 2a: Latex templating in acid

Silica shells can also be created by a heterogeneous templating method, making the subsequent removal of the core easier. Silica coated latex beads can be hollowed either by dissolution of the core in a solvent, or by calcination at a temperature, 550°C, which will remove the organic matter and leave the silica intact. This method was therefore attempted with modifications of reference [285], as illustrated in Figure 6.2.

Amine-modified beads had poly-L-lysine deposited on their surface. Freshly hydrolysed silicate species were then added in acidic solution, which crosslinked to form a silica shell, catalysed by the poly-L-lysine. The core was removed by stirring with toluene or dichloromethane. It is worth noting that the poly-L-lysine may still be present in the silica shell unless the particles are calcined, which may or may not be desirable. This could be verified in a hollow particle suspension by zeta potential measurements.

The starting silane was varied from the tetraethyl orthosilicate to the tetramethyl orthosilicate as it was thought that the different hydrolysis rates might affect the shell formation so reduce the amount of debris.



Figure 6.2: Illustration of the formation of hollow nanoparticles templated by a latex sphere. A polystyrene latex bead is coated in polymer, coated in silicic acid. The core and polymer are then calcined or dissolved away.

Method 2b: Latex templating in base

Amine-modified latex beads may also be coated with silica in basic solution according to reference [286]. The latex beads are dispersed in an ammonia alcohol solution and the silica precursor added in the same manner as a Stober synthesis. The latex core can then be removed as above, by calcining or solvent extraction.

Method 3: Selective etching

Hollow particles can also be created by the selective etching of silica nanoparticles in a heated basic solution [282]. Solid spheres are created according to a Stober type synthesis then coated with a shell incorporating C₁₈ chains as porogens. After washing, particles are etched in base, washed and calcined to remove the C₁₈ chains. This process is illustrated in Figure 6.3.



Figure 6.3: Illustration of the selective etching of silica nanoparticles. A silica nanoparticle is coated with organically modified silanes, the core is etched away, and the particle is calcined leaving a hollow porous shell.

Loading of imaging agents

The first step in adding imaging functionality to the hollow particles was coating the surface with gadolinium complexes, producing gadolinium-functionalised hollow nanoparticles (GdHSNPs). In this case the gadolinium complex was the same GdDTPA-APTES silane that was used in Chapter 4. This would add proton MRI contrast enhancement, while leaving the core of the GdHSNPs to be filled with other agents.

Loading of imaging agents into the core was then attempted with the most promising silica shells, as indicated in Figure 6.4. The imaging agents used for the filling must be: smaller in diameter than the nanoparticle; capable of either being trapped during the synthesis or being introduced afterwards (e.g. through pores in the shell). They must also not require interaction with the bulk of the solvent, since they would be limited in interaction to the contents of the shell.

In this work, PFOB was used as a ^{19}F MRI tracer which is immiscible with water and has previously been clinically approved. The immiscibility should reduce leakage from the nanoparticle into aqueous media, and the previous clinical approval is an indication of the capability for it to be manufactured to GMP standards, and of its bio-inert properties.

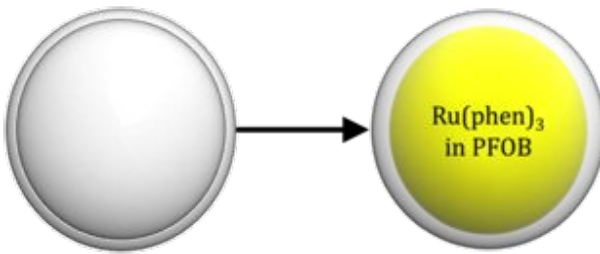


Figure 6.4: Illustration of the loading of hollow nanoparticles with imaging agents.

Other design considerations

Using a removable heterogeneous template to form hollow silica nanoparticles has been investigated in the literature with magnetic [285], calcium carbonate [287] and carbon [288] nanoparticle templates. These hollow particles tend to be anywhere between 10-200 nm in diameter, depending strongly on the size of the template, with rough surfaces, as

frequently seen by electron microscopy.

In order to minimise the surface area to volume ratio, hence increasing the volume of cargo the particle can contain (see Figure 6.5), it is desirable to use larger hollow particles. This is limited however by the size of particles that cells can internalise readily, and the associated cytotoxicities, as discussed in Section 1.5.

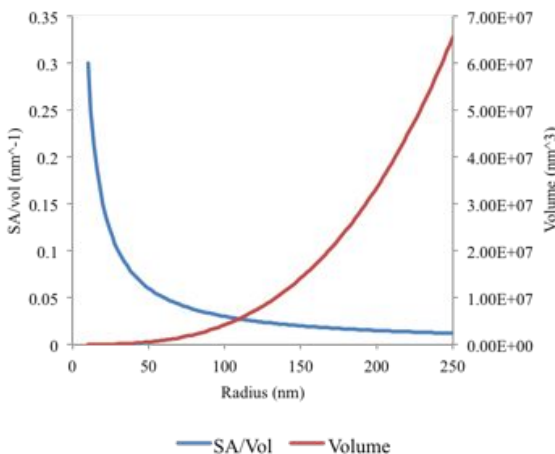


Figure 6.5: Plot showing the relation between surface area to volume ratio and the core volume for a range of sphere radii.

Large hollow nanoparticles or microparticles (in the range of 200 nm to micrometers in diameter) have also been reported [289, 290]. These are often created around latex bead templates, the polydispersity of which determine the polydispersity of the hollow structures. At these sizes, the surfaces seem to be more readily controlled, providing the possibility of smooth solid surfaces or rougher more porous shells as required.

Particles in the range of 100-150 nm in diameter would be interesting vehicles, and a range of the reported methods were investigated. They have a relatively low surface area to volume ratio, but may still be readily internalised by the cells. The aim at first was therefore to create nanoparticles in this size range, and although the final trimodal particles in this work are larger, the eventual goal would be to reduce the size back to this range if the loading of fluorinated species were sufficient for MRI.

Other design considerations are that the shells should allow the imaging agents to enter or be trapped, but in this case must also minimise leakage. Design features to allow

this could include:

- Favourable interactions (hydrophobicity, electrostatic or covalent) to hold the agents inside;
- Capping of the nanoparticle surface once the agents are trapped;
- Incorporating the agents in a liquid medium that subsequently gels or solidifies, thus reducing their diffusion rate, though this would probably require UTE pulse sequences for the fluorine MRI.

The first option was used in this work in that a hydrophobic fluorous solvent filled the shells which were suspended in aqueous solvents, though the other methods could be interesting avenues for future work depending on the imaging agents of interest.

6.3 Experimental details

Experimental information included here is specific to this chapter. All other details can be found in the general experimental details section in Chapter 2.

6.3.1 Materials

Octadecyltrimethoxysilane (C_{18} TMS) (90%) was purchased from Sigma-Aldrich (UK) and warmed to 25°C prior to use if necessary to ensure the product was fully liquid.

Sodium carbonate (Na_2CO_3 , purum) was purchased from Fisher Scientific (UK).

Polyvinyl pyrrolidone (average molecular weight 58 kDa) was purchased from VWR. Sodium borohydride (98%), tetramethyl orthosilicate (98%) and poly-L-lysine hydrobromide powder (70-150 kDa) were purchased from Sigma Aldrich.

Aliphatic amine latex beads ($0.1\ \mu m$, 2% w/v) were purchased from Life Technologies.

6.3.2 Hollow silica nanoparticle syntheses

The synthetic methods for creating hollow silica nanoparticles are described in this section. Various syntheses were attempted by a range of methods: dissolution and regrowth, heterogeneous templating by latex beads, and selective etching.

Synthesis by dissolution and regrowth

Silica nanoparticles were formed by a modification of the Stober synthesis.

A solution of 2.8 ml of NH₄OH (28-32%), 30.6 ml distilled water and 16.6 ml of ethanol was rapidly mixed with a solution of 4.5 ml of TEOS and 45.5 ml of ethanol. The mixture was stirred for 6 hours at 800 rpm, but became turbid within minutes.

The nanoparticles were washed by centrifugation and resuspension in ethanol twice and water twice. The nanoparticles were concentrated to 30 mg/ml by centrifugation and resuspension. This suspension was split into 10 ml aliquots to test different methods of forming the shell.

One 10 ml aliquot of the nanoparticle suspension was placed in a plastic centrifuge tube and 600 mg of NaBH₄ was added. The suspension was left for 10 days with occasional shaking to resuspend the nanoparticles.

Another 10 ml aliquot of the 30 mg/ml nanoparticle suspension was used for a more rapid reaction. The nanoparticles were centrifuged and resuspended in a 2.9% polyvinyl pyrrolidone solution (291 mg PVP, 58 kDa, in 10 ml of distilled water). 600 mg of NaBH₄ was added. A gas evolved rapidly causing foaming. The suspension was transferred to a 500 ml round bottomed flask and stirred while heating to 50°C. It was held at this temperature for 6 hours then washed in water three times.

Synthesis by latex templating in acid

1 M silicic acid was prepared from TEOS by stirring 230 μ l of TEOS in 0.01 M HCl for 20 minutes.

625 μ l of aliphatic amine latex spheres (0.1 μ m) were mixed with 10 ml of PBS and 2 ml of 0.1% poly-L-lysine (70-150kDa) in PBS and sonicated briefly. 250 μ l of 1 M silicic acid was then added, and the mixture was stirred for at least 10 minutes. The particles were washed with water then re-suspended in toluene. The toluene suspension was stirred for 24 hours, washed into fresh toluene and stirred for a further 24 hours. The particles were then washed with ethanol three times and water three times, and dried in a glass vial in an oven.

Surface modification of the HSNPs latex-templated in acid

The HSNPs were prepared as for the plain HSNPs, then resuspended at 10 mg/ml in ethanol.

Meanwhile 177 mg (295 μ mol) of APTES-DTPA was dissolved for 30 minutes in 600 μ l of 1 M NaOH. 400 μ l (200 μ mol) of 0.5 M GdCl₃ in distilled water was added and allowed to dissolve for two hours. The 250 μ l (50 μ mol of Gd) of the ligand solution was then added to the nanoparticle suspension and stirred over night.

The resulting particles were washed by centrifugation and resuspension in ethanol three times and water three times.

Synthesis by latex templating in base

1.3 ml of aliphatic amine polystyrene beads, 6.7 ml of water and 40 ml of 2-propanol were placed in a round-bottomed flask. 1 ml of NH₄OH was added, and the pH was verified as being between 11 and 12. 219 μ l of TEOS was added and the suspension was stirred at 800 rpm for 3 hours. The particles were washed with propanol, then resuspended in toluene and stirred for 24 hours.

The particles were purified by centrifugation and resuspension in ethanol three times then water three times.

Synthesis 1 by selective etching

36 ml of ethanol, 5 ml of deionised water and 1.6 ml of ammonium hydroxide (NH_4OH 28-32%) were stirred in a 250 ml round-bottomed flask for 30 minutes. 3 ml of TEOS were added and the solution was stirred for a further 1 hour, during which it became turbid.

1 ml of C_{18}TMS and 2.5 ml of TEOS were mixed and added to the suspension, then stirring continued for a further 1 hour.

The nanoparticles were then washed three times by centrifugation, decantation of the supernatant and resuspension to the same volume in ethanol. They were finally washed and resuspended in approximately 100 ml of 0.6 M Na_2CO_3 and transferred to a 500 ml round-bottomed flask.

The basic nanoparticle suspension was heated to 80°C while stirring, and maintained at that temperature for 30 minutes.

The particles were then again washed in distilled water three times before drying in a glass petri dish at room temperature or vial in a drying oven.

The dried nanoparticles were calcined for 6 hours at 550°C in air (ramp rate 5°C/min) and allowed to cool to room temperature overnight.

Synthesis 2 by selective etching

The solid and coated silica particles were created as for synthesis 1.

The nanoparticles were then washed three times by centrifugation, decantation of the supernatant and resuspension to the same volume in ethanol. They were finally washed and resuspended in approximately 200 ml of 0.6 M Na_2CO_3 and transferred to a 500 ml round-bottomed flask.

The basic nanoparticle suspension was heated to 80°C while stirring, and maintained at that temperature for 4 hours.

The particles were washed, dried and calcined as for synthesis 1.

Surface functionalisation of HSNPs produced by selective etching (synthesis 2) with gadolinium

APTES-DTPA was synthesised as in Section 4.2.

88 mg (22 µmol) of APTES-DTPA was dissolved for 30 minutes in 180 µl of 1 M NaOH. 18.6 mg (50 µmol) of $\text{GdCl}_3 \cdot 6\text{H}_2\text{O}$ was added and allowed to dissolve for 30 minutes. The ligand solution was then added to a HSNP suspension of 300 mg in 30 ml of ethanol. The particles were stirred over night at 800 rpm, then washed twice with ethanol and twice with water by centrifugation at 4000 x g, decantation of the supernatant and resuspension.

Filling the cores of HSNPs produced by selective etching (synthesis 2) with ruthenium tris-phenanthroline and PFOB

0.5 mg of $[\text{Ru}(\text{phen})_3](\text{PF}_6)_2$ was suspended in 0.5 ml of PFOB by sonication. 225µl of this suspension was added, in aliquots of 25µl with sonication for roughly ten seconds after each addition, to 10 mg of dried HSNPs or GdHSNPs in a glass vial. The liquid appeared to be absorbed by the solid after each addition, with the final addition seeming to reach the saturation point, thus creating RuPFOBHSNPs or RuPFOBGdHSNPs.

The particles were then suspended in 1 ml of PBS with minimal agitation or sonication.

6.3.3 Hollow nanoparticle characterisation

Light scattering (DLS)

Hollow nanoparticles are not reliably characterisable by DLS, since the calculations involved rely on the density and optical properties of the sphere, which will be different for nanoparticles of varying shell thickness and composition.

Zeta potential measurements were nevertheless carried out for the sake of comparison between the charges of the functionalised and non-functionalised surfaces. These were carried out as detailed in Section 2.2.1.

Electron microscopy (TEM and SEM)

TEM samples were prepared as in other chapters, as detailed in Section 2.2.2.

For scanning electron microscopy (SEM), samples were placed on an adhesive carbon pad on a sample stub. The surface was sputter coated under vacuum with gold at 25mA (Emscope SC500). The preparation was then imaged in a Philips XL30 ESEM-FEG.

Density, luminescence spectroscopy and ICP-MS

The density of samples was measured by helium pycnometry as described in Section 2.2.3. All of the density measurements were carried out by Dr. R. Williams.

Luminescence spectra were recorded as for the other chapters, as described in Section 2.2.5

ICP-MS samples were prepared and analysed as in other chapters according to Section 2.2.4

6.4 Synthesis and characterisation results

Method 1 is a modification of a reported process of dissolving nanoparticles for the silicate species to redeposit on the surface thus creating shells [284]. The solid nanoparticles were first created with a deliberately low density silica matrix by a rapid form of the Stober synthesis. The silane molecules are given less time to hydrolyse before being incorporated, so making the matrix in the core weaker and more susceptible to hydrolysis. After coating with a stabilising polymer and addition of borohydride, the rehydrolysed silicate species reportedly deposit on the surface of the particle, thus regrowing the silica matrix [284]. The method was mainly developed and reported for larger particles. Here the aim was to modify this method for roughly 100 nm nanoparticles. No hollow particles were visibly produced however, see Section 6.4.1, so further techniques were explored.

Next heterogeneous templating was tried in order to form the silica shells. Aminated polystyrene latex beads were coated with silica, structured around poly-L-lysine deposited

on the latex surface, with the coating step occurring in either an acidic or basic solution. Using an acidic solution has the advantage of maintaining the stability of the latex spheres, but requires the shells to be in a basic solution for further functionalisation with metal complexes. Using a basic solution has the opposite benefits and disadvantages. This did produce hollow particles, but debris mixed with the particles makes purification difficult. Modifications to the surface made this problem worse, as shown in Section 6.4.2, suggesting that the technique would need considerable optimisation to make it feasible.

Hollow nanoparticles were also created according to a selective etching protocol [282]. In a similar way to method 1, a particle is formed with a silica core, but in this case the surface layer is interspersed with lipophilic areas formed from a silane with an 18-carbon chain, $C_{18}TMS$. The less well-condensed core is more susceptible to base catalysed hydrolysis than the surface, allowing the selective removal of the core, followed by calcination of the C_{18} chains. This method showed more promising results, so these were developed as a basis for creating trimodal imaging agents. The particles were surface-functionalised with gadolinium complexes, and filled with a perfluorocarbon fluorophore suspension. The synthesis and characterisation of this trimodal imaging agent is described in Section 6.4.3.

6.4.1 Hollow particle synthesis by dissolution-regrowth

Nanoparticles were initially created by a rapid version of the Stober process. According to reports in [284] they could then be etched by reaction with sodium borohydride, either at ambient temperature over 10 days or at a higher temperature within an hour.

This is an attractive method because it appears to produce highly regular particles with a highly controllable shell thickness and core size.

Unfortunately however the results reported in [284] could not be reproduced for particles with roughly 100-200 nm diameters. The sodium borohydride appeared to have no effect, either at ambient temperature, or at higher temperature.

Light scattering (DLS and zeta potential measurements)

The nanoparticles before the dissolving process had a mean diameter of $160\text{ nm} \pm 40\text{ nm}$ (by number distribution), or $190\text{ nm} \pm 44\text{ nm}$ (by intensity distribution), with a polydispersity index of 0.023. These particles therefore have a corresponding radius $80\text{ nm} \pm 20\text{ nm}$. This would be a suitable size to allow for the reduction in diameter seen during dissolution process in the original article.

The zeta potential was $-5 \pm 2\text{ mV}$, which is surprisingly low for a silica nanoparticle, and possibly due to terminal OEt groups on the surface where the silane was not fully hydrolysed.

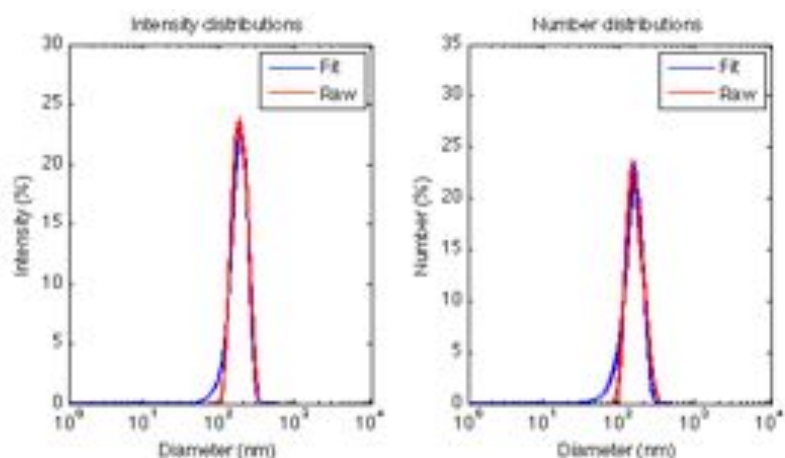


Figure 6.6: DLS intensity (left) and number (right) distributions for the silica nanoparticles prior to the borohydride treatment.

Electron microscopy (TEM and SEM)

Characterisation was principally carried out by TEM to assess the effectiveness of the synthesis as this gives a clear outline of the particle and an indication of its morphology.

The particles used as the base structures varied in size, but had a clear solid morphology, as shown in Figure 6.7 with the measured size distribution plotted in Figure 6.8. The mean radius was $76\text{ nm} \pm 9\text{ nm}$ based on 398 particles detected in the TEM images, analysed by the method described in Section 7.1.

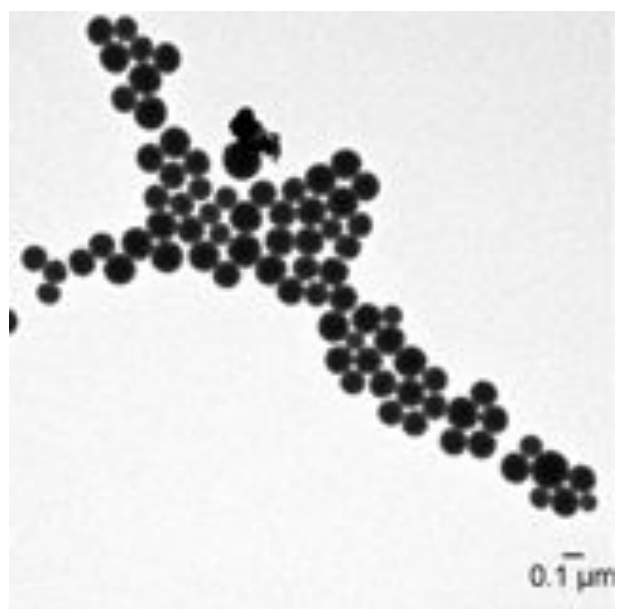


Figure 6.7: TEM image of silica nanoparticles used as the initial particles for the synthesis of hollow silica nanoparticles by dissolution and regrowth.

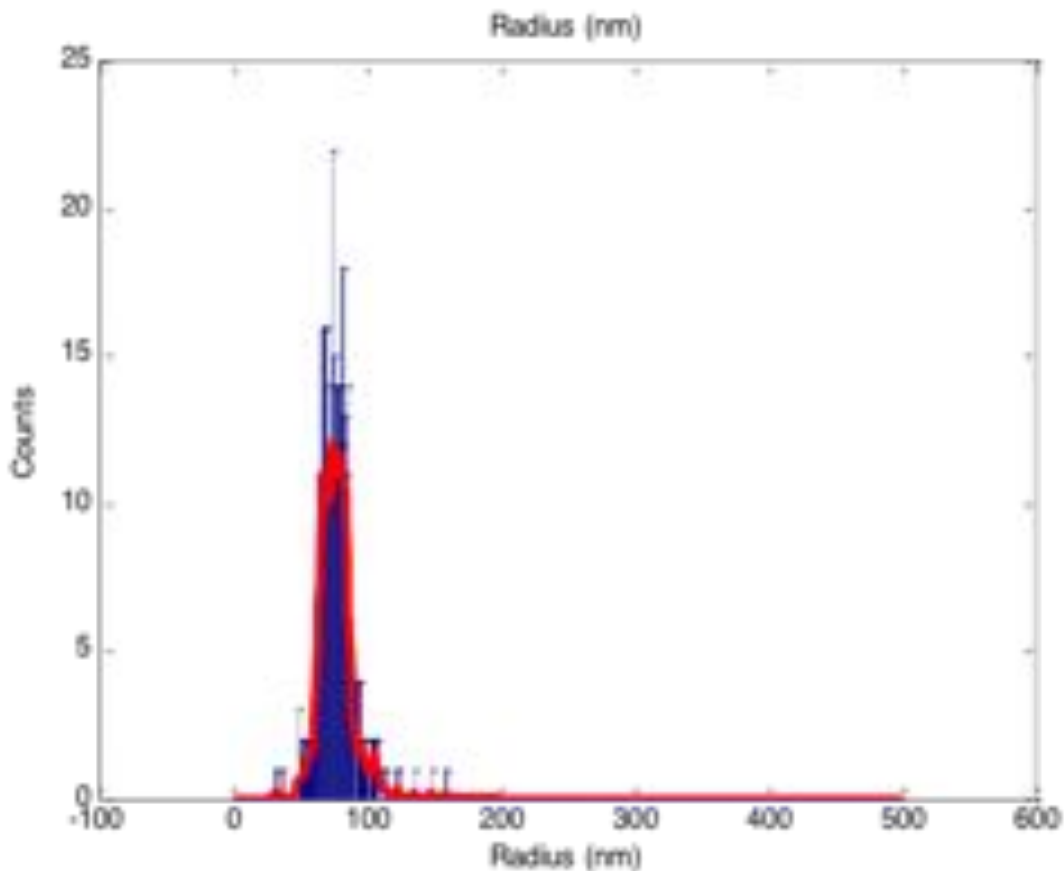


Figure 6.8: Histogram of SiNPs' radii measured from TEM images by automated segmentation. The red line shows the fitted Gaussian distribution.

These SiNPs were considerably smaller than those in the original article, but formed by a similar method. Their composition was therefore expected to be similar, so subject to the same reactions.

After the dissolution-regrowth treatment step the particles contained more debris and had less well defined morphology, suggesting that a reaction with the silica was occurring. They did not however appear to contain any cavities, as shown in Figure 6.9.

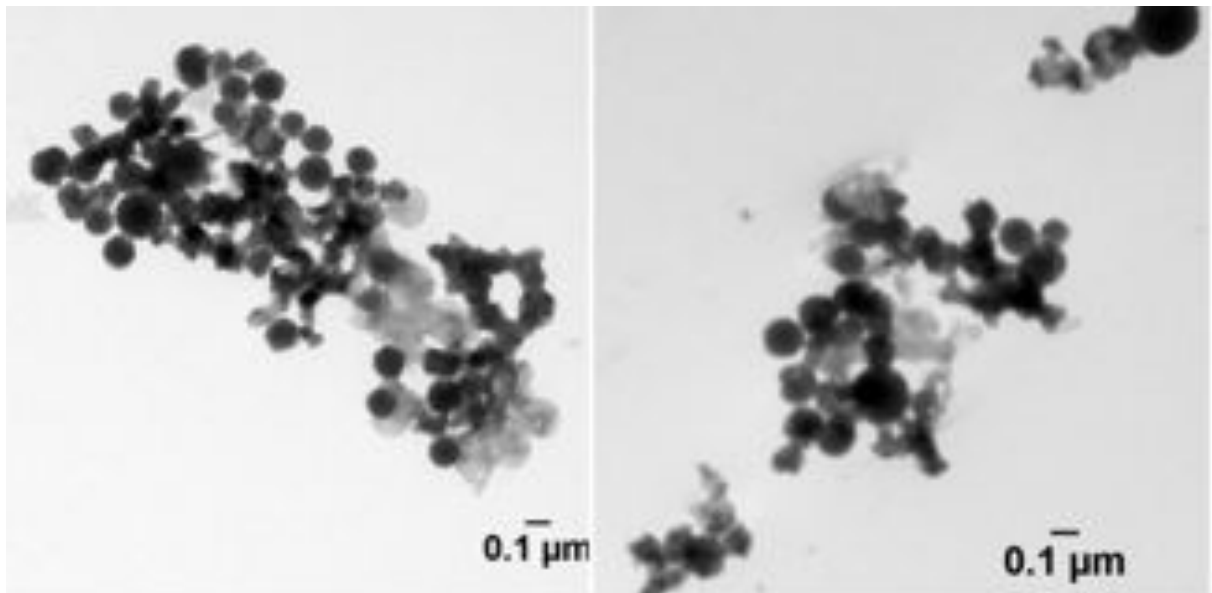


Figure 6.9: TEM images of silica nanoparticles after the dissolution-regrowth treatment intended to create hollow SiNPs.

Conclusions

The results reported in [284] could not be reproduced for nanoparticles of roughly 160 nm diameters. The sodium borohydride appeared to have no hollowing effect, either at ambient temperature, or at higher temperature. This synthesis was therefore not pursued.

6.4.2 Hollow particle synthesis by latex templating

Polystyrene latex nanoparticles, with poly-L-lysine first deposited on the surface, were coated with silanes to produce a silica shell. The poly-L-lysine would provide extra positively charged amine groups for the deposition of the silicate species. The latex core

was then dissolved away using organic solvents, leaving a hollow silica shell.

The benefit of this method is that the latex templates are available in highly monodisperse suspensions, thus creating silica shells with very readily controlled sizes. The template can also be readily removed, either by calcination or by dissolution in organic solvent. While calcination can be more effective at removing the core than solvents [285], it was found that, with the quantities handled during these experiments, less of the sample was lost by the solvent extraction method. If a similar synthesis were scaled up in future work calcination would be an important route to explore in order to maximise the cavity's volume.

Coating in acidic solution: electron microscopy (TEM)

The synthesis was explored using both TEOS and tetramethyl orthosilicate (TMOS) as silane precursors, pre-hydrolysed in acidic solution for 30 minutes. Characterisation was carried out by TEM to assess the effectiveness of the synthesis. The electron microscopy images of the resultant silica shells after dissolution of the cores are shown in Figures 6.10 (TEOS) and 6.11 (TMOS).

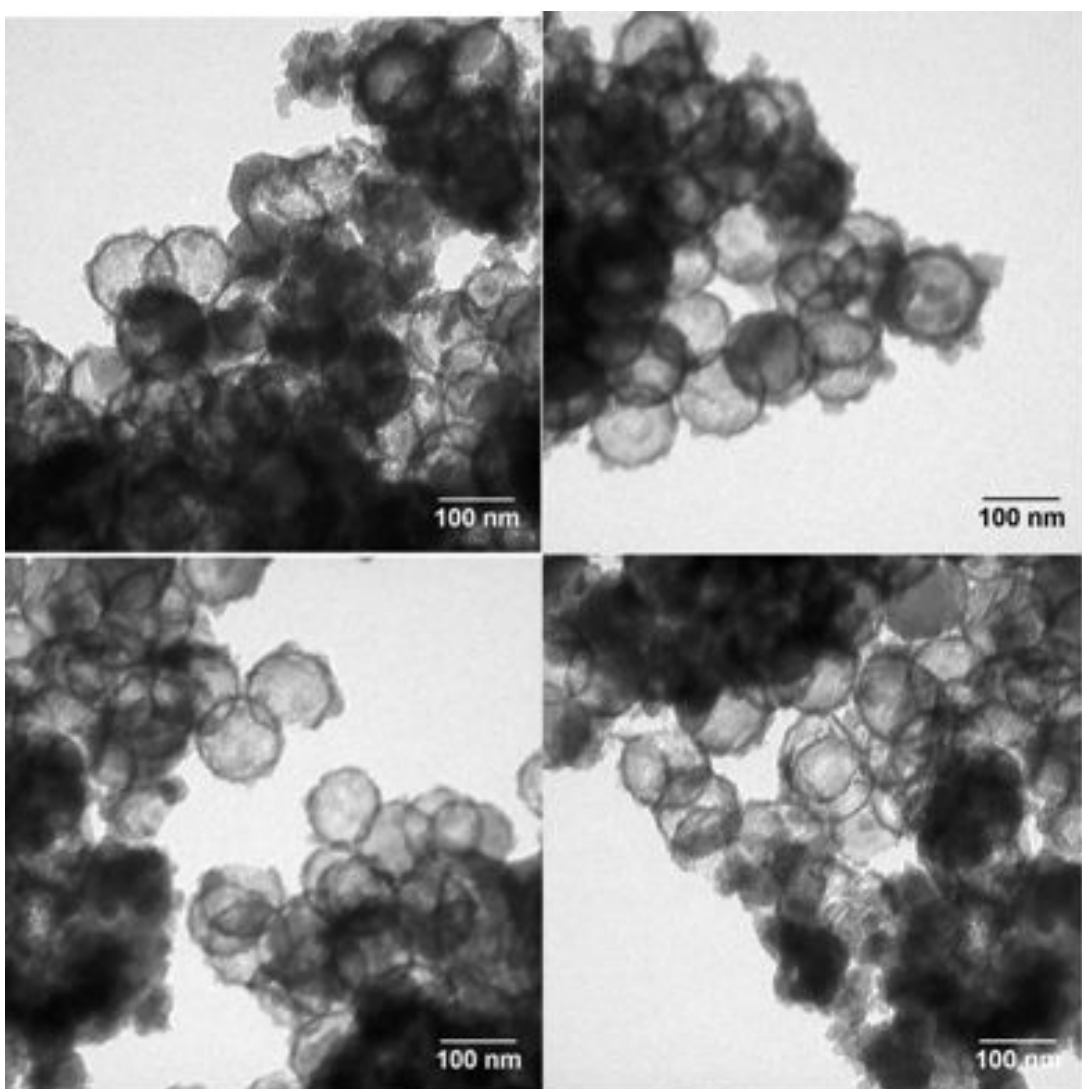


Figure 6.10: TEM images of HSNPs created by latex templating from TEOS in acidic solution.

The TEOS HSNPs were found to have a mean radius of $59 \text{ nm} \pm 3 \text{ nm}$. They appeared to have poorly defined silica shells, making shell thickness determination difficult. There is also a significant amount of debris present which could not be readily separated from the nanoparticles during purification. Though this could simply be nanoparticle aggregates, so potentially capable of trapping PFCs in their core, this would be problematic for cell uptake. One point to note is that there were no obvious secondary solid particles observed.

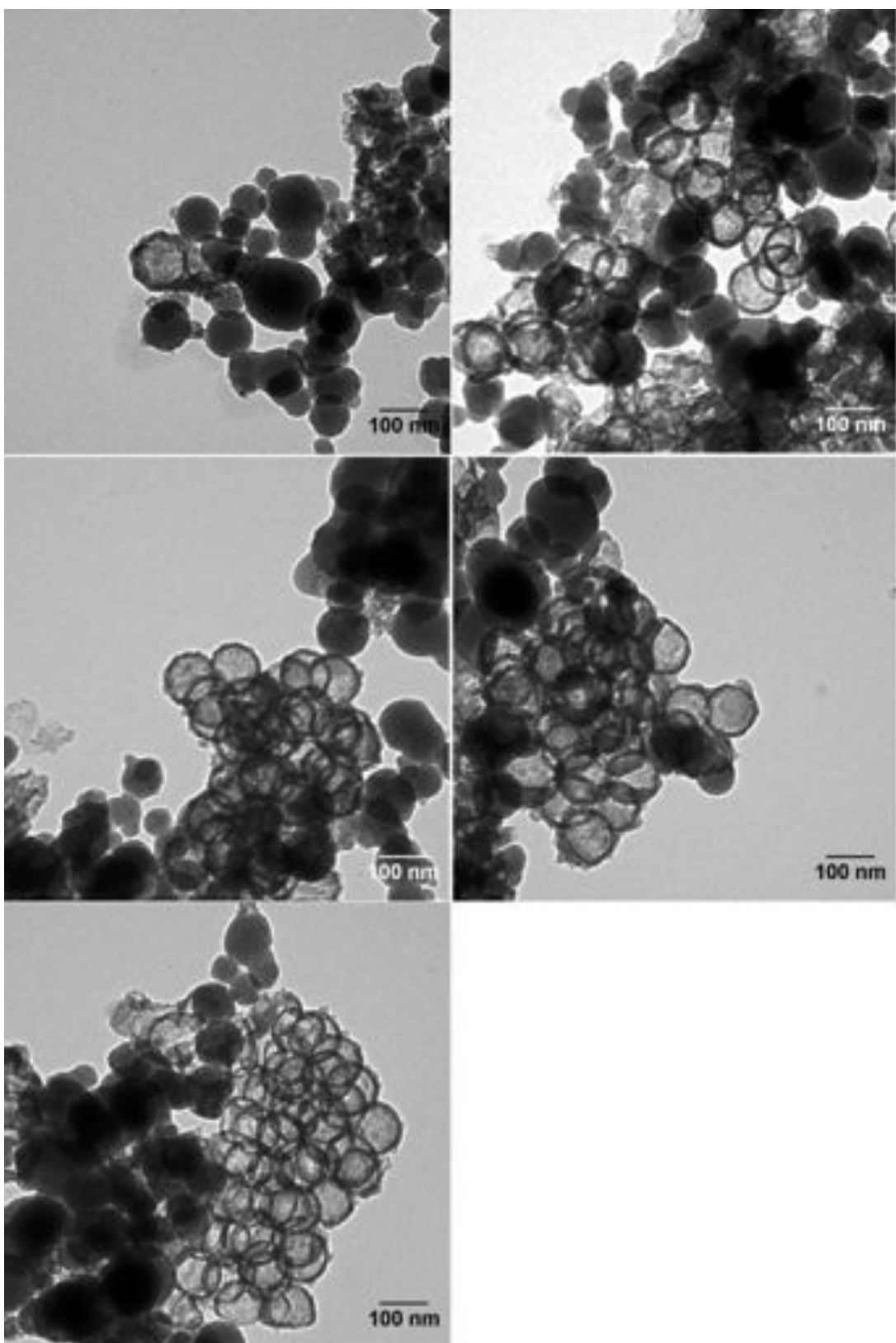


Figure 6.11: TEM images of HSNPs created by latex templating from TMOS in acidic solution.

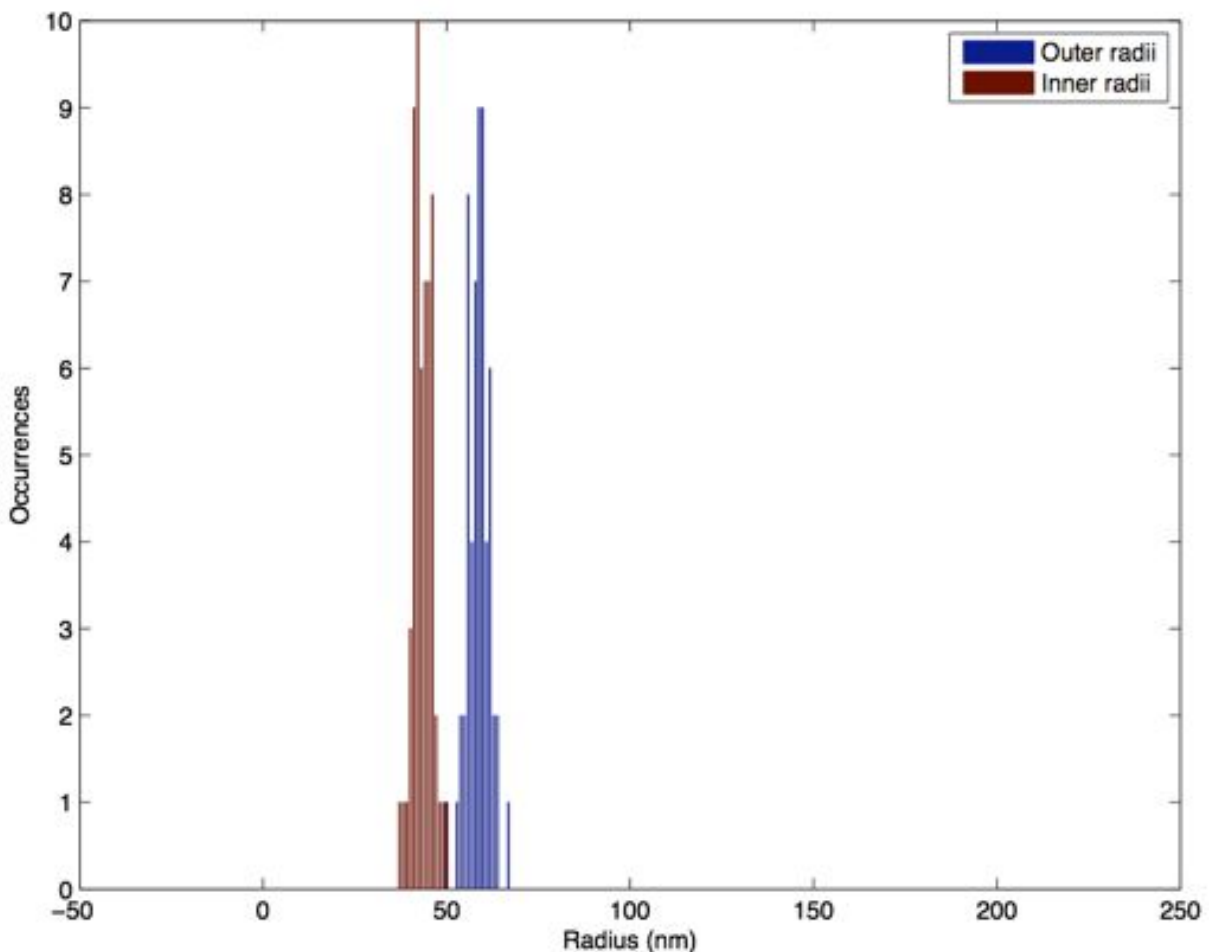


Figure 6.12: Histogram of inner and outer radii of HSNPs created by acidic latex templating using TMOS, as measured from TEM images.

The TMOS HSNPs were found to have a mean radius of $59 \text{ nm} \pm 3 \text{ nm}$, with a shell thickness of $15 \text{ nm} \pm 2 \text{ nm}$. The HSNPs made using TMOS have better-defined shells than above, possibly due to the slower hydrolysis rate of TEOS leading to a lower concentration of silicic acid than with TMOS. There are also solid silica nanoparticles visible which would be difficult to separate from the HSNPs. The formation of silica particles in acidic solution have been reported in other work [291], showing it can be a common problem with this method and adding considerable challenges to the production of pure shells.

This synthetic route did reliably produce monodisperse nanoparticles with a relatively thin shell, with different potential options for development through the variation of the

silanes. If the synthesis could be modified to improve the purity of the nanoparticles for the TMOS nanoparticles, or to produce smoother shells for the TEOS nanoparticles, this would be a promising method for producing silica shells. This may be solved by carrying out the hydrolysis in the presence of the templates, allowing the silicate species to deposit on the surface immediately and reduce the concentration available for forming secondary particles. A low concentration layer-by-layer approach may also be effective.

It is also worth noting that these reactions were carried out on a small scale, and the scale up of this synthesis could be costly due to the need for monodisperse polystyrene particles as the template.

Light scattering (zeta potential measurements)

Although dynamic light scattering is a flawed method for analysing hollow nanoparticles so the results should be approached with some caution, zeta potential measurements were carried out in order to examine the surface charge of the HSNPs created by acidic latex templating.

The particles were found to have a surface charge of 36 ± 0.4 mV. This positive surface charge is to be expected due to the poly-L-lysine embedded in the shell, and would be potentially beneficial for uptake of the HSNPs by cells. One consideration for future work is that this advantage might be removed by calcination if it were used instead of solvent extraction to remove the core.

Surface modification of latex-templated HSNPs: electron microscopy (TEM)

As the most robust in appearance of the latex-templated particles, the TMOS-coated HSNPs were selected for treatment with GdDTPA-APTES in order to add proton MRI contrast enhancement.

As can be seen in Figure 6.13, functionalising the surface of the latex templated HSNPs with further silanes has, in this case, degraded the morphology of the particles. While hollow structures are still clearly visible, the edges appear to be much rougher, with some

possibly fused together.

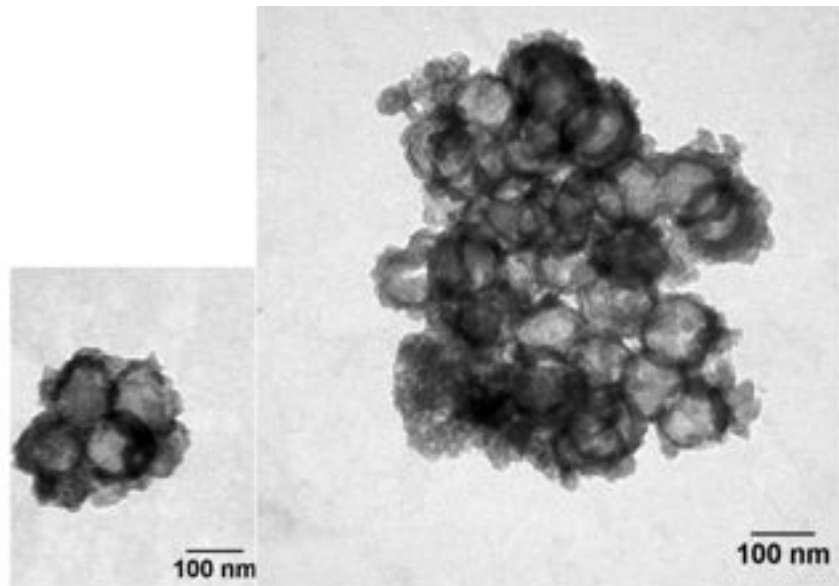


Figure 6.13: TEM images of HSNPs created by latex templating from TMOS in acidic solution, then functionalised with gadolinium functionalised silanes.

This synthesis was therefore not pursued, though it could have been an interesting alternative avenue.

Coating in basic solution: electron microscopy (TEM)

This synthesis was attempted as an alternative route to the acidic latex templating method described above. Shells here are also templated by the latex beads, but with the reaction solution basic, and similar in composition to the Stober synthesis.

The electron microscopy images are displayed in Figure 6.14.

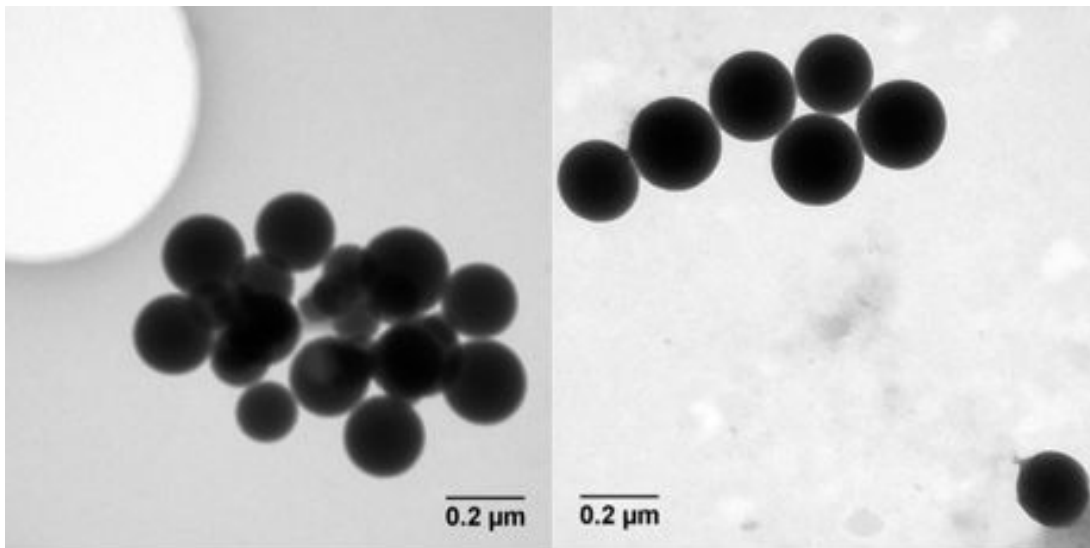


Figure 6.14: TEM images of HSNPs created by latex templating in basic solution.

The nanoparticles produced by this method distinctly resembled standard Stober silica nanoparticles rather than Hollow nanoparticles. No other structures such as collapsed silica shells were found. Modification of the image intensities revealed no further structures either.

The latex beads used did recommend maintaining a neutral to low pH medium for the particle suspension, so the templates may have collapsed before the silica could be deposited. This synthesis was not pursued further.

Conclusions

HSNPs were readily formed when templated in acidic solution, although the method has some disadvantages. One in particular is that the synthesis of a gadolinium functionalised version could not be performed without washing the particles, since the gadolinium will be released from the complex at low pHs. This adds considerable time and material costs since there is often a loss of material during the washing steps. Another disadvantage is the cost of the latex beads, which limits the scale of the reaction and which are unrecoverable.

These methods would be of interest for further work however if various problems

could be overcome. The main challenges are the purification from debris, or minimising the aggregation of the particles, as well as the optimisation of the particle coating process, which would ideally lead to discrete and smooth particles. In view of this other syntheses were explored.

6.4.3 Hollow particle synthesis by selective etching

Silica nanoparticles as sacrificial templates were created by the Stober method, then coated with a co-condensed mixture of silanes, thus incorporating porogenic C₁₈ chains. The core was etched away in 0.6 M Na₂CO₃ for 30 minutes at 80°C leaving a silica shell, with hydrophobic regions on the surface. The C₁₈ chains were then removed by calcination, leaving hollow porous silica shells.

This method is attractive because it uses only silanes to form the shell, avoiding the need for additional surfactants, polymers or a heterogeneous core. Hollow nanoparticles were formed using this synthesis which were further developed into proof-of-concept trimodal imaging agents for fluorescence, ¹H MRI and ¹⁹F MRI.

Synthesis 1: electron microscopy (TEM)

Characterisation was carried out by TEM to assess the effectiveness of the syntheses. Hollow nanoparticles were produced, though with a varying size distribution, see Figure 6.15.

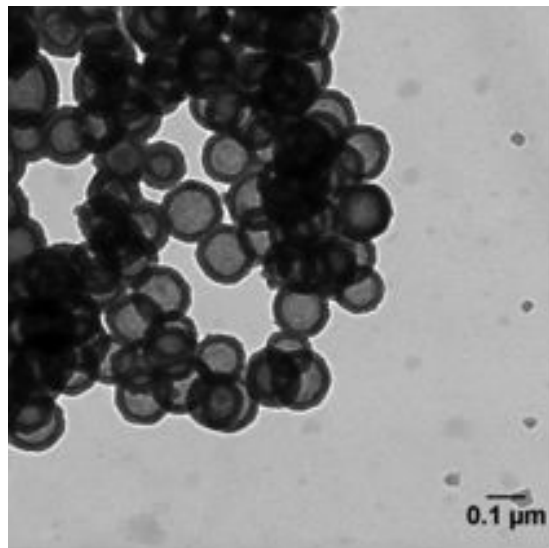


Figure 6.15: TEM image of HSNPS created by selective etching by synthesis 1.

It was however unreliable in producing these results reproducibly. An example of the incomplete etching is illustrated in Figure 6.16. A range of etching results, from solid particles and rattle-type particles to hollow nanoparticles, can be seen. There is also a significant amount of debris present. This would be unacceptable for progress towards clinical use, and would lead to inefficient loading of imaging agents.

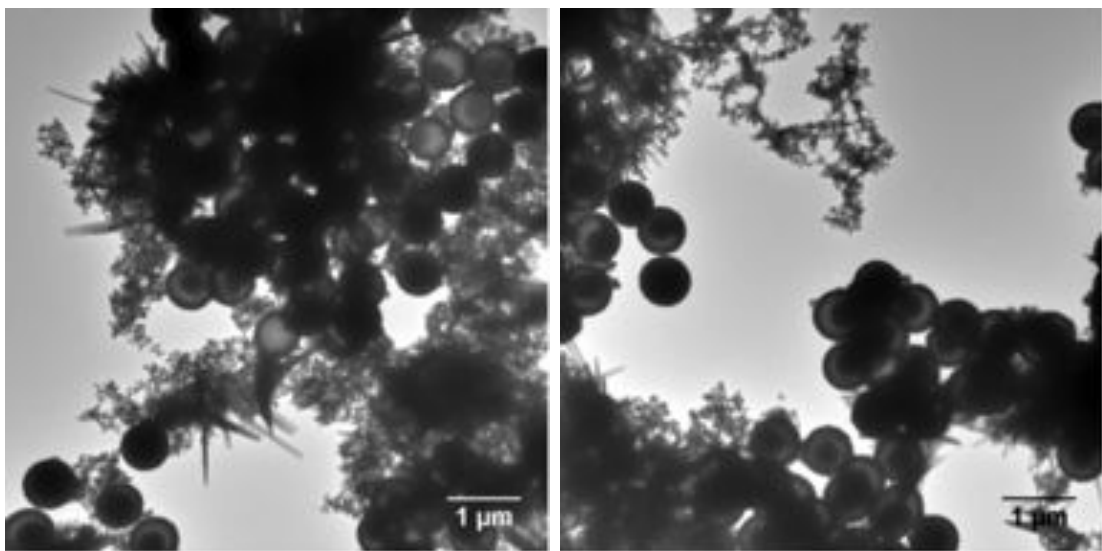


Figure 6.16: TEM image of HSNPS created by incomplete selective etching by synthesis 1.

Synthesis 2: electron microscopy (TEM and SEM)

Another article [292] by some of the same authors as for synthesis 1 [282] details a slightly modified version of the selective etching synthesis used above. The most significant difference was a longer etching time being used and a stated etchant volume, and two concentrations of etchant were investigated.

The particles were also formed with greater diameters in order to verify the method according to the original procedure. The electron microscopy images from these particles before and after calcination are presented in Figures 6.17 and 6.19 respectively (for particles hollowed in 0.6 M etchant). The contrast in all these figures has been altered for clarity, causing noticeably reduced background noise. This has been necessary due to the size of the silica shells leading to a higher volume of silica being present, and hence a greater attenuation of the electron beam.

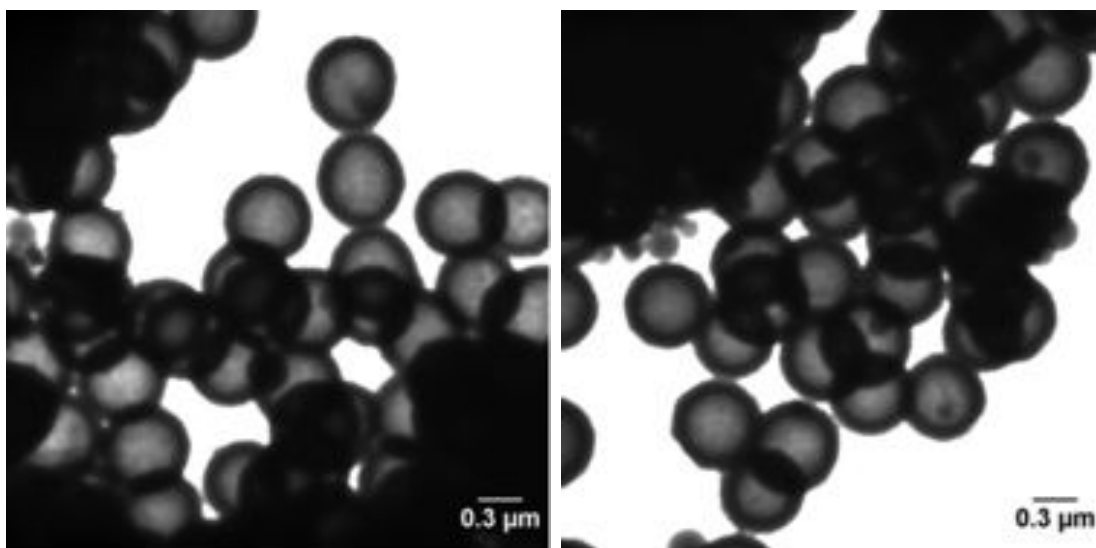


Figure 6.17: TEM image of HSNPS created by selective etching by synthesis 2 before calcination.

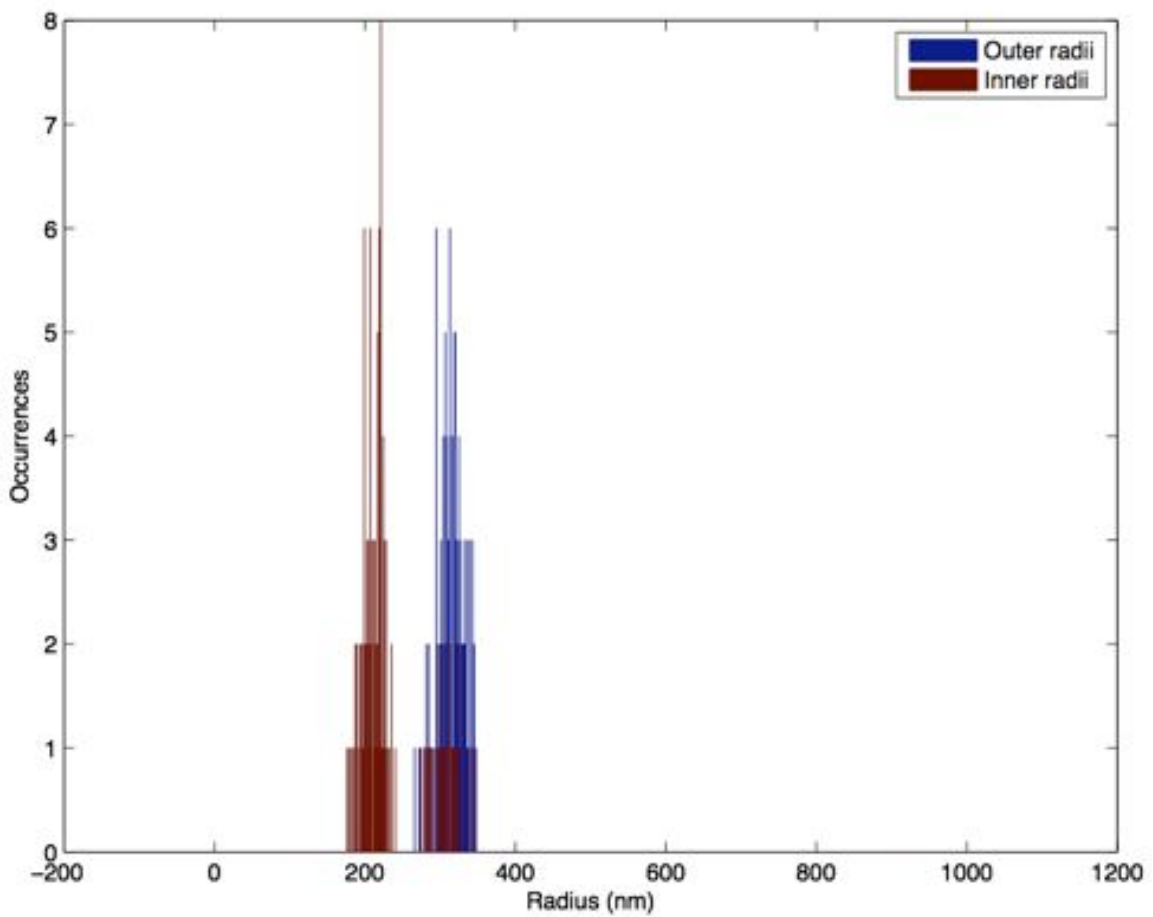


Figure 6.18: Histograms of the inner and outer radii of the HSNP shells, based on 127 particles.

The uncalcined particles have well defined morphology and a limited amount of debris present. The outer mean radius was $315 \text{ nm} \pm 18 \text{ nm}$, and the inner radius was $235 \text{ nm} \pm 43 \text{ nm}$, giving a shell thickness of 80 nm.

There are some solid $81 \text{ nm} \pm 19 \text{ nm}$ (based on 28 NPs) secondary particles present, though these were not as obviously widespread as in the following modifications to the particles. This could be due to the solid particles being trapped in aggregates; this is discussed further below.

There are dark areas visible in the image, and the presence of debris in these areas cannot be ruled out. Examining some of the dark areas did however show that at least some of these are composed of hollow silica nanoparticle aggregates, since the same pat-

terns of overlaid circles could be seen with extreme alteration of the contrast. Aggregates could be expected in this uncalcined sample since the particles have hydrophobic surfaces, and are suspended in water for the TEM sample preparation.

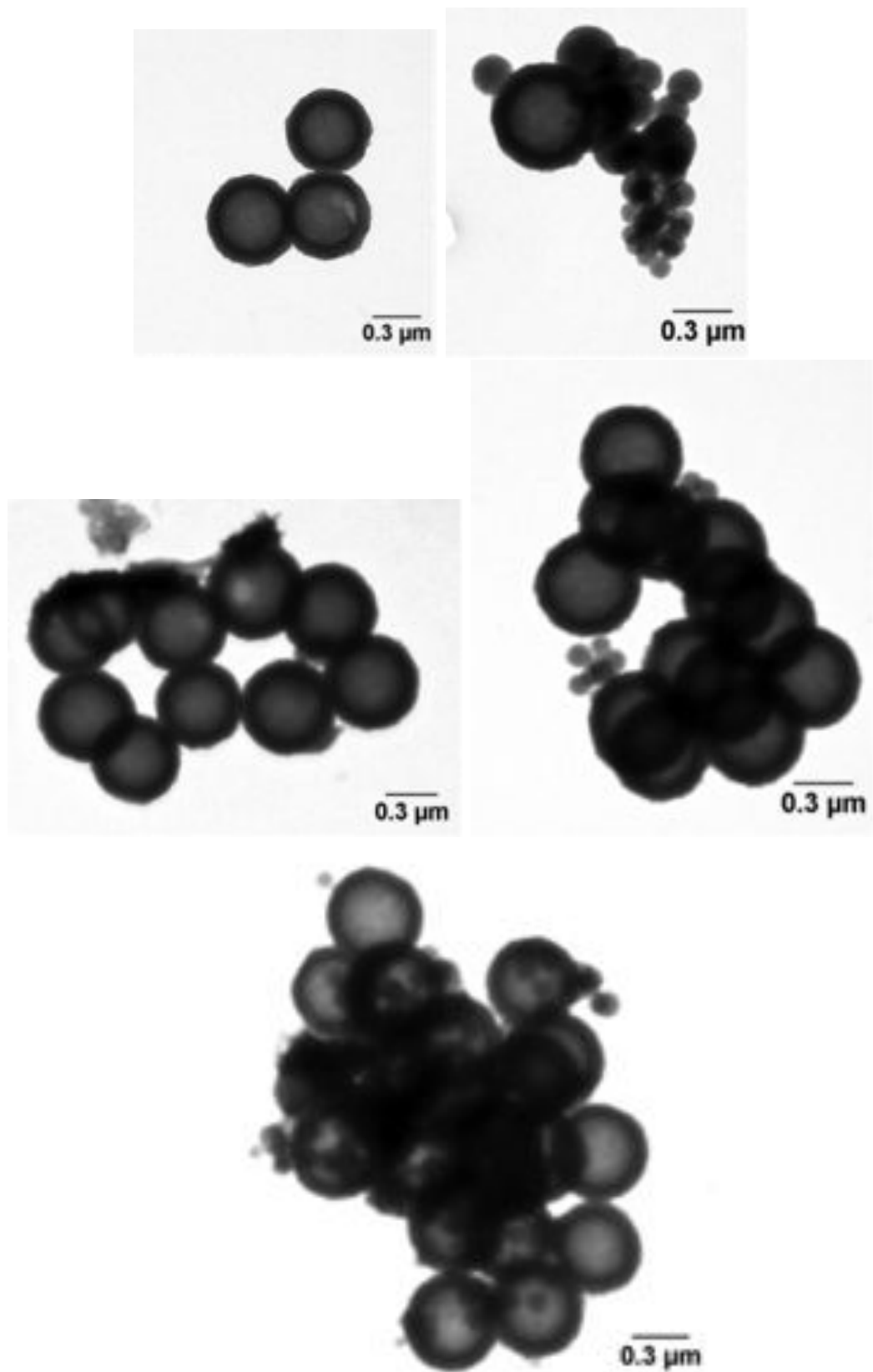


Figure 6.19: TEM image of HSNPs created by selective etching by synthesis 2 after calcination.

After calcination fewer large aggregates were visible, see Figure 6.19, and the HSNPs tended to be in small generally flat clusters, as shown in the top images. The smaller clusters allow closer analysis of the debris present, which mostly consists of small solid particles. Some of these appear to be closely associated with the surface of hollow particles, where they might have been seeded. This is indicated partly by the multiple small dark areas on the particles visible at the bottom of the fifth image, and the ‘raspberry-like’ effect on the particle in the second image.

The radius of these particles has reduced somewhat during the calcination process, measuring $258 \text{ nm} \pm 11 \text{ nm}$ with a shell thickness of $87 \text{ nm} \pm 14 \text{ nm}$ (based on 85 HSNPs) after calcination.

These particles were also analysed by scanning electron microscopy (SEM). The aims were to confirm their hollow character, examine the surface morphology, and to determine the nature of the aggregates visible by TEM.

The hollow nature of the particles can be seen by examining broken particles, as shown in Figure 6.20, where a clear cavity is visible inside the broken shells.

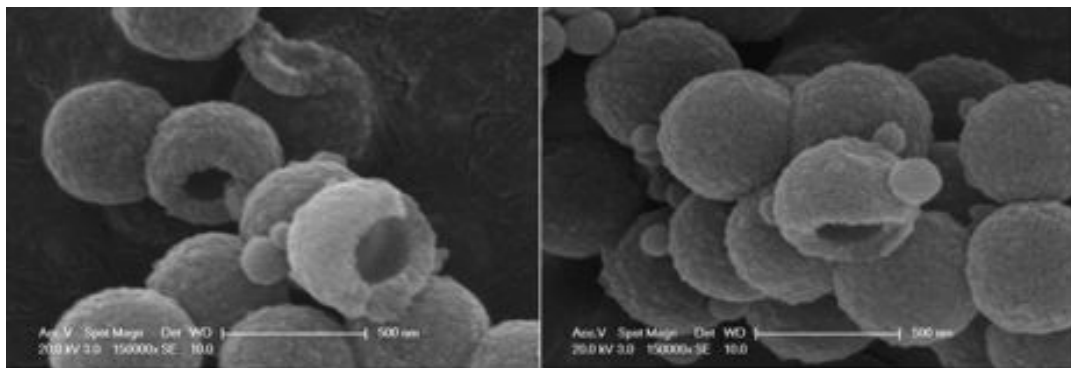


Figure 6.20: SEM image of HSNPs showing the hollow cavity in broken particles.

The surface morphology can be seen in Figure 6.21, which shows a more representative proportion of broken to non-broken particles (the majority appeared to have whole shells). There is some roughness on the surface, as would be expected for a porous surface with an etched core, though some of this could also be due to the sputter coating. The roughness is similar to that observed in SEM images from the original article [282].

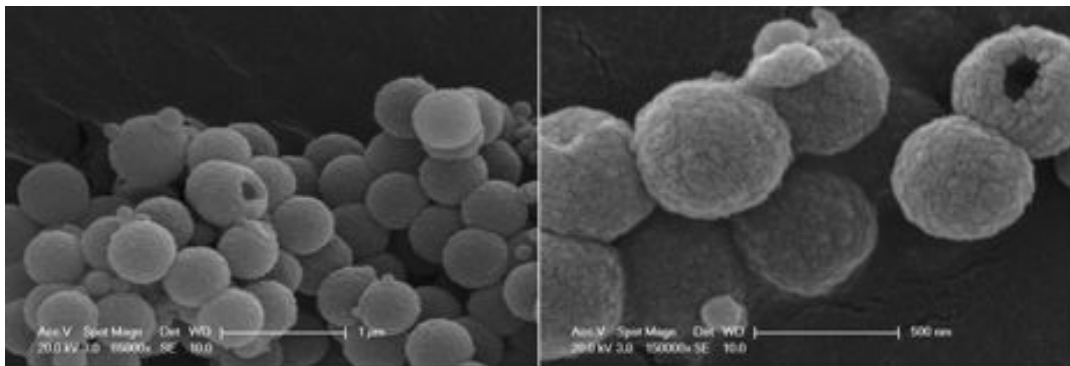


Figure 6.21: SEM image of HSNPs showing the rough surface morphology.

The aggregates visible only as dark areas by TEM are seen by SEM to be aggregates of spherical particles, as seen in Figure 6.22. Though the largest aggregates could not be imaged due to charge build-up causing local image noise, the aggregates shown here would not have been characterisable by TEM. It is worth noting that none of the large particles observed by TEM were solid, suggesting that the vast majority of the large spheres seen in Figure 6.22 will be hollow particles.

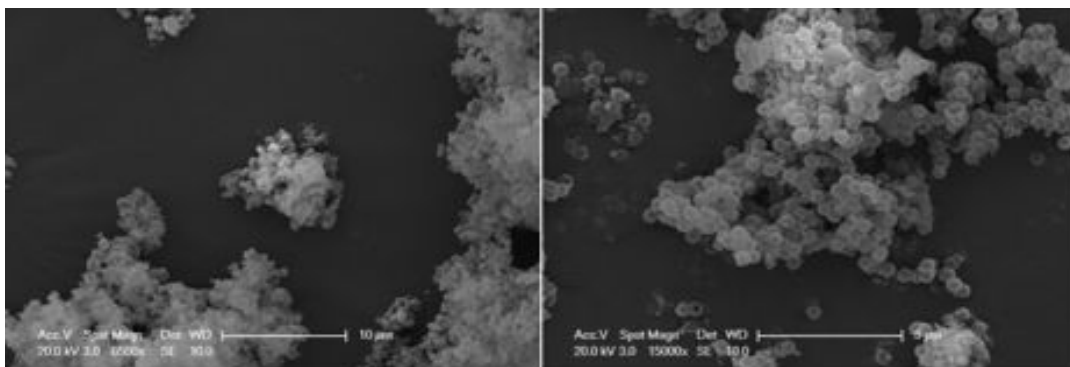


Figure 6.22: SEM image of HSNPs showing the surface morphology of the clusters of particles.

Another point to note is that small particles, often located on the surface of the large hollow particles, are visible in these images as in the TEM images. Though they are less prevalent than the large particles, they could affect the bioactivity of the system, and thus would need to be purified if possible, or ideally eliminated through optimisation of the synthesis. This would be a crucial point to be addressed in future work.

A long etching time of 3 hours and a higher concentration of etchant (1.2 M NaHCO_3) was also explored. This produced particles which were clearly hollow from the TEM images, though some smaller particles are still visible, see Figure 6.23.

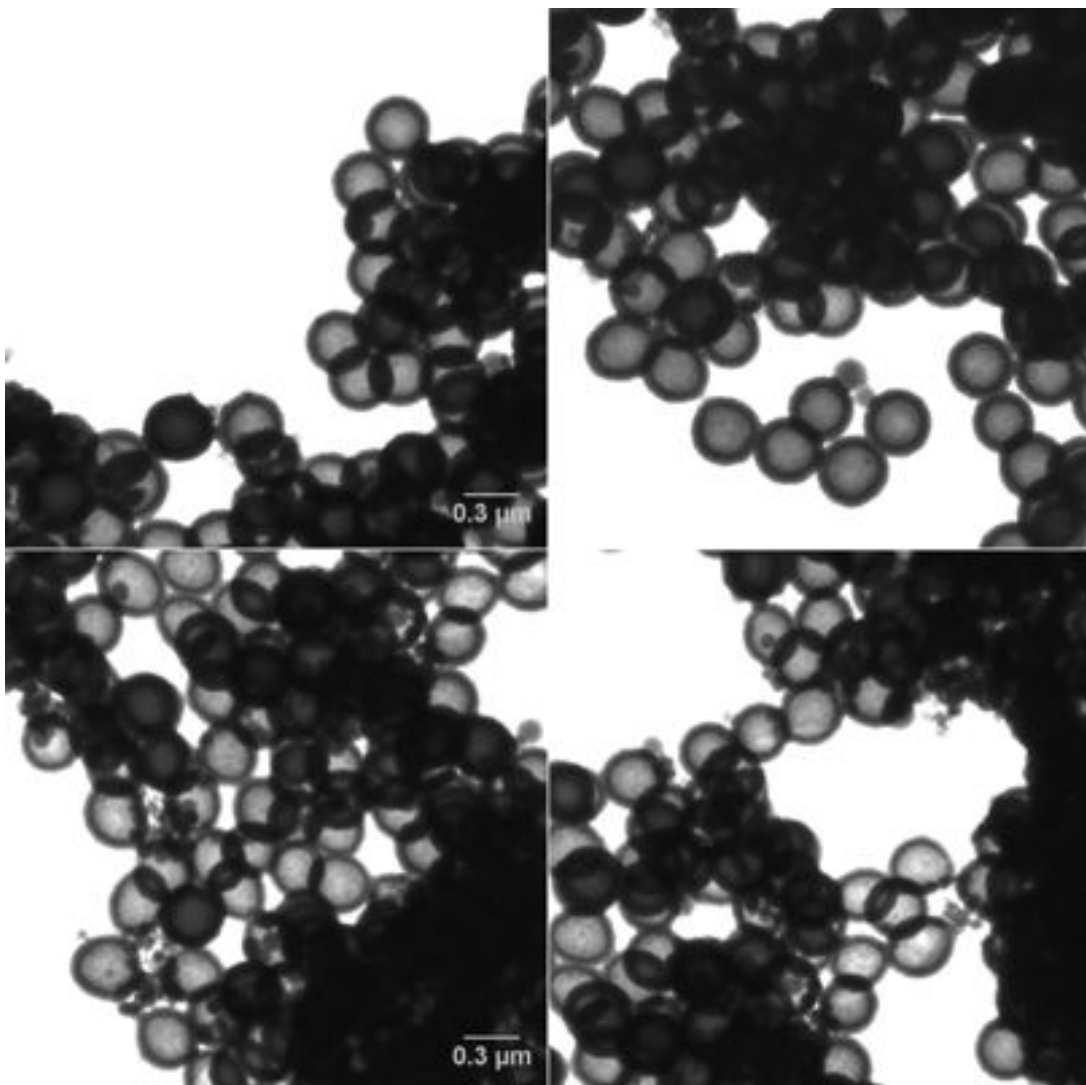


Figure 6.23: TEM image of HSNPs created by selective etching using synthesis 1 but with a higher concentration etchant (1.2 M).

There is little obvious difference between the HSNPs produced by the different concentrations of etchant, though further characterisation would help clarify the differences if it became of interest. For example SEM would help determine the surface morphology, and nitrogen absorption or helium pycnometry would indicate the density of the shell walls. For the purposes of this work however the HSNPs hollowed with 0.6 M etchant

were investigated further as they appeared to be similar while less debris (in the form of secondary particles) was visible when compared to the 1.2 M etched HSNPs.

Surface modification of the HSNPs: electron microscopy (TEM and SEM)

The HSNPs created by synthesis 2 with 0.6 M etchant were coated with GdDTPA-APTES, a gadolinium functionalised silane. The resulting GdHSNPs were examined by TEM and SEM.

After the gadolinium modification the particles are still spherical and hollow, with an outer radius of $266\text{ nm} \pm 16\text{ nm}$ and a shell thickness of $92\text{ nm} \pm 18\text{ nm}$, as would be expected from the extra silanation step. They do however have a greater predominance of debris visible. The particles also seem to be thicker in terms of the beam attenuation since a change in the contrast was necessary for showing the hollow character of the particles (rather than preferable for clarity as above). Characteristic images are shown in Figure 6.24, and the corresponding histograms are in Figure 6.25. The lower images show the original image on the left, where the debris is seen to be solid spherical particles, and the contrast-adjusted images are on the right showing the hollowness of the large particles. One of the HSNPs in the bottom images appears to have a hole in the surface, where there is an area of higher intensity, supporting the assertion that these are hollow spherical particles.

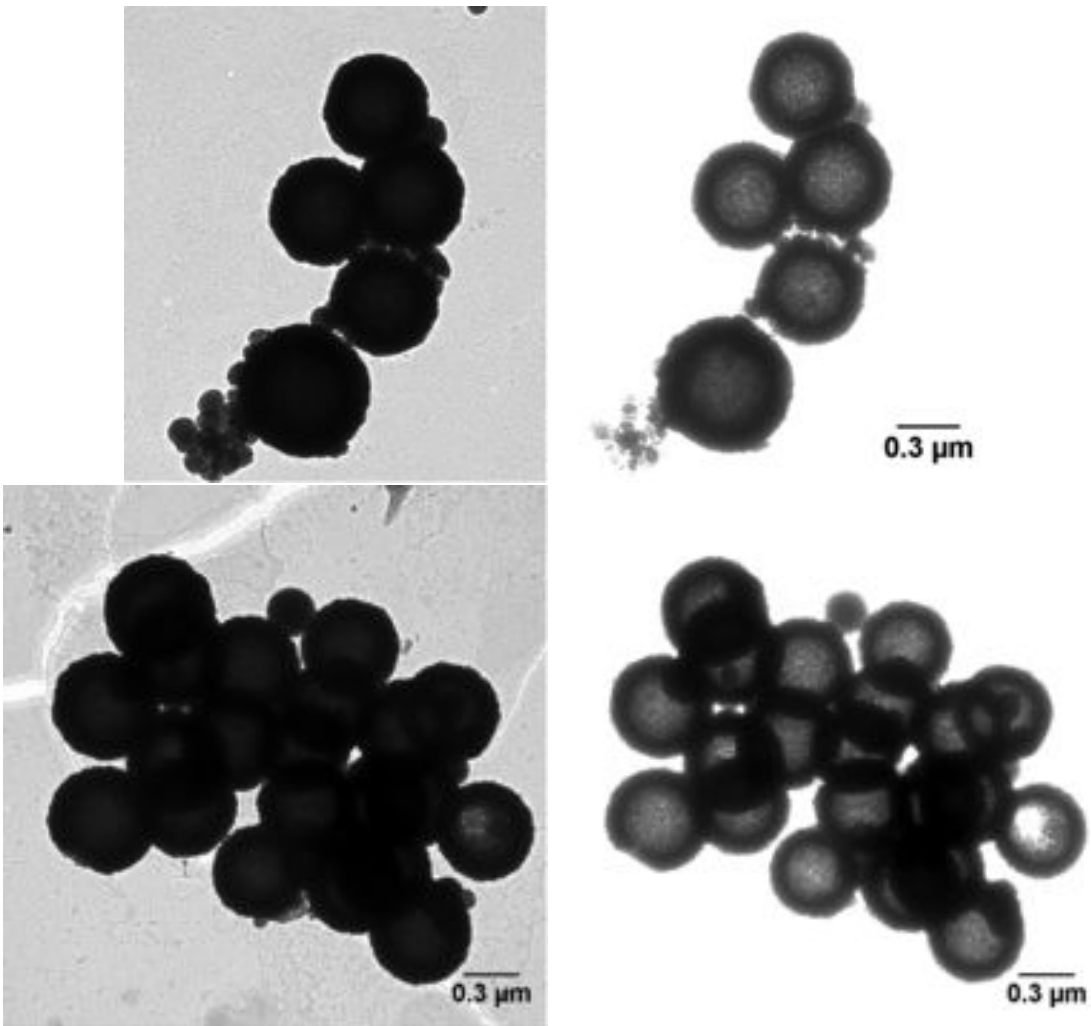


Figure 6.24: TEM images of GdHNSPs. The original images are shown on the left, while the contrast enhanced version showing the hollow cores are on the right.

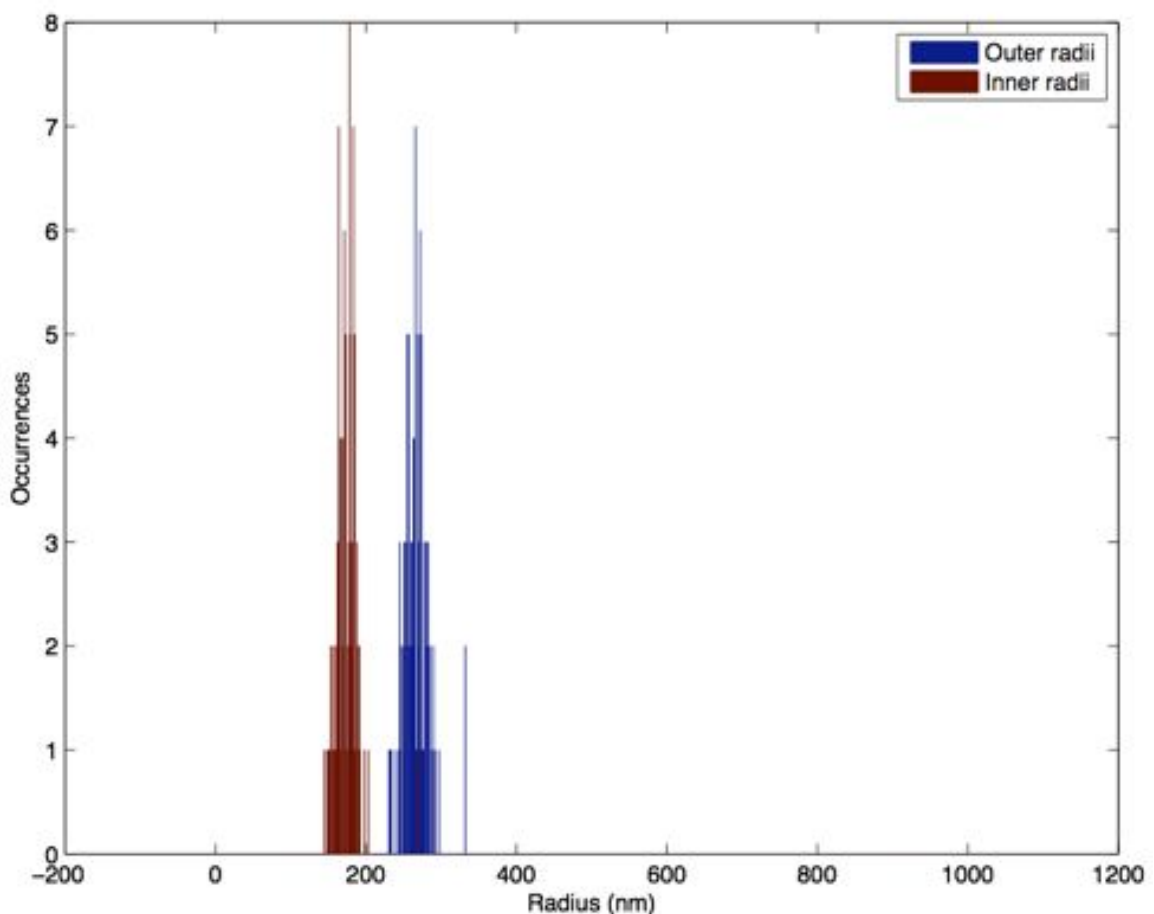


Figure 6.25: Histograms of the GdHSNP inner and outer radii as measured from TEM images.

These particles were also analysed by SEM after the gadolinium functionalisation step. The aim was to observe any consequent changes in the particles and their surface morphology. Figure 6.26 shows characteristic SEM images of the GdHSNPs. The spheres are still clearly distinct from each other with a spherical morphology. Some are broken but most have no visible holes.

The surface modification appears to have made the surface rougher, with more prominent bumps, as shown in Figure 6.26. These could be nucleation sites for further particle growth.

Some of the breaks in the nanoparticle shells have more irregular morphologies than the non-functionalised particles. These could be an indication of the holes being closed by

further functionalisation. This is particularly of interest as further work on these particles could consist of capping the particles in order to minimise leakage of loaded imaging agents. An interesting computational aspect of future work would also be to automate quantifying the holes in the particles, though this would not be a trivial challenge.

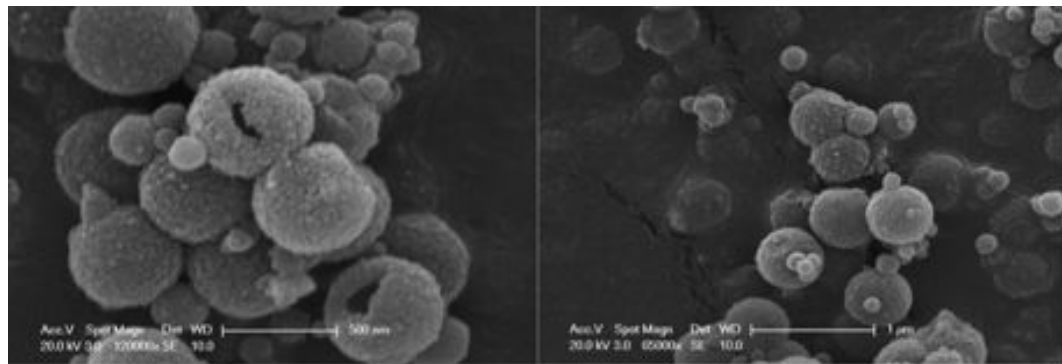


Figure 6.26: SEM images of GdHSNPs.

Light scattering (zeta potential measurements)

Light scattering measurements were of limited use for the hollow nanoparticles since the calculation of the size distribution depends upon the particle being a homogenous material with a known refractive index and dielectric constant. With hollow nanoparticles the scattering of the shell and the core will be different, producing overall unreliable results.

Zeta potential measurements are also flawed for the same reasons as sizing calculations. Measurements were nevertheless carried out for the HSNPs and GdHSNPs created by selective etching (synthesis 2 with 0.6 M etchant). Values are provided for comparison purposes as the change in the zeta potential, see Table 6.1, gives an indication of the successful surface coating.

NPs	Mean zeta potential (mV)	Standard deviation
HSNPs	-35.1	0.833
GdHSNPs	-5.07	0.52

Table 6.1: Zeta potential measurements for HSNPs and GdHSNPs.

These numbers are as expected considering the more neutral layer presented by the GdDTPA complexes than by the terminal silanol groups. The reduction in zeta potential does however suggest that the GdHSNPs should be considerably less stable in suspension than the HSNPs since a higher surface charge enables colloidal stability. A further development of these particles would therefore involve finding a balance of functionalisation to tune the surface charge while maintaining water access to the gadolinium ions.

Density

The density of the shell walls of the HSNPs and GdHSNPs, both created by selective etching (synthesis 2 with 0.6 M etchant), were measured by helium pycnometry as described in Section 2.2.3.

The HSNPs had a shell wall density of 2.9 g/ml, with a standard deviation of 1.2 g/cm³. The GdHSNPs had a lower density of 1.46 g/cm³, with a standard deviation of 0.003 g/ml. Both of these values fall outside typical ranges for silica nanoparticles, which are reported in the range of 1.9 - 2.2 g/cm³ [293, 72]. Some drop in density due to the surface modification would not be surprising since the incomplete hydrolysis of silanes during a Stober-like process would lead to a less well ordered matrix. The extent of this reduction is however unexpected, and suggests a very low density addition to the composition of the particles, or a structural change in the shells during the surface modification.

Binding of gadolinium

The concentration of gadolinium in dissolved GdHSNP samples created by selective etching (synthesis 2 with 0.6 M etchant) was measured by ICP-MS. An average of 59.3 mg (Gd)/l, with a standard deviation of 43.13 mg/l was found from triplicates of each samples. This corresponds to a mean of 0.38 mM gadolinium, with a standard deviation of 0.27 mM.

Luminescence

The HSNPs created by selective etching (synthesis 2 with 0.6 M etchant) were infused by sonication with $[\text{Ru}(\text{phen})_3]^{+2}$ suspended in PFOB. These RuPFOBHSNPs were then suspended in PBS for further analysis.

The luminescence excitation and emission spectra of the RuPFOBHSNPs are presented in Figure 6.27, along with the spectra of $[\text{Ru}(\text{phen})_3]^{+2}$ for comparison.

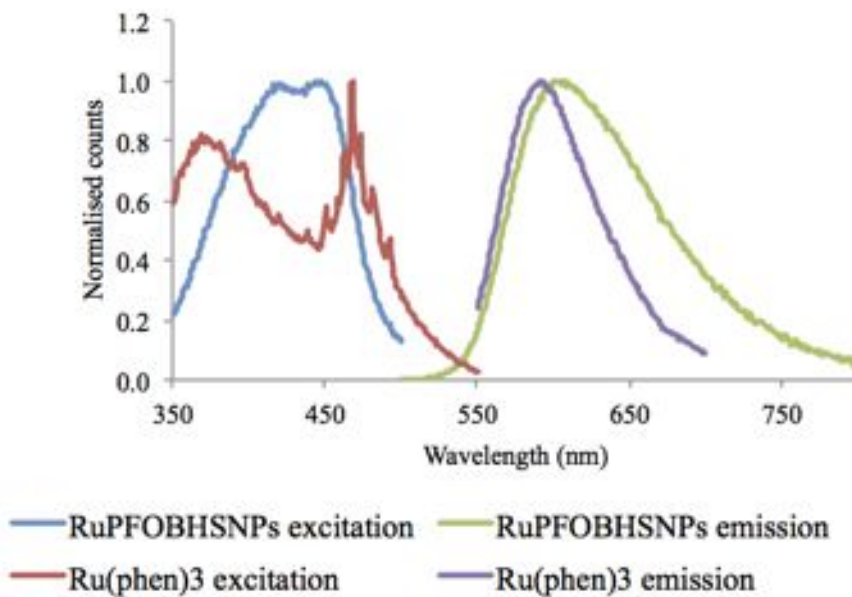


Figure 6.27: Luminescence excitation and emission spectra of RuPFOBHSNPs and $[\text{Ru}(\text{phen})_3]^{+2}$ for comparison.

The excitation spectrum of the RuPFOBHSNPs shows greater than 95% excitation between 415-455 nm. The $[\text{Ru}(\text{phen})_3]^{+2}$ excitation spectrum has two more distinct peaks, with maxima at 369 and 468 nm.

The RuPFOBHSNPs have a broad excitation range, making them suitable for excitation by 405 nm or 458 nm light sources.

The emission spectra show broadening on the $[\text{Ru}(\text{phen})_3]^{+2}$ being suspended in PFOB, with the emission maximum shifting from 590 nm for the free dye to 609 nm for the trapped dye.

¹H MRI contrast enhancement

MRI was carried out on aqueous suspensions of GdHSNPs alongside water and gadolinium complex (Primovist) controls in order to determine the sample relaxation rates. An image and diagram describing sample placement is shown in Figure 6.28.

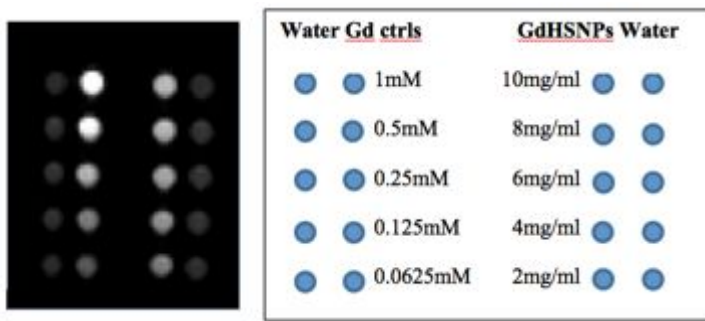


Figure 6.28: (Left) MRI image of GdHSNPs alongside gadolinium controls and water controls. (Right) Diagram showing the corresponding placement and concentration of samples, with water samples down both sides, gadolinium controls of decreasing concentration down the central left column, and GdHSNPs of decreasing concentration down the central right column.

It might be noted that the image above only shows clear contrast from the gadolinium controls. The relaxivities obtained from the series of images however indicate that there is concentration-dependent contrast enhancement from the GdHSNPs.

Direct comparison of the relaxation rates suggests that the gadolinium concentration of the GdHSNPs at 10 mg/ml is roughly 0.3 mM. This agrees with the ICP-MS data which indicates that it is 0.38 mM.

The relaxivity plots are shown in Figure 6.29. The slopes of the fitted lines indicate a relaxivity of $7.64 \text{ mM}^{-1}\text{s}^{-1}$ for the Primovist controls and $5.04 \text{ mM}^{-1}\text{s}^{-1}$ for the GdHSNP samples.

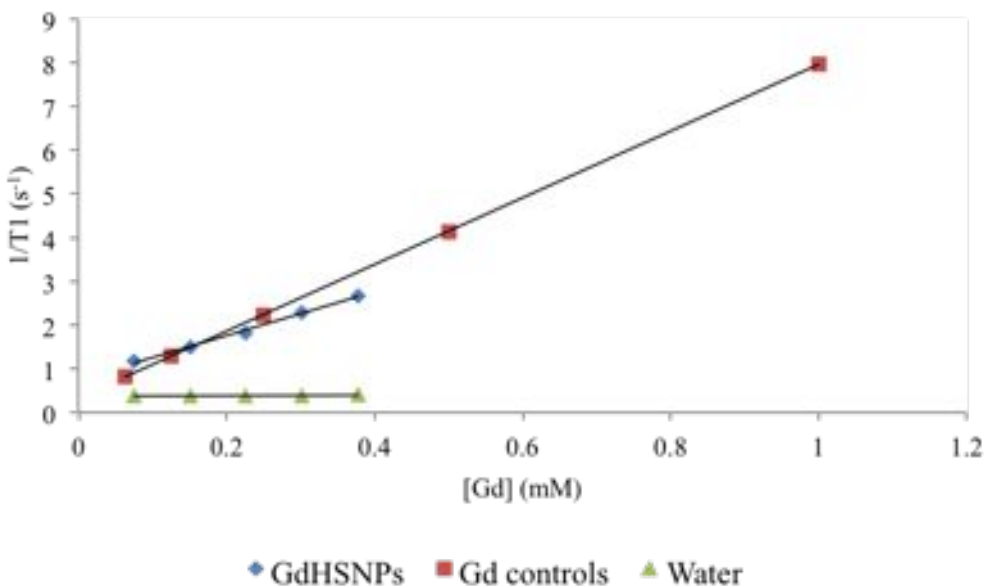


Figure 6.29: Plot of the relaxation rate against the gadolinium concentration in the GdHSNP and gadolinium control samples. the water is plotted as if it had the same Gd concentrations for comparison. The slopes of the lines give the corresponding relaxivities.

The relaxivity of the GdHSNPs is therefore in the same range as the clinically available contrast agents. Given the similar structure of the complex, this is not surprising, though there appears to be no significant increase due to the slowed tumbling, as could be hoped. The tumbling rate however is likely to vary once the nanoparticles are filled and in a stable suspension, so this may vary as the particles develop.

Both HSNPs and GdHSNPs were filled with a $[\text{Ru}(\text{phen})_3]^{+2}$ PFOB suspension by sonication of the dry particles with the suspension, and the relaxation times measured. Unfortunately however the particles were insufficiently stable when suspended in PBS to allow reliable imaging. The particles were therefore suspended in gelatin as an initial indication of what the contrast enhancement would be if they could be stabilised. The relaxivity is illustrated in Figure 6.30.

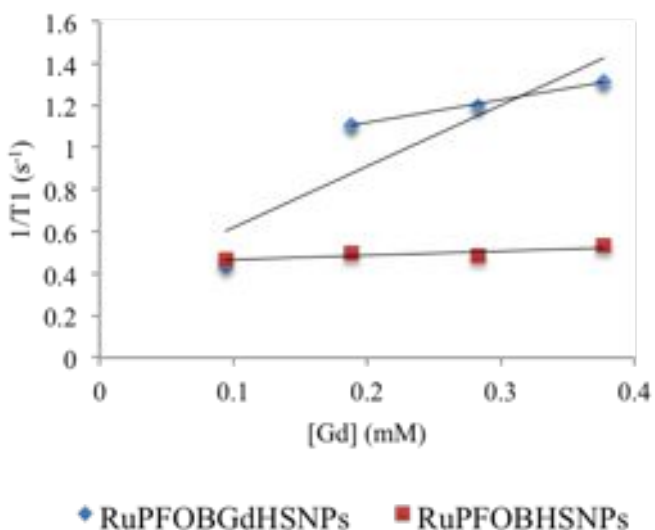


Figure 6.30: Plot of the relaxation rate against the gadolinium concentration in the RuPFOBGdHSNPs. The RuPFOBHSNPs, which contained the same weight of nanoparticles before filling, are plotted as if they had equivalent Gd concentrations for comparison. The slopes of the lines give the corresponding relaxivities. Two trendlines are shown for the RuPFOBHSNPs data, one excluding the lowest concentration point (see main text for reasoning).

The slopes in Figure 6.30 indicate a relaxivity of $0.20 \text{ mM}^{-1}\text{s}^{-1}$ for the RuPFOBHSNPs and $2.91 \text{ mM}^{-1}\text{s}^{-1}$ for the gadolinium functionalised RuPFOBGdHSNPs. The difference between them is to be expected due to the presence of the gadolinium in the latter. The data does not fit well with the trend line for the RuPFOBGdHSNPs. This was a preliminary experiment however, and there may have been an inhomogeneous distribution of the nanoparticles in the gelatin for the lowest concentration sample resulting in the relaxation rate similar to those with no Gd. If this sample result is excluded therefore a relaxivity of $1.09 \text{ mM}^{-1}\text{s}^{-1}$ is obtained.

While either of the relaxivities for the RuPFOBGdHSNPs are unexpectedly low compared to the unfilled nanoparticle, with a reduction in the relaxivity from 5.04 to $1.09 \text{ mM}^{-1}\text{s}^{-1}$ (in the worse case), some important points should be noted.

There are multiple sources of possible error: the surfaces of the particles may not be uniformly coated as suggested by the variation in the ICP-MS results (see Section 6.4.3) the sample may not have been uniformly distributed in the gelatin, as noted above from

the seemingly anomalous result for the lowest concentration RuPFOBGdHSNP sample; there may be partial volume effects in the MRI measurements if small air bubbles were present in the gelatin. No bubbles were clearly visible, but this should be taken into consideration.

The relaxivity for the RuPFOBGdHSNPs is of the same order of magnitude as clinically approved gadolinium agents, but is distinctly lower than the particles' unfilled equivalents, as measured above. This could be due to the need to suspend the particles in gelatin when filled, which could affect the movement of the particles. It could also be due to the limited colloidal stability of the particles which may result in them clustering and hence not tumbling as readily. The unfilled GdHSNPs also has a low surface charge as found by zeta potential in Section 6.4.3. There could therefore by a wetting effect, with the PFOB covering the outside surface of the particles as well as filling the cores. This would explain the low colloidal stability, which is more severe than that seen with the unfilled GdHSNPs. It would also result in reduced water access to gadolinium complexes, which would explain the lower relaxivity.

There is nevertheless a clear difference in the relaxation rates between the Gd functionalised RuPFOBGdHSNPs and the non-functionalised RuPFOBHSNPs. While this should be reproduced in future work, this lays the groundwork for a promising and versatile ^1H MRI contrast agent.

^{19}F MRI signal in dual modal nanoparticles

Having created these trimodal particles, RuPFOBGdHSNPs, the aim was to assess whether they could be imaged by both ^1H and ^{19}F MRI, and to identify any challenges facing this process. 10 mg of GdHSNPs and 10 mg of HSNPs were therefore again filled with the perfluorocarbon PFOB followed by suspension in PBS. Gelatin was added again at 10% w/v to maintain the suspension. The $[\text{Ru}(\text{phen})_3]^{+2}$ was excluded here however to avoid any effects it may have, though none are anticipated. These PFOBGdHSNPs and the corresponding particles with no gadolinium bound to the surface, PFOBHSNPs,

were imaged by two modes of MRI: ^1H MRI and ^{19}F MRI.

The sample images are presented in Figure 6.31 with the HSNP samples indicated with arrows. The surrounding samples are control samples containing gadolinium (the small samples on the right) and trifluoroethanol (the smaller samples on the left). The large circles are tubes of water added to aid in localisation in the scanner.

The gadolinium samples were not all clearly visible in the same slice as the HSNPs due to the sample containers being of different heights. This slice shown in on the left of Figure 6.31 was selected to illustrate the clear difference between the PFOBGdHSNPs and the PFOBHSNPs in the ^1H MR image.

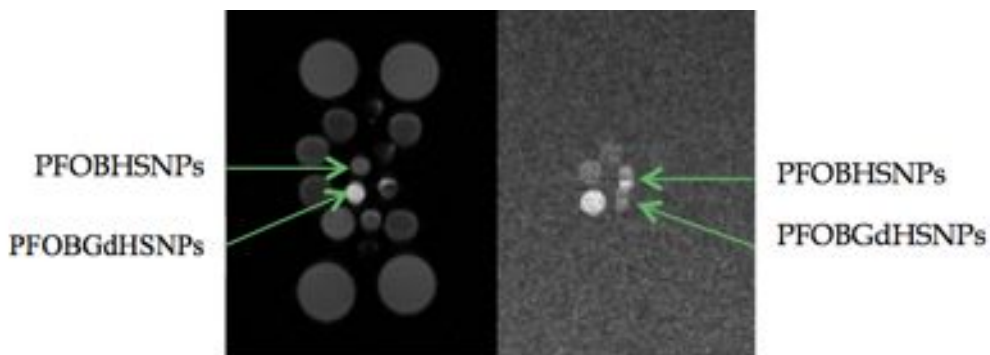


Figure 6.31: ^1H and ^{19}F MR images of PFOBHSNPs and RuPFOBGdHSNPs; the samples are indicated with green arrows.

The location of the TFE samples on the left of the slice shows the relative location of the PFOBHSNP samples. The HSNP samples themselves are slightly overlapping due to chemical shift artefacts, which PFOB is susceptible to producing. A simple SNR analysis of the ^{19}F image however shows a clear difference in mean intensity between the two HSNP samples. A plot of the SNRs of the TFE samples is shown in Figure 6.32, and the HSNP SNRs were mapped onto this line to back calculate an estimate of the concentration.

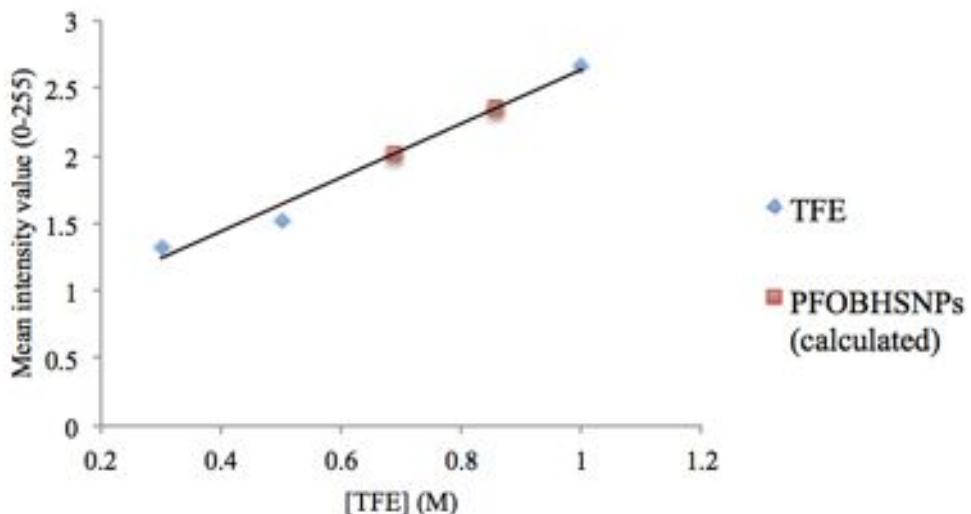


Figure 6.32: Plot of the mean intensity of the trifluoroethanol samples against the sample concentration (blue diamonds), and the calculated concentrations of the PFOB in the PFOBHSNP samples.

The PFOBHSNPs theoretically contain 0.87 mM PFOB based on the volume of PFOB added. Back calculation estimates a concentration of 0.86 mM, and incomplete trapping of the PFOB or low levels of leakage can readily explain the difference between the two values. The PFOBGdHSNPs however showed a much lower SNR, despite having been loaded with the same volume and concentration as the others.

A number of factors could be involved in this observation. The gadolinium on the surface may be exerting a paramagnetic relaxation effect on the fluorine. Since the echo times used in this sequence are too long to detect rapidly relaxing fluorine, these atoms would appear to be quenched, leading to a loss of signal. This theory is supported by a similar system, which was reported during the preparation of this thesis: a complete signal quenching of a perfluorocarbon nanoparticles was claimed to be due to gadolinium relaxation enhancement [294].

There is a further consideration in this project, which is that the gadolinium functionalisation may be shrinking the nanoparticle surface pores, and therefore allow lower PFOB uptake in some particles. This could be tested in future work by the removal of the gadolinium ions in acidic solution after initial imaging to observe any restoration of

the signal.

This proof-of-concept experiment indicates that this dual modal imaging can be carried out with these nanoparticles.

This experiment also highlighted various challenges. The slice size and thickness could not be copied between the ^1H and ^{19}F MRI protocols used here. If this were possible, perhaps by careful selection of the sequences and various parameters involved, the process of co-registering the images would be trivial. On the other hand if, as may be more likely, this is a systematic problem, there would need to be robust co-registration algorithms in place before this technique could be considered clinically. This problem is made more difficult by the ‘hotspot’ nature of the technique, which would mean that suitable fiducial markers would need to be included in both scans for co-registration to succeed. With a surface coil of limited depth penetration this could be challenging to overcome, since any inclusion of extra vials, for example, would necessarily entail a lower penetration to areas in the body of interest, and therefore lower sensitivity of an already insensitive technique.

6.5 Conclusions

Hollow silica nanoparticles have been shown to form an excellent vehicle for multiple imaging agents. The surface functionalisation combined with the inner cavity can separate agents that have negative interactions while simultaneously forming a multimodal nanoparticle. They are moreover highly versatile in that the imaging agents could be swapped for suitable alternatives.

Different syntheses were attempted to create the hollow shells. The most effective was found to be the method of selectively etching the silane core from a porous shell. It was noted however that careful control of the conditions was necessary, especially in terms of the base etchant volume to nanoparticle ratio.

Other syntheses resulted in considerable amounts of amorphous material and sometimes no hollow shapes could be found. The method of using a latex bead as a template,

while expensive due to the cost of the latex beads, provided highly uniform sizes of shells. These may be preferable for clinical development than the selective etching particles, since the Stober synthesis of the templates naturally results in some polydispersity. In this work however the amorphous material was not readily separable from the nanoparticles, and therefore was considered too problematic to pursue. If this could be resolved by modification of the conditions or suitable purification in future work then this method would be very attractive.

Trapping in nanoparticle cores can therefore be considered a valuable tool for the delivery of imaging agents. The hydrophobicity of the perfluorocarbon was used in this case to maintain the trapping. There is no reason however why other hydrophobic liquids and suspensions should not replace the perfluorocarbon in further work, thus increasing the range of agents or drugs that could be transported in the core. Similarly, the surface functionalisation of these hollow particles was used to create proton MRI contrast. They could however be modified to carry luminescent complexes to provide multicolour luminescence.

Another aspect that would be of interest in future work would be to consider capping the nanoparticles, either with more silane, or possibly with a heterogeneous layer of gold, for example. Using a metal or a hydrophobic material could be beneficial as it would create a less permeable barrier to leakage, though in this case a further hydrophilic layer would be necessary to allow cell treatment. Similar work has been carried out with solid particles [295, 296], and the techniques from layer-by-layer assembly [297] mean this process could be finely controlled.

CHAPTER 7

IMAGE ANALYSIS METHODS

This chapter describes the image analysis that has been carried out on the TEM and MRI data during this project. The processes and algorithms involved are discussed.

7.1 Automated particle sizing from TEM images

In order to extract meaningful information from transmission electron microscopy (TEM), many particles must be imaged, ideally from different locations on the sample grid. According to the National Institute of Standards and Technology at least “200 discrete particles should be measured from each of at least two widely separated regions of the sample.” [298]. The analysis of these images could be carried out by hand. That is, if investigating the size of nanoparticles, each circular shape could be delineated manually and the diameter measured. This can however be a lengthy task considering the number of nanoparticle measurements necessary, so the automation of detection of the nanoparticles’ edges, and hence their size, is a useful tool. As well as the time benefits, it also adds consistency and removes bias, depending only on the images themselves rather than experimenter’s perception.

This problem usually breaks down into two components; edge detection in order to threshold a greyscale image, thus delineating the nanoparticles, and circle detection in the binary image in order to model and recognise the shape of the nanoparticles, thus

finding their sizes.

Two methods were implemented in this project. Particular challenges arose from overlapping nanoparticles, where there is not a whole circle to be detected, only an arc, and hollow nanoparticles, which made both the edge detection and circle detection more complex.

7.1.1 Background and overview

In TEM images where there is high contrast between the nanoparticles and the background, simple thresholding is often sufficient to segment out the ROIs. From a binary image, tools such as ImageJ's Analyse Particles function can often be sufficient to extract information on the particle sizes and circularities. Alternatively, particles can be manually delineated, and the size of the selections analysed. These are simple methods, though time consuming in the latter case. Their perception of being trivial may help to explain why very few papers state the method used for their TEM image analysis.

It was found during this project however that particles were sometimes not readily segmented by simple thresholding, either due to low contrast, rough edges, varying background (though this was generally rectified at the imaging stage), or hollow structures. Since manual delineation of the particles would be time consuming and subject to user bias, more complex algorithms were explored in order to move towards automation of the measurement.

The first method used was rapid circle detection (RCD), as described in reference [299]. The second, referred to as compass gradients edge detection (CGED) involves more sophisticated edge detection, using the vertical, horizontal and diagonal gradients of the image.

The RCD method is a heuristic which has considerable advantages over methods such as the circular Hough transforms in terms of processing power and memory efficiency [299]. This primarily addresses the circle detection problem, and was initially combined with simple Sobel edge detection, as implemented in Matlab.

The second method developed improved the edge detection part of the process. Sobel edge detection is based on convolution with vertical and horizontal gradient kernels, so detects vertical and horizontal lines readily, but is less suited to circular shapes. In order to cover more of the circle perimeter, eight points of the compass were used, adding the diagonals to the analysis.

It was noted that information on the direction of the gradient, as well as its magnitude, would be of use, since the gradients would converge on the centre of the circle. A Robinson compass type kernel [300] was therefore used as a basis for the image analysis.

Both algorithms aided in the detection of the nanoparticles, and were therefore combined for the analysis of the TEM images presented in the previous chapters.

The methods are discussed in detail below.

7.1.2 Algorithm I: Rapid circle detection (RCD)

Rapid circle detection (RCD) uses basic edge detection to distinguish the edges of the circle. Random points selected from the edges are then tested for co-circularity. If the points then meet certain other criteria, the circle is counted as a distinct nanoparticle.

This approach has the advantage that arcs can also be detected, so overlapping nanoparticles should therefore not be problematic. It is also relatively rapid to run, as the calculation is running based on four coordinates rather than a whole image.

Algorithm

The images are smoothed using a Gaussian filter. A threshold level is calculated by Otsu's method [301], and the intensity threshold used to segment out the nanoparticles. The edges of the nanoparticles are then detected using a Sobel operator.

Circles in the image of the edges are then distinguished by a modification of the method proposed in reference [299]. An edge pixel, v₁, is randomly selected, and the set of other edge pixels within a threshold distance calculated. Two other pixels, v₂ and v₃,

are randomly selected from the subset, and the centre of the circle formed by these three pixels is calculated. A fourth pixel, v4, is also randomly selected from the subset, and tested for co-circularity, as illustrated in Figure 7.1.

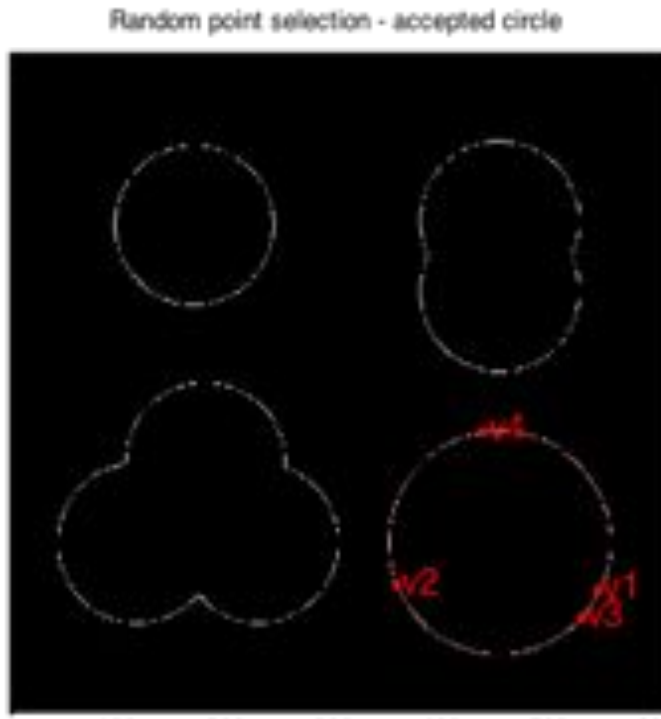


Figure 7.1: Image illustrating the algorithm requirements of co-circularity for circle detection.

If v4 does not fall on the perimeter of the circle the subset is re-tested a certain number of times, proportionally to the number of edge pixels contained in it.

If v1-4 all fall on the perimeter of a circle, the number of other edge pixels approximately close to the perimeter of the circle is determined. This number is compared to the number of pixels expected to lie there in order to ensure the presence of at least an arc.

Circles are accepted if they satisfy the following criteria:

- All 4 pixels are on or close to the edge of the circle;
- The radius is above a minimum threshold;
- There is a high proportion of the expected number of perimeter pixels present;
- The centre of the circle is within the image.

If any further circles are selected which have a centre close to one that has already been accepted, the one with the higher proportion of expected edge pixels present is retained.

This process is repeated until failure thresholds are met; these consist of a certain number of failed attempts at finding circles, or too few edge pixels being left in the subset.

The sizes of the detected circles from all the images are aggregated, presented as a histogram, and the mean and standard deviation of the values are returned.

Some user bias can be removed by setting the threshold distance for the subset of edge pixels around v1 to a very high value. Using a lower threshold can however speed up the algorithm as there are fewer edge pixels to test with, and those in the subset are more likely to be relevant.

Testing

With real data where the nanoparticles are well contrasted with the background and well defined, this analysis detects 89% of the nanoparticles when run on single images (tested 3 times each on 4 images), and 86% when run on a stack of 10 images (run 3 times). Nanoparticles were considered to be detected if, by inspection, the same centre would have been selected if the process were carried out manually. The details are summarised in table 7.1. An example of a typical image with the detected circles and the resulting histogram is shown in Figures 7.2 and 7.3.

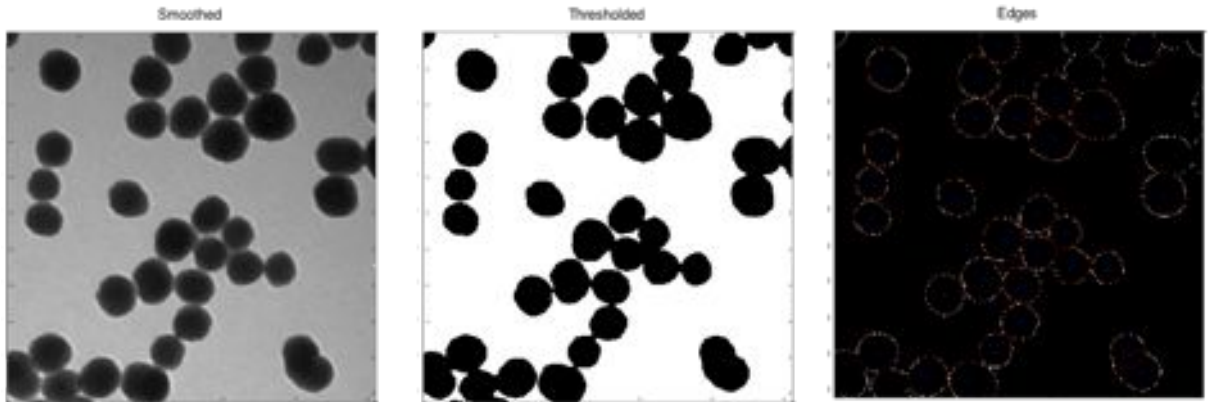


Figure 7.2: Image illustrating stages of the algorithm being used on real data: the smoothed image (left), the binary image (centre), and the results of the RCD detection (right).

Images analysed per run	Time taken	NP detection sensitivity	False positives
1	7.52s	89.03%	2
10	71.90s	86.20%	3

Table 7.1: Results of testing the RCD algorithm on real data. The values for 1 image (top row) are a mean of the results from three runs, each carried out on 4 different images. The values for 10 images are a mean of the results from three runs using a stack of 10 images.

With sufficient nanoparticles visible in the TEM images, reliably detecting 86% of the particles would give a reasonably accurate representation of the size distribution.

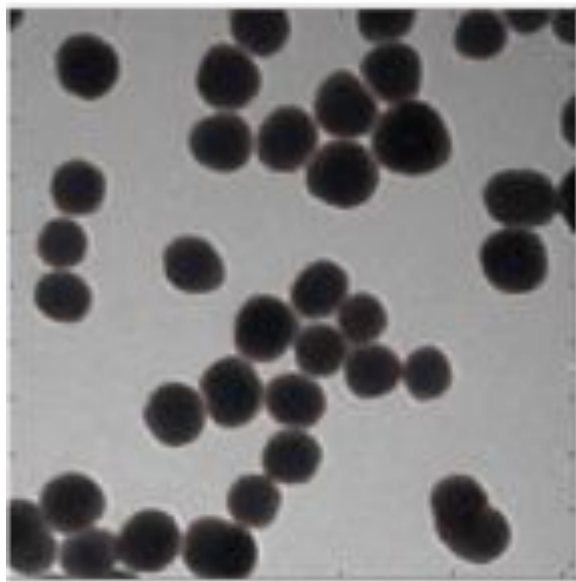


Figure 7.3: Typical image with the centres of the detected circles overlaid as blue crosses.

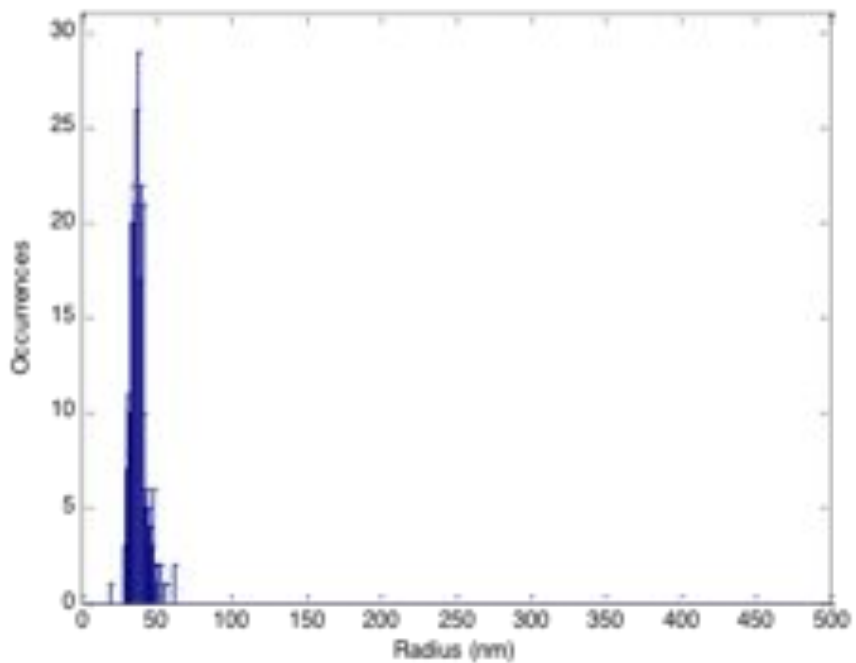


Figure 7.4: Histogram of the detected circles' radii.

This algorithm does however have some flaws, as illustrated in Figure 7.5.

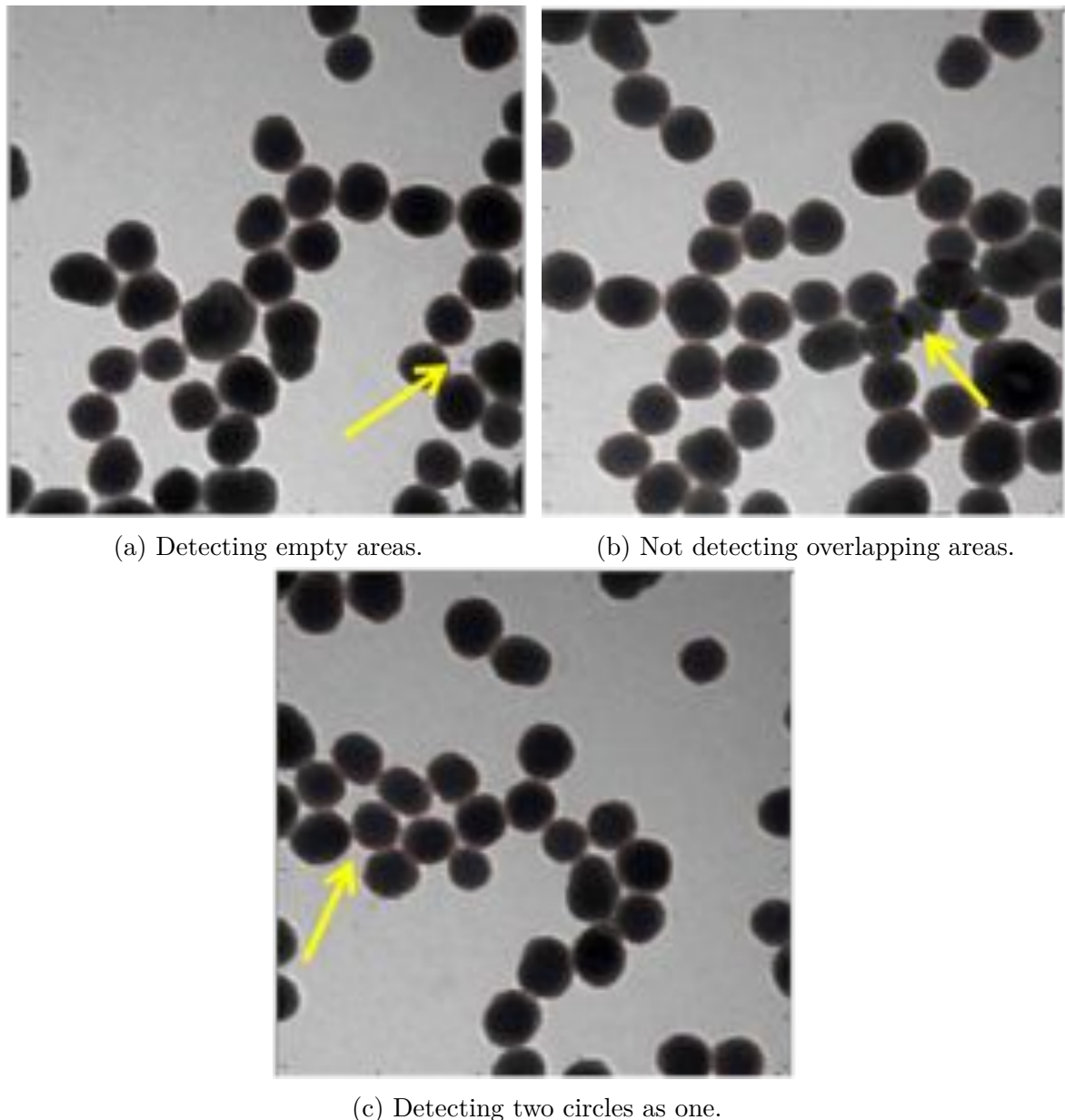


Figure 7.5: Illustrations of problems with the RCD algorithm.

1. False positives can arise when nanoparticles are arranged so that there is a similarly sized gap between them (see Figure 7.5a). This could be minimised by selection of a higher minimum radius threshold, but this risks losing true positive smaller particles, so biasing the distribution. It could also be solved by increasing the threshold for the proportion of expected pixels present. This however risks the non-detection of overlapping or non-spherical particles.
2. Overlapping particles are sometimes however still not detected, especially when

they fall in a row, as in Figure 7.5b with significant overlap. This is attributable to the edge detection, which does not detect the edges of the overlap.

3. False positives can also occur when multiple particles fall within the range of allowed radii (which should be large to avoid bias). This occurs especially when there are other suitably placed nanoparticles that can provide extra edge pixels, as seen in Figure 7.5c.

In conclusion, this method can provide effective circle detection provided with suitable images and parameter selection. It could be improved with extra information being extracted from the image. This is addressed by the following algorithm, which examines the intensity gradients.

7.1.3 Algorithm 2: Compass gradients edge detection (CGED)

Standard edge detection using gradients often only uses the horizontal and vertical intensity gradients of the image. For circular structure detection however more complex analysis is desirable to allow for more rounded structures [300]. This method also has the advantage that the gradient directions should be symmetrical, in that both opposite edges of the nanoparticle will exhibit a similar and inverse gradients.

Algorithm

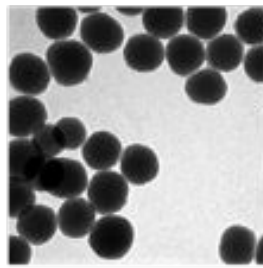
Using the eight points of the compass as opposed to just the four has been proposed as a method for edge detection [300]. Gradients along the horizontal, vertical and both diagonals are examined for both their magnitude and direction. This is achieved by convolution of the smoothed image with a rotating 3x3 kernel, with the direction of each kernel pointing in one compass direction, as shown in Figure 7.6. The result is maps of the gradient magnitude and gradient directions, as shown in Figure 7.7.

$$E = \begin{bmatrix} -1 & 0 & 1 \\ -2 & 0 & 2 \\ -1 & 0 & 1 \end{bmatrix}, SE = \begin{bmatrix} -2 & -1 & 0 \\ -1 & 0 & 1 \\ 0 & 1 & 2 \end{bmatrix}, S = \begin{bmatrix} -1 & -2 & -1 \\ 0 & 0 & 0 \\ 1 & 2 & 1 \end{bmatrix}, SW = \begin{bmatrix} 0 & -1 & -2 \\ 1 & 0 & -1 \\ 2 & 1 & 0 \end{bmatrix},$$

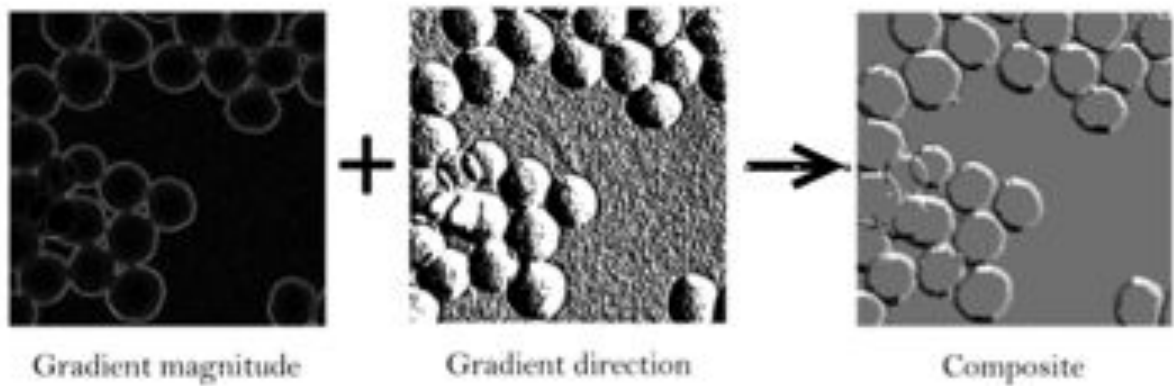
$$W = \begin{bmatrix} 1 & 0 & -1 \\ 2 & 0 & -2 \\ 1 & 0 & -1 \end{bmatrix}, NW = \begin{bmatrix} 2 & 1 & 0 \\ 1 & 0 & -1 \\ 0 & -1 & -2 \end{bmatrix}, N = \begin{bmatrix} 1 & 2 & 1 \\ 0 & 0 & 0 \\ -1 & -2 & -1 \end{bmatrix}, NE = \begin{bmatrix} 0 & 1 & 2 \\ -1 & 0 & 1 \\ -2 & -1 & 0 \end{bmatrix}$$

Figure 7.6: Robinson kernels for edge detection

The gradient magnitude image already produces useful information on the location of the edges. With an applied threshold, the magnitude image can act as a mask to limit the interference of noise in further processing. The gradient direction image can however also be used to direct the circle detection. For any increasing gradient there should be a corresponding decrease in the gradient with equal and opposite direction. A composite image is therefore formed from the magnitude and direction images that incorporates both sets of information, as illustrated in Figure 7.7.



(a) Original image



(b) Components of the composite image

Figure 7.7: Illustration of the results of convolution with the compass-gradient kernels, decomposed into magnitude and direction, then recombined.

Projections are then taken along each compass direction through the composite image, e.g. Figure 7.8. Whenever two corresponding (equal and opposite) gradients are detected along the projection, the centre point is calculated and the size noted. When the four directions are combined these central points form star shapes, with the lines crossing at the centre of each circle.

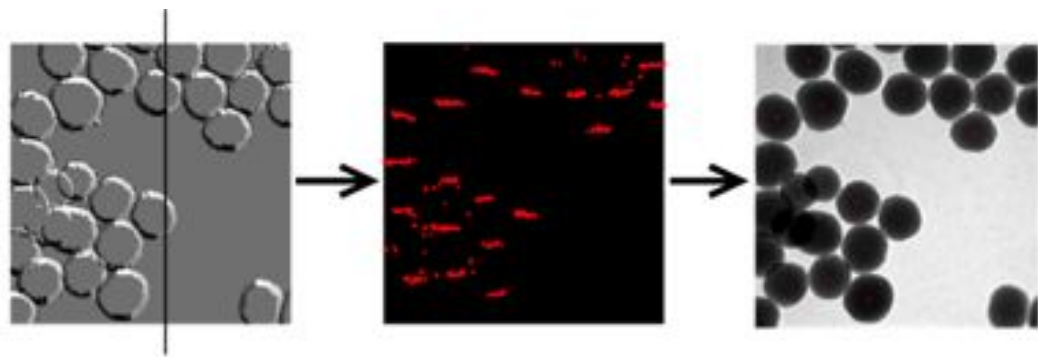


Figure 7.8: Illustration of projections taken across the composite image (left), the consequently detected central points in one direction (centre), and the resulting NP centres from combining the four directions.

Once tidied up using mathematical morphology and control criteria the circles in the image are characterised, and a histogram of the sizes can be produced, such as in Figure 7.9.

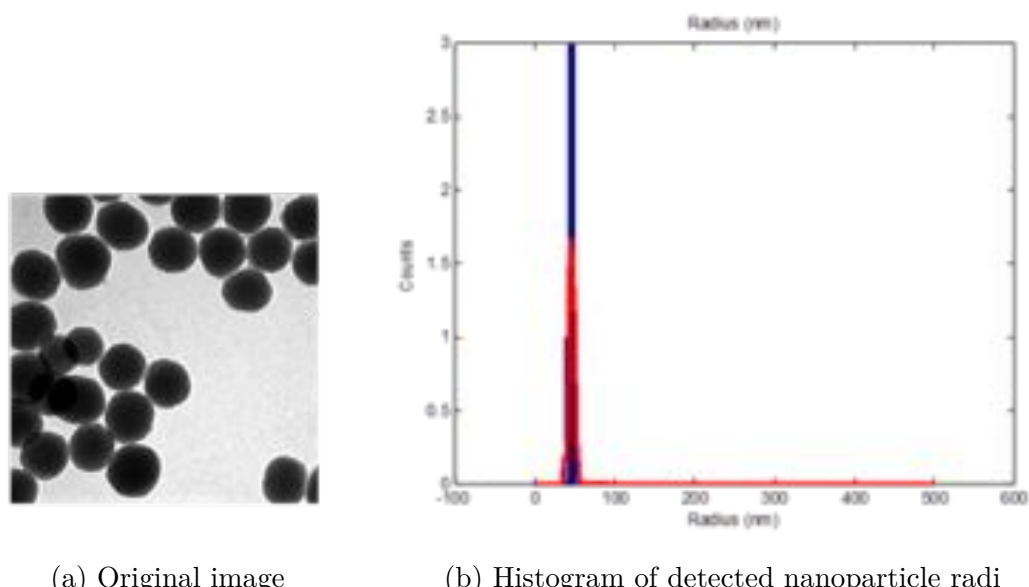


Figure 7.9: The results of the CGED algorithm, showing the original image and the histogram of radii obtained.

Testing

With the use of real data, it was found that the method worked reliably on clean images consistently as shown in Figure 7.9. Certain flaws in the method were noted with less ideal images.

When the particles imaged are of more irregular shapes, the algorithm produced less reliable results, as shown in Figure 7.10. Multiple particles can be counted as one particle and small particles are detected which are probably only due to roughness in the particle surface. The cause of this can be seen in the noisier gradient direction image, since the edge gradients will not be as well defined with irregular shapes.

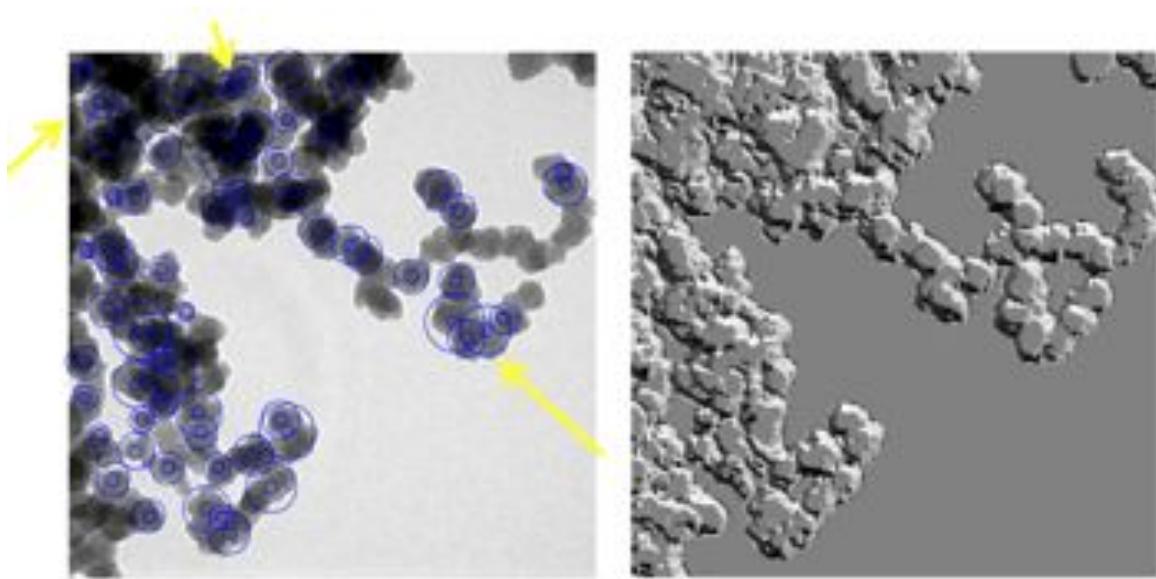


Figure 7.10: Problems with the CGED algorithm when tested with more complex data (original image, with the detected circles marked in blue, and problems highlighted with yellow arrows), and the corresponding composite image.

In general however, though this method could be of use, it did not contain true information about the circularity of the particles. This method was therefore combined with the RCD method above, which provides greater use of the circularity of the particles detected. The combined algorithm is described below.

7.1.4 Combined algorithms: StarRCD

The methods described above, the CGED and the RCD, improve different components of the analysis. They were therefore combined to produce an effective method for analysing TEM images, referred to as the StarRCD method.

Algorithm

The image intensity values are mapped to values between 0 and 1, then smoothed using a Gaussian filter to eliminate some of the noise. At this stage, if necessary, further image processing such as background correction can be carried out. This was generally unnecessary, but depended on the image quality.

The edges and gradients of the edges are detected as for the compass gradients method (see section 7.1.3). Briefly, the image is convolved with a rotating 3x3 kernel, which maps the magnitude and direction of edges.

The magnitude image is segmented by a threshold value, calculated by Otsu's method, and the lines are thinned to create more closely fitted edges. The thresholded magnitude image is then multiplied by the direction map.

Circles in the edges image are detected by the RCD method as described in section 7.1.2 and expended here.

Some threshold values are set:

- A failure threshold is set as an exit criteria in case no circles can be found.
- Thresholds are also set to limit the minimum and maximum distances between the first three randomly selected pixels. This is included for time benefits, though the values must be selected carefully so as not to bias the results.
- There is a third threshold set to limit the distance that the 4th randomly selected pixel can be from the test circle made by the first three.
- The fourth threshold determines the acceptable ratio between the number of edge pixels on the perimeter of the test circle and the theoretical number of edge pixels of the test circle's radius.

Three pixels are then randomly selected from the subset of edge pixels. The circle they form is determined (referred to as the test circle). A fourth pixel is then also randomly selected and is tested for whether it also falls on the perimeter of the test circle.

Some false positives need to be filtered out; this method is susceptible to detecting a circle which encompasses either zero or multiple nanoparticles. Where there is no

nanoparticle in the circle and the edges are made up of multiple true nanoparticles, the results can be filtered out by reference to the composite image. Therefore, once a list of possible circles has been obtained, the gradients around the edges of each of the centres are verified in the composite image. Potential circles are kept if they have the correct gradient directions at 2 or more compass points. This threshold could be increased for greater accuracy but would risk losing some circles with more irregular shapes.

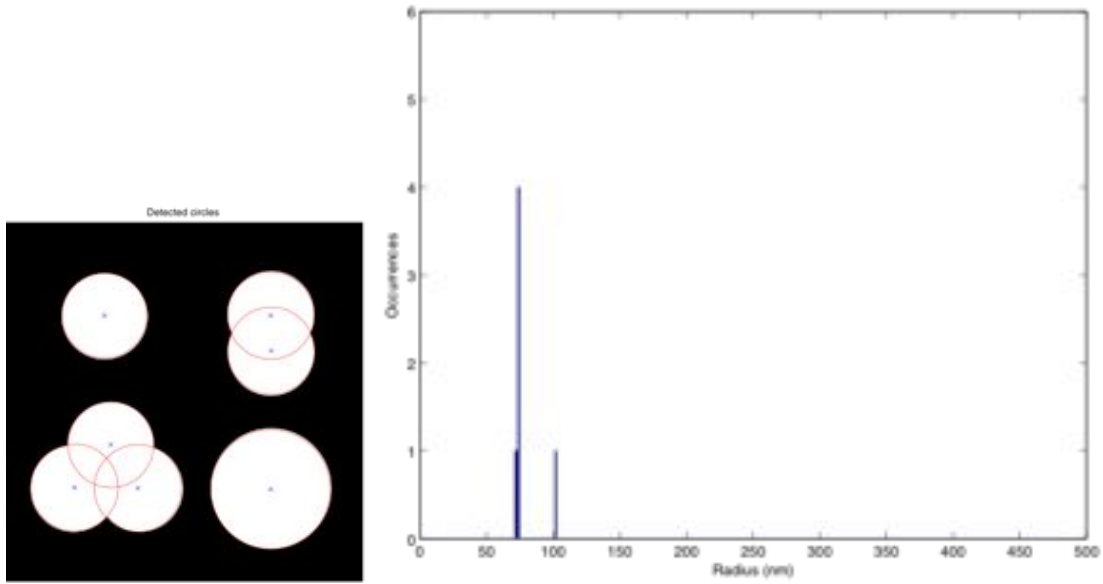
A histogram of the circle radii and a mean radius is then calculated.

Validation

The algorithm was run on a phantom image to test its capabilities. All seven of the phantom circles were detected, and the radii detected accurately represent the radii of the circles, see Figure 7.11.

It should be noted however that careful parameter selection is required. Though there are several checks carried out during the detection, there is a vulnerability to duplicate detections, as discussed below, if the threshold parameters are too broad.

The average radius detected was 78 pixels, with two separate size peaks at 74 and 100 as expected.



(a) Detected circles

(b) Histogram of radii of detected circles.

Figure 7.11: Results of the star RCD algorithm tested on a model image.

Testing

SiNP images On well-contrasted images, such as those of the RuSiNPs, the algorithm readily detected structures, and the perimeters visually matched well with what would be selected manually, as shown in Figure 7.12, with the associated histogram shown in Figure 7.13.

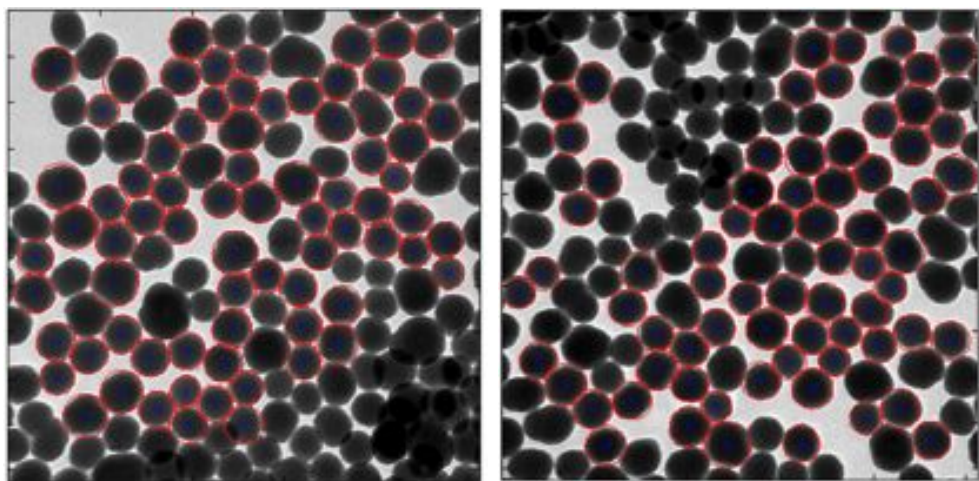


Figure 7.12: Typical images of SiNPs showing the overlaid circles detected by automated analysis by the StarRCD method. Circle perimeters are shown in red, and centres in blue.

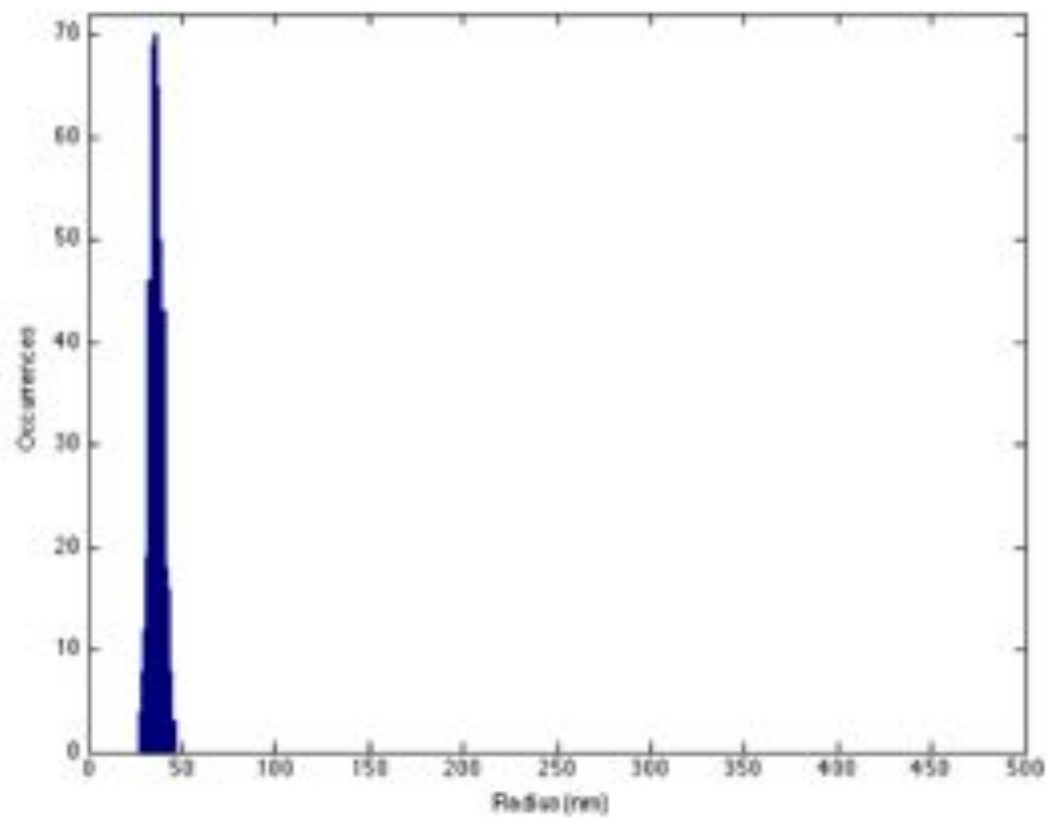


Figure 7.13: Histogram of the results of SiNP radii by automated analysis by the StarRCD method.

When measured by the algorithm a mean radius of 37 nm with a standard deviation of 4 nm was calculated, based on 368 measured NPs.

The mean radius of the particles measured manually is 37 nm with a standard deviation of 17 nm when 260 nanoparticles were included. The means are the same for manual measurement as for the algorithm's result suggesting that both methods produce similar results. When measuring manually a wide range of particles were selected. In the images in Figure 7.12 however, with the results from the algorithm, some of the larger particles seem to have been missed, which accounts for the smaller standard deviation. This could be due to parameter selection, as there is no other intrinsic reason the algorithm should miss them.

AuNP images AuNPs are also well-contrasted images, since the gold highly attenuates the electron beam. The difference between AuNPs and SiNPs is usually the size, so it was of interest to also test the algorithm on small particles. While it is possible to compensate for this by magnification on some microscopes, the scale will be limited for older models, with AuNPs falling at the low end of the spectrum, and therefore they often comprise fewer pixels than the SiNPs.

A mean radius of 8 nm, with a standard deviation of 1 nm was found using the algorithm, which detected 339 NPs. The histogram showing the distribution of sizes is shown in Figure 7.14.

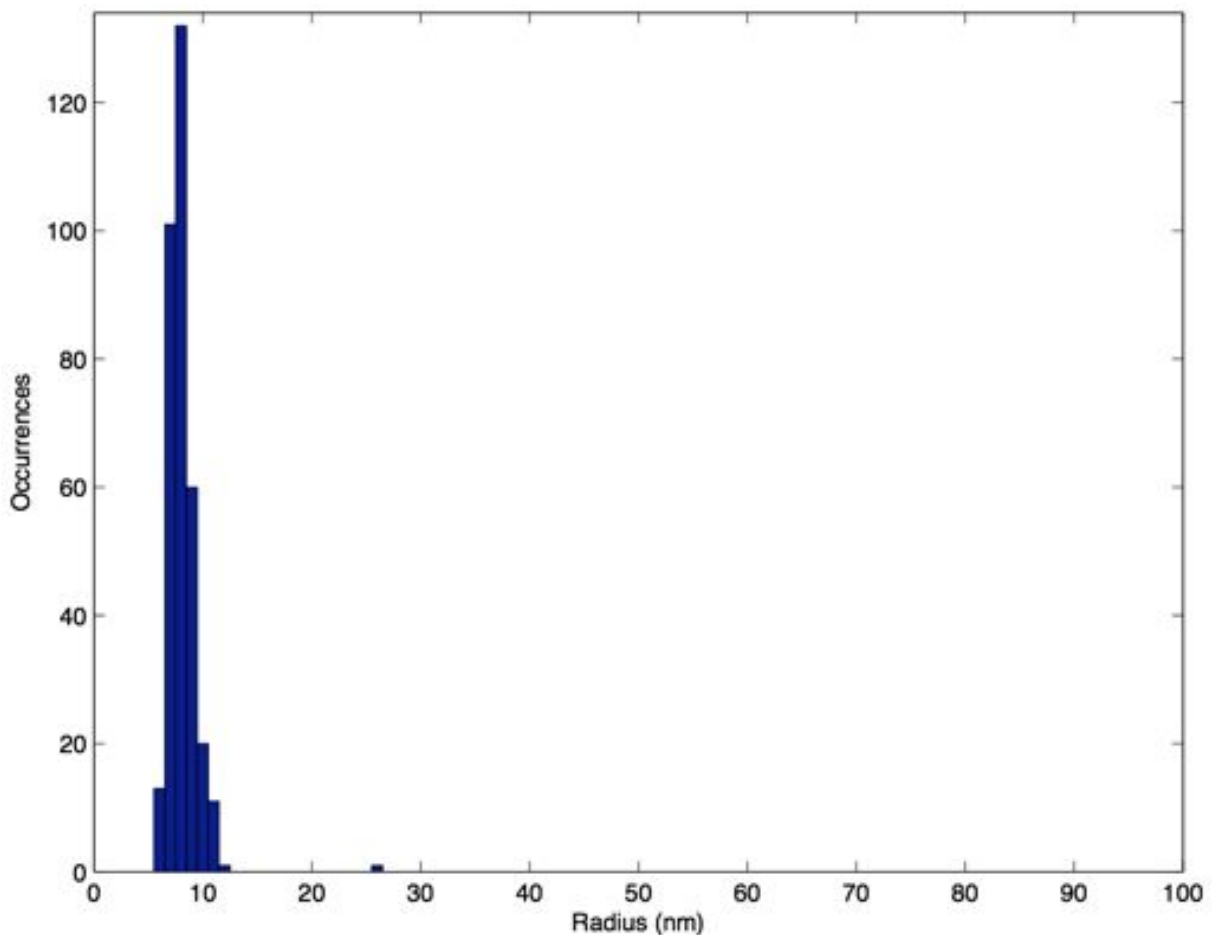


Figure 7.14: Histogram of the results of AuNP radii by automated analysis by the Star RCD method. The x-axis was expanded for clarity as the higher radius bins were empty.

The detected particles are shown in Figure 7.15, with the second image zoomed in for clarity.

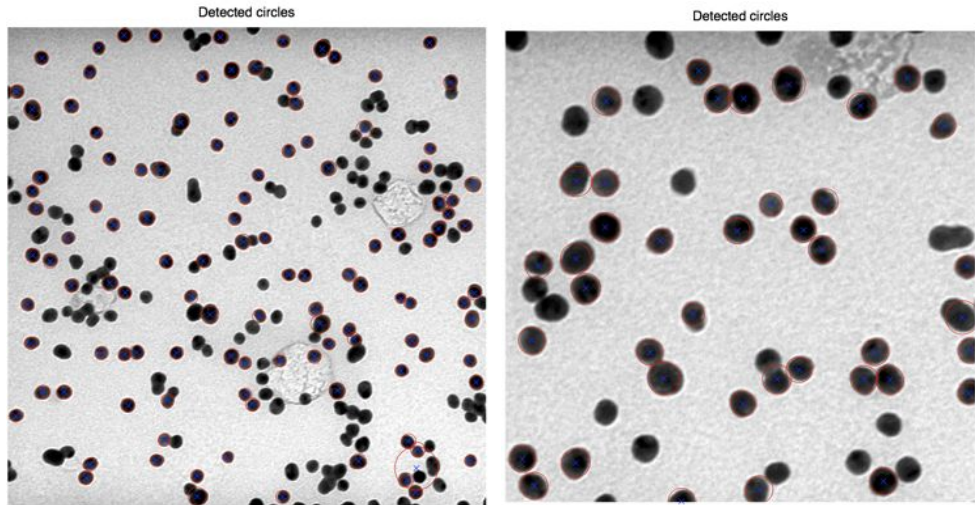


Figure 7.15: Typical images of AuNPs showing overlaid circles detected by automated analysis by the Star RCD method. Circle perimeters are shown in red, and centres in blue.

By measuring 100 AuNPs in the same images manually, a radius of 9 nm with a standard deviation of 4 nm was obtained. These values are similar to each other and probably within experimental error due to focusing and aberrations, so the difference can be considered acceptable and the results of the algorithm for these small particles comparable to those measured manually.

ASiNP images For ASiNPs, which had irregular morphologies, the algorithm detected some circles which would be selected manually, but struggled to reliably detect nanoparticles, see Figures 7.16 and 7.17. This could partly be due to the aggregation and poor contrast of the particles, which leads to non-discrete shapes on the TEM image.

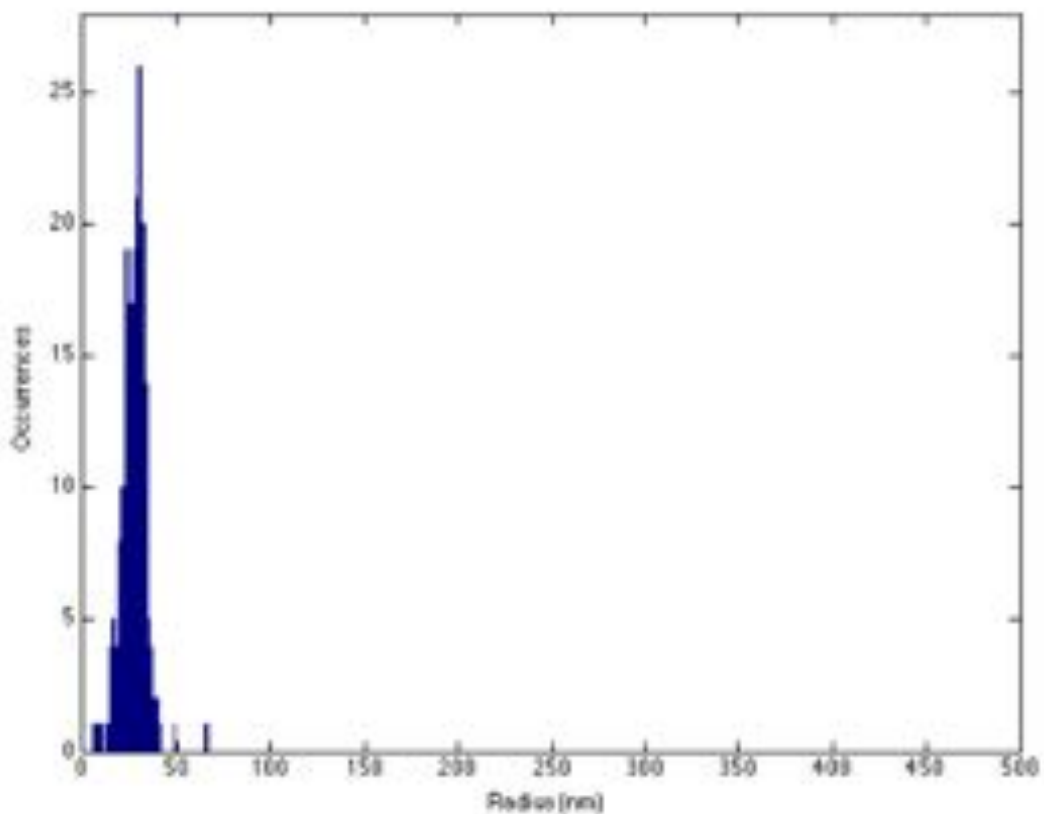


Figure 7.16: Histogram of the results of ASiNP radii by automated analysis by the Star RCD method.

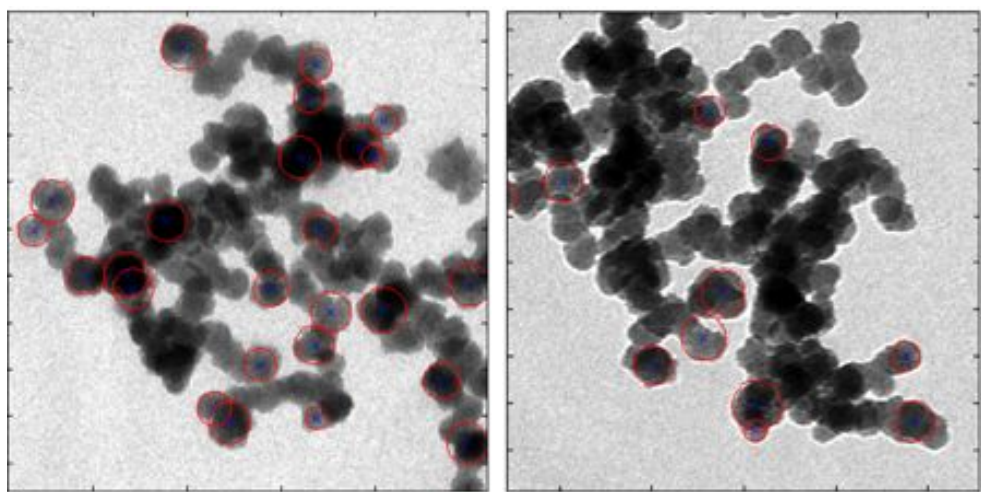


Figure 7.17: Typical images of ASiNPs showing overlaid as circles detected by automated analysis by the Star RCD method. Circle perimeters are shown in red, and centres in blue.

Automated detection resulted in a mean radius of 34 nm and a standard deviation of

10 nm, from 618 NPs.

Manual selection of 109 circular structures from the same images however produced a mean radius of 27 nm with a standard deviation of 14 nm. The mean obtained by the automated method was within a standard deviation of that found by manual selection, but there is considerable variation, so this method should be used with caution on such images. There is some ambiguity in the nanoparticle edges which both measurements will be subject to, but taking a fraction of the time does add some value to the computational method.

One compromise between these two methods would be to run the algorithm with loose parameters then to confirm or reject every selected circle manually. While this is similarly tedious, it would speed up the task compared to drawing every ROI.

HSNP images In the case of the hollow silica nanoparticles the algorithm was able to detect the nanoparticle outer edges in a small test sample, as shown in Figures 7.18 and 7.19. None of the inner circles produced by the cavity in the nanoparticle core were delineated, as expected since the gradient direction is controlled. There are some small structures delineated, which shifts the histogram and mean. These could be excluded by parameter selection, but should not be to avoid arbitrary bias. It is clear from this example though that the algorithm can distinguish overlapping hollow particles as long as the edges are clear.

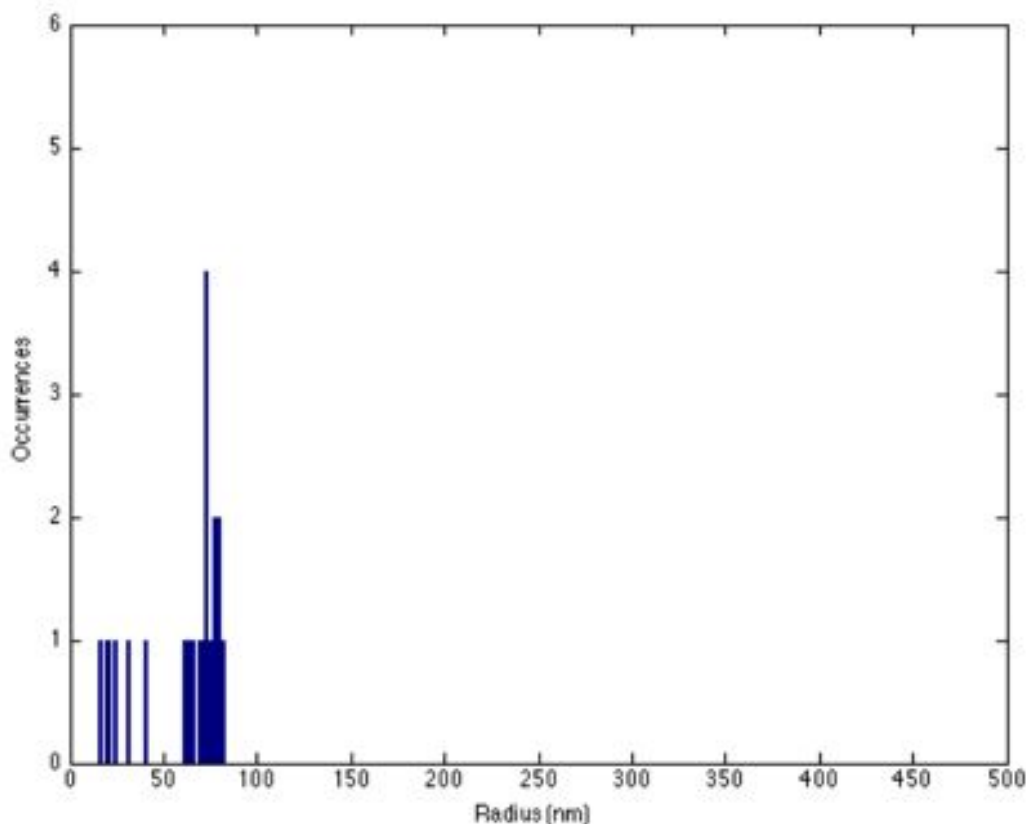


Figure 7.18: Histogram of the results of HSiNP radii by automated analysis by the Star RCD method.

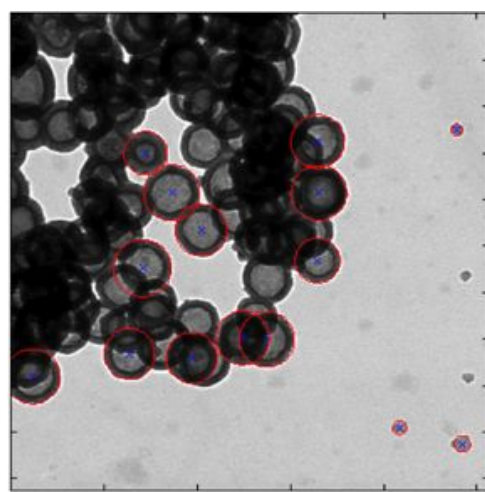


Figure 7.19: Typical image of HSiNPs showing overlaid as circles detected by automated analysis by the Star RCD method. Circle perimeters are shown in red, and centres in blue.

Further testing would indicate the limits of this algorithm with respect to hollow

particles, but this illustrates the effectiveness of the concept.

Discussion

The StarRCD is rapid and effective given sufficient runs for the selections to be optimised. It does however require good edge detection. The use of the compass gradients then has the advantage of providing the directions too. This means that it is the intrinsic image information that is being used to filter out false positives circles rather than arbitrary distance values.

7.2 Automated relaxation time calculation from MR images

This section describes the automated sorting and analysis of the proton MRI images carried out during this project.

7.2.1 Background and overview

Magnetic resonance images are formed through a balance of the effects of the relaxation times (T_1 and T_2) and the proton density of the sample. The relaxation time T_1 can be determined from a series of inversion recovery images with varying inversion time (TI), or saturation recovery images with varying repetition times [111].

The images in recovery sequences were acquired with the inversion or repetition times in a non-ordered series. This reduces the risk of accumulating errors from incomplete relaxation from the previous sequences. The images must therefore be sorted for analysis according to both the series to which they belong, and the order of the image stack according to inversion time.

The regions of interest (ROI) can then be segmented and the intensities of the ROIs averaged for each slice through the stack of images, which is ordered by inversion or

repetition time.

The intensity of the image at a given coordinate will correspond to the signal intensity at that point, which will recover through the series according to the equation (7.1) for inversion recovery, or equation (7.2) for saturation recovery.

$$Intensity_{sample,IR}(TI) = M_0 \left[e^{-\frac{TI}{T_1}} (-2 + e^{-\frac{TR}{T_1}}) + 1 \right] \quad (7.1)$$

$$Intensity_{sample,SR}(TR) = M_0 \left[1 - e^{-\frac{TR}{T_1}} + k \right] \quad (7.2)$$

The intensity of the image coordinates can therefore be fitted to equations (7.1) or (7.2) to calculate the T_1 . This is a complex problem with multiple unknown variables, so most easily addressed computationally.

One standard method of fitting is to use a Levenberg-Marquart nonlinear-least-squares minimisation of three parameters [302, 303, 304]. Other methods, such as that used here, have been reported which can save on computation time and have been found to be more robust [305].

In this work the intensity data has been fitted to the recovery curve by a Nelder-Mead simplex minimisation [306] of the squared difference between theoretical model values and the experimental data. This is a non-linear multivariate optimisation algorithm, and while it is a heuristic method, it is relatively simple and produced excellent results for this purpose.

7.2.2 Algorithm

The algorithm used to sort and analyse the MR images are described below. The methods for analysing inversion recovery and saturation recovery data are very similar, with only the model equation for the fitting differing. Both are therefore presented together below.

The algorithm is summarised in Figure 7.20.

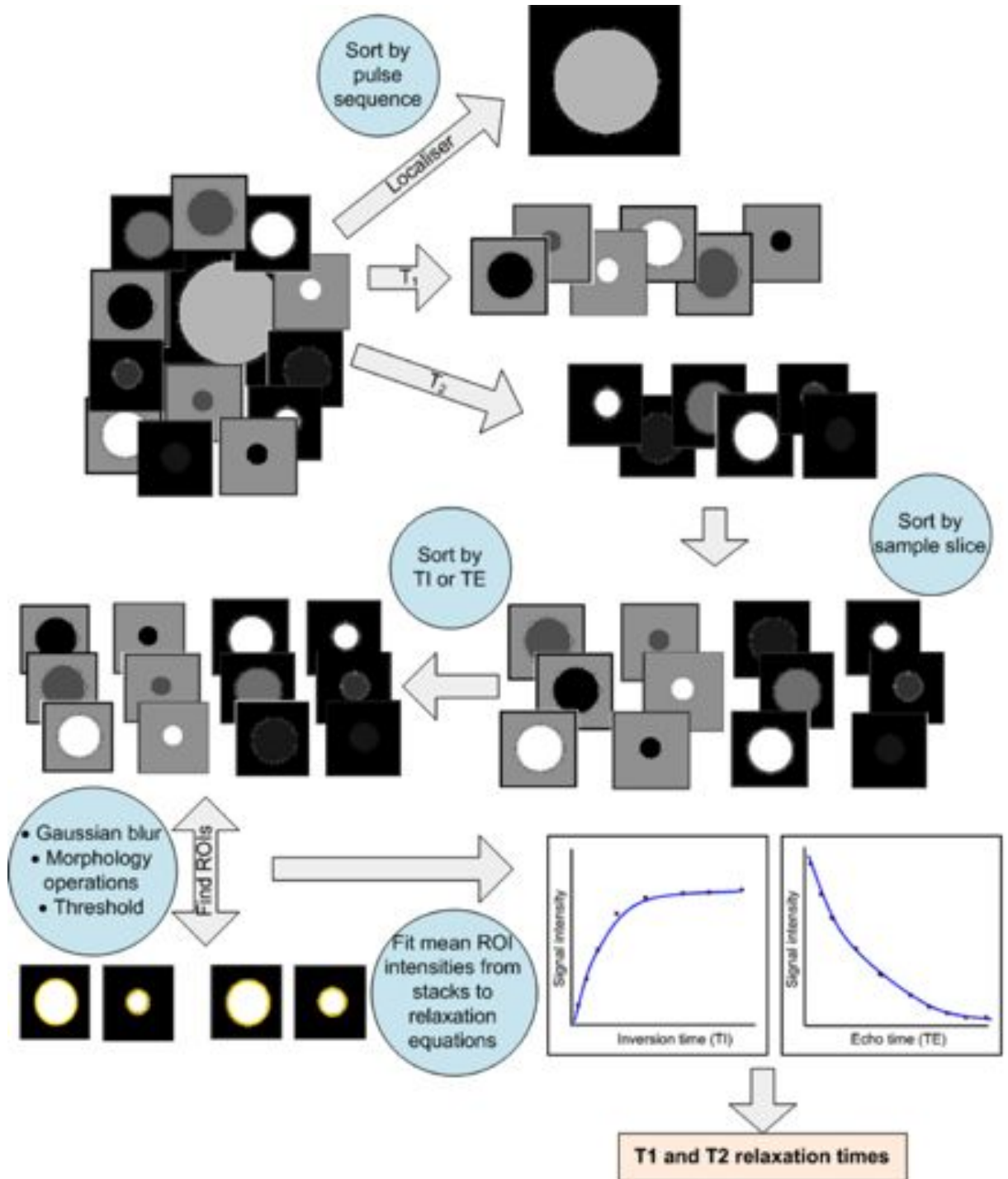


Figure 7.20: Workflow for the automated calculation of relaxation times from DICOM format MR images.

The raw images are sorted according to their DICOM header information. This includes the sequence name, which is used to distinguish initially whether the images are relevant for T₁ calculations. They are then sorted according to the series they were

acquired in, and ordered according to their inversion time.

This produces a set of image stacks for each image slice. The optimal slice for selecting regions of interest is then selected manually. Usually this will be the image with the highest inversion time as the samples should all be fully relaxed, and therefore show the highest and most uniform contrast.

A threshold might be directly applicable, but there may also be a need to first apply mathematical morphology operations to better delineate the regions of interest. The variables used in these operations are at present set manually as appropriate. The mean intensity value for each region of interest is then calculated, providing the data for the curve fitting.

A test function is estimated to model the shape of the relaxation curve, either for equation (7.1) or (7.2) above depending on whether the sequence was inversion or saturation recovery. Signal recovery estimates for different relaxation times are calculated from this model, which are compared to the real data. The difference between the test data and real data is minimised by changes to the test function until either a threshold number of attempts is exceeded or a minimum is found. The minimisation is carried out by a Nelder-Mead simplex minimisation [306, 305].

The starting values for the test function must be supplied. Given the knowledge of MRI sample properties however, reasonable estimates for each value have been used and consistently provided closely fitted results.

7.2.3 Discussion

In general this algorithm has been highly effective, and has routinely been used to analyse MRI images throughout this project. Once a suitable region of interest has been selected, the sorting and fitting processes produce reliable results which are consistent with expected values.

Any problems that have arisen have been in region of interest (ROI) segmentation, especially where there is an uneven background due to other objects in the scanner. For

example, in one early experiment samples tubes were placed in a sponge for support and submerged in water to reduce surface-air artefacts. The sponge however created a rough background, from which it was difficult to segment the sample tubes.

There is also currently no fully automated function for ROI detection integrated into the algorithm. Parameters must be provided with an approximate size of the ROIs in order for any morphology operations to be carried out. Future work on this script could include automating an approximation of the ROI size.

Other problems that have arisen have been due to incomplete data sets. This arose from samples completely relaxing before the minimum available inversion time. This would lead to increased error in samples with high contrast agent concentrations, so these samples should be treated with caution during the analysis.

The other occasion for incomplete data so poor fitting occurred when samples had an unexpectedly long relaxation time, so were not sufficiently relaxed to model the curve. This was resolved however by re-scanning the samples with increased repetition times.

7.3 Conclusions

In conclusion, two effective algorithms have been developed during this project that considerably reduced the processing time for extracting information from the images. They have been used throughout this report where relevant, and were found, despite some limitations, to be highly useful tools.

Some problems have been noted and discussed. Overcoming these would be an interesting route for future work since these algorithms could be useful for many people undertaking such analyses manually or producing their own similar algorithms.

CHAPTER 8

CONCLUSIONS AND FURTHER WORK

In this work, the possibilities of multimodal imaging of *in vivo* immune cells have been investigated on several levels. The design of an appropriate imaging agent system first required a focus on suitable techniques, then incorporated the many requirements they entailed. For example, a gadolinium agent should have ready solvent access to allow efficient exchange, whereas fluorophores are often better protected from the oxygen in the solvent to avoid quenching.

The most challenging aspect was however incorporating fluorinated agents into the structure. In order to design a suitable vehicle, one unknown factor was how readily the agents could be examined by ^{19}F MRI. The capabilities of the MR imaging equipment available were therefore investigated to help establish the requirements for multimodal imaging agents to be developed. It was found that the SNR increased linearly with fluorine concentration for a given compound, as expected. The trend of the SNR against fluorine concentration *between* compounds however was not linear, which was attributed to the properties of the molecules and the medium such as the relaxation times and the viscosity.

This data suggests a strong caveat for future research, in that the signal may not vary as expected when comparing two fluorine tracers in different tissue compartments, but also when comparing agents in tissue and in a reference standard.

Another caveat highlighted in this section is the variation in the signal that can arise

both laterally and vertically with respect to the coil. This is most significant when a vial adjacent to a sample is used as a reference, since the coil sensitivity may well vary over this area. While this effect is most pronounced with a surface coil due to its simple structure, it was also demonstrated that there can be considerable variation within a birdcage coil too. Consequently careful thought should be given to mapping the regions of interest onto a sensitivity profile.

Next the design of a multimodal vehicle was considered. Of the various ways that imaging agents can be incorporated into a nanoparticle, three were explored in this project: trapping imaging agents inside the matrix of a particle, binding agents onto a nanoparticle surface, and trapping agents in the core of nanoparticles. Using multimodal molecules was briefly explored but their usefulness was limited by the inability to tune the different imaging agent concentrations as required by the different techniques.

8.1 Trapping imaging agents in a nanoparticle matrix

A novel dual-modal nanoparticle was created which incorporated both fluorescein for fluorescence techniques and gadolinium for proton MRI, denoted as FlGdASiNPs. The particles' morphologies were investigated by electron microscopy. The shape was found to be uneven, and with distinguishable but aggregated particles, which explained the polydispersity observed by light scattering.

The FlGdASiNPs were characterised in relation to their effectiveness as imaging agents. The luminescence was spectrally similar to the free dye, though the lifetime suggested there would be a reduction to the quantum yield. Given the high sensitivity of fluorophores and fluorescence techniques this was not considered to be a problem since the particles were visibly fluorescent. The MR relaxivity was comparable to commercially available MRI contrast agents.

Having shown both luminescence and MR contrast enhancement, PBMCs were treated with the FlGdASiNPs to assess how they are taken up into the various cell types. Flow

cytometry indicated that there was uptake both into monocytes and lymphocytes, though with labelling starting at different concentrations. Microscopy however demonstrated one significant challenge with these nanoparticles, which is that the aggregation severely increased in cell medium, and that the consequent problems were exacerbated by slide preparation techniques such as cytopinning. Separation of the aggregates from the cells is challenging as both settled rapidly, and the cells were used at too low a concentration for recovery from a density-gradient column. The FlGdASiNP-labelled PBMCs also showed no contrast enhancement by MRI. This is at least partly explained by the limited uptake and labelling observed by flow cytometry.

Trapping imaging agents in the matrix has therefore been shown to be of potential use for cell labelling by fluorescence and novel nanoparticles demonstrating this have been created in Chapter 3 of this work. The advantage of this method is that it preserves the structures of the imaging agents with no chemical modification required. It is important to note that the fluorescence was quenched to some extent by the trapping process, and although it was not significant in this context it should be borne in mind for future work.

Another aspect to be investigated in future systems with using this method is the degree of leakage from the nanoparticles. No leakage of fluorescent compounds was evident by observation either during these experiments or afterwards, but if the system were to be carried forward this should be investigated thoroughly.

Fluorinated species could not readily be incorporated by trapping in the matrix, which effectively limits these particles to being dual-modality agents for the techniques of interest. This was a limitation that led to other methods being explored. In future work however other designs, such as using SPIOs and negative proton MRI contrast, could replace the fluorine MRI and hence the requirement for fluorinated species. This is discussed further below.

An attempt was made to improve the trapping and increase the surface charge by using a quaternary aminated silane instead of a primary silane. The method used however produced only gels which may have some function in other work, but were not considered

viable for this project since they could not be characterised as nanostructures.

Strategies for improving the trapping of imaging agents in ASiNPs in further work would therefore include developing the synthesis to achieve colloidal stability in cell medium. While replacing all of the aminated silane was not useful, if the particles could be dispersed and coated with a layer of pure silane, the core would still retain the effective trapping observed here, while the surface could stabilise the particles and be further functionalised. The question arising from this would be whether the gadolinium would still have sufficient access to water in the core, or whether it would have to be conjugated to the surface.

8.2 Binding imaging agents to a nanoparticle surface

Two nanoparticle systems were created in this chapter. Ruthenium-tris-phenanthroline-doped silica nanoparticles, RuSiNPs were further functionalised with gadolinium to form RuGdSiNPs. Iridium bipyridyl and gadolinium DTPA-functionalised gold nanoparticles, IrGdAuNPs, were also explored.

The RuGdSiNPs were useful as a reference point as similar particles have been reported to show good uptake into cells [236]. The RuGdSiNPs were therefore used for developing protocols and setting baseline expectations for novel systems.

The RuGdSiNPs showed a regular morphology and low dispersity by both electron microscopy and light scattering. The luminescence of the ruthenium complex was comparable to literature values and MRI contrast enhancement was comparable to commercially available contrast agents. Treatment of PBMCs with the RuGdSiNPs resulted in effective fluorescence labelling, as measured by flow cytometry and observed by microscopy. The labelling was not however high enough to observe contrast enhancement by MRI.

The IrGdAuNPs were novel structures, designed in the context of stabilised gold nanoparticles [261], and offering a greater surface to volume ratio than the silica nanoparticle. In this system however the gadolinium complexes, instead of a surfactant, stabilised

the particles before the iridium complexes were incorporated. Electron microscopy and light scattering showed a regular morphology and low dispersity, as expected with gold nanoparticles. The luminescence was spectrally comparable with literature values, and the MR relaxivity was greater than that of current commercially available contrast agents. When PBMCs were treated with the IrGdAuNPs however, there was no uptake observed by microscopy, and very limited contrast enhancement by MRI.

The IrGdAuNPs did suffer from a limited stability, so further development could be of interest as a means to improve the interaction with cells.

More generally, binding imaging agents to nanoparticle surfaces is attractive due to easy characterisation and simple functionalisation reactions. There was however no obvious way to incorporate fluorinated species into these simple systems without reducing the ^{19}F relaxation time to an undetectable level or without more specialised pulse sequences. As an approach it is therefore insufficient, alone, to create a trimodal imaging agent for cell tracking for the modalities of choice in this work, but it is a useful component in the nanoparticle toolkit.

8.3 Multimodal imaging agent molecules

In this chapter AFC was explored as a potential multimodal agent for fluorescence techniques and ^{19}F MRI. The fluorescence was found to be in a suitable range for most fluorescence techniques, and the SNR of the fluorine MRI signal at various concentrations was measured. Based on the MRI measurements, it was considered unlikely that treatment of PBMCs with AFC would lead to effective labelling. Indeed in cell tests it was found that, while the molecule was very effective as a cell label for fluorescence techniques, the labelling of PBMCs was not sufficient to allow effective detection by ^{19}F MRI.

It was noted however that this molecule could be a useful component for future larger multimodal systems; For example, if a high concentration of the dye could be trapped inside a nanoparticle shell, there may be sufficient signal for observation by fluorine MRI,

and consequently tracking.

In general combining fluorine MRI and fluorescent agents in one molecule will always suffer from a need to balance the number of fluorines in the structure and the solubility of molecule. An interesting but complex option would be to develop dendrimers, which could simultaneously incorporate both agents with tuning of the ratios, have a stabilising moieties on its surface to improve the solubility, and the added benefit of monodispersity. The design, synthesis and purification of such a system would however be very challenging.

8.4 Trapping imaging agents in nanoparticle cores

In Chapter 6 nanoparticles were explored further, in this case as hollow shells to be filled with imaging agents. This method proved more successful, with the development of a novel dual modal particle by trapping ruthenium tris-phenanthroline suspended in PFOB in a silica shell, which could be pre-functionalised with gadolinium to add the third modality of proton MRI contrast. Both the suspension of fluorophores in perfluorocarbons and its subsequent trapping inside a silica shell has been demonstrated here for the first time (to the author's knowledge).

This is an exciting and relatively unexplored area of nanoscience, where the many opportunities need to be balanced by robustness in the development process. For example, careful consideration needs to be given to the choice between calcination and solvent extraction. Solvent extraction is effective on smaller scale quantities of particles, whereas calcination has been shown to be more efficient in the removal of organic material. This is important for confidence in the purity of the shells, where residues of surfactants can make a significant difference to the physicochemical properties of the particle such as the surface charge or the porosity.

Similarly the choice of synthesis would be important for future work as each have their advantages. In this work latex templating produced interesting results, such as the positive surface charge and the relative monodispersity and uniform shell thickness. The

positive surface charge, while potentially improving the cell uptake, does however show that the poly-l-lysine is thoroughly incorporated into the shell. Calcination would remove the polymer, so solvent extraction might be preferable, but then there is a concern for robust characterisation of the shell contents and residual latex in the core reducing the loading capacity. Another complication of future work is that the latex beads would need to be produced in-house in order to make the synthesis financially viable, especially when scaled up.

Homogeneous templating, with selective etching to remove the core of a nanoparticle, was therefore explored further here. Large scale production was possible, which produced stocks for further experimentation. These hollow structures were then filled with perfluoroctyl bromide as a fluorine MRI agent.

It was found that $[\text{Ru}(\text{phen})_3](\text{PF}_6)_2$ could be suspended in the PFOB while maintaining its fluorescence, thus creating a dual modal suspension without any further functionalisation. This $[\text{Ru}(\text{phen})_3](\text{PF}_6)_2$ -labelled PFOB (RuPFOB) was then introduced into hollow nanoparticles.

Filling the GdHSNPs with RuPFOB, the suspension mentioned above, led to nanoparticles which could be viewed by proton MRI, fluorine MRI and fluorescence techniques. A difference was noted however between the fluorine signal from the Gd-functionalised and unfunctionalised PFOB-filled HSNPs. This suggests that the gadolinium may be having a relaxation enhancing effect on the fluorines in the core, making them relax faster than they can be observed by standard MR sequences.

Multiple routes for further work could stem from this section. The most pressing would be to optimise the silica shells themselves. While they show good colloidal stability after calcination, both surface functionalisation with the gadolinium and filling with the perfluorocarbon disrupt the stability. Further surface functionalisation would therefore be useful in order to increase the surface charge. Filling of the nanoparticles poses a greatest problem in that currently the nanoparticle pores expose the PFOB to the aqueous medium, so causing aggregation. Capping the particles with either a further silane layer,

a layer of metal, or a polymer brush to cover the pores, could potentially all improve the stability of the filled shells.

Another aspect would be incorporating more gadolinium onto the surface to increase the proton MRI contrast, either through using multiple layers of gadolinium complexes, through conjugation to a longer structure polymeric structure [236, 195], or through increasing the surface area to volume ratio. The latter option would however reduce the volume available for the PFOB, which is also subject to low sensitivity.

A third route is to explore other fluorescent or luminescent dyes and perfluorocarbon suspensions, especially those with a high hydrophobicity, to find other dyes which might be incorporated into the silica shells. This, in addition to the capping, would further minimise the risk of leakage from the shell.

8.5 Image analysis

A large volume of image data was collected over the course of this project, with no readily available tools for easily carrying out analysis to extract useful information. The two principal areas where this was found were in electron microscopy and MRI.

8.5.1 Electron microscopy image analysis

For TEM images, the goal was to develop an algorithm to automatically analyse a stack of microscopy images in order to measure the size of the nanoparticles. Essentially the required task was circle detection, which was implemented by a rapid randomized method [299]. The edge detection was not sufficient however so a more sophisticated edge detection method was added, which also provided information on the direction as well as the magnitude of the gradient. The extra checks the gradient direction information produced was found to often be effective at minimising the detection of false-positive circles. This method was shown to be effective on a range of nanoparticle images, so could be a useful tool for others in the analysis of similar images.

Future work for this algorithm would be to generalise it so that it can accept a wider variety of images, and to add a user interface so that it could be used by others without requiring knowledge of Matlab, or the costly licence fee for the software.

8.5.2 MRI image analysis

In a similar way, T_1 mapping is a common task, but there were no readily available tools which could extract relaxivity information from the image stacks. A method was therefore developed in Matlab which would accept read in DICOM files, detect regions of interest, then fit T_1 values to the data.

This method was found to provide reliable results, and was used with different pulse sequences. This versatility is useful as the only input needed to measure values from a new sequence is the equation for the fitting.

This algorithm could also be developed into a more widely applicable tool. Firstly, a method selecting regions of interest would be required, then a way to input and validate new equations would be useful. Lastly a user-interface would make this accessible to those without Matlab licenses.

8.6 Future directions

To develop this project further capping of the pores with imaging agents inside the shells would be a priority future work. The most important consideration would be to provide greater colloidal stability by increasing the surface charge, preferably with a positive charge, while minimising leakage. This would give greater confidence in the reliability and clinical translatability of the system.

The next steps would involve tuning the size and polydispersity in order to optimise the surface area to volume ratio, and hence the ratio of agents for proton and fluorine MRI. This would have to be done in combination with cell studies to ensure that the sizes are appropriate for efficient uptake and minimal cytotoxicity.

Another interesting aspect would be to determine whether the quenching of the fluorine MRI signal by the gadolinium could be reduced with either thicker shells or a spacer molecule and for example polymer brush adding distance between the gadolinium and the fluorine species. Alternatively if different pulse sequences became available it would be useful to explore shorter echo times, and hence the use of less mobile fluorine molecules.

An alternative route could involve incorporating SPIOs by trapping them in the matrix of a nanoparticle shell, as an extension of trapping in the bulk matrix of the particle [307, 308] or in the core during synthesis as a rattle-type particle [309, 310]. This could have multiple potential benefits: it would add negative proton MRI contrast to the system; it could add an extra check of the cell quantification by comparison with the fluorine quantification result; it would demonstrate that the core was co-localised with the shell itself; it could also enable magnetic purification of the shells.

To conclude, the main challenge in this work is the low sensitivity of MRI, especially of fluorine MRI, which may require a technological breakthrough rather than a chemical solution to make clinical translatability feasible. This work however has systematically investigated several ways to label immune cells using nanotechnology, and has explored novel formulations and structures for imaging by multiple modalities. The combination of the different approaches, *i.e.* trapping in the matrix, binding to the surface, and using the core of the particle, allows a varied design to accommodate the different agents' needs, which is crucial for building an effective system. A proof-of-concept system has been presented here, which lays important ground work for developing an innovative multi-modal system for immune cell tracking.

Appendices

APPENDIX A

FLOW CYTOMETRY OF IRGDAUNPS IN PBMCS

This appendix illustrates the flow cytometry of IrGdAuNP-treated PBMCs. No signal was detected, though the limited iridium luminescence around 405nm could be an important factor in this. The data is included here for completeness.

The forward scatter and side scatter plots of the cells are shown in figure A.1.

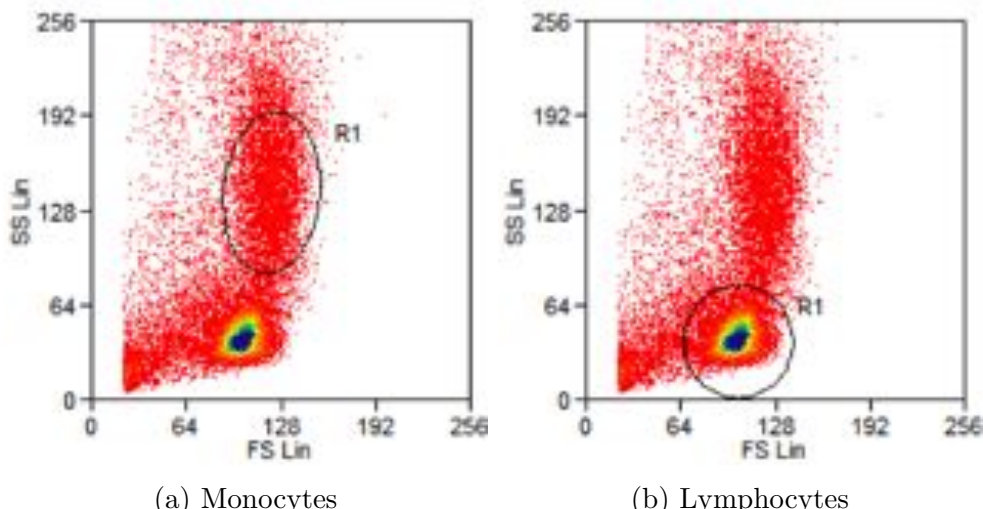


Figure A.1: Forward scatter vs. side scatter plots of PBMCs labelled with IrGdAuNPs. The overlaid ellipses mark the gates used to define the monocyte and lymphocyte clouds respectively.

There is no clear trend in this data. A significant point to note is that the count of labelled lymphocytes appears to be high for the treated cells, suggesting some of the cells are labelled. This is probably due to a misplaced fluorescence gate however, as supported by the lack of change in the median channel fluorescence.

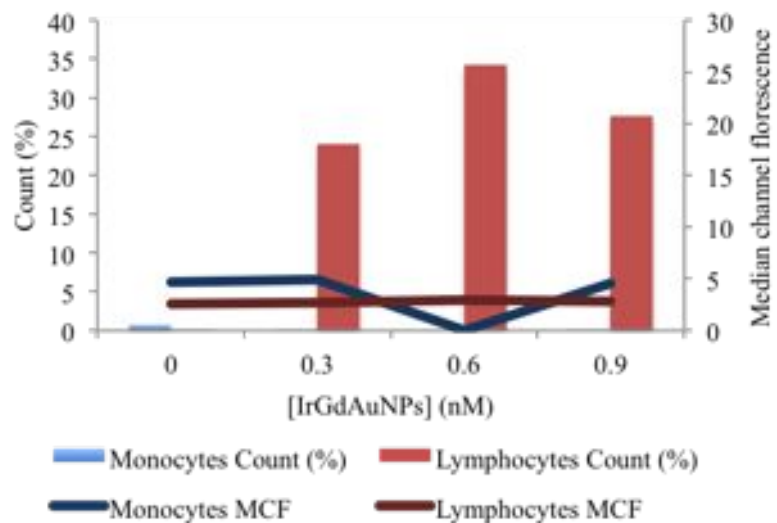


Figure A.2: The percentage of cells with increased fluorescence (the percentage of the cell count), and the median channel fluorescence (arbitrary scale) of the cells within the fluorescence gate, if any.

APPENDIX B

CHARACTERISATION DATA FOR SYNTHESISED MOLECULES

This appendix contains the nuclear magnetic resonance spectroscopy (NMR), electrospray ionisation mass spectrometry (ESI-MS) and Fourier transform infrared spectroscopy (FT-IR) spectra which were summarised in the relevant experimental sections.

B.1 Diethylenetriamine tetraacetic acid 3-amidopropyl triethoxysilane

B.1.1 NMR

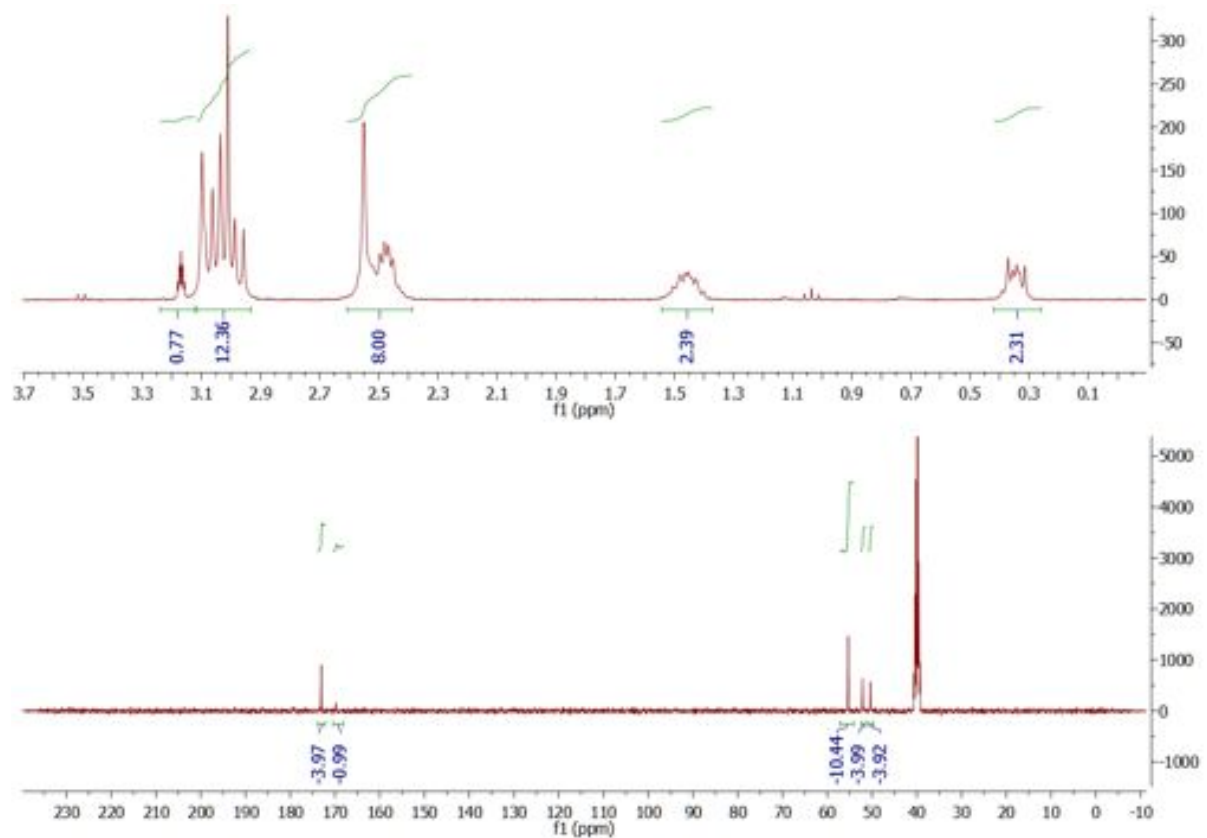


Figure B.1: ^1H (top) and ^{13}C (bottom) NMR spectra of APTES-DTPA.

B.1.2 ESI-MS

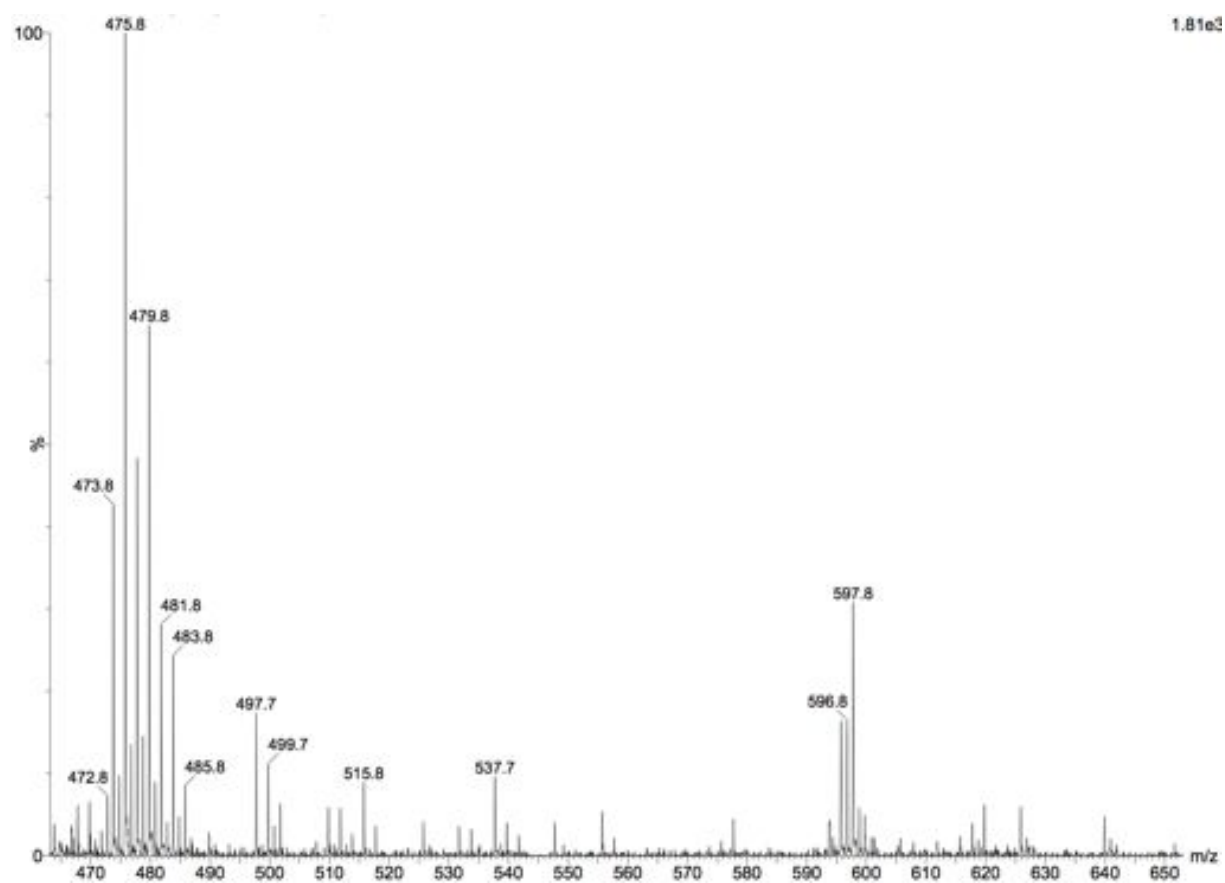


Figure B.2: ESI-MS spectrum of APTES-DTPA.

B.1.3 FT-IR

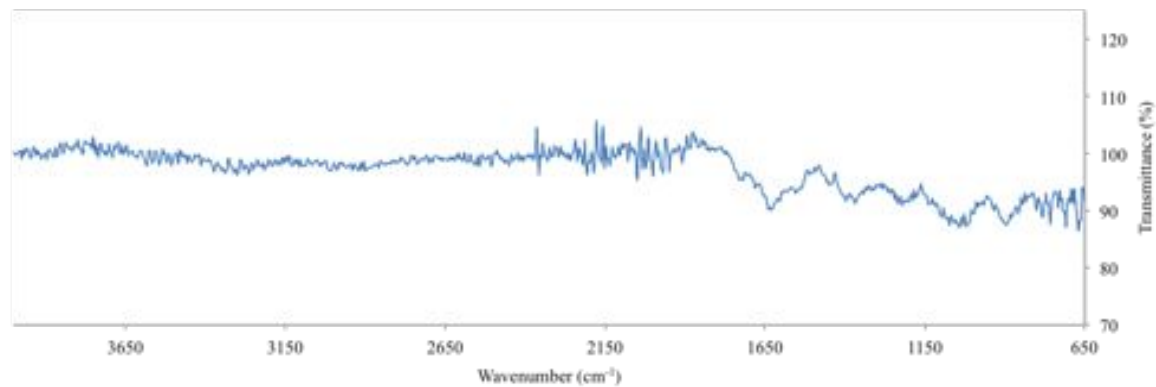


Figure B.3: FT-IR spectra of APTES-DTPA.

LIST OF REFERENCES

- [1] D. M. Clifford, S. A. Fisher, S. J. Brunskill, C. Doree, A. Mathur, S. Watt, and E. Martin-Rendon, “Stem cell treatment for acute myocardial infarction,” in *Cochrane Database of Systematic Reviews*, 1996.
- [2] K. Palucka and J. Banchereau, “Cancer immunotherapy via dendritic cells,” *Nature Reviews Cancer*, vol. 12, pp. 265–277, Apr. 2012.
- [3] C. C. Gross and H. Wiendl, “Dendritic cell vaccination in autoimmune disease:,” *Current Opinion in Rheumatology*, vol. 25, pp. 268–274, Mar. 2013.
- [4] S. C. Knight, R. Hunt, C. Dore, and P. B. Medawar, “Influence of dendritic cells on tumor growth,” *Proceedings of the National Academy of Sciences*, vol. 82, pp. 4495–4497, July 1985.
- [5] F. O. Nestle, S. Alijagic, M. Gilliet, Y. Sun, S. Grabbe, R. Dummer, G. Burg, and D. Schadendorf, “Vaccination of melanoma patients with peptide- or tumorlysate-pulsed dendritic cells,” *Nature Medicine*, vol. 4, pp. 328–332, Mar. 1998.
- [6] L. Fong and E. G. Engleman, “Dendritic cells in cancer immunotherapy,” *Annual Review of Immunology*, vol. 18, no. 1, pp. 245–273, 2000.
- [7] M. F. Kircher, S. S. Gambhir, and J. Grimm, “Noninvasive cell-tracking methods,” *Nature Reviews Clinical Oncology*, vol. 8, pp. 677–688, Nov. 2011.
- [8] V. Mailänder and K. Landfester, “Interaction of Nanoparticles with Cells,” *Biomacromolecules*, vol. 10, no. 9, pp. 2379–2400, 2009.
- [9] A. Verma and F. Stellacci, “Effect of Surface Properties on Nanoparticle–Cell Interactions,” *Small*, vol. 6, no. 1, pp. 12–21, 2010.

- [10] A. Albanese, P. S. Tang, and W. C. Chan, “The Effect of Nanoparticle Size, Shape, and Surface Chemistry on Biological Systems,” *Annual Review of Biomedical Engineering*, vol. 14, no. 1, pp. 1–16, 2012.
- [11] M. Srinivas, P. A. Morel, L. A. Ernst, D. H. Laidlaw, and E. T. Ahrens, “Fluorine-19 MRI for visualization and quantification of cell migration in a diabetes model,” *Magnetic Resonance in Medicine*, vol. 58, no. 4, pp. 725–734, 2007.
- [12] J. M. Janjic, M. Srinivas, D. K. K. Kadakkara, and E. T. Ahrens, “Self-delivering nanoemulsions for dual fluorine-19 MRI and fluorescence detection,” *Journal of the American Chemical Society*, vol. 130, no. 9, pp. 2832–2841, 2008.
- [13] P. Boehm-Sturm, M. Aswendt, A. Minassian, S. Michalk, L. Mengler, J. Adamczak, L. Mezzanotte, C. Löwik, and M. Hoehn, “A multi-modality platform to image stem cell graft survival in the naïve and stroke-damaged mouse brain,” *Biomaterials*, vol. 35, pp. 2218–2226, Feb. 2014.
- [14] C. Jacoby, S. Temme, F. Mayenfels, N. Benoit, M. P. Krafft, R. Schubert, J. Schrader, and U. Flögel, “Probing different perfluorocarbons for in vivo inflammation imaging by 19f MRI: image reconstruction, biological half-lives and sensitivity,” *NMR in Biomedicine*, vol. 27, no. 3, pp. 261–271, 2014.
- [15] J. D. Christensen, D. A. Yurgelun-Todd, S. M. Babb, S. A. Gruber, B. M. Cohen, and P. F. Renshaw, “Measurement of human brain dextroamphetamine concentration by 19f magnetic resonance spectroscopy,” *Brain Research*, vol. 834, pp. 1–5, July 1999.
- [16] S. Langereis, J. Keupp, J. L. J. van Velthoven, I. H. C. de Roos, D. Burdinski, J. A. Pikkemaat, and H. Grüll, “A Temperature-Sensitive Liposomal 1h CEST and 19f Contrast Agent for MR Image-Guided Drug Delivery,” *Journal of the American Chemical Society*, vol. 131, pp. 1380–1381, Feb. 2009.
- [17] K. C. Partlow, J. Chen, J. A. Brant, A. M. Neubauer, T. E. Meyerrose, M. H. Creer, J. A. Nolta, S. D. Caruthers, G. M. Lanza, and S. A. Wickline, “19f magnetic resonance imaging for stem/progenitor cell tracking with multiple unique perfluorocarbon nanobeacons,” *The FASEB Journal*, vol. 21, pp. 1647–1654, June 2007.
- [18] F. Aversa, A. Tabilio, A. Velardi, I. Cunningham, A. Terenzi, F. Falzetti, L. Ruggeri, G. Barbabietola, C. Aristei, P. Latini, Y. Reisner, M. F. Martelli, R. Felicini, F. Falconi, A. Carotti, K. Perruccio, S. Ballanti, A. Santucci, and C. Gambelunghe, “Treatment of High-Risk Acute Leukemia with T-Cell–Depleted Stem Cells from

Related Donors with One Fully Mismatched HLA Haplotype," *New England Journal of Medicine*, vol. 339, pp. 1186–1193, Oct. 1998.

- [19] R. H. Buckley, S. E. Schiff, R. I. Schiff, M. L. Markert, L. W. Williams, J. L. Roberts, L. A. Myers, and F. E. Ward, "Hematopoietic Stem-Cell Transplantation for the Treatment of Severe Combined Immunodeficiency," *New England Journal of Medicine*, vol. 340, pp. 508–516, Feb. 1999.
- [20] R. R. Jenq and M. R. M. van den Brink, "Allogeneic haematopoietic stem cell transplantation: individualized stem cell and immune therapy of cancer," *Nature Reviews Cancer*, vol. 10, pp. 213–221, Mar. 2010.
- [21] J. Ankrum and J. M. Karp, "Mesenchymal stem cell therapy: Two steps forward, one step back," *Trends in Molecular Medicine*, vol. 16, pp. 203–209, May 2010.
- [22] C. Lo Celso, H. E. Fleming, J. W. Wu, C. X. Zhao, S. Miake-Lye, J. Fujisaki, D. Côté, D. W. Rowe, C. P. Lin, and D. T. Scadden, "Live-animal tracking of individual haematopoietic stem/progenitor cells in their niche," *Nature*, vol. 457, pp. 92–96, Jan. 2009.
- [23] S. Méndez-Ferrer, T. V. Michurina, F. Ferraro, A. R. Mazloom, B. D. MacArthur, S. A. Lira, D. T. Scadden, A. Ma'ayan, G. N. Enikolopov, and P. S. Frenette, "Mesenchymal and haematopoietic stem cells form a unique bone marrow niche," *Nature*, vol. 466, pp. 829–834, Aug. 2010.
- [24] C. E. Murry, M. H. Soonpaa, H. Reinecke, H. Nakajima, H. O. Nakajima, M. Rubart, K. B. S. Pasumarthi, J. Ismail Virag, S. H. Bartelmez, V. Poppa, G. Bradford, J. D. Dowell, D. A. Williams, and L. J. Field, "Haematopoietic stem cells do not transdifferentiate into cardiac myocytes in myocardial infarcts," *Nature*, vol. 428, pp. 664–668, Apr. 2004.
- [25] M. H. Vandsburger, M. Radoul, B. Cohen, and M. Neeman, "MRI reporter genes: applications for imaging of cell survival, proliferation, migration and differentiation," *NMR in Biomedicine*, vol. 26, pp. 872–884, July 2013.
- [26] S. C. Berman, C. Galpoththawela, A. A. Gilad, J. W. M. Bulte, and P. Walczak, "Long-term MR cell tracking of neural stem cells grafted in immunocompetent versus immunodeficient mice reveals distinct differences in contrast between live and dead cells," *Magnetic Resonance in Medicine*, vol. 65, pp. 564–574, Feb. 2011.

- [27] J. Banchereau and R. M. Steinman, “Dendritic cells and the control of immunity,” *Nature*, vol. 392, pp. 245–252, Mar. 1998.
- [28] B. Thurner, I. Haendle, C. Röder, D. Dieckmann, P. Keikavoussi, H. Jonuleit, A. Bender, C. Maczek, D. Schreiner, P. v. d. Driesch, E. B. Bröcker, R. M. Steinman, A. Enk, E. Kämpgen, and G. Schuler, “Vaccination with Mage-3a1 Peptide–Pulsed Mature, Monocyte-Derived Dendritic Cells Expands Specific Cytotoxic T Cells and Induces Regression of Some Metastases in Advanced Stage IV Melanoma,” *The Journal of Experimental Medicine*, vol. 190, pp. 1669–1678, Dec. 1999.
- [29] K. Palucka and J. Banchereau, “Dendritic-cell-based therapeutic cancer vaccines,” *Immunity*, vol. 39, pp. 38–48, July 2013.
- [30] L. J. Zhou and T. F. Tedder, “CD14+ blood monocytes can differentiate into functionally mature CD83+ dendritic cells,” *Proceedings of the National Academy of Sciences*, vol. 93, pp. 2588–2592, Mar. 1996.
- [31] B. León, M. López-Bravo, and C. Ardavín, “Monocyte-derived dendritic cells,” *Seminars in Immunology*, vol. 17, pp. 313–318, Aug. 2005.
- [32] J. M. Timmerman, MD and R. Levy, MD, “Dendritic Cell Vaccines for Cancer Immunotherapy,” *Annual Review of Medicine*, vol. 50, no. 1, pp. 507–529, 1999.
- [33] J. F. Banchereau, M. Montes, A. K. Palucka, L. M. Sloan, and Y. Levy, “Dendritic Cell Vaccines,” July 2011. US20110182937 A1.
- [34] I. J. M. d. Vries, D. J. E. B. Krooshoop, N. M. Scharenborg, W. J. Lesterhuis, J. H. S. Diepstra, G. N. P. v. Muijen, S. P. Strijk, T. J. Ruers, O. C. Boerman, W. J. G. Oyen, G. J. Adema, C. J. A. Punt, and C. G. Figdor, “Effective Migration of Antigen-pulsed Dendritic Cells to Lymph Nodes in Melanoma Patients Is Determined by Their Maturation State,” *Cancer Research*, vol. 63, pp. 12–17, Jan. 2003.
- [35] D. A. Mitchell, K. A. Batich, M. D. Gunn, M.-N. Huang, L. Sanchez-Perez, S. K. Nair, K. L. Congdon, E. A. Reap, G. E. Archer, A. Desjardins, *et al.*, “Tetanus toxoid and ccl3 improve dendritic cell vaccines in mice and glioblastoma patients,” *Nature*, vol. 519, no. 7543, pp. 366–369, 2015.
- [36] J. Tel, E. H. J. G. Aarntzen, T. Baba, G. Schreibelt, B. M. Schulte, D. Benitez-Ribas, O. C. Boerman, S. Croockewit, W. J. G. Oyen, M. v. Rossum, G. Winkels,

- P. G. Coulie, C. J. A. Punt, C. G. Figdor, and I. J. M. d. Vries, “Natural Human Plasmacytoid Dendritic Cells Induce Antigen-Specific T-Cell Responses in Melanoma Patients,” *Cancer Research*, vol. 73, pp. 1063–1075, Feb. 2013.
- [37] A. Vasaturo, M. Verdoes, J. de Vries, R. Torensma, and C. G. Figdor, “Restoring immunosurveillance by dendritic cell vaccines and manipulation of the tumor microenvironment,” *Immunobiology*, vol. 220, pp. 243–248, Feb. 2015.
- [38] A. B. van der Waart, H. Fredrix, R. van der Voort, N. Schaap, W. Hobo, and H. Dolstra, “sirna silencing of pd-1 ligands on dendritic cell vaccines boosts the expansion of minor histocompatibility antigen-specific cd8+ t cells in nod/scid/il2rg (null) mice,” *Cancer Immunology, Immunotherapy*, pp. 1–10, 2015.
- [39] L. A. Johnson, R. A. Morgan, M. E. Dudley, L. Cassard, J. C. Yang, M. S. Hughes, U. S. Kammula, R. E. Royal, R. M. Sherry, J. R. Wunderlich, C.-C. R. Lee, N. P. Restifo, S. L. Schwarz, A. P. Cogdill, R. J. Bishop, H. Kim, C. C. Brewer, S. F. Rudy, C. VanWaes, J. L. Davis, A. Mathur, R. T. Ripley, D. A. Nathan, C. M. Laurencot, and S. A. Rosenberg, “Gene therapy with human and mouse T-cell receptors mediates cancer regression and targets normal tissues expressing cognate antigen,” *Blood*, vol. 114, pp. 535–546, July 2009.
- [40] T. N. M. Schumacher, “T-cell-receptor gene therapy,” *Nature Reviews Immunology*, vol. 2, pp. 512–519, July 2002.
- [41] C. H. June, “Adoptive T cell therapy for cancer in the clinic,” *Journal of Clinical Investigation*, vol. 117, pp. 1466–1476, June 2007.
- [42] M. A. Pulè, K. C. Straathof, G. Dotti, H. E. Heslop, C. M. Rooney, and M. K. Brenner, “A Chimeric T Cell Antigen Receptor that Augments Cytokine Release and Supports Clonal Expansion of Primary Human T Cells,” *Molecular Therapy*, vol. 12, pp. 933–941, Nov. 2005.
- [43] M. V. Maus, A. K. Thomas, D. G. B. Leonard, D. Allman, K. Addya, K. Schlienger, J. L. Riley, and C. H. June, “Ex vivo expansion of polyclonal and antigen-specific cytotoxic T lymphocytes by artificial APCs expressing ligands for the T-cell receptor, CD28 and 4-1bb,” *Nature Biotechnology*, vol. 20, pp. 143–148, Feb. 2002.
- [44] J. A. Bluestone, “Regulatory T-cell therapy: is it ready for the clinic?,” *Nature Reviews Immunology*, vol. 5, pp. 343–349, Apr. 2005.

- [45] M. H. Kershaw, J. A. Westwood, L. L. Parker, G. Wang, Z. Eshhar, S. A. Mavroukakis, D. E. White, J. R. Wunderlich, S. Canevari, L. Rogers-Freezer, C. C. Chen, J. C. Yang, S. A. Rosenberg, and P. Hwu, “A Phase I Study on Adoptive Immunotherapy Using Gene-Modified T Cells for Ovarian Cancer,” *Clinical Cancer Research*, vol. 12, pp. 6106–6115, Oct. 2006.
- [46] J. Kuyama, A. McCormack, A. J. T. George, B. T. Heelan, S. Osman, J. R. Batchelor, and A. M. Peters, “Indium-111 labelled lymphocytes: isotope distribution and cell division,” *European Journal of Nuclear Medicine*, vol. 24, pp. 488–496, May 1997.
- [47] C. H. Dodd, H.-C. Hsu, W.-J. Chu, P. Yang, H.-G. Zhang, J. D. Mountz Jr., K. Zinn, J. Forder, L. Josephson, R. Weissleder, J. M. Mountz, and J. D. Mountz, “Normal T-cell response and in vivo magnetic resonance imaging of T cells loaded with HIV transactivator-peptide-derived superparamagnetic nanoparticles,” *Journal of Immunological Methods*, vol. 256, pp. 89–105, Oct. 2001.
- [48] G. Koehne, M. Doubrovin, E. Doubrovina, P. Zanzonico, H. F. Gallardo, A. Ivanova, J. Balatoni, J. Teruya-Feldstein, G. Heller, C. May, V. Ponomarev, S. Ruan, R. Finn, R. G. Blasberg, W. Bornmann, I. Riviere, M. Sadelain, R. J. O'Reilly, S. M. Larson, and J. G. Gelovani Tjuvajev, “Serial in vivo imaging of the targeted migration of human HSV-TK-transduced antigen-specific lymphocytes,” *Nature Biotechnology*, vol. 21, pp. 405–413, Apr. 2003.
- [49] P. Dubey, H. Su, N. Adonai, S. Du, A. Rosato, J. Braun, S. S. Gambhir, and O. N. Witte, “Quantitative imaging of the T cell antitumor response by positron-emission tomography,” *Proceedings of the National Academy of Sciences*, vol. 100, pp. 1232–1237, Feb. 2003.
- [50] A. J. Korman, K. S. Peggs, and J. P. Allison, “Checkpoint Blockade in Cancer Immunotherapy,” in *Advances in Immunology* (G. D. James P. Allison, and Frederick W. Alt, ed.), vol. 90 of *Cancer Immunotherapy*, pp. 297–339, Academic Press, 2006.
- [51] Y. Iwai, M. Ishida, Y. Tanaka, T. Okazaki, T. Honjo, and N. Minato, “Involvement of PD-L1 on tumor cells in the escape from host immune system and tumor immunotherapy by PD-L1 blockade,” *Proceedings of the National Academy of Sciences*, vol. 99, pp. 12293–12297, Sept. 2002.
- [52] D. M. Pardoll, “The blockade of immune checkpoints in cancer immunotherapy,” *Nature Reviews Cancer*, vol. 12, pp. 252–264, Apr. 2012.

- [53] D. Zamarin and M. A. Postow, “Immune checkpoint modulation: Rational design of combination strategies,” *Pharmacology and Therapeutics*, 2015.
- [54] S. Spranger and T. Gajewski, “Rational combinations of immunotherapeutics that target discrete pathways,” *Journal for ImmunoTherapy of Cancer*, vol. 1, p. 16, Sept. 2013.
- [55] I. J. M. de Vries, W. J. Lesterhuis, J. O. Barentsz, P. Verdijk, J. H. van Krieken, O. C. Boerman, W. J. G. Oyen, J. J. Bonenkamp, J. B. Boezeman, G. J. Adema, J. W. M. Bulte, T. W. J. Scheenen, C. J. A. Punt, A. Heerschap, and C. G. Figdor, “Magnetic resonance tracking of dendritic cells in melanoma patients for monitoring of cellular therapy,” *Nature Biotechnology*, vol. 23, pp. 1407–1413, Nov. 2005.
- [56] M. J. Pittet, J. Grimm, C. R. Berger, T. Tamura, G. Wojtkiewicz, M. Nahrendorf, P. Romero, F. K. Swirski, and R. Weissleder, “In vivo imaging of T cell delivery to tumors after adoptive transfer therapy,” *Proceedings of the National Academy of Sciences*, vol. 104, pp. 12457–12461, July 2007.
- [57] T.-C. Yeh, W. Zhang, S. T. Ildstad, and C. Ho, “In Vivo Dynamic MRI Tracking of Rat T-Cells Labeled with Superparamagnetic Iron-Oxide Particles,” *Magnetic Resonance in Medicine*, vol. 33, pp. 200–208, Feb. 1995.
- [58] H. Em, R. Rb, and E. Bl, “Subcellular localization of indium-111 in indium-111-labeled platelets.,” *The Journal of laboratory and clinical medicine*, vol. 97, pp. 577–582, Apr. 1981.
- [59] M. R. Puncher and P. J. Blower, “Frozen section microautoradiography in the study of radionuclide targeting: application to indium-111-oxine-labeled leukocytes,” *Journal of Nuclear Medicine*, vol. 36, pp. 499–505, Mar. 1995.
- [60] D. Blocklet, M. Toungouz, R. Kiss, M. Lambermont, T. Velu, D. Duriau, M. Goldman, and S. Goldman, “¹¹¹In-oxine and ⁹⁹mtc-HMPAO labelling of antigen-loaded dendritic cells: in vivo imaging and influence on motility and actin content,” *European Journal of Nuclear Medicine and Molecular Imaging*, vol. 30, pp. 440–447, Mar. 2003.
- [61] M. E. Roddie, A. M. Peters, H. J. Danpure, S. Osman, B. L. Henderson, J. P. Lavender, M. J. Carroll, R. D. Neirinckx, and J. D. Kelly, “Inflammation: imaging with ^{Tc-99m} HMPAO-labeled leukocytes.,” *Radiology*, vol. 166, pp. 767–772, Mar. 1988.

- [62] M. R. B. Puncher and P. J. Blower, “Autoradiography and density gradient separation of technetium-99m-Exametazime (HMPAO) labelled leucocytes reveals selectivity for eosinophils,” *European Journal of Nuclear Medicine*, vol. 21, pp. 1175–1182, Nov. 1994.
- [63] F. Demaimay, A. Roucoux, L. Dazord, N. Noiret, A. Moisan, and H. Patin, “Studies of technetium-99m nitridobisdithiocarboxylate leucocyte specific radiopharmaceutical: [99mtcn(DTCX)2], DTCX = CH₃(CH₂)₈cs₂. the cellular and subcellular distribution in human blood cells, and chemical behaviour. synthesis of the analogous rhenium-188 radiopharmaceutical,” *Nuclear Medicine and Biology*, vol. 26, pp. 225–231, Feb. 1999.
- [64] W. J. Kang, H.-J. Kang, H.-S. Kim, J.-K. Chung, M. C. Lee, and D. S. Lee, “Tissue Distribution of 18f-FDG-Labeled Peripheral Hematopoietic Stem Cells After Intracoronary Administration in Patients with Myocardial Infarction,” *Journal of Nuclear Medicine*, vol. 47, pp. 1295–1301, Aug. 2006.
- [65] B. Doyle, B. J. Kemp, P. Chareonthaitawee, C. Reed, J. Schmeckpeper, P. Sorajja, S. Russell, P. Araoz, S. J. Riederer, and N. M. Caplice, “Dynamic Tracking During Intracoronary Injection of 18f-FDG-Labeled Progenitor Cell Therapy for Acute Myocardial Infarction,” *Journal of Nuclear Medicine*, vol. 48, pp. 1708–1714, Oct. 2007.
- [66] D. L. Kraitchman, M. Tatsumi, W. D. Gilson, T. Ishimori, D. Kedziorek, P. Walczak, W. P. Segars, H. H. Chen, D. Fritzges, I. Izbudak, R. G. Young, M. Marcelino, M. F. Pittenger, M. Solaiyappan, R. C. Boston, B. M. W. Tsui, R. L. Wahl, and J. W. M. Bulte, “Dynamic Imaging of Allogeneic Mesenchymal Stem Cells Trafficking to Myocardial Infarction,” *Circulation*, vol. 112, pp. 1451–1461, Sept. 2005.
- [67] H. M. Prince, D. M. Wall, D. Ritchie, D. Honemann, S. Harrrison, H. Quach, M. Thompson, R. Hicks, E. Lau, J. Davison, M. Loudovaris, J. Moloney, B. Love-land, J. Bartholeyns, A. Katsifis, and L. Mileshtkin, “In vivo tracking of dendritic cells in patients with multiple myeloma:,” *Journal of Immunotherapy*, vol. 31, pp. 166–179, Feb. 2008.
- [68] W. Brenner, A. Aicher, T. Eckey, S. Massoudi, M. Zuhayra, U. Koehl, C. Heeschen, W. U. Kampen, A. M. Zeiher, S. Dimmeler, and E. Henze, “111in-Labeled CD34+ Hematopoietic Progenitor Cells in a Rat Myocardial Infarction Model,” *Journal of Nuclear Medicine*, vol. 45, pp. 512–518, Mar. 2004.
- [69] R. Bhorade, R. Weissleder, T. Nakakoshi, A. Moore, and C.-H. Tung, “Macrocyclic Chelators with Paramagnetic Cations Are Internalized into Mammalian Cells

via a HIV-Tat Derived Membrane Translocation Peptide,” *Bioconjugate Chemistry*, vol. 11, pp. 301–305, May 2000.

- [70] S. Heckl, J. Debus, J. Jenne, R. Pipkorn, W. Waldeck, H. Spring, R. Rastert, C. W. v. d. Lieth, and K. Braun, “CNN-Gd³⁺ Enables Cell Nucleus Molecular Imaging of Prostate Cancer Cells: The Last 600 nm,” *Cancer Research*, vol. 62, pp. 7018–7024, Dec. 2002.
- [71] D. L. J. Thorek, A. K. Chen, J. Czupryna, and A. Tsourkas, “Superparamagnetic Iron Oxide Nanoparticle Probes for Molecular Imaging,” *Annals of Biomedical Engineering*, vol. 34, pp. 23–38, Feb. 2006.
- [72] D. L. J. Thorek and A. Tsourkas, “Size, charge and concentration dependent uptake of iron oxide particles by non-phagocytic cells,” *Biomaterials*, vol. 29, pp. 3583–3590, Sept. 2008.
- [73] M. Mikhaylova, D. K. Kim, C. C. Berry, A. Zagorodni, M. Toprak, A. S. G. Curtis, and M. Muhammed, “Immobilization on Amine-Functionalized Superparamagnetic Iron Oxide Nanoparticles,” *Chemistry of Materials*, vol. 16, pp. 2344–2354, June 2004.
- [74] M. V. Yigit, D. Mazumdar, and Y. Lu, “Detection of Thrombin with Aptamer Functionalized Superparamagnetic Iron Oxide Nanoparticles,” *Bioconjugate Chemistry*, vol. 19, pp. 412–417, Feb. 2008.
- [75] E. V. Groman, J. C. Bouchard, C. P. Reinhardt, and D. E. Vaccaro, “Ultrasmall Mixed Ferrite Colloids as Multidimensional Magnetic Resonance Imaging, Cell Labeling, and Cell Sorting Agents,” *Bioconjugate Chemistry*, vol. 18, pp. 1763–1771, Nov. 2007.
- [76] F. Kratz, P. Senter, and H. Steinhagen, *Drug Delivery in Oncology: From Basic Research to Cancer Therapy, 3 Volume Set*. Sept. 2013.
- [77] H. E. Daldrup-Link, M. Rudelius, R. A. J. Oostendorp, M. Settles, G. Piontek, S. Metz, H. Rosenbrock, U. Keller, U. Heinzmann, E. J. Rummeny, J. Schlegel, and T. M. Link, “Targeting of Hematopoietic Progenitor Cells with MR Contrast Agents,” *Radiology*, vol. 228, pp. 760–767, Sept. 2003.
- [78] M. Lewin, N. Carlesso, C. H. Tung, X. W. Tang, D. Cory, D. T. Scadden, and R. Weissleder, “Tat peptide-derivatized magnetic nanoparticles allow in vivo track-

- ing and recovery of progenitor cells," *Nature Biotechnology*, vol. 18, pp. 410–414, Apr. 2000.
- [79] P. Smirnov, E. Lavergne, F. Gazeau, M. Lewin, A. Boissonnas, B.-T. Doan, B. Gillet, C. Combadière, B. Combadière, and O. Clément, "In vivo cellular imaging of lymphocyte trafficking by MRI: A tumor model approach to cell-based anticancer therapy," *Magnetic Resonance in Medicine*, vol. 56, pp. 498–508, Sept. 2006.
- [80] A. V. Naumova, H. Reinecke, V. Yarnykh, J. Deem, C. Yuan, and C. E. Murry, "Ferritin Overexpression for Noninvasive MRI-Based Tracking of Stem Cells Transplanted into the Heart," *Molecular imaging*, vol. 9, pp. 201–210, Aug. 2010.
- [81] A. E. Deans, Y. Z. Wadghiri, L. M. Bernas, X. Yu, B. K. Rutt, and D. H. Turnbull, "Cellular MRI contrast via coexpression of transferrin receptor and ferritin," *Magnetic Resonance in Medicine*, vol. 56, pp. 51–59, July 2006.
- [82] G. Genove, U. DeMarco, H. Xu, W. F. Goins, and E. T. Ahrens, "A new transgene reporter for in vivo magnetic resonance imaging," *Nature Medicine*, vol. 11, pp. 450–454, Apr. 2005.
- [83] M. Campan, V. Lionetti, G. D. Aquaro, F. Forini, M. Matteucci, L. Vannucci, F. Chiuppesi, C. D. Cristofano, M. Faggioni, M. Maioli, L. Barile, E. Messina, M. Lombardi, A. Pucci, M. Pistello, and F. A. Recchia, "Ferritin as a reporter gene for in vivo tracking of stem cells by 1.5-T cardiac MRI in a rat model of myocardial infarction," *American Journal of Physiology - Heart and Circulatory Physiology*, vol. 300, pp. H2238–H2250, June 2011.
- [84] J. Liu, E. C. Cheng, R. C. Long, S.-H. Yang, L. Wang, P.-H. Cheng, J. Yang, D. Wu, H. Mao, and A. W. Chan, "Noninvasive Monitoring of Embryonic Stem Cells In Vivo with MRI Transgene Reporter," *Tissue Engineering Part C: Methods*, vol. 15, pp. 739–747, Mar. 2009.
- [85] A. V. Naumova, N. Balu, V. L. Yarnykh, H. Reinecke, C. E. Murry, and C. Yuan, "Magnetic Resonance Imaging Tracking of Graft Survival in the Infarcted Heart Iron Oxide Particles Versus Ferritin Overexpression Approach," *Journal of Cardiovascular Pharmacology and Therapeutics*, vol. 19, pp. 358–367, July 2014.
- [86] H. S. Kim, J. Woo, J. H. Lee, H. J. Joo, Y. Choi, H. Kim, W. K. Moon, and S. J. Kim, "In vivo Tracking of Dendritic Cell using MRI Reporter Gene, Ferritin," *PloS One*, vol. 10, no. 5, p. e0125291, 2015.

- [87] G. Santyr, M. Fox, K. Thind, E. Hegarty, A. Ouriadov, M. Jensen, T. J. Scholl, J. Van Dyk, and E. Wong, “Anatomical, functional and metabolic imaging of radiation-induced lung injury using hyperpolarized MRI,” *NMR in Biomedicine*, vol. 27, pp. 1515–1524, Dec. 2014.
- [88] S. Klippel, J. Döpfert, J. Jayapaul, M. Kunth, F. Rossella, M. Schnurr, C. Witte, C. Freund, and L. Schröder, “Cell Tracking with Caged Xenon: Using Cryptophanes as MRI Reporters upon Cellular Internalization,” *Angewandte Chemie*, vol. 126, pp. 503–506, Jan. 2014.
- [89] T. Jonischkeit, U. Bommerich, J. Stadler, K. Woelk, H. G. Niessen, and J. Bargon, “Generating long-lasting H₁ and C₁₃ hyperpolarization in small molecules with parahydrogen-induced polarization,” *The Journal of Chemical Physics*, vol. 124, p. 201109, May 2006.
- [90] E. Rej, T. Gaebel, T. Boele, D. E. J. Waddington, and D. J. Reilly, “Hyperpolarized Nanodiamond with Long Spin Relaxation Times,” *arXiv preprint arXiv:1502.06214*, Feb. 2015.
- [91] A. Viale and S. Aime, “Current concepts on hyperpolarized molecules in MRI,” *Current Opinion in Chemical Biology*, vol. 14, pp. 90–96, Feb. 2010.
- [92] M. T. McMahon, A. A. Gilad, M. A. DeLiso, S. M. Cromer Berman, J. W. Bulte, and P. C. van Zijl, “New “multicolor” polypeptide diamagnetic chemical exchange saturation transfer (DIACEST) contrast agents for MRI,” *Magnetic Resonance in Medicine*, vol. 60, pp. 803–812, Oct. 2008.
- [93] A. A. Gilad, M. T. McMahon, P. Walczak, P. T. Winnard, V. Raman, H. W. M. van Laarhoven, C. M. Skoglund, J. W. M. Bulte, and P. C. M. van Zijl, “Artificial reporter gene providing MRI contrast based on proton exchange,” *Nature Biotechnology*, vol. 25, pp. 217–219, Feb. 2007.
- [94] S. Zhang, M. Merritt, D. E. Woessner, R. E. Lenkinski, and A. D. Sherry, “PARACEST Agents: Modulating MRI Contrast via Water Proton Exchange,” *Accounts of Chemical Research*, vol. 36, pp. 783–790, Oct. 2003.
- [95] E. Terreno, D. D. Castelli, and S. Aime, “Encoding the frequency dependence in MRI contrast media: the emerging class of CEST agents,” *Contrast Media and Molecular Imaging*, vol. 5, pp. 78–98, Mar. 2010.

- [96] S. Aime, C. Carrera, D. Delli Castelli, S. Geninatti Crich, and E. Terreno, “Tunable Imaging of Cells Labeled with MRI-PARACEST Agents,” *Angewandte Chemie International Edition*, vol. 44, pp. 1813–1815, Mar. 2005.
- [97] G. Ferrauto, D. D. Castelli, E. Terreno, and S. Aime, “In vivo MRI visualization of different cell populations labeled with PARACEST agents,” *Magnetic Resonance in Medicine*, vol. 69, pp. 1703–1711, June 2013.
- [98] J. V. Frangioni and R. J. Hajjar, “In Vivo Tracking of Stem Cells for Clinical Trials in Cardiovascular Disease,” *Circulation*, vol. 110, pp. 3378–3383, Nov. 2004.
- [99] J. W. M. Bulte, “In Vivo MRI Cell Tracking: Clinical Studies,” *AJR. American journal of roentgenology*, vol. 193, pp. 314–325, Aug. 2009.
- [100] I. Veilleux, J. Spencer, D. Biss, D. Côté, and C. Lin, “In Vivo Cell Tracking With Video Rate Multimodality Laser Scanning Microscopy,” *IEEE Journal of Selected Topics in Quantum Electronics*, vol. 14, pp. 10–18, Jan. 2008.
- [101] N. A. Christian, F. Benencia, M. C. Milone, G. Li, P. R. Frail, M. J. Therien, G. Coukos, and D. A. Hammer, “In Vivo Dendritic Cell Tracking Using Fluorescence Lifetime Imaging and Near-Infrared-Emissive Polymersomes,” *Molecular Imaging and Biology*, vol. 11, pp. 167–177, Feb. 2009.
- [102] X. Michalet, F. F. Pinaud, L. A. Bentolila, J. M. Tsay, S. Doose, J. J. Li, G. Sundaresan, A. M. Wu, S. S. Gambhir, and S. Weiss, “Quantum Dots for Live Cells, in Vivo Imaging, and Diagnostics,” *Science*, vol. 307, pp. 538–544, Jan. 2005.
- [103] Y. Lei, H. Tang, L. Yao, R. Yu, M. Feng, and B. Zou, “Applications of Mesenchymal Stem Cells Labeled with Tat Peptide Conjugated Quantum Dots to Cell Tracking in Mouse Body,” *Bioconjugate Chemistry*, vol. 19, pp. 421–427, Feb. 2008.
- [104] A.-K. Hadjantonakis and V. E. Papaioannou, “Dynamic in vivo imaging and cell tracking using a histone fluorescent protein fusion in mice,” *BMC Biotechnology*, vol. 4, p. 33, Dec. 2004.
- [105] Y. Tang, K. Shah, S. M. Messerli, E. Snyder, X. Breakefield, and R. Weissleder, “In Vivo Tracking of Neural Progenitor Cell Migration to Glioblastomas,” *Human Gene Therapy*, vol. 14, pp. 1247–1254, Sept. 2003.

- [106] A. M. Derfus, W. C. W. Chan, and S. N. Bhatia, “Intracellular Delivery of Quantum Dots for Live Cell Labeling and Organelle Tracking,” *Advanced Materials*, vol. 16, pp. 961–966, June 2004.
- [107] V. Ntziachristos, C. Bremer, and R. Weissleder, “Fluorescence imaging with near-infrared light: new technological advances that enable *in vivo* molecular imaging,” *European Radiology*, vol. 13, pp. 195–208, Jan. 2003.
- [108] M. Oheim, E. Beaurepaire, E. Chaigneau, J. Mertz, and S. Charpak, “Two-photon microscopy in brain tissue: parameters influencing the imaging depth,” *Journal of Neuroscience Methods*, vol. 111, Oct. 2001.
- [109] D. Kobat, N. G. Horton, and C. Xu, “*In vivo* two-photon microscopy to 1.6-mm depth in mouse cortex,” *Journal of Biomedical Optics*, vol. 16, no. 10, pp. 106014–106014–4, 2011.
- [110] J. Ruiz-Cabello, B. P. Barnett, P. A. Bottomley, and J. W. Bulte, “Fluorine (19f) MRS and MRI in biomedicine,” *NMR in Biomedicine*, vol. 24, no. 2, pp. 114–129, 2011.
- [111] W. S. Hinshaw and A. H. Lent, “An introduction to NMR imaging: From the Bloch equation to the imaging equation,” *Proceedings of the IEEE*, vol. 71, pp. 338–350, Mar. 1983.
- [112] M. M. Martin and L. Lindqvist, “The pH dependence of fluorescein fluorescence,” *Journal of Luminescence*, vol. 10, pp. 381–390, July 1975.
- [113] W.-C. Sun, K. R. Gee, D. H. Klaubert, and R. P. Haugland, “Synthesis of Fluorinated Fluoresceins,” *The Journal of Organic Chemistry*, vol. 62, pp. 6469–6475, Sept. 1997.
- [114] E. C. Butcher, R. G. Scollay, and I. L. Weissman, “Direct fluorescent labeling of cells with fluorescein or rhodamine isothiocyanate. II. Potential application to studies of lymphocyte migration and maturation,” *Journal of Immunological Methods*, vol. 37, pp. 109–121, Oct. 1980.
- [115] C. R. Parish, “Fluorescent dyes for lymphocyte migration and proliferation studies,” *Immunology and Cell Biology*, vol. 77, pp. 499–508, Dec. 1999.

- [116] A. B. Lyons and C. R. Parish, “Determination of lymphocyte division by flow cytometry,” *Journal of Immunological Methods*, vol. 171, pp. 131–137, May 1994.
- [117] P. Hossain, J. Liversidge, M. J. Cree, A. Manivannan, P. Vieira, P. F. Sharp, G. C. Brown, and J. V. Forrester, “In vivo cell tracking by scanning laser ophthalmoscopy: quantification of leukocyte kinetics.,” *Investigative Ophthalmology and Visual Science*, vol. 39, pp. 1879–1887, Sept. 1998.
- [118] S. A. Weston and C. R. Parish, “New fluorescent dyes for lymphocyte migration studies: Analysis by flow cytometry and fluorescence microscopy,” *Journal of Immunological Methods*, vol. 133, pp. 87–97, Oct. 1990.
- [119] J. R. S. Hoult and M. Payá, “Pharmacological and biochemical actions of simple coumarins: Natural products with therapeutic potential,” *General Pharmacology: The Vascular System*, vol. 27, pp. 713–722, June 1996.
- [120] V. Gurtu, S. R. Kain, and G. Zhang, “Fluorometric and Colorimetric Detection of Caspase Activity Associated with Apoptosis,” *Analytical Biochemistry*, vol. 251, pp. 98–102, Aug. 1997.
- [121] K. K.-W. Lo, A. W.-T. Choi, and W. H.-T. Law, “Applications of luminescent inorganic and organometallic transition metal complexes as biomolecular and cellular probes,” *Dalton Transactions*, vol. 41, no. 20, p. 6021, 2012.
- [122] J. K. Barton, A. Danishefsky, and J. Goldberg, “Tris(phenanthroline)ruthenium(II): stereoselectivity in binding to DNA,” *Journal of the American Chemical Society*, vol. 106, no. 7, pp. 2172–2176, 1984.
- [123] S. Satyanarayana, J. C. Dabrowiak, and J. B. Chaires, “Neither .DELTA.- nor .LAMBDA.-tris(phenanthroline)ruthenium(II) binds to DNA by classical intercalation,” *Biochemistry*, vol. 31, pp. 9319–9324, Oct. 1992.
- [124] A. Shulman, G. M. Laycock, and T. R. Bradley, “Action of 1,10-phenanthroline transition metal chelates on P388 mouse lymphocytic leukaemic cells,” *Chemico-Biological Interactions*, vol. 16, pp. 89–99, Jan. 1977.
- [125] F. R. Svensson, M. Abrahamsson, N. Strömberg, A. G. Ewing, and P. Lincoln, “Ruthenium(II) Complex Enantiomers as Cellular Probes for Diastereomeric Interactions in Confocal and Fluorescence Lifetime Imaging Microscopy,” *The Journal of Physical Chemistry Letters*, vol. 2, pp. 397–401, Mar. 2011.

- [126] J. D. Slinker, A. A. Gorodetsky, M. S. Lowry, J. Wang, S. Parker, R. Rohl, S. Bernhard, and G. G. Malliaras, “Efficient Yellow Electroluminescence from a Single Layer of a Cyclometalated Iridium Complex,” *Journal of the American Chemical Society*, vol. 126, pp. 2763–2767, Mar. 2004.
- [127] Q. Zhao, M. Yu, L. Shi, S. Liu, C. Li, M. Shi, Z. Zhou, C. Huang, and F. Li, “Cationic Iridium(III) Complexes with Tunable Emission Color as Phosphorescent Dyes for Live Cell Imaging,” *Organometallics*, vol. 29, pp. 1085–1091, Mar. 2010.
- [128] K. K.-W. Lo, M.-W. Louie, and K. Y. Zhang, “Design of luminescent iridium(III) and rhenium(I) polypyridine complexes as *in vitro* and *in vivo* ion, molecular and biological probes,” *Coordination Chemistry Reviews*, vol. 254, pp. 2603–2622, Nov. 2010.
- [129] K. K.-W. Lo, S. P.-Y. Li, and K. Y. Zhang, “Development of luminescent iridium(III) polypyridine complexes as chemical and biological probes,” *New Journal of Chemistry*, vol. 35, pp. 265–287, Feb. 2011.
- [130] L. Xiong, Q. Zhao, H. Chen, Y. Wu, Z. Dong, Z. Zhou, and F. Li, “Phosphorescence Imaging of Homocysteine and Cysteine in Living Cells Based on a Cationic Iridium(III) Complex,” *Inorganic Chemistry*, vol. 49, pp. 6402–6408, July 2010.
- [131] C. Li, M. Yu, Y. Sun, Y. Wu, C. Huang, and F. Li, “A Nonemissive Iridium(III) Complex That Specifically Lights-Up the Nuclei of Living Cells,” *Journal of the American Chemical Society*, vol. 133, pp. 11231–11239, July 2011.
- [132] N. J. Rogers, *The development of gold nanoparticles labelled with transition metal complexes for imaging applications*. Ph.D., University of Birmingham, 2014.
- [133] M. R. Gill, J. Garcia-Lara, S. J. Foster, C. Smythe, G. Battaglia, and J. A. Thomas, “A ruthenium(II) polypyridyl complex for direct imaging of DNA structure in living cells,” *Nature Chemistry*, vol. 1, pp. 662–667, Nov. 2009.
- [134] C. A. Puckett and J. K. Barton, “Targeting a ruthenium complex to the nucleus with short peptides,” *Bioorganic and Medicinal Chemistry*, vol. 18, pp. 3564–3569, May 2010.
- [135] C. A. Puckett and J. K. Barton, “Mechanism of Cellular Uptake of a Ruthenium Polypyridyl Complex†,” *Biochemistry*, vol. 47, pp. 11711–11716, Nov. 2008.

- [136] C. A. Puckett, R. J. Ernst, and J. K. Barton, “Exploring the cellular accumulation of metal complexes,” *Dalton Transactions*, vol. 39, no. 5, pp. 1159–1170, 2010.
- [137] H.-J. Weinmann, G. Schuhmann-Giampieri, H. Schmitt-Willich, H. Vogler, T. Frenzel, and H. Gries, “A new lipophilic gadolinium chelate as a tissue-specific contrast medium for MRI,” *Magnetic Resonance in Medicine*, vol. 22, pp. 233–237, Dec. 1991.
- [138] H. S. Thomsen, S. K. Morcos, T. Almén, M.-F. Bellin, M. Bertolotto, G. Bongartz, O. Clement, P. Leander, G. Heinz-Peer, P. Reimer, *et al.*, “Nephrogenic systemic fibrosis and gadolinium-based contrast media: updated esur contrast medium safety committee guidelines,” *European radiology*, vol. 23, no. 2, pp. 307–318, 2013.
- [139] P. Caravan, J. J. Ellison, T. J. McMurry, and R. B. Lauffer, “Gadolinium(III) Chelates as MRI Contrast Agents: Structure, Dynamics, and Applications,” *Chemical Reviews*, vol. 99, pp. 2293–2352, Sept. 1999.
- [140] C. Cabella, S. G. Crich, D. Corpillo, A. Barge, C. Ghirelli, E. Bruno, V. Lorusso, F. Uggeri, and S. Aime, “Cellular labeling with Gd(III) chelates: only high thermodynamic stabilities prevent the cells acting as ‘sponges’ of Gd³⁺ ions,” *Contrast Media and Molecular Imaging*, vol. 1, pp. 23–29, Jan. 2006.
- [141] L. Biancone, S. G. Crich, V. Cantaluppi, G. M. Romanazzi, S. Russo, E. Scalabrino, G. Esposito, F. Figliolini, S. Beltramo, P. C. Perin, G. P. Segoloni, S. Aime, and G. Camussi, “Magnetic resonance imaging of gadolinium-labeled pancreatic islets for experimental transplantation,” *NMR in Biomedicine*, vol. 20, pp. 40–48, Feb. 2007.
- [142] M. Modo, D. Cash, K. Mellodew, S. C. R. Williams, S. E. Fraser, T. J. Meade, J. Price, and H. Hodges, “Tracking Transplanted Stem Cell Migration Using Bi-functional, Contrast Agent-Enhanced, Magnetic Resonance Imaging,” *NeuroImage*, vol. 17, pp. 803–811, Oct. 2002.
- [143] S. A. Anderson, K. K. Lee, and J. A. Frank, “Gadolinium-fullerenol as a paramagnetic contrast agent for cellular imaging,” *Investigative Radiology*, vol. 41, pp. 332–338, Mar. 2006.
- [144] J. Bernardou, R. Martino, M. C. Malet-Martino, A. Lopez, and J. P. Armand, “Fluorine-19 NMR: a technique for metabolism and disposition studies of fluorinated drugs,” *Trends in Pharmacological Sciences*, vol. 6, pp. 103–105, 1985.

- [145] J. G. Riess and M. Le Blanc, “Perfluoro Compounds as Blood Substitutes,” *Angewandte Chemie International Edition in English*, vol. 17, pp. 621–634, Sept. 1978.
- [146] R. Díaz-López, N. Tsapis, and E. Fattal, “Liquid Perfluorocarbons as Contrast Agents for Ultrasonography and 19f-MRI,” *Pharmaceutical Research*, vol. 27, pp. 1–16, Nov. 2009.
- [147] M. Srinivas, L. J. Cruz, F. Bonetto, A. Heerschap, C. G. Figdor, and I. J. M. de Vries, “Customizable, multi-functional fluorocarbon nanoparticles for quantitative in vivo imaging using 19f MRI and optical imaging,” *Biomaterials*, vol. 31, pp. 7070–7077, Sept. 2010.
- [148] H. W. Kim and A. G. Greenburg, “Artificial Oxygen Carriers as Red Blood Cell Substitutes: A Selected Review and Current Status,” *Artificial Organs*, vol. 28, pp. 813–828, Sept. 2004.
- [149] D. M. Freeman, H. H. Muller, R. E. Hurd, and S. W. Young, “Rapid 19f magnetic resonance imaging of perfluorooctyl bromide in vivo,” *Magnetic Resonance Imaging*, vol. 6, no. 1, pp. 61–64, 1988.
- [150] E. Pisani, N. Tsapis, B. Galaz, M. Santin, R. Berti, N. Taulier, E. Kurtisovski, O. Lucidarme, M. Ourevitch, B. T. Doan, J. C. Beloeil, B. Gillet, W. Urbach, S. L. Bridal, and E. Fattal, “Perfluorooctyl Bromide Polymeric Capsules as Dual Contrast Agents for Ultrasonography and Magnetic Resonance Imaging,” *Advanced Functional Materials*, vol. 18, pp. 2963–2971, Oct. 2008.
- [151] R. Mattrey, “Perfluorooctylbromide: a new contrast agent for CT, sonography, and MR imaging,” *American Journal of Roentgenology*, vol. 152, pp. 247–252, Feb. 1989.
- [152] D. K. Kadayakkara, K. Damodaran, T. K. Hitchens, J. W. M. Bulte, and E. T. Ahrens, “19f spin-lattice relaxation of perfluoropolyethers: Dependence on temperature and magnetic field strength (7.0-14.1 T),” *Journal of Magnetic Resonance*, vol. 242, pp. 18–22, May 2014.
- [153] F. Schweighardt and J. Rubertone, *Perfluoro-crown ethers in fluorine magnetic resonance imaging*. June 1989. US Patent 4,838,274.
- [154] Y. T. Lim, Y.-W. Noh, J.-N. Kwon, and B. H. Chung, “Multifunctional perfluorocarbon nanoemulsions for 19f-based magnetic resonance and near-infrared optical imaging of dendritic cells,” *Chemical Communications*, pp. 6952–6954, Nov. 2009.

- [155] I. Tirotta, A. Mastropietro, C. Cordigliani, L. Gazzera, F. Baggi, G. Baselli, M. G. Bruzzone, I. Zucca, G. Cavallo, G. Terraneo, F. Baldelli Bombelli, P. Metrangolo, and G. Resnati, “A Superfluorinated Molecular Probe for Highly Sensitive in Vivo¹⁹f-MRI,” *Journal of the American Chemical Society*, vol. 136, pp. 8524–8527, June 2014.
- [156] M. Srinivas, P. Boehm-Sturm, C. G. Figdor, I. J. de Vries, and M. Hoehn, “Labeling cells for in vivo tracking using ¹⁹f MRI,” *Biomaterials*, vol. 33, pp. 8830–8840, Dec. 2012.
- [157] B. P. Barnett, J. Ruiz-Cabello, P. Hota, R. Ouwerkerk, M. J. Shambrott, C. Lauzon, P. Walczak, W. D. Gilson, V. P. Chacko, D. L. Kraitchman, A. Arepally, and J. W. Bulte, “Use of perfluorocarbon nanoparticles for non-invasive multimodal cell tracking of human pancreatic islets,” *Contrast Media and Molecular Imaging*, vol. 6, pp. 251–259, July 2011.
- [158] A. S. Kabalnov and E. D. Shchukin, “Ostwald ripening theory: applications to fluorocarbon emulsion stability,” *Advances in Colloid and Interface Science*, vol. 38, pp. 69–97, Mar. 1992.
- [159] M. Geiser, B. Rothen-Rutishauser, N. Kapp, S. Schürch, W. Kreyling, H. Schulz, M. Semmler, V. I. Hof, J. Heyder, and P. Gehr, “Ultrafine Particles Cross Cellular Membranes by Nonphagocytic Mechanisms in Lungs and in Cultured Cells,” *Environmental Health Perspectives*, vol. 113, pp. 1555–1560, Nov. 2005.
- [160] B. M. Rothen-Rutishauser, S. Schürch, B. Haenni, N. Kapp, and P. Gehr, “Interaction of Fine Particles and Nanoparticles with Red Blood Cells Visualized with Advanced Microscopic Techniques†,” *Environmental Science and Technology*, vol. 40, pp. 4353–4359, July 2006.
- [161] T. Wang, J. Bai, X. Jiang, and G. U. Nienhaus, “Cellular Uptake of Nanoparticles by Membrane Penetration: A Study Combining Confocal Microscopy with FTIR Spectroelectrochemistry,” *ACS Nano*, vol. 6, pp. 1251–1259, Feb. 2012.
- [162] K. Unfried, C. Albrecht, L.-O. Klotz, A. Von Mikecz, S. Grether-Beck, and R. P. Schins, “Cellular responses to nanoparticles: Target structures and mechanisms,” *Nanotoxicology*, vol. 1, pp. 52–71, Jan. 2007.
- [163] W. Stöber, A. Fink, and E. Bohn, “Controlled growth of monodisperse silica spheres in the micron size range,” *Journal of Colloid and Interface Science*, vol. 26, pp. 62–69, Jan. 1968.

- [164] Z. Wu, H. Xiang, T. Kim, M.-S. Chun, and K. Lee, “Surface properties of sub-micrometer silica spheres modified with aminopropyltriethoxysilane and phenyltriethoxysilane,” *Journal of Colloid and Interface Science*, vol. 304, pp. 119–124, Dec. 2006.
- [165] L. M. Rossi, L. Shi, F. H. Quina, and Z. Rosenzweig, “Stöber synthesis of monodispersed luminescent silica nanoparticles for bioanalytical assays,” *Langmuir*, vol. 21, no. 10, pp. 4277–4280, 2005.
- [166] G. Canton, R. Riccò, F. Marinello, S. Carmignato, and F. Enrichi, “Modified Stöber synthesis of highly luminescent dye-doped silica nanoparticles,” *Journal of Nanoparticle Research*, vol. 13, pp. 4349–4356, May 2011.
- [167] Y. Takeda, Y. Komori, and H. Yoshitake, “Direct stöber synthesis of monodisperse silica particles functionalized with mercapto-, vinyl- and aminopropylsilanes in alcohol–water mixed solvents,” *Colloids and Surfaces A: Physicochemical and Engineering Aspects*, vol. 422, pp. 68–74, Apr. 2013.
- [168] I. I. Slowing, J. L. Vivero-Escoto, C.-W. Wu, and V. S. Y. Lin, “Mesoporous silica nanoparticles as controlled release drug delivery and gene transfection carriers,” *Advanced Drug Delivery Reviews*, vol. 60, pp. 1278–1288, Aug. 2008.
- [169] K. M. L. Taylor, J. S. Kim, W. J. Rieter, H. An, W. Lin, and W. Lin, “Mesoporous Silica Nanospheres as Highly Efficient MRI Contrast Agents,” *Journal of the American Chemical Society*, vol. 130, pp. 2154–2155, Feb. 2008.
- [170] C.-H. Lee, S.-H. Cheng, Y.-J. Wang, Y.-C. Chen, N.-T. Chen, J. Souris, C.-T. Chen, C.-Y. Mou, C.-S. Yang, and L.-W. Lo, “Near-infrared mesoporous silica nanoparticles for optical imaging: Characterization and in vivo biodistribution,” *Advanced Functional Materials*, vol. 19, no. 2, pp. 215–222, 2009.
- [171] J. Wang, S. Chu, F. Kong, L. Luo, Y. Wang, and Z. Zou, “Designing a smart fluorescence chemosensor within the tailored channel of mesoporous material for sensitively monitoring toxic heavy metal ions Pb(II),” *Sensors and Actuators B: Chemical*, vol. 150, pp. 25–35, Sept. 2010.
- [172] J. M. Rosenholm, C. Sahlgren, and M. Lindén, “Towards multifunctional, targeted drug delivery systems using mesoporous silica nanoparticles – opportunities and challenges,” *Nanoscale*, vol. 2, pp. 1870–1883, Oct. 2010.

- [173] A. Galarneau, H. Cambon, F. D. Renzo, R. Ryoo, M. Choi, and F. Fajula, “Micro-porosity and connections between pores in SBA-15 mesostructured silicas as a function of the temperature of synthesis,” *New Journal of Chemistry*, vol. 27, pp. 73–79, Jan. 2003.
- [174] P. I. Ravikovitch and A. V. Neimark, “Characterization of Micro- and Mesoporosity in SBA-15 Materials from Adsorption Data by the NLDFT Method,” *The Journal of Physical Chemistry B*, vol. 105, pp. 6817–6823, July 2001.
- [175] M. Ben Ezra, O. Penate-Medina, P. B. Zanzonico, D. Schaer, H. Ow, A. Burns, E. DeStanchina, V. Longo, E. Herz, S. Iyer, J. Wolchok, S. M. Larson, U. Wiesner, and M. S. Bradbury, “Multimodal silica nanoparticles are effective cancer-targeted probes in a model of human melanoma,” *The Journal of Clinical Investigation*, vol. 121, pp. 2768–2780, July 2011.
- [176] J. M. Rosenholm, A. Meinander, E. Peuhu, R. Niemi, J. E. Eriksson, C. Sahlgren, and M. Lindén, “Targeting of Porous Hybrid Silica Nanoparticles to Cancer Cells,” *ACS Nano*, vol. 3, pp. 197–206, Jan. 2009.
- [177] L. Pan, Q. He, J. Liu, Y. Chen, M. Ma, L. Zhang, and J. Shi, “Nuclear-Targeted Drug Delivery of TAT Peptide-Conjugated Monodisperse Mesoporous Silica Nanoparticles,” *Journal of the American Chemical Society*, vol. 134, pp. 5722–5725, Apr. 2012.
- [178] J. Turkevich, “Colloidal gold. Part I,” *Gold Bulletin*, vol. 18, pp. 86–91, Sept. 1985.
- [179] J. Turkevich, P. C. Stevenson, and J. Hillier, “A study of the nucleation and growth processes in the synthesis of colloidal gold,” *Discussions of the Faraday Society*, vol. 11, pp. 55–75, Jan. 1951.
- [180] P. Ghosh, G. Han, M. De, C. K. Kim, and V. M. Rotello, “Gold nanoparticles in delivery applications,” *Advanced Drug Delivery Reviews*, vol. 60, pp. 1307–1315, Aug. 2008.
- [181] E. E. Connor, J. Mwamuka, A. Gole, C. J. Murphy, and M. D. Wyatt, “Gold Nanoparticles Are Taken Up by Human Cells but Do Not Cause Acute Cytotoxicity,” *Small*, vol. 1, pp. 325–327, Mar. 2005.
- [182] B. D. Chithrani and W. C. W. Chan, “Elucidating the Mechanism of Cellular Uptake and Removal of Protein-Coated Gold Nanoparticles of Different Sizes and Shapes,” *Nano Letters*, vol. 7, pp. 1542–1550, June 2007.

- [183] E. Dulkeith, M. Ringler, T. A. Klar, J. Feldmann, A. Muñoz Javier, and W. J. Parak, “Gold Nanoparticles Quench Fluorescence by Phase Induced Radiative Rate Suppression,” *Nano Letters*, vol. 5, pp. 585–589, Apr. 2005.
- [184] T. L. Jennings, M. P. Singh, and G. F. Strouse, “Fluorescent Lifetime Quenching near $d = 1.5$ nm Gold Nanoparticles: Probing NSET Validity,” *Journal of the American Chemical Society*, vol. 128, pp. 5462–5467, Apr. 2006.
- [185] C. M. Goodman, C. D. McCusker, T. Yilmaz, and V. M. Rotello, “Toxicity of Gold Nanoparticles Functionalized with Cationic and Anionic Side Chains,” *Bioconjugate Chemistry*, vol. 15, pp. 897–900, July 2004.
- [186] Y. Pan, S. Neuss, A. Leifert, M. Fischler, F. Wen, U. Simon, G. Schmid, W. Brandau, and W. Jahnens-Decent, “Size-Dependent Cytotoxicity of Gold Nanoparticles,” *Small*, vol. 3, pp. 1941–1949, Nov. 2007.
- [187] Y. Cheng, A. C. Samia, J. D. Meyers, I. Panagopoulos, B. Fei, and C. Burda, “Highly Efficient Drug Delivery with Gold Nanoparticle Vectors for in Vivo Photodynamic Therapy of Cancer,” *Journal of the American Chemical Society*, vol. 130, pp. 10643–10647, Aug. 2008.
- [188] G. Han, P. Ghosh, and V. M. Rotello, “Functionalized gold nanoparticles for drug delivery,” *Nanomedicine*, vol. 2, pp. 113–123, Feb. 2007.
- [189] I. H. El-Sayed, X. Huang, and M. A. El-Sayed, “Selective laser photo-thermal therapy of epithelial carcinoma using anti-EGFR antibody conjugated gold nanoparticles,” *Cancer Letters*, vol. 239, pp. 129–135, July 2006.
- [190] X. Huang, P. K. Jain, I. H. El-Sayed, and M. A. El-Sayed, “Plasmonic photothermal therapy (pptt) using gold nanoparticles,” *Lasers in medical science*, vol. 23, no. 3, pp. 217–228, 2008.
- [191] S. M. Janib, A. S. Moses, and J. A. MacKay, “Imaging and drug delivery using theranostic nanoparticles,” *Advanced Drug Delivery Reviews*, vol. 62, pp. 1052–1063, Aug. 2010.
- [192] D. N. Heo, D. H. Yang, H.-J. Moon, J. B. Lee, M. S. Bae, S. C. Lee, W. J. Lee, I.-C. Sun, and I. K. Kwon, “Gold nanoparticles surface-functionalized with paclitaxel drug and biotin receptor as theranostic agents for cancer therapy,” *Biomaterials*, vol. 33, pp. 856–866, Jan. 2012.

- [193] R. Goel, N. Shah, R. Visaria, G. F. Paciotti, and J. C. Bischof, “Biodistribution of TNF- α -coated gold nanoparticles in an in vivo model system,” *Nanomedicine*, vol. 4, pp. 401–410, June 2009.
- [194] D. R. McCormack, K. Bhattacharyya, R. Kannan, K. Katti, and J. A. Viator, “Enhanced photoacoustic detection of melanoma cells using gold nanoparticles,” *Lasers in Surgery and Medicine*, vol. 43, pp. 333–338, Apr. 2011.
- [195] Y. Song, X. Xu, K. W. MacRenaris, X.-Q. Zhang, C. A. Mirkin, and T. J. Meade, “Multimodal Gadolinium-Enriched DNA–Gold Nanoparticle Conjugates for Cellular Imaging,” *Angewandte Chemie International Edition*, vol. 48, pp. 9143–9147, Nov. 2009.
- [196] A. Irure, M. Marradi, B. Arnáiz, N. Genicio, D. Padro, and S. Penadés, “Sugar/gadolinium-loaded gold nanoparticles for labelling and imaging cells by magnetic resonance imaging,” *Biomaterials Science*, vol. 1, pp. 658–668, May 2013.
- [197] J. S. Gebauer, M. Malissek, S. Simon, S. K. Knauer, M. Maskos, R. H. Stauber, W. Peukert, and L. Treuel, “Impact of the Nanoparticle–Protein Corona on Colloidal Stability and Protein Structure,” *Langmuir*, vol. 28, pp. 9673–9679, June 2012.
- [198] D. Napierska, L. C. J. Thomassen, V. Rabolli, D. Lison, L. Gonzalez, M. Kirsch-Volders, J. A. Martens, and P. H. Hoet, “Size-Dependent Cytotoxicity of Monodisperse Silica Nanoparticles in Human Endothelial Cells,” *Small*, vol. 5, pp. 846–853, Apr. 2009.
- [199] F. Lu, S.-H. Wu, Y. Hung, and C.-Y. Mou, “Size Effect on Cell Uptake in Well-Suspended, Uniform Mesoporous Silica Nanoparticles,” *Small*, vol. 5, pp. 1408–1413, June 2009.
- [200] W.-C. Sun, K. R. Gee, and R. P. Haugland, “Synthesis of novel fluorinated coumarins: Excellent UV-light excitable fluorescent dyes,” *Bioorganic and Medicinal Chemistry Letters*, vol. 8, pp. 3107–3110, Nov. 1998.
- [201] L. F. Mottram, S. Boonyarattanakalin, R. E. Kovel, and B. R. Peterson, “The Pennsylvania Green Fluorophore: A Hybrid of Oregon Green and Tokyo Green for the Construction of Hydrophobic and pH-Insensitive Molecular Probes,” *Organic Letters*, vol. 8, pp. 581–584, Feb. 2006.

- [202] G. Ulrich, R. Ziessel, and A. Harriman, “The Chemistry of Fluorescent Bodipy Dyes: Versatility Unsurpassed,” *Angewandte Chemie International Edition*, vol. 47, pp. 1184–1201, Feb. 2008.
- [203] R. Ziessel, G. Ulrich, and A. Harriman, “The chemistry of Bodipy: A new El Dorado for fluorescence tools,” *New Journal of Chemistry*, vol. 31, pp. 496–501, Apr. 2007.
- [204] M. Srinivas, M. S. Turner, J. M. Janjic, P. A. Morel, D. H. Laidlaw, and E. T. Ahrens, “In vivo cytometry of antigen-specific t cells using 19f MRI,” *Magnetic Resonance in Medicine*, vol. 62, no. 3, pp. 747–753, 2009.
- [205] S. D. Caruthers, A. M. Neubauer, F. D. Hockett, R. Lamerichs, P. M. Winter, M. J. Scott, P. J. Gaffney, S. A. Wickline, and G. M. Lanza, “In Vitro Demonstration Using 19f Magnetic Resonance to Augment Molecular Imaging With Paramagnetic Perfluorocarbon Nanoparticles at 1.5 Tesla:,” *Investigative Radiology*, vol. 41, pp. 305–312, Mar. 2006.
- [206] W. G. Schreiber, B. Eberle, S. Laukemper-Ostendorf, K. Markstaller, N. Weiler, A. Scholz, K. Bürger, C. P. Heussel, M. Thelen, and H.-U. Kauczor, “Dynamic 19f-MRI of pulmonary ventilation using sulfur hexafluoride (SF6) gas,” *Magnetic Resonance in Medicine*, vol. 45, pp. 605–613, Apr. 2001.
- [207] S. Laukemper-Ostendorf, A. Scholz, K. Bürger, C. P. Heussel, M. Schmittner, N. Weiler, K. Markstaller, B. Eberle, H.-U. Kauczor, M. Quintel, M. Thelen, and W. G. Schreiber, “19f-MRI of perflubron for measurement of oxygen partial pressure in porcine lungs during partial liquid ventilation,” *Magnetic Resonance in Medicine*, vol. 47, pp. 82–89, Jan. 2002.
- [208] G. N. Holland, P. A. Bottomley, and W. S. Hinshaw, “19f magnetic resonance imaging,” *Journal of Magnetic Resonance (1969)*, vol. 28, pp. 133–136, Oct. 1977.
- [209] M. E. Henry, M. E. Schmidt, J. Hennen, R. A. Villafuerte, M. L. Butman, P. Tran, L. T. Kerner, B. Cohen, and P. F. Renshaw, “A comparison of brain and serum pharmacokinetics of r-fluoxetine and racemic fluoxetine: A 19-f MRS study,” *Neuropharmacology*, vol. 30, pp. 1576–1583, May 2005.
- [210] N. R. Bolo, Y. Hodé, and J.-P. Macher, “Long-term sequestration of fluorinated compounds in tissues after fluvoxamine or fluoxetine treatment: a fluorine magnetic resonance spectroscopy study in vivo,” *Magnetic Resonance Materials in Physics, Biology and Medicine*, vol. 16, pp. 268–276, Mar. 2004.

- [211] E. T. Ahrens, R. Flores, H. Xu, and P. A. Morel, “In vivo imaging platform for tracking immunotherapeutic cells,” *Nature Biotechnology*, vol. 23, pp. 983–987, Aug. 2005.
- [212] J. D. Christensen, S. M. Babb, B. M. Cohen, and P. F. Renshaw, “Quantitation of dfenfluramine/d-norfenfluramine concentration in primate brain using ^{19}F NMR spectroscopy,” *Magnetic Resonance in Medicine*, vol. 39, pp. 149–154, Jan. 1998.
- [213] R. Nyffenegger, C. Quellet, and J. Ricka, “Synthesis of fluorescent, monodisperse, colloidal silica particles,” *Journal of Colloid and Interface Science*, vol. 159, pp. 150–157, Aug. 1993.
- [214] A. Van Blaaderen and A. Vrij, “Synthesis and characterization of colloidal dispersions of fluorescent, monodisperse silica spheres,” *Langmuir*, vol. 8, no. 12, pp. 2921–2931, 1992.
- [215] N. Shanker and S. L. Bane, “Basic aspects of absorption and fluorescence spectroscopy and resonance energy transfer methods,” *Methods in Cell Biology*, vol. 84, pp. 213–242, 2008.
- [216] B. Quan, K. Choi, Y.-H. Kim, K. W. Kang, and D. S. Chung, “Near infrared dye indocyanine green doped silica nanoparticles for biological imaging,” *Talanta*, vol. 99, pp. 387–393, Sept. 2012.
- [217] X. Gao, J. He, L. Deng, and H. Cao, “Synthesis and characterization of functionalized rhodamine b-doped silica nanoparticles,” *Optical Materials*, vol. 31, pp. 1715–1719, Sept. 2009.
- [218] D. R. Larson, H. Ow, H. D. Vishwasrao, A. A. Heikal, U. Wiesner, and W. W. Webb, “Silica Nanoparticle Architecture Determines Radiative Properties of Encapsulated Fluorophores,” *Chemistry of Materials*, vol. 20, pp. 2677–2684, Apr. 2008.
- [219] H. Wang, J. Fang, T. Cheng, J. Ding, L. Qu, L. Dai, X. Wang, and T. Lin, “One-step coating of fluoro-containing silica nanoparticles for universal generation of surface superhydrophobicity,” *Chemical Communications*, pp. 877–879, Feb. 2008.
- [220] A. Kumar, “Use of dyes in ophthalmology,” *Journal of Clinical Ophthalmology and Research*, vol. 1, no. 1, pp. 55–58, 2013.

- [221] I. A. Rahman, M. Jafarzadeh, and C. S. Sipaut, “Synthesis of organo-functionalized nanosilica via a co-condensation modification using γ -aminopropyltriethoxysilane (APTES),” *Ceramics International*, vol. 35, July 2009.
- [222] R. Pecora, “Dynamic Light Scattering Measurement of Nanometer Particles in Liquids,” *Journal of Nanoparticle Research*, vol. 2, pp. 123–131, June 2000.
- [223] H. Shi, X. He, K. Wang, Y. Yuan, K. Deng, J. Chen, and W. Tan, “Rhodamine b isothiocyanate doped silica-coated fluorescent nanoparticles (RBTC-DSFNPs)-based bioprobes conjugated to annexin v for apoptosis detection and imaging,” *Nanomedicine: Nanotechnology, Biology and Medicine*, vol. 3, pp. 266–272, Dec. 2007.
- [224] R. Kumar, I. Roy, T. Y. Ohulchanskky, L. A. Vathy, E. J. Bergey, M. Sajjad, and P. N. Prasad, “In vivo biodistribution and clearance studies using multimodal organically modified silica nanoparticles,” *ACS Nano*, vol. 4, no. 2, pp. 699–708, 2010.
- [225] Y. Wang, Y. Wang, and B. Liu, “Fluorescent detection of ATP based on signaling DNA aptamer attached silica nanoparticles,” *Nanotechnology*, vol. 19, p. 415605, Oct. 2008.
- [226] E. Izak-Nau, M. Voetz, S. Eiden, A. Duschl, and V. F. Puntes, “Altered characteristics of silica nanoparticles in bovine and human serum: the importance of nanomaterial characterization prior to its toxicological evaluation,” *Particle and Fibre Toxicology*, vol. 10, pp. 1–12, Nov. 2013.
- [227] I. Lynch and K. A. Dawson, “Protein-nanoparticle interactions,” *Nano Today*, vol. 3, pp. 40–47, Feb. 2008.
- [228] A. A. Golub, A. I. Zubenko, and B. V. Zhmud, “\gamma-APTES modified silica gels: The structure of the surface layer,” *Journal of Colloid and Interface Science*, vol. 179, pp. 482–487, May 1996.
- [229] F. J. d. Sousa, G. P. A. d. Lima, L. R. Ávila, K. J. Ciuffi, P. S. Calefi, and E. J. Nas-sar, “Incorporation of europium III complex into nanoparticles and films obtained by the Sol-Gel methodology,” *Materials Research*, vol. 13, pp. 71–75, Mar. 2010.
- [230] X.-J. Wu, Y. Wang, W. Yang, B.-H. Xie, M.-B. Yang, and W. Dan, “A rheological study on temperature dependent microstructural changes of fumed silica gels in dodecane,” *Soft Matter*, vol. 8, pp. 10457–10463, Sept. 2012.

- [231] N. Klonis and W. H. Sawyer, “Spectral properties of the prototropic forms of fluorescein in aqueous solution,” *Journal of Fluorescence*, vol. 6, pp. 147–157, Sept. 1996.
- [232] D. Magde, G. E. Rojas, and P. G. Seybold, “Solvent Dependence of the Fluorescence Lifetimes of Xanthene Dyes,” *Photochemistry and Photobiology*, vol. 70, pp. 737–744, Nov. 1999.
- [233] H. Elmgren, “The fluorescence lifetime of free and conjugated fluorescein in various environments,” *Journal of Polymer Science: Polymer Letters Edition*, vol. 18, no. 12, pp. 815–822, 1980.
- [234] L. Wang, Y. Shao, J. Zhang, and M. Anpo, “Study on the fluorescence properties of fluorescein dye incorporated into SBA-15,” *Optical Materials*, vol. 28, pp. 1232–1234, July 2006.
- [235] A. Imhof, M. Megens, J. J. Engelberts, D. T. N. de Lang, R. Sprik, and W. L. Vos, “Spectroscopy of Fluorescein (FITC) Dyed Colloidal Silica Spheres,” *The Journal of Physical Chemistry B*, vol. 103, pp. 1408–1415, Mar. 1999.
- [236] W. J. Rieter, J. S. Kim, K. M. L. Taylor, H. An, W. Lin, T. Tarrant, and W. Lin, “Hybrid Silica Nanoparticles for Multimodal Imaging,” *Angewandte Chemie International Edition*, vol. 46, pp. 3680–3682, May 2007.
- [237] J. S. Ananta, B. Godin, R. Sethi, L. Moriggi, X. Liu, R. E. Serda, R. Krishnamurthy, R. Muthupillai, R. D. Bolkar, L. Helm, M. Ferrari, L. J. Wilson, and P. Decuzzi, “Geometrical confinement of gadolinium-based contrast agents in nanoporous particles enhances T1 contrast,” *Nature Nanotechnology*, vol. 5, pp. 815–821, Nov. 2010.
- [238] M. Mooney, “The viscosity of a concentrated suspension of spherical particles,” *Journal of Colloid Science*, vol. 6, pp. 162–170, Apr. 1951.
- [239] S. Santra, P. Zhang, K. Wang, R. Tapec, and W. Tan, “Conjugation of Biomolecules with Luminophore-Doped Silica Nanoparticles for Photostable Biomarkers,” *Analytical Chemistry*, vol. 73, pp. 4988–4993, Oct. 2001.
- [240] T. Yu, A. Malugin, and H. Ghandehari, “Impact of Silica Nanoparticle Design on Cellular Toxicity and Hemolytic Activity,” *ACS Nano*, vol. 5, pp. 5717–5728, July 2011.

- [241] D. Zhang, Z. Wu, J. Xu, J. Liang, J. Li, and W. Yang, “Tuning the emission properties of ru(phen)₃²⁺ doped silica nanoparticles by changing the addition time of the dye during the stöber process,” *Langmuir*, vol. 26, no. 9, pp. 6657–6662, 2010.
- [242] D. J. Lewis, T. M. Day, J. V. MacPherson, and Z. Pikramenou, “Luminescent nanobeads: attachment of surface reactive Eu(III) complexes to gold nanoparticles,” *Chemical Communications*, pp. 1433–1435, Mar. 2006.
- [243] R. B. P. Elmes, K. N. Orange, S. M. Cloonan, D. C. Williams, and T. Gunnlaugsson, “Luminescent Ruthenium(II) Polypyridyl Functionalized Gold Nanoparticles; Their DNA Binding Abilities and Application As Cellular Imaging Agents,” *Journal of the American Chemical Society*, vol. 133, pp. 15862–15865, Oct. 2011.
- [244] C. Alric, J. Taleb, G. L. Duc, C. Mandon, C. Billotey, A. L. Meur-Herland, T. Brochard, F. Vocanson, M. Janier, P. Perriat, S. Roux, and O. Tillement, “Gadolinium Chelate Coated Gold Nanoparticles As Contrast Agents for Both X-ray Computed Tomography and Magnetic Resonance Imaging,” *Journal of the American Chemical Society*, vol. 130, pp. 5908–5915, May 2008.
- [245] L. Moriggi, C. Cannizzo, E. Dumas, C. R. Mayer, A. Ulianov, and L. Helm, “Gold Nanoparticles Functionalized with Gadolinium Chelates as High-Relaxivity MRI Contrast Agents,” *Journal of the American Chemical Society*, vol. 131, pp. 10828–10829, Aug. 2009.
- [246] J. Kimling, M. Maier, B. Okenve, V. Kotaidis, H. Ballot, and A. Plech, “Turkevich Method for Gold Nanoparticle Synthesis Revisited,” *The Journal of Physical Chemistry B*, vol. 110, pp. 15700–15707, Aug. 2006.
- [247] M. Brust, M. Walker, D. Bethell, D. J. Schiffrin, and R. Whyman, “Synthesis of thiol-derivatised gold nanoparticles in a two-phase Liquid-Liquid system,” *Journal of the Chemical Society, Chemical Communications*, no. 7, p. 801, 1994.
- [248] M. N. Martin, J. I. Basham, P. Chando, and S.-K. Eah, “Charged Gold Nanoparticles in Non-Polar Solvents: 10-min Synthesis and 2d Self-Assembly,” *Langmuir*, vol. 26, pp. 7410–7417, May 2010.
- [249] A. Guerrero-Martínez, J. Pérez-Juste, and L. M. Liz-Marzán, “Recent Progress on Silica Coating of Nanoparticles and Related Nanomaterials,” *Advanced Materials*, vol. 22, pp. 1182–1195, Mar. 2010.

- [250] E. Mine, A. Yamada, Y. Kobayashi, M. Konno, and L. M. Liz-Marzán, “Direct coating of gold nanoparticles with silica by a seeded polymerization technique,” *Journal of Colloid and Interface Science*, vol. 264, pp. 385–390, Aug. 2003.
- [251] K. Tanaka, A. Narita, N. Kitamura, W. Uchiyama, M. Morita, T. Inubushi, and Y. Chujo, “Preparation for Highly Sensitive MRI Contrast Agents Using Core/Shell Type Nanoparticles Consisting of Multiple SPIO Cores with Thin Silica Coating,” *Langmuir*, vol. 26, pp. 11759–11762, July 2010.
- [252] D. Gerion, F. Pinaud, S. C. Williams, W. J. Parak, D. Zanchet, S. Weiss, and A. P. Alivisatos, “Synthesis and Properties of Biocompatible Water-Soluble Silica-Coated CdSe/ZnS Semiconductor Quantum Dots†,” *The Journal of Physical Chemistry B*, vol. 105, pp. 8861–8871, Sept. 2001.
- [253] S. T. Selvan, P. K. Patra, C. Y. Ang, and J. Y. Ying, “Synthesis of Silica-Coated Semiconductor and Magnetic Quantum Dots and Their Use in the Imaging of Live Cells,” *Angewandte Chemie*, vol. 119, pp. 2500–2504, Mar. 2007.
- [254] S. Santra, R. P. Bagwe, D. Dutta, J. T. Stanley, G. A. Walter, W. Tan, B. M. Moudgil, and R. A. Mericle, “Synthesis and Characterization of Fluorescent, Radio-Opaque, and Paramagnetic Silica Nanoparticles for Multimodal Bioimaging Applications,” *Advanced Materials*, vol. 17, pp. 2165–2169, Sept. 2005.
- [255] L. Kong, E. Mume, G. Triani, and S. V. Smith, “Optimizing Radiolabeling Amine-Functionalized Silica Nanoparticles Using SarAr-NCS for Applications in Imaging and Radiotherapy,” *Langmuir*, vol. 29, pp. 5609–5616, May 2013.
- [256] K. D. Hartlen, A. P. T. Athanasopoulos, and V. Kitaev, “Facile Preparation of Highly Monodisperse Small Silica Spheres (15 to >200 nm) Suitable for Colloidal Templating and Formation of Ordered Arrays,” *Langmuir*, vol. 24, pp. 1714–1720, Mar. 2008.
- [257] H. Yamauchi, T. Ishikawa, and S. Kondo, “Surface characterization of ultramicro spherical particles of silica prepared by w/o microemulsion method,” *Colloids and Surfaces*, vol. 37, pp. 71–80, 1989.
- [258] F. J. Arriagada and K. Osseo-Asare, “Synthesis of Nanosize Silica in Aerosol OT Reverse Microemulsions,” *Journal of Colloid and Interface Science*, vol. 170, pp. 8–17, Mar. 1995.

- [259] R. P. Bagwe, C. Yang, L. R. Hilliard, and W. Tan, “Optimization of Dye-Doped Silica Nanoparticles Prepared Using a Reverse Microemulsion Method,” *Langmuir*, vol. 20, pp. 8336–8342, Sept. 2004.
- [260] T. Sato, “Volatilization behaviour of ruthenium from boiling nitric acid,” *Journal of Radioanalytical and Nuclear Chemistry*, vol. 129, Jan. 1989.
- [261] Z. Pikramenou and N. Rogers, “Coated nanoparticles,” July 2014. US20140212497 A1.
- [262] K. K.-W. Lo, J. S.-W. Chan, C.-K. Chung, V. W.-H. Tsang, and N. Zhu, “Synthesis, photophysical and electrochemical properties, and biological labelling studies of luminescent cyclometallated iridium(III) bipyridine–aldehyde complexes,” *Inorganica Chimica Acta*, vol. 357, pp. 3109–3118, July 2004.
- [263] D. J. Lewis, V. Dore, N. J. Rogers, T. K. Mole, G. B. Nash, P. Angeli, and Z. Pikramenou, “Silica Nanoparticles for Micro-Particle Imaging Velocimetry: Fluorosurfactant Improves Nanoparticle Stability and Brightness of Immobilized Iridium(III) Complexes,” *Langmuir*, vol. 29, pp. 14701–14708, Nov. 2013.
- [264] S. J. Adams, D. J. Lewis, J. A. Preece, and Z. Pikramenou, “Luminescent Gold Surfaces for Sensing and Imaging: Patterning of Transition Metal Probes,” *ACS Applied Materials and Interfaces*, vol. 6, pp. 11598–11608, July 2014.
- [265] D. C. Peters, “A comparison of mercury arc lamp and laser illumination for flow cytometers.,” *Journal of Histochemistry and Cytochemistry*, vol. 27, pp. 241–245, Jan. 1979.
- [266] B. L. Diffey, “Sources and measurement of ultraviolet radiation,” *Methods*, vol. 28, pp. 4–13, Sept. 2002.
- [267] C. Kielbassa, L. Roza, and B. Epe, “Wavelength dependence of oxidative DNA damage induced by UV and visible light.,” *Carcinogenesis*, vol. 18, pp. 811–816, Apr. 1997.
- [268] N. Fatin-Rouge, E. Tóth, R. Meuli, and J.-C. G. Bünzli, “Enhanced imaging properties of a GdIII complex with unusually large relaxivity,” *Journal of Alloys and Compounds*, vol. 374, pp. 298–302, July 2004.

- [269] Y.-S. Lin, Y. Hung, J.-K. Su, R. Lee, C. Chang, M.-L. Lin, and C.-Y. Mou, “Gadolinium(III)-Incorporated Nanosized Mesoporous Silica as Potential Magnetic Resonance Imaging Contrast Agents,” *The Journal of Physical Chemistry B*, vol. 108, pp. 15608–15611, Oct. 2004.
- [270] I. Canton and G. Battaglia, “Endocytosis at the nanoscale,” *Chemical Society Reviews*, vol. 41, pp. 2718–2739, Mar. 2012.
- [271] J. Chen and P. R. Selvin, “Synthesis of 7-amino-4-trifluoromethyl-2-(1h)-quinolinone and its use as an antenna molecule for luminescent europium polyaminocarboxylates chelates,” *Journal of Photochemistry and Photobiology A: Chemistry*, vol. 135, pp. 27–32, June 2000.
- [272] S. Mizukami, R. Takikawa, F. Sugihara, M. Shirakawa, and K. Kikuchi, “Dual-Function Probe to Detect Protease Activity for Fluorescence Measurement and ¹⁹F MRI,” *Angewandte Chemie*, vol. 121, pp. 3695–3697, May 2009.
- [273] B. Annabi, M.-P. Lachambre, K. Plouffe, R. Moumdjian, and R. Bélineau, “Propranolol adrenergic blockade inhibits human brain endothelial cells tubulogenesis and matrix metalloproteinase-9 secretion,” *Pharmacological Research*, vol. 60, pp. 438–445, Nov. 2009.
- [274] N. S. Nagaraj, K. R. Anilakumar, and O. V. Singh, “Diallyl disulfide causes caspase-dependent apoptosis in human cancer cells through a Bax-triggered mitochondrial pathway,” *The Journal of Nutritional Biochemistry*, vol. 21, pp. 405–412, May 2010.
- [275] M. Ito, A. Shibata, J. Zhang, M. Hiroshima, Y. Sako, Y. Nakano, K. Kojima-Aikawa, B. Mannervik, S. Shuto, Y. Ito, R. Morgenstern, and H. Abe, “Universal Caging Group for the in-Cell Detection of Glutathione Transferase Applied to ¹⁹F NMR and Bioluminogenic Probes,” *ChemBioChem*, vol. 13, pp. 1428–1432, July 2012.
- [276] M. Oishi, S. Sumitani, and Y. Nagasaki, “On-Off Regulation of ¹⁹F Magnetic Resonance Signals Based on pH-Sensitive PEGylated Nanogels for Potential Tumor-Specific Smart ¹⁹F MRI Probes,” *Bioconjugate Chemistry*, vol. 18, pp. 1379–1382, Sept. 2007.
- [277] F. Schmid, C. Höltke, D. Parker, and C. Faber, “Boosting ¹⁹F MRI—SNR efficient detection of paramagnetic contrast agents using ultrafast sequences,” *Magnetic Resonance in Medicine*, vol. 69, pp. 1056–1062, Apr. 2013.

- [278] J. E. Lee, N. Lee, T. Kim, J. Kim, and T. Hyeon, “Multifunctional Mesoporous Silica Nanocomposite Nanoparticles for Theranostic Applications,” *Accounts of Chemical Research*, vol. 44, pp. 893–902, Oct. 2011.
- [279] M. B. Kok, A. de Vries, D. Abdurrachim, J. J. Prompers, H. Grüll, K. Nicolay, and G. J. Strijkers, “Quantitative 1h MRI, 19f MRI, and 19f MRS of cell-internalized perfluorocarbon paramagnetic nanoparticles,” *Contrast Media and Molecular Imaging*, vol. 6, pp. 19–27, Jan. 2011.
- [280] A. Radu, C. Eleonora, A. Lucian, C. Georgeta, V. Virginia, and T. Cristiana, “In vitro biocompatibility testing of implantable biomaterials,” *Roumanian Biotechnological Letters*, vol. 13, no. 4, pp. 3863–72, 2008.
- [281] L. L. Hench and J. Wilson, “Biocompatibility of silicates for medical use,” in *Silicon Biochemistry*, pp. 231–246, John Wiley New York, USA, 1986.
- [282] X. Wang, H. Chen, Y. Chen, M. Ma, K. Zhang, F. Li, Y. Zheng, D. Zeng, Q. Wang, and J. Shi, “Perfluorohexane-Encapsulated Mesoporous Silica Nanocapsules as Enhancement Agents for Highly Efficient High Intensity Focused Ultrasound (HIFU),” *Advanced Materials*, vol. 24, pp. 785–791, Feb. 2012.
- [283] J. Yang, J. U. Lind, and W. C. Trogler, “Synthesis of Hollow Silica and Titania Nanospheres,” *Chemistry of Materials*, vol. 20, pp. 2875–2877, May 2008.
- [284] T. Zhang, J. Ge, Y. Hu, Q. Zhang, S. Aloni, and Y. Yin, “Formation of Hollow Silica Colloids through a Spontaneous Dissolution–Regrowth Process,” *Angewandte Chemie*, vol. 120, pp. 5890–5895, July 2008.
- [285] J. Yang, J. Lee, J. Kang, K. Lee, J.-S. Suh, H.-G. Yoon, Y.-M. Huh, and S. Haam, “Hollow Silica Nanocontainers as Drug Delivery Vehicles,” *Langmuir*, vol. 24, pp. 3417–3421, Apr. 2008.
- [286] Y. Lu, J. McLellan, and Y. Xia, “Synthesis and Crystallization of Hybrid Spherical Colloids Composed of Polystyrene Cores and Silica Shells,” *Langmuir*, vol. 20, pp. 3464–3470, Apr. 2004.
- [287] M. Fuji, T. Shin, H. Watanabe, and T. Takei, “Shape-controlled hollow silica nanoparticles synthesized by an inorganic particle template method,” *Advanced Powder Technology*, vol. 23, pp. 562–565, Sept. 2012.

- [288] Y. Zhu, Y. Fang, L. Borchardt, and S. Kaskel, “PEGylated hollow mesoporous silica nanoparticles as potential drug delivery vehicles,” *Microporous and Mesoporous Materials*, vol. 141, pp. 199–206, May 2011.
- [289] J. J. L. M. Cornelissen, E. F. Connor, H.-C. Kim, V. Y. Lee, T. Magibitang, P. M. Rice, W. Volksen, L. K. Sundberg, and R. D. Miller, “Versatile synthesis of nanometer sized hollow silica spheres,” *Chemical Communications*, pp. 1010–1011, Apr. 2003.
- [290] M. Chen, L. Wu, S. Zhou, and B. You, “A Method for the Fabrication of Monodisperse Hollow Silica Spheres,” *Advanced Materials*, vol. 18, pp. 801–806, Mar. 2006.
- [291] E. Rampazzo, F. Boschi, S. Bonacchi, R. Juris, M. Montalti, N. Zaccheroni, L. Prodi, L. Calderan, B. Rossi, S. Becchi, and A. Sbarbati, “Multicolor core/shell silicananoparticles for in vivo and ex vivo imaging,” *Nanoscale*, vol. 4, no. 3, pp. 824–830, 2012.
- [292] Y. Chen, C. Chu, Y. Zhou, Y. Ru, H. Chen, F. Chen, Q. He, Y. Zhang, L. Zhang, and J. Shi, “Reversible Pore-Structure Evolution in Hollow Silica Nanocapsules: Large Pores for siRNA Delivery and Nanoparticle Collecting,” *Small*, vol. 7, pp. 2935–2944, Oct. 2011.
- [293] C. A. R. Costa, C. A. P. Leite, and F. Galembeck, “Size Dependence of Stöber Silica Nanoparticle Microchemistry,” *The Journal of Physical Chemistry B*, vol. 107, pp. 4747–4755, May 2003.
- [294] T. Nakamura, H. Matsushita, F. Sugihara, Y. Yoshioka, S. Mizukami, and K. Kikuchi, “Activatable 19f MRI Nanoparticle Probes for the Detection of Reducing Environments,” *Angewandte Chemie International Edition*, vol. 54, pp. 1007–1010, Jan. 2015.
- [295] T. Pham, J. B. Jackson, N. J. Halas, and T. R. Lee, “Preparation and Characterization of Gold Nanoshells Coated with Self-Assembled Monolayers,” *Langmuir*, vol. 18, pp. 4915–4920, June 2002.
- [296] M. S. Fleming and D. R. Walt, “Stability and Exchange Studies of Alkanethiol Monolayers on Gold-Nanoparticle-Coated Silica Microspheres,” *Langmuir*, vol. 17, pp. 4836–4843, Aug. 2001.
- [297] X. Xia, Y. Liu, V. Backman, and G. A. Ameer, “Engineering sub-100 nm multi-layer nanoshells,” *Nanotechnology*, vol. 17, p. 5435, Nov. 2006.

- [298] John E. Bonevich and W. K. Haller, “Measuring the Size of Nanoparticles Using Transmission Electron Microscopy (TEM),” *NIST - NCL Joint Assay Protocol*, vol. PCC-7, Mar. 2010.
- [299] T.-C. Chen and K.-L. Chung, “An Efficient Randomized Algorithm for Detecting Circles,” *Computer Vision and Image Understanding*, vol. 83, pp. 172–191, Aug. 2001.
- [300] G. S. Robinson, “Edge detection by compass gradient masks,” *Computer Graphics and Image Processing*, vol. 6, pp. 492–501, Oct. 1977.
- [301] N. Otsu, “A threshold selection method from gray-level histograms,” *IEEE Transactions on Systems, Man and Cybernetics*, vol. 9, pp. 62–66, Jan. 1979.
- [302] M. A. Goldberg, P. F. Hahn, S. Saini, M. S. Cohen, P. Reimer, T. J. Brady, and P. R. Mueller, “Value of T1 and T2 relaxation times from echoplanar MR imaging in the characterization of focal hepatic lesions.,” *American Journal of Roentgenology*, vol. 160, pp. 1011–1017, May 1993.
- [303] T. S. Ahearn, R. T. Staff, T. W. Redpath, and S. I. K. Semple, “The use of the Levenberg–Marquardt curve-fitting algorithm in pharmacokinetic modelling of DCE-MRI data,” *Physics in Medicine and Biology*, vol. 50, p. N85, May 2005.
- [304] D. M. Higgins, J. P. Ridgway, A. Radjenovic, U. M. Sivananthan, and M. A. Smith, “T1 measurement using a short acquisition period for quantitative cardiac applications,” *Medical Physics*, vol. 32, pp. 1738–1746, June 2005.
- [305] D. L. Buckley, R. W. Kerslake, S. J. Blackband, and A. Horsman, “Quantitative analysis of multi-slice Gd-DTPA enhanced dynamic MR images using an automated simplex minimization procedure,” *Magnetic Resonance in Medicine*, vol. 32, pp. 646–651, Nov. 1994.
- [306] J. Lagarias, J. Reeds, M. Wright, and P. Wright, “Convergence Properties of the Nelder–Mead Simplex Method in Low Dimensions,” *SIAM Journal on Optimization*, vol. 9, pp. 112–147, Jan. 1998.
- [307] M. Stjerndahl, M. Andersson, H. E. Hall, D. M. Pajerowski, M. W. Meisel, and R. S. Duran, “Superparamagnetic Fe₃O₄/SiO₂ Nanocomposites: Enabling the Tuning of Both the Iron Oxide Load and the Size of the Nanoparticles,” *Langmuir*, vol. 24, pp. 3532–3536, Apr. 2008.

- [308] A. Gole, N. Agarwal, P. Nagaria, M. D. Wyatt, and C. J. Murphy, “One-pot synthesis of silica-coated magnetic plasmonic tracer nanoparticles,” *Chemical Communications*, no. 46, p. 6140, 2008.
- [309] Y.-S. Lin, S.-H. Wu, C.-T. Tseng, Y. Hung, C. Chang, and C.-Y. Mou, “Synthesis of hollow silica nanospheres with a microemulsion as the template,” *Chemical Communications*, pp. 3542–3544, June 2009.
- [310] Y. Chen, H. Chen, L. Guo, Q. He, F. Chen, J. Zhou, J. Feng, and J. Shi, “Hollow/Rattle-Type Mesoporous Nanostructures by a Structural Difference-Based Selective Etching Strategy,” *ACS Nano*, vol. 4, pp. 529–539, Jan. 2010.